GEOCHEMICAL AND MINERALOGICAL CHARACTERIZATION OF THE ARBUCKLE AQUIFER: STUDYING MINERAL REACTIONS AND ITS IMPLICATIONS FOR CO_2 SEQUESTRATION

by

ROBINSON BARKER

B.S., Georgia College and State University, 2008

A THESIS

submitted in partial fulfillment of the requirements for the degree

MASTER OF SCIENCE

Department of Geology
College of Arts and Sciences

KANSAS STATE UNIVERSITY
Manhattan, Kansas

2012

Approved by:

Major Professor
Saugata Datta

Abstract

In response to increasing concerns over release of anthropogenic greenhouse gases the Arbuckle saline aquifer in south-central Kansas has been proposed as a potential site for geologic storage for CO_2. Two wells (KGS 1-32 and 1-28) have been drilled to provide data for site specific determination of the storage potential of the Arbuckle. Cores from specific depths within Arbuckle (4164`-5130`) were utilized for study and flow-through experiments. Examination of formation rocks by thin section studies, SEM, XRD and CT scans was carried out to characterize the mineralogy of the core.

Dominant mineralogy throughout the formation is dolomite with large chert nodules and occasional zones with pyrite and argillaceous minerals. Carbonate-silica contacts contain extensive heterogeneity with sulfide minerals and argillaceous material in between. Extensive vugs and microfractures are common. This study focuses on three zones of interest: the Mississippian pay zone (3670`-3700`), a potential baffle in Arbuckle (4400`-4550`) and the proposed CO_2 injection zone (4900`-5050`).

Drill stem tests and swabbed brine samples collected from 13 depths throughout the aquifer reveal a saline brine (~50,000-190,000 TDS) dominated by Na^+, Ca^{2+} and Cl^-. Elemental ratios of major cations with Cl^- demonstrate a typical saline aquifer system. Cl/Br ratios reveal mixing between primary and secondary brines within the aquifer. Ca/Cl and Mg/Cl ratios suggest effect of dolomitization within the brines. $\delta^{18}O$ and $\delta^{2}H$ isotopes and Li/Cl ratios in the brine suggest the separation of upper and lower Arbuckle by a baffle zone. Swabbed waters provide Fe speciation data and reveal the importance of it in the system.

Laboratory experiments carried out at 40°C and 2100 psi using formation core plug and collected brine identify reaction pathways to be anticipated when supercritical CO_2 is injected. Results showed fluctuating chemistries of elements with Ca^{2+}, Mg^{2+}, Na^+ and Cl^- increasing during the first 15 hours, while Fe, S, and SO_4^{2-} decrease. For the next 15 hours a reverse trend of the same elements were observed. Alkalinity and pH show inverse relationship throughout the experiment. We conclude that dominant reactions will occur between brine, CO_2 and dolomite, calcite, chert, pyrite and argillaceous minerals. There is no perceived threat to freshwater resources in Kansas due to CO_2 injection.

Table of Contents

List of Figures

List of Tables

Acknowledgements

I would like to express my gratitude to many people who have helped me in the two years I have been at Kansas State University. Firstly, I would like to extend a huge thanks to Dr. Lynn Watney from the Kansas Geological Survey (KGS) for sharing his seemingly endless knowledge of Kansas geology and of the project, for his help in obtaining field data and for the countless opportunities he has allowed for me to present my research to a diversity of audiences. I would also like to thank other working at/with the KGS that have provided help including Saibal Bhattacharyya, Jason Rush, Dave Newell, Dave Laflen, Eugene Holubnyak, and Tiraz Birdie. From the University of Kansas I would like to thank Jennifer Roberts and Aimee Scheffer, who spent many long, cold nights with me on the rig collecting samples.

A special thanks to Dana Wreath, Vice President of Berexco, for working with us to provide ample opportunity to collect water samples from the Arbuckle. The Beredco drilling crew also helped tremendously in aiding the collection of rock and water samples during and after the drilling process and for providing entertainment through long, snow filled nights. Jason Bruns of Beredco deserves a special thank you for going out of his way to accommodate our sampling procedure and for the opportunity to operate equipment on the drill site. I would also like to thank Kent Crisler, on site geologist for KGS 1-32 and 1-28, for helping obtain core samples and for providing valuable experiential insight into the drilling/coring process and knowledge of Kansas Geology. Thanks to Trilobite Testing and Devilbliss Coring Services for helping sample brine and core samples in the snowy January weather.

I would like to thank Brian Strazisar at the National Energy Technology Laboratory in Pittsburgh, PA for allowing me access to the Flow Lab as a visiting researcher. Other people who helped me at NETL are: Timothy Murin, who was my shadow and guide throughout the learning and experimental process; Barbara Kutchko, who helped take beautiful SEM images of my samples; and Dustin Crandall, who took wonderful CT scans.

I would like to thank Eric Hoffman and the staff at Activation Laboratories for the great job in analyzing our high salinity samples. I would like to thank Michael DePhanger at Spectrum Petrographics for making beautiful thin sections of our core samples.

At K-State, I would like to thank Mickey Ransom for providing access to the XRD machine in the Department of Agronomy; and Angela Tran for assisting in the operation of the

XRD machine. I would like to thank Troy Ocheltree and Jesse Nippert of the Department of Biology for assisting in analyzing my samples for stable isotopes.

I would like to thank several people within the Geology Department. Firstly, I would like to thank Paul and Deana Strunk for providing me with a generous scholarship to continue my thesis research. I would like to thank George Clark for providing funding for several trips to field work, national laboratories and conferences. Thanks to Lori Page-Wilyard for administrative assistance. I would like to thank the K-State graduate students for their support, particularly Derek Ohl, Bobby Ford, Tyler Hill, Drew Evans, Randi Isham, O.C. Eke, Andrea Leggit, Charlotte Phillips, Sankar M.S., and Andrew Ingalls; and specifically Andy Neal and Munson for helping me get set up in Manhattan and showing me the cool places; Zac Hasten for providing numerous hours of research discussion, and for making office 6 the best office in Thompson Hall; Jeff Bridges for keeping me on my toes; and Chad Hobson for providing housing while the thesis was finished. I would like to extend a huge thank you to Sophia Ford, Logan Kelly and Guilherme Hoerlle for assisting during the long hours of core plug descriptions and assistance in field work.

I would like to give a special thanks to my committee members: Dr. Matthew Brueseke for numerous discussions on mineralogy and home brewing and for allowing me access to his microscope and camera; and Dr. Sambhudas Chaudhuri for numerous research discussions, engaging philosophical quandaries and making sure I did not work too hard.

I would like to thank my parents, Pam and Bruce Barker for their undying support throughout my life and especially during my graduate career. Special thanks also goes to my sister, Greta Barker for her humor and words of wisdom; and the Barker-Brown family in Tribune, Kansas for providing support while I lived in Kansas. My long time friends Matt Nordgren, Tip Whatley and Weston Lewis have encouraged me throughout the two years.

Finally, but not least of all, I would like to extend a heartfelt thank you to my advisor, Dr. Saugata Datta: for the opportunity to pursue a masters degree; for early morning meetings; for providing the opportunity to travel to conferences in Denver, Minneapolis, San Francisco, Canada, Oklahoma and North Carolina; for countless research discussions; for delicious Tandoori Chicken; for continuous encouragement; and for always thinking of his students best interests.

Chapter 1 - Introduction

Scientists have documented a rise in atmospheric CO_2 over the past few decades that can be attributed to anthropogenic inputs via power plants, industries and automobiles. The concentration of CO_2 in the atmosphere has increased from the preindustrial value of 280 ppm to 380 ppm in 2005 (Bachu, 2008) to its current value of 392 ppm in August 2012 (NOAA, 2012). Continuing emissions of CO_2 could have widespread effect on changing global weather patterns, ocean acidity and sea level rise (IPCC, 2007). In addition to advances in efficiency and development in renewable sources of energy, multiple mitigation techniques have been suggested for limiting future emissions of CO_2 into the atmosphere. Earth systems have naturally balanced the concentration of atmospheric CO_2 with sinks such as terrestrial plants and the ocean. Rates of deforestation that exceed reforestation is decreasing the ability of trees and soil to take CO_2 from the atmosphere (Rittenhouse et al, 2012). The ocean is the biggest sink of CO_2 with the biologic pump driving the absorption of CO_2 from the atmosphere and converting it to organic matter where it can be secured in ocean sediments for millions of years (DeVries et al, 2012). Increasing the storage capacity of the oceans by injecting anthropogenic CO_2 into the deep ocean is being examined but has serious limitations. It is considered a temporary option due to susceptibility to leakage and the potential to oversaturate the ocean with regard to CO_2. The effect of sudden increases of CO_2 on the ocean biosphere is not well understood (`, 2012). Considering the limitations of natural CO_2 sinks to handle anthropogenic increases of CO_2, is has been proposed to sequester, or securely store as the long term in geologic formations (IPCC, 2005; Gunter et al, 1997; Bachu, 2008).

Not all geologic settings have the necessary characteristics to store CO_2 (Gunter et al, 2004). Large igneous provinces and sedimentary basins have been demonstrated to hold the greatest potential to sequester CO_2. Mafic igneous rocks, for example the Columbia Flood basalt and the Deccan Traps, could sequester significant amounts of CO_2 (McGrail et al, 2006). Sedimentary basins hold the greatest potential for the stable sequestration of CO_2 for geologically significant time periods (Gunter et al, 2004). Sedimentary basins of interest include un-minable coal seams, depleted oil and gas fields and deep saline aquifers (Xu et al, 2004). CO_2 injected in coal seams preferentially replaces methane trapped in pores and

adsorbed to organic matter. Capturing the ejected methane is difficult and necessary in offsetting greenhouse gasses emitted to the atmosphere (Bachu, 2007).

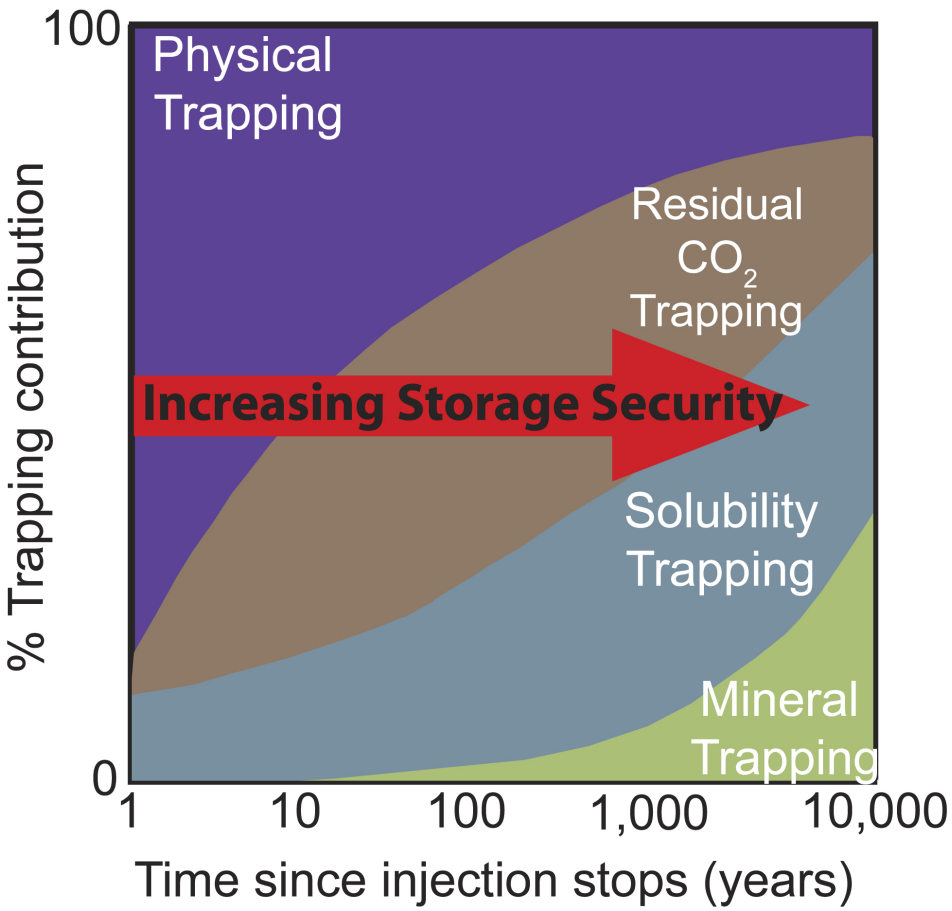

Figure 1-1. Security of CO_2 trapping mechanisms as a percentage of contribution and time (IPCC, 2005).

Saline aquifers hold the greatest sequestration potential, estimated between 1,000 and 10,000 billion tons globally (IPCC, 2005). As seen in Figure 1-1 from the IPCC report, mineral trapping is the most secure mechanism of CO_2 storage over geologically significant time periods, converting gaseous CO_2 into carbonate minerals. Physical, residual and solubility trapping are other trapping mechanisms that are important in the short and medium term. This study examines the potential for the Arbuckle aquifer, a deep saline system in south-central Kansas, to sequester CO_2 through mineralization reactions.

This study, a US Department of Energy funded collaboration between the Kansas Geological Survey, Kansas State University, BEREXCO, Inc (among other industry partners) and the University of Kansas has focused on the Wellington Field, Sumner County, Kansas,

and integrates seismic, geologic, and engineering approaches to evaluate miscible CO_2-EOR and tertiary oil recovery potential in the Mississippian chat reservoir and CO_2 sequestration potential in the underlying Arbuckle Group saline aquifer. The expected outcome of this work is to provide a geochemical database to aid in the development of a regional geosequestration model of a 17+ county area (centered on the Sedgwick Basin) in south-central Kansas to estimate regional CO_2 sequestration potential in the Arbuckle Group (saline) aquifer.

The key scientific theme of the overall project is to understand the geologic fundamentals behind the internal stratal architecture, structural deformation, and sediment diagenesis and to evaluate their role on flow units, cap rock integrity, aquifer storage, and identification of reservoir compartments and barriers to flow in the Arbuckle. High injectivity zones are being tested to determine aquifer/aquitard-specific geochemistry. Ultimately, reservoir simulation studies will be carried out in Computer Modeling Group's Generalized Equation-of-State Model Compositional Reservoir Simulator (CMG-GEM) to determine CO_2 injectivity in aquifers, possible tonnage of CO_2 sequestered in solution, residual gas saturation, and mineral precipitates. It will evaluate seal integrity in overcoming pressure increase upon injection, seal porosity changes due to geochemical reactions, and estimate CO_2 leakage as a fraction of injection. Short and long-term simulations will be carried out to quantify free phase CO_2, its distribution, and time for its dissipation, to understand plume growth, its area of influence and attenuation in presence of multiple aquitards and background aquifer flow, and movement in contact with fault zones.

The aspect of this project delegated to the Kansas State University-Geochemistry group is to examine the geochemical aspects of a CO_2 injection into the saline reservoir. The main concepts of this project include the geochemistry of the aquifer formation water, mineralogy of the aquifer formation, major reaction pathways of CO_2-water-rock interactions and modeling these reactions over geologically significant time periods.

For this work, 1600 feet of core from the Arbuckle and overlying Mississippian formation have been obtained and described. 179 core plug were taken from this core for detailed mineralogical description by thin section and X-ray diffraction, assisted by SEM-EDX analyses and CT scan tomographies. Investigations focused on the proposed CO_2 injection zone of 4900`-5050`. Brine samples were obtained from 8 drill stem tests and 5 swab tests to characterize the major and minor element chemistry and stable isotopic composition of

the Arbuckle brines. Supercritical flow experiments with collected core plugs and brine allowed the determination of key CO_2-brine-mineral reactions at relevant temperature and pressure conditions within the Arbuckle aquifer.

Chapter 2 - Background

While this research area is relatively new, numerous papers have been published in the past 15 years that address the issues involved with carbon capture and storage (CCS). This topic involves many disciplines and avenues of research including engineering, geochemistry, environmental impacts, human impacts and regulatory issues. This project is focused on the geochemical aspects of CCS, in particular to understand the reactions that take place after injection of CO_2 into a saline aquifer. An overview of important CO_2 sequestration concepts and current research on mineral sequestration in saline aquifers is summarized below.

CO_2 Trapping Mechanisms

Mechanisms of CO_2 sequestration in sedimentary basins can be of two general types, physical and geochemical (Han et al, 2010; Matter et al, 2007). Physical mechanisms include residual trapping of CO_2 in the pore spaces of the formation as it migrates, or as a plume trapped by a structural feature such as a caprock. Physical trapping mechanisms do not have long term storage potentials or cover regional basins (Bradshaw et al, 2007). Geochemical trapping involves the dissolution of CO_2 in water or brine, dissolution of the host rock and finally the precipitation of carbonate minerals that are stable over geologically significant time periods (Gunter et al, 2004).

Sequestration through mineralization reactions is the most stable form of geologic storage, but it takes the longest time for precipitation reactions to occur (Bachu, 2002). Mineral trapping can occur in several geologic settings appropriate for the sequestration of carbon dioxide. Basalts, sandstone aquifers, and carbonate aquifers each have variable potential to store CO_2 as a mineral phase (Gunter et al, 2004). After the CO_2 has been injected into a formation it will react with the water to form carbonic acid (reactions 1 & 2). The carbonic acid will dissociate into bicarbonate ions and finally carbonate ions, which will increase the reactivity of the fluid (reactions 3 & 4).

$CO_2(g) \rightarrow CO_2(aq)$ …… (1)

$CO_{2(aq)} + H_2O \rightarrow H_2CO_{3(aq)}$ …… (2)

$H_2CO_3 \rightarrow H^+ + HCO_3^-$ …… (3)

$HCO_3^- \rightarrow CO_3^{2-} + H^+$…… (4)

The acidified brine will react with the surrounding formation rock and, depending on the mineralogy of the formation, dissolve certain cations (predominantly alkali earth elements), serving as a buffer to the pH. The increased pH reduces the solubility of carbonate minerals, inducing saturation and precipitation (Newell et al, 2008). Some common dissolution-precipitation reactions and their relation to CO_2 sequestration sites are described below.

Basaltic rocks have high concentrations of mafic minerals (such as forsteriteand when dissolved into CO_2 saturated water, will introduce divalent cations into solution (Matter, 2007, McGrail et al, 2006). These cations act as a buffer, raising the pH until carbonate precipitation can begin. Laboratory experiments have shown that the dissolution of forsteritic olivine by CO_2 will release Mg^{2+} ions and amorphous silica (reaction 5) which react with bicarbonate to form magnesite (reaction 6).

$$Mg_2SiO_4(s) + 4H^+ \rightarrow 2Mg^{2+} + 2H_2O + SiO_2 \ldots\ldots\ldots (5)$$

$$Mg^{2+} + HCO_3^- \rightarrow MgCO_3 + H^+ \ldots\ldots\ldots (6)$$

Geochemical reaction rates leading to carbonate mineral precipitation are faster in mafic rocks than sedimentary rocks (Garcia et al, 2010). Basaltic rocks are very attractive for sequestration projects because of large concentrations of Ca^{2+}, Mg^{2+} and Fe^{3+} and low silica concentrations that enable fast reaction rates. Ca^{2+} and Mg are readily dissolved from basaltic rocks but Fe requires reducing conditions to allow for high concentrations to dissolve (Gislason et al, 2010). Massive flood basalts are found around the world in proximity to point sources of CO_2 and could serve as sequestration targets (McGrail et al, 2006). While basalts are attractive locations for CO_2 mineral sequestration, storage capacity may be limited due to low permeability throughout the formation. This low permeability may be offset by fractures and cavities in the basalt, but these features are hard to quantify in a subsurface setting (McGrail et al, 2006).

In addition to basalt formations, deep saline aquifers hold potential to sequester large amounts of CO_2 through mineralization reactions. These sedimentary formations have high porosity and permeability which allow CO_2 to spread through the formation and through large reactive surface area to facilitate mineral reactions. Saline sedimentary aquifers are usually overlain by an impermeable layer such as shale or an evaporite which serves as a caprock, securing injected CO_2 in the injection zone (Gunter et al, 2004). The two types of deep

sedimentary aquifers that have been examined are sandstone and carbonate formations. Siliciclastic/sandstone formations that have high amounts of quartz and low amounts of aluminosilicate minerals (e.g. quartz arenites) may have the correct temperature and pressure conditions to allow CO_2 to exist as a supercritical fluid, but could lack sufficient alkali earth elements needed to buffer the pH of the CO_2-brine (Matter et al., 2007). If the pH is not buffered by these alkali earth elements (e.g. Ca^{2+} and Mg^{2+}), CO_2 solubility will decrease and carbonate precipitation will be limited (Newell, 2008). However arkosic sandstone aquifers have high concentrations of aluminosilicate minerals, such as feldspars with some micas, that could facilitate mineralization reactions. Reaction 7 shows a generalized plagioclase feldspar dissolution and carbonate precipitation (Gunter et al, 2004).

anorthite + CO_2 + $2H_2O$ → kaolinite + calcite…… (7)

Another reaction with feldspar that could serve as a CO_2 trapping mechanism is the carbonation of albite into dawsonite and the formation of chalcedony through the following reaction (Gaus, 2010):

$NaAlSi_3O_8 + CO_2 + H_2O \leftrightarrow NaAlCO_3(OH)_2 + 3SiO_2$ …… (8)

Saline aquifers which have considerable carbonate formations have many alkali earth elements available to buffer the pH and allow CO_2 solubility to increase (Gunter, 2004; Matter et al, 2007). Dissolution of Fe hydroxides, clays, calcite and dolomite can provide divalent ions needed to facilitate mineralization reactions. Dissimilatory reductive dissolution of a common Fe hydroxide mineral is shown in reaction 9 below (Li, 2008).

$FeOOH(s) + 1/8CH_3COO^- + 15/8H^+ \leftrightarrow Fe^{2+} + 1/4HCO_3^- + 3/2H_2O$…… (9)

The reduction of Fe^{3+} to Fe^{2+} is necessary in order for the precipitation of Fe carbonate minerals such as siderite (Gislason et al, 2010). The dissolution of clay minerals can be important in providing divalent cations that enable carbonate mineralization. An example reaction of the dissolution of chlorite and calcite yielding siderite, dolomite, kaolinite and chalcedony is given below (Gaus et al, 2010):

$Fe_{2.5}Mg_{2.5}Al_2Si_3O_{10}(OH)_8 + 2.5CaCO_3 + 5CO_2 \leftrightarrow 2.5FeCO_3 + 2.5MgCa(CO_3) + Al_2Si_2O_5(OH)_4 + SiO_2 + 2H_2O$…… (10)

The dissolution of carbonate minerals such as calcite or dolomite will release bicarbonate ions along with Ca^{2+} or Mg^{2+} along three parallel reactions (reactions 11-13 from Li, 2008):

$(Ca, Mg)CO_3 + H^+ \rightarrow (Ca^{2+}, Mg^{2+}) + HCO_3^-$ …… (11)

$(Ca, Mg)CO_3 + H_2CO_3 \rightarrow (Ca^{2+}, Mg^{2+}) + 2HCO_3^-$…… (12)

$(Ca, Mg)CO_{3(s)} \rightarrow (Ca^{2+}, Mg^{2+}) + CO_3^{2-}$…… (13)

The release of carbonate ions from minerals could lead to a reduction in the mineralization capacity of carbonate aquifers (Bachu et al, 2002; Thibeau et al, 2007). However, the buffering effect of these carbonate minerals could increase the solubility of CO_2, increasing solubility trapping mechanisms (Lagneau et al, 2005). Mineral sequestration in carbonate aquifers is still a viable option if sufficient non carbonate mineral phases are present. Clays, micas, chlorites and silicates can provide cations needed to facilitate carbonation reactions (Gunter, 2004; Shao, 2010). Cations present in aquifer brine can also contribute to mineralization reactions (Druckenmiller et al, 2005). Mineralogical description of these carbonate aquifers allow insight into the amounts of non carbonate minerals available to provide the cations for carbonate precipitation. The expected carbonate mineralization reactions that form calcite, siderite, magnesite and dolomite (respectively) are shown below:

$Ca^{2+} + HCO_3^- \leftrightarrow CaCO_3 + H^+$…… (14)

$Fe^{2+} + HCO_3^- \leftrightarrow FeCO_3 + H^+$…… (15)

$Mg^{2+} + HCO_3^- \leftrightarrow MgCO_3 + H^+$…… (16)

$Ca^{2+} + Mg^{2+} + HCO_3^- \leftrightarrow CaMgCO_3 + H^+$…… (17)

Mineralogical sequestration is important because it has the potential to securely store CO_2 over geologically significant time periods. Physical trapping mechanisms and even solubility trapping can eventually lead to leaking of the CO_2 plume into potable aquifers. Reducing this leakage threat is a driving force in examining the permanent aspects to geologic sequestration, namely mineral trapping. The geochemical reactions leading to CO_2 sequestration through mineral precipitation in a carbonate aquifer are the focus of this work. Exact timing and extent of the reactions is uncertain because of the large uncertainties that surround the kinetics of water (brine)-rock-CO_2 reactions at supercritical temperatures and pressures.

The concept of geological storage of CO_2 is to evolve into a viable solution strategy for the problem of carbon dioxide emissions, and a series of issues need to be addressed, among them the most potential is for monitoring CO_2 leakage from the injection formation (

and Adams, 2003). CO_2 injected in sedimentary basins will always be lighter than formation water (Bachu and Adams, 2003), and hence the potential for upward leakage is enhanced by CO_2 buoyancy. And because initial deep injection of CO_2 is likely to occur in mature basins using existing infrastructure, possible leakage through existing wells needs to be considered.

CO_2 injection projects

Aquifers with total dissolved solid values higher that 10,000 mg/L are not considered sources of potable water by the US Environmental Protection Agency. This makes them good targets for disposal wells and for CO_2 sequestration (Xu et al, 2003). Saline aquifers have been used for years as disposal wells for hazardous materials, oilfield brines, acid gas (H_2S + CO_2) and as injection wells for enhanced oil recovery (EOR) (Nordbotten et al, 2005). Temperatures and pressures found in saline aquifers indicate that they can withstand the injection of CO_2 and allow it to exist as a supercritical fluid (Basbug et al, 2005). Current research into CO_2 sequestration sites is focused on saline aquifers with several pilot projects underway in the US and Canada.

A pilot CO_2 injection project into the Frio formation in Texas has provided in situ chemical data and insights into monitoring the CO_2 plume. This pilot project is located near major sources of CO_2 near the Gulf of Mexico in Texas. In 2004, 1600 tons of CO_2 (food grade) was injected into a sandstone aquifer. The 24 m thick injection zone is generally described as a cemented, sub-arkosic sandstone (Kharaka et al, 2006). The injection well was drilled for this project and intervals of the well were cored to provide lithology, mineralogy and fracture data. Core plugs from this well were used in laboratory flow through experiments, similar to the experiment described in Chapter 4 of this work (Sakurai, 2006, Xu. 2010). Water samples were collected before injection to provide baseline data, during and after to monitor the CO_2 plume and to measure geochemical changes. The samples were collected from an observation well 30 meters up-dip from the injection site (Kharaka et al, 2006). Collected waters show a decrease in pH and a small increase in electrical conductivity as the CO_2 plume reached the observation well two days after injection (Kharaka et al, 2006; Sakurai et al, 2006). Chemical analysis of the water indicated rapid dissolution rates which was confirmed with laboratory tests and geochemical modeling. Measured pH values after injection were around 3, which drastically increased the dissolution rates (Kharaka et al,

2009). These rapid dissolution reactions have implications for the long term security of CO_2. Dissolution of the caprock could create leakage pathways and transport toxic metals and organic compounds into drinking water (Kharaka et al, 2006, 2009). The plume of CO_2 was successfully monitored through the analysis of $\delta^{18}O$. This has positive implications for the monitoring of future injection projects (Kharaka et al, 2006).

A large scale CO_2 injection project occurred in Saskatchewan, Canada in the Weyburn oil field. The Weyburn field is part of the Williston basin in north central US and southern Canada and has been producing oil for many decades. It is a well studied oil field and is notable for its horizontal drilling and successful secondary recovery methods. In 1964 water flooding began to improve oil recovery. In 2000 a tertiary enhanced oil recovery (EOR) technique was employed, the injection of CO_2. 5000 tons of CO_2 was injected per day for an estimated total of 20 million tons (Preston et al, 2005). Forty three wells across the basin were analyzed for baseline data and were measured periodically after injection. Water flooding activities are suspected to have diluted the salinity of the formation water and transported some mobile ions out of the solution. Monitoring wells documented a small decrease in pH, a small increase in Ca, and a doubling of bicarbonate ions. Salinity increased due to the dissolution of minerals that had not been leached by the water flood (Emberley et al, 2004). Geochemical modeling was performed using PHREEQC (Parkhurst and Apello, 1999) and data collected from the monitoring wells. The modeling results were compared to observational data and validated to reduce the uncertainties involved with modeling subsurface reactions (Cantucci et al, 2009). From the results of this project, the researchers concluded that an EOR project can safely accompany a CO_2 storage project (Preston et al, 2005).

Properties of Supercritical CO_2

The behavior of CO_2 as a supercritical fluid and how it will interact with water and the formation rock is an important step in determining the reaction kinetics of a CO_2 system. CO_2 solubility in brine and its migration path are critical in evaluating the sequestration potential of a deep saline aquifer (Bachu, 2002). The properties of supercritical CO_2 and its solubility are discussed below.

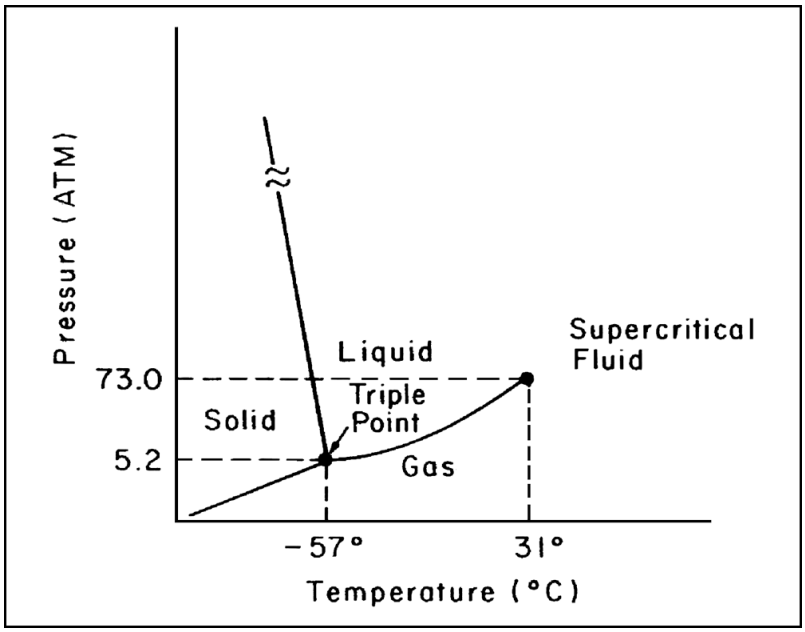

Figure 2-1. Pressure and temperature phase diagram of CO_2 showing the critical point at 31°C and 73 ATM (~7 MPa) *(Bachu, 2008)*.

Before CO_2 can react with the host rock, it must react with the formation brine and dissolve. The issue of CO_2 solubility in regards to CCS is further complicated by variations in temperature, pressure and salinity that can be found in saline aquifers. Injected CO_2 will be present as a supercritical fluid to avoid separation into liquid and gas phases which could cause injection problems (Basbug et al, 2005). This unique phase allows CO_2 to act as a fluid (high density) and a gas (fills available volume, low viscosity). The critical point for CO_2 is found at a temperature of 31.1°C and a pressure of 7.38 MPa (Fig. 2-1). This is much lower than the supercritical conditions for water (374.2°C, 22.05 MPa) (Kaszuba et al, 2005). Pressure and temperature conditions needed for CO_2 to exist in a supercritical phase begin at about 800 m (2625`) below the surface. Below this depth CO_2 has a density similar to (but less than) water (Gunter et al, 2004). The properties of supercritical CO_2 ($scCO_2$) control how it behaves in an aquifer setting. The density of $scCO_2$ can vary between 0.1 to 1.1 g/cm^3 depending on the temperature and pressure. The density decreases with temperature and increases with pressure like a liquid (Fig. 2-2). The density of $scCO_2$ is less than water, so it will be buoyant and will flow toward the caprock. The liquid-like density also allows $scCO_2$ to solubilize ions much better, increasing mineral dissolution. $scCO_2$ also has gas-like properties of low viscosity and diffusivity. These properties allow the supercritical fluid to

flow quicker through permeable zones. Any ions that dissolve into the fluid will be diffused much quicker throughout the solution (Kaszuba et al, 2005).

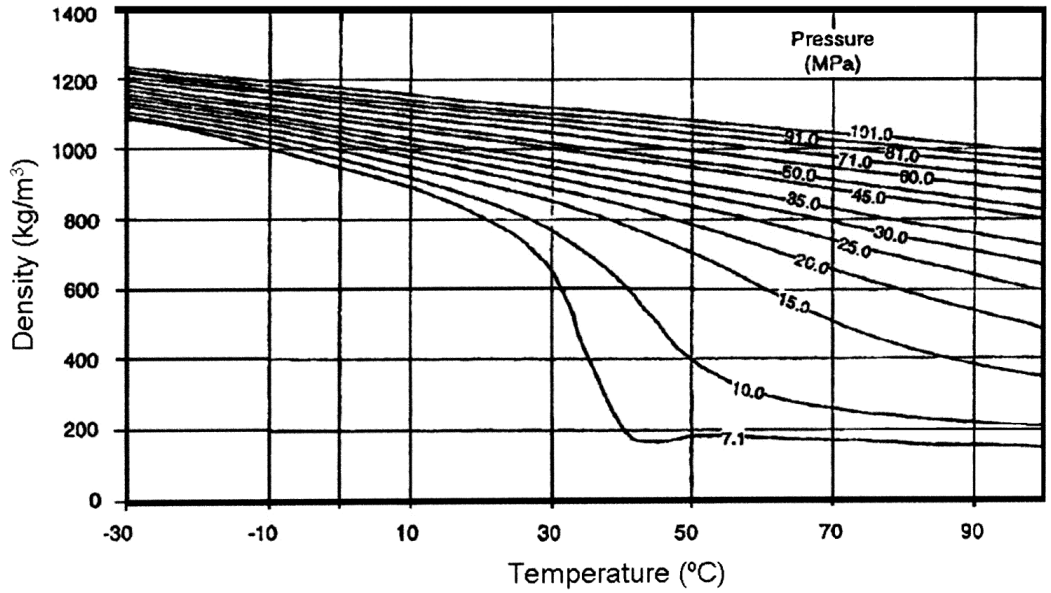

Figure 2-2. Density variation of CO_2 with temperature at various pressures *(Bachu, 2008)*.

As $scCO_2$ is injected into the aquifer, it comes in contact with the formation brine. At first the two fluids are immiscible and the CO_2 rises above the water due to differences in buoyancy. The interface between the $scCO_2$ and brine is the mixing zone, where CO_2 will dissolve into the brine and the brine dissolves into $scCO_2$. This zone shows decreasing pH as carbonic acid is produced. Chalbaud et al. (2010) examined the interfacial tension (IFT) between CO_2 and brine. It was found that an underestimation of IFT would lead to an underestimation of CO_2 storage capacity because more mixing would seem to occur. However this same underestimation of IFT could lead to an overestimation of brine displacement which could lead to lower storage capacity. IFT helps define capillary pressure which is an important factor in modeling how displaced brine and injected CO_2 will flow through the formation (Espinoza et al, 2010). The mixing zone travels further away from the injection zone toward the caprock as the $scCO_2$ is transported by gravity override (Taberner et al, 2009).

The ability of the CO_2 to become soluble in water depends also on the temperature, pressure and salinity of the formation in question. Portier et al (2005) have presented CO_2 solubility data for a range of temperatures, pressures and salinities. These results have been used to validate the ability of models to predict the solubility of CO_2 up to an ionic strength of

3. Another important aspect is how supercritical CO_2 will react with brine and what its threshold of solubility is. This concept was examined by Kaszuba et al (2005) when his research group reacted supercritical CO_2, brine and rock. It was found that once the CO_2 has been added, the fluid phase would dominate the direction of the reactions that occur within the formation over the solid mineral phases. Therefore, understanding the interaction of brine and CO_2 is an important first step in understanding the geochemistry of the system. Although much work has been done to provide experimental results pertaining to CO_2 solubility in brine and how it will affect CCS, it is clear that this topic needs to be examined for each proposed CCS site to ensure proper model parameters.

Laboratory Investigations

Once the CO_2 has dissolved into the formation brine it will become a reactive solution with a low pH and will begin to react with the host rock. This aspect of CCS has been examined using a variety of laboratory studies as well as geochemical models. In a classic sequestration paper, Gunter et al (1997) reacts synthetic brine with crushed lab grade minerals to examine the CO_2-water-rock reaction rates. Smyth et al (2008) describe a batch experiment where rock chips are exposed to brine and CO_2 in a flask at atmospheric temperature and pressure. Both researchers found that pH will decrease and cation concentrations will increase with exposure over time. These basic results have been expanded upon by research groups who have executed batch experiments at supercritical temperatures and pressures (Sorai et al, 2007). These experiments provide data on dissolution rates, but fail to account for the effect of flow through an aquifer.

Numerous studies provide reaction data from flow through experiments (Wigand et al, 2009; Pfingsten et al, 2006). These studies provide data that help to reduce uncertainty by closely emulating in situ conditions. Shao et al (2010) and Thibeau et al (2007) use lab grade minerals to provide thermodynamic and kinetic information on mineralization rates. This data is important in comparing lab experiments using in situ material. The majority of these studies have used a synthesized brine to conduct the flow and batch experiments (Tarkowski and Wdowin, 2011; Fischer et al, 2010; Gledhill et al, 2006; Liu et al, 2010, Birkle et al, 2008). This provides a high level of experimental control but fails to mimic the complexity of natural formation waters. Liu et al (2010) examined the suitability of synthetic brines to conduct

experiments examining the effects of CO_2 on pH and carbonation reactions. They found the pH was not significantly affect, but these brines do not have trace metal concentrations found in natural brines that could have effects on mineral carbonation reactions. Results from flow experiments have been used to constrain a reactive transport model in Wellman et al (2003). Xu et al (2003, 2004) and Lagneau et al (2005) examine mineral trapping mechanisms through geochemical models. Geochemical models are important because they can extrapolate reactions over timescales that are impossible in a laboratory setting.

Research is ongoing in the investigation of leakage pathways the CO_2 plume could take and how it would affect potable water sources. Experiments have shown that CO_2 dissolved in brine have a high reactivity and mobilize heavy metals (Little et al, 2010). If the CO_2 rich waters encounter an unplugged well, fracture or other pathways these ions could intrude into freshwater sources (Gunter et al, 2004). Salt water intrusion along these same pathways due to increased pressure from CO_2 injection can also lead to potable water contamination (Kalunka et al, 2010). Trace metal contamination is a possibility in a CO_2 leakage scenario. Site specific characterization and experiments utilizing in situ minerals and brine are needed to quantify this risk (Lemieux et al, 2011). It has been shown that if a CO_2 plume leaked from the storage formation and entered a freshwater supply the pH would decrease and total dissolved solid concentration would increase (Little et al, 2010). However, it has not been demonstrated in the laboratory or through geochemical models that CO_2-rock interactions will create leakage pathways through dissolution reactions alone. The pathways could be enlarged by reactions, but not created (Gaus et al, 2010). Limited data exists on caprock reactivity and more needs to be done in this area to determine the security of a formation over thousand year time frames (Liu et al, 2012). This is why determining the integrity of the cap rock is important in characterizing a potential CO_2 storage site.

Current sequestration research is providing results that can be used as experimental comparison and to validate models. Each proposed site is different and needs to be individually assessed using comprehensive methods (Brosse et al, 2010). In order to reduce uncertainty in the site assessment, care needs to be taken to mimic as close as possible the conditions found at the injection site. This includes using formation brine, studying rock cores from the area and performing flow through experiments at injection temperature and pressure.

Chapter 3 - Geologic Setting

Geologic History

A geologic history of the region is given here according to a paleohydrologic study conducted by Jorgensen (1989), one of the most classical works in this area. The rocks of the Arbuckle are late Cambrian to early Ordovician in age and were deposited over Precambrian basement. The Precambrian basement rock in Kansas, and throughout the central US, is igneous and metamorphic. The top of the basement is a major unconformity with variable topography. The unconformity occurred while the mid continent of the USA was above sea level during the early to mid Cambrian and exposed to weathering and erosion. The "granite wash" refers to a permeable, fractured and weathered rock along the surface of the Precambrian basement. In the late Cambrian the central USA was inundated by a shallow sea and the Lamotte and Reagan sandstones were deposited over the basement rock. Cambro-Ordovician rocks were deposited when the central USA was dominated by cyclic, shallow seas (Fig. 3-1). During this time thick beds of carbonate were deposited and lithified into limestone as sediment started to accumulate. During periods of regression the rocks are thought to have come into contact with meteoric water which led to dissolution along fractures and initiated dolomitization of the limestone (Jorgensen, 1989). During Silurian and Devonian times most of the mid-continent, USA was uplifted above sea level and underwent extensive erosion. This erosion resulted in extensional fracturing and the development of a regional hydrologic system. The influx of meteoric waters into Cambrian and Ordovician rocks is thought to have resulted in the flushing of formation water from the rocks (Jorgensen, 1989). As the Devonian transitioned into the early Mississippian, the area was again inundated by a shallow equatorial sea. Sand and clay layers were deposited above the Cambro-Ordovician rocks as the sea transgressed into the mid continental basin. Calcareous deposits dominated Mississippian time in the cyclic sea.

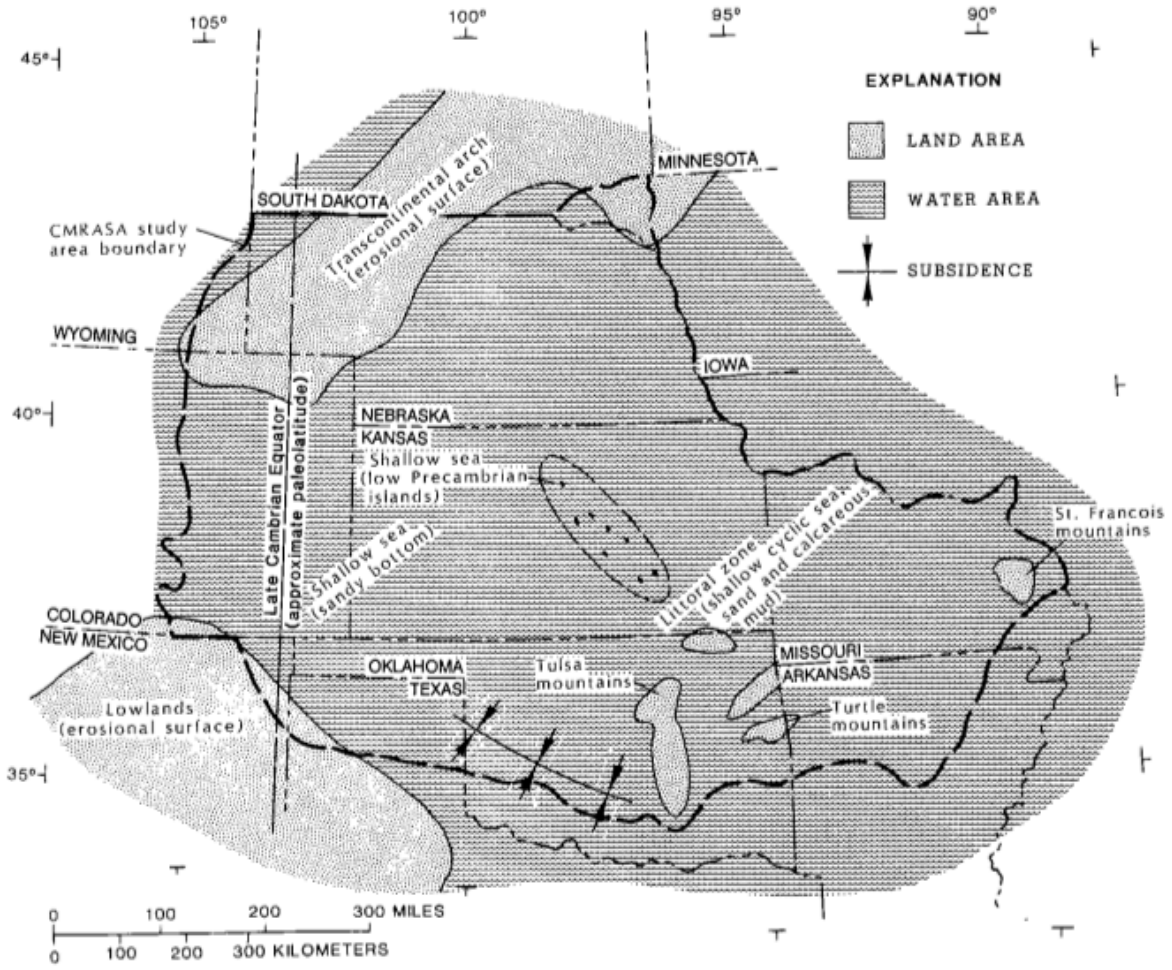

Figure 3-1. Extent of the Cambrian seas in the central US (Jorgensen, 1989).

There was major deposition of mainly clays onto the Pennsylvanian seas and the development of a shale layer above the Mississippian carbonate. During the Permian a rain shadow developed due to the Appalachian and Ouachita uplifts resulting in the formation of extensive evaporite deposits. These evaporite deposits and the Pennsylvanian shale effectively isolated the Cambro-Ordovician and Mississippian carbonates from local meteoric water influence and it wasn't until the Laramide Orogeny that there was a significant change in the hydrologic flow regime. As the front range and the Rocky mountains were uplifted in the late Cretaceous, the flow regime shifted from east-west to west-east. This led to the hydrologic flow regime we see today (Jorgensen, 1989).

Stratigraphy

The Arbuckle Group consists of porous dolomitic carbonates with interbedded shaly aquitards (Merriam, 1963). The Arbuckle formation extends laterally across much of Kansas except for structural highs in the central Kansas and Nemaha Uplifts. The top of the Arbuckle formation can be reached at depth of 500-7000 feet and thickens from the north to the south (Franseen et al, 2003). The rocks of the Arbuckle are typically divided into five groups. The Bonneterra and Eminence Dolomites are Cambrian and are excluded from the Arbuckle formation description in this work. The Glasconade, Roubidoux and Jefferson City Dolomites are Ordovician. The Arbuckle formation in Kansas can generally be considered to be all the rocks between the Simpson Group (above) and Reagan Sandstone (below) (Merriam, 1963). Arbuckle group rocks are overlain by the Chattanooga shale (upper Devonian) and the Mississippian carbonate aquifer that contains large oil and gas reservoirs. Shales of Pennsylvanian age lie above and confine the Mississippian reservoir. The Mississippian and Arbuckle saline reservoirs make up the Ozark Plateau Aquifer System (OPAS) in Kansas (MacFarlane, 2000).

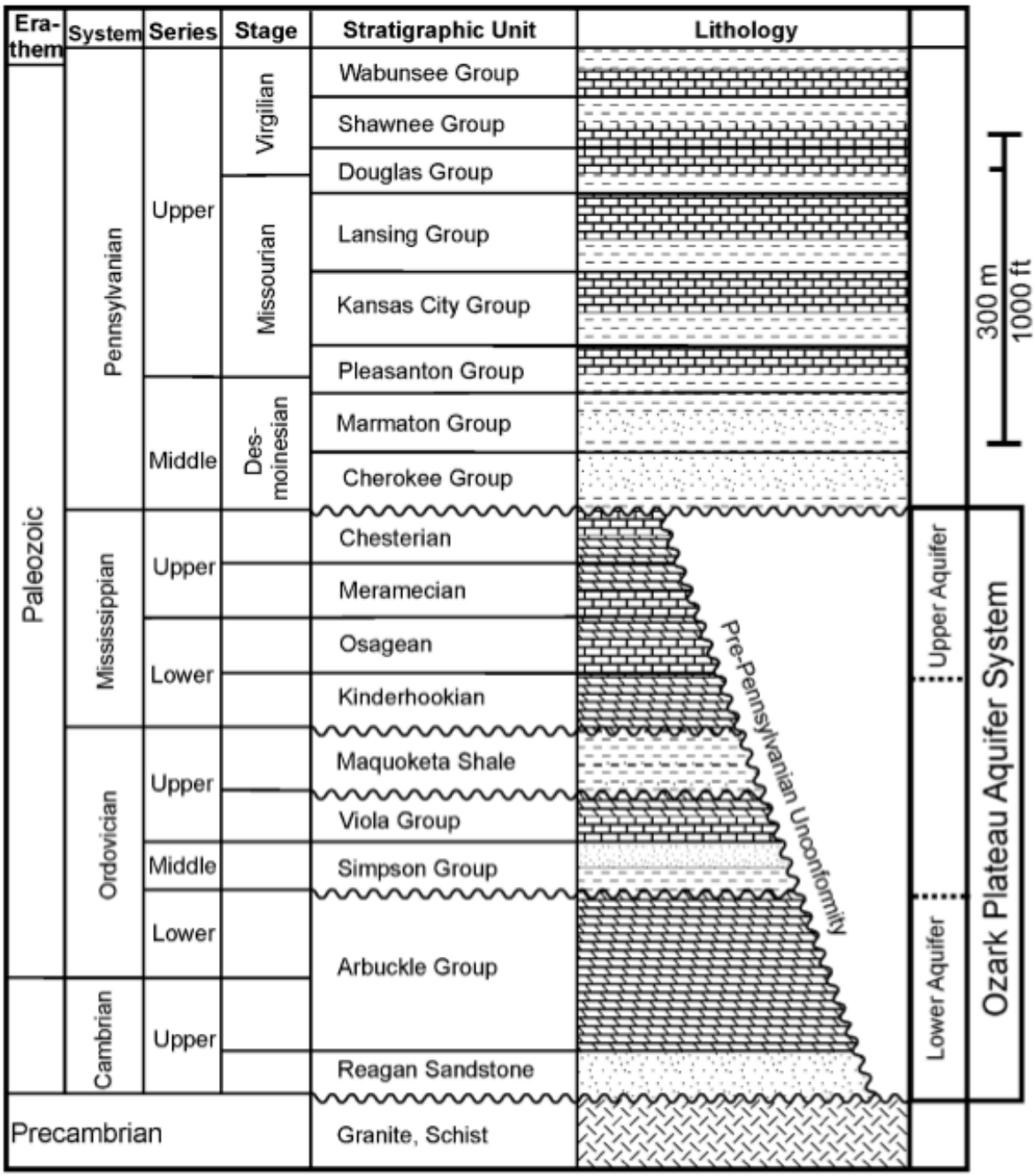

Figure 3-2. Stratigraphic column for Paleozoic rocks in Kansas. ***(From Carr, 2005)***

Project Location

Data gathered for this work was collected from two wells drilled in Sumner county, KS near the town of Wellington. Two wells (KGS 1-32 and KGS 1-32) were drilled 945 yards apart. Figure 1-3 shows the project location on a isopach map of Kansas showing thickness of

the Arbuckle aquifer throughout the state. The inset graph shows a satellite image of the location with the distance between the two wells.

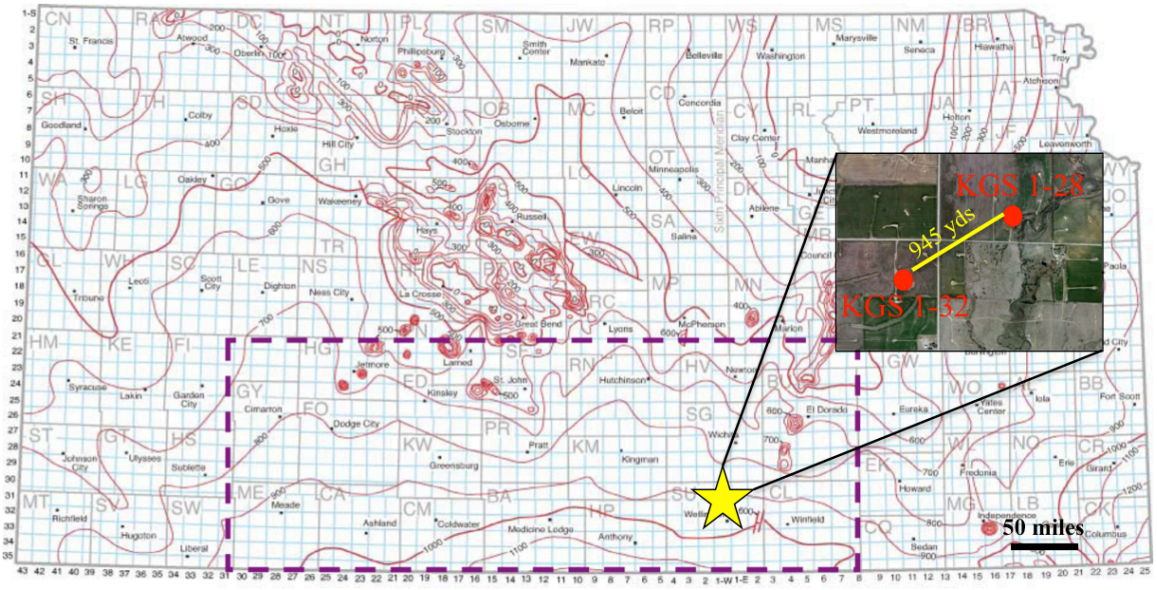

Figure 3-3. Isopach map of Kansas showing the thickness of Arbuckle Aquifer and project location (yellow star). Purple dashed polygon represents the regional study area of the project. Inset map is satellite image of well location with distance between wells marked.

Stratigraphic profiles compiled from core description and well logs are displayed in Figure 3-3. The thick Pennsylvanian shale that lies above the Mississippian reservoir is included because it is considered the secondary caprock. The Mississippian carbonate reservoir is ~400 feet thick in KGS 1-32. The Chattanooga shale is present as only a thin formation in 1-32 while it is much thicker in 1-28. The top of the Arbuckle is at 4164` and the bottom is about 5130` where it transitions into the Reagan sandstone/granite wash. The stratigraphy of the two wells is similar with the main difference being the absence of the Chattanooga shale in 1-32.

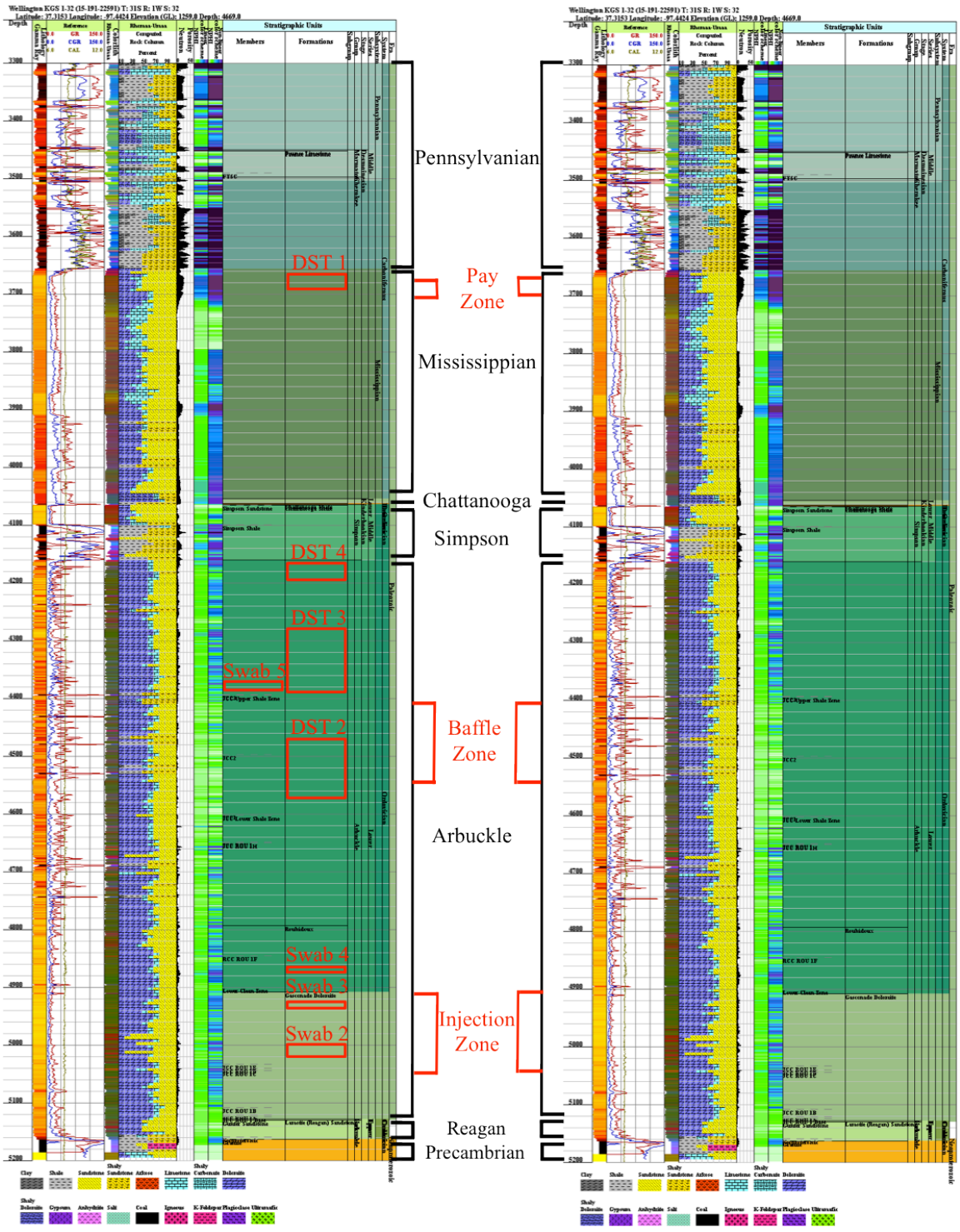

Figure 3-4. Stratigraphic profiles of KGS 1-32 (left) and 1-28 (right) compiled from well logs and core description by Kansas Geological Survey. Major stratigraphic units are labeled in black in the center. DST and Swab test intervals are denoted by red boxes. The pay zone, baffle zone and injection zone are labeled in red in the center.

The detailed lithological column compiled from core description of KGS 1-32 is displayed in Figure 3-5. Missing sections represent intervals of no core recovery. The top of the Arbuckle at 4164` in KGS 1-32 lies below a thin layer of Cherokee shale and a thicker Simpson sandstone. The first 70 feet of the Arbuckle is a shaley limestone that transitions into a 20` thick siltstone before becoming exclusively dolomite. 4320` through 4550` is a argillaceous dolomite and represents a low porosity baffle zone within the Arbuckle. 4550` to 4580` is a brecciated dolomite transitioning into a chert dolomite between 4580` and 4720`. Another brecciated zone at 4730` to 4750` lies above a slightly argillaceous dolomite from 4750 to 4900. The 4900` to 4950` zone is the proposed CO_2 injection zone. The upper portion of this zone (4900` to 4980`) is a dolomitic packstone-wackstone. A 10 foot brecciated zone at 4980` is followed by a cherty dolomite from 4990`-5030`. Below 5030` the formation is a argillaceous dolomite transitioning into the Reagan sandstone. The Precambrian granitoid basement was reached at ~5170` in KGS 1-32.

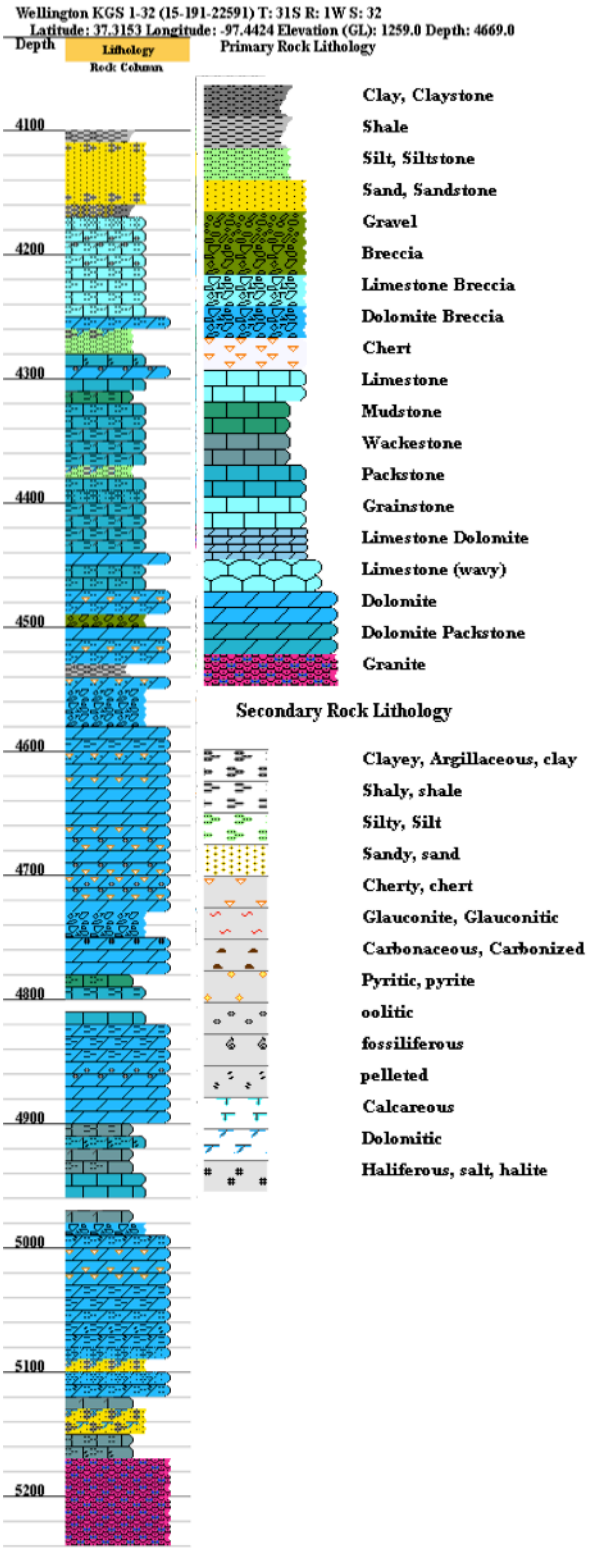

Figure 3-5. Lithology of KGS 1-32 compiled with well log data and whole core description.

Hydrogeology

The Ozark Plateau Aquifer System (OPAS) in south-central Kansas is well suited for supercritical CO_2 sequestration in its deep saline aquifers because of its depth (4164`), thickness (~1000`), and isolation from shallow freshwater aquifers by regional caprock, the Chattanooga Shale (thickness ≈ 50`). Another caprock of lower Pennsylvanian shale overlie the Mississippian carbonates (thicknesses in 10's of ft). The groundwater in the Arbuckle is saline and ranges in total dissolved solids concentration (TDS) from 10,000 to 250,000 ppm. Variable vertical connectivity has been observed between the upper and lower Arbuckle, indicative of stratigraphic, diagenetic and structural controls (Franseen et al, 2003). Ground water flow in the OPAS is to the east from CO and to the south east from NE, with Precambrian topography locally controlling flow regimes. (Jorgensen, 1989). Flow through the aquifer is thought to be slow and the current hydrologic regime is thought to have been in place about 65 m.y. ago. The saline Western Interior Plains aquifer is connected to the freshwater Ozark Plateau aquifer system to the east (Jorgensen, 1989). The Arbuckle has been a productive petroleum reservoir and is utilized as an injection zone for class I and II wastes. The integrity of the formation to trap petroleum and other wastes and close proximity to major point sources of CO_2 emissions make it a viable candidate for CO_2 sequestration (Carr et al, 2005).

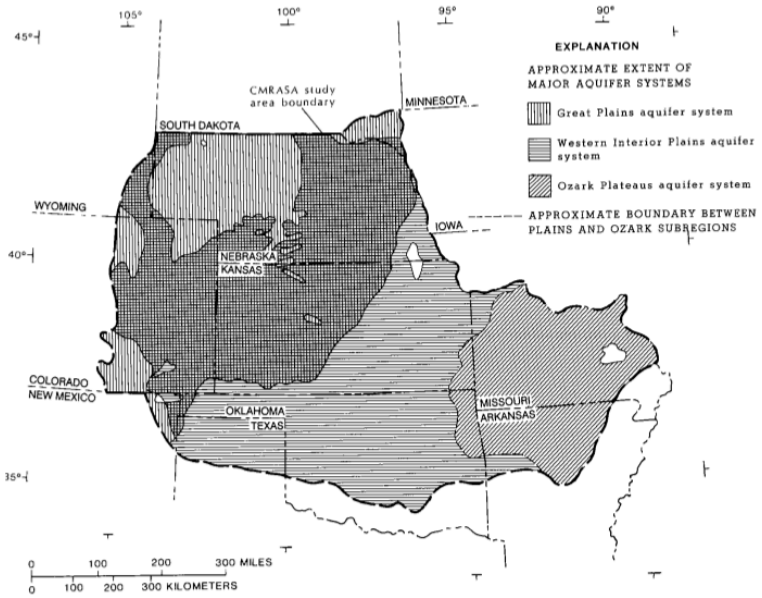

Figure 3-6. Map of regional aquifer systems in the central US *(Jorgensen, 1989).*

Origin of Brines in Sedimentary Basins

The origin of brines in sedimentary basins have been the focus of many studies through the years due to the importance in understanding oil formation and migration (Carpenter, 1978; Tan et al, 2011). While the focus of this work is not to determine the origin of the Arbuckle brine, collected data provide insight into this topic. This section will address the background research on the origin of brines and the discussion section will address the implications of the data to the origin of Arbuckle brines.

Controls on the chemical composition of brines associated with sedimentary basins are complex diverse and include physical and chemical processes, regional and local groundwater flow, mixing between brines and diagenetic reactions (Hanor et al, 1994). Brines are typically defined as solutions with greater than 100,000 ppm total dissolved solids (Carpenter, 1978). This is significantly greater than the sea water value of 35,000 ppm. Several mechanisms for the concentration of brines have been proposed: evaporation of seawater, dissolution of halite, or shale membrane filtration. The latter has been demonstrated in the laboratory by Kharaka and Smalley (1976) but difficulty arises when applying the laboratory results to natural conditions. Shale membrane filtration requires high pressure to force massive volumes of water through relatively impermeable shale. This process has not been documented in nature and is generally ruled out as a significant factor in the origin of brines found in sedimentary basins (Carpenter, 1978).

The evaporation of seawater and dissolution of halite to form brines are the most likely to occur and can be traced using the conservative elements of chloride and bromide. These elemental concentrations are not affected by mineral precipitation reactions or diagenetic processes. Only mixing between solutions of different composition can have a significant impact on Cl^- and Br^- concentrations (Fontes and Matray, 1993). Brine formed through the dissolution of halite will show an enrichment in Cl^- and Na^+ while other elements will be depleted (relative to seawater). Br^- concentrations in halite are low, so concentrations in brine will not significantly increase (Carpenter, 1978). However, brines formed from the evaporation of seawater will show distinct trends in major element behavior and follow the evaporation path described by previous researchers, compiled and summarized in Fontes and Matray (1993). Primary brines are described as those originating from the evaporation of normal seawater while secondary brines are those produced from the dissolution of evaporite

minerals (Fontes and Matray, 1993). Brines of primary and secondary origins are not mutually exclusive in a reservoir and commonly brines are mixtures of two end members (Chi et al, 1997). The mixing can be interpreted using Cl/Br ratios and $\delta^{18}O$ and $\delta^{2}H$ isotope data. Original connate brines may have been displaced by meteoric waters, creating distinct mixing signatures that can be quite complex and difficult to interpret (Domenico et al, 1985)

Some element's concentrations such as Ca^{2+}, Mg^{2+}, Na^{+} and K^{+} can be altered by diagenetic processes, and produce interpretable trends. As seawater evaporates minerals become saturated in a specific order and precipitate out, affecting the chemistry of the brine. The first mineral to reach saturation is gypsum, followed by halite, Mg-sulfates and finally K-salts (Fontes and Matray, 1993). The precipitation of these salts deplete the brine of the major cation associated with that mineral. Diagenetic processes such as dolomitization, albitization of feldspars and the alteration of clay minerals to K-feldspars can further affect the concentrations of brines relative to seawater. The alteration of clay minerals to form illite and K-feldspar can deplete a brine in K^{+} ions. Ca^{2+} and Na^{+} concentrations in brines are mainly controlled through buffering action between minerals and brine solutions (Houston et al, 2011). Albitization of feldspars can cause a reduction in the concentration of Na^{+} in brine. This process occurs in siliciclastic reservoirs where feldspar is an abundant mineral. In carbonate reservoirs, dolomitization results in enrichment of Ca^{2+} and depletion of Mg^{2+} due to the replacement reaction:

$$2CaCO_3 + Mg^{2+} \rightarrow CaMg(CO_3)_2 + Ca^{2+} \quad \ldots\ldots\ldots(18)$$

Comparing the ratio of major elements to chloride against the seawater evaporation curve provides useful information to the origin of brine and the diagenetic processes that have affected the brine as it reacts with reservoir rock. Another useful calculation that provides information on diagenetic reactions is the excess-deficit plot developed by Davisson (1994) and expanded upon by Birkle et al (2009). They developed two equations that define the Ca^{2+} excess and Na^{+} deficit commonly seen in sedimentary brines:

$$\mathrm{Na}_{deficit} = \frac{1}{22.99}\left(\left(\frac{\mathrm{Na}}{\mathrm{Cl}}\right)_{sw}[\mathrm{Cl}]_{meas} - [\mathrm{Na}]_{meas}\right) \quad \ldots\ldots\ldots (19)$$

$$\mathrm{Ca}_{excess} = \frac{2}{40.08}\left([\mathrm{Ca}]_{meas} - \left(\frac{\mathrm{Ca}}{\mathrm{Cl}}\right)_{sw}[\mathrm{Cl}]_{meas}\right) \ldots\ldots\ldots (20)$$

These equations sought to determine a relationship between Ca^{2+}, Na^{+} and Cl^{-} for basinal fluids. The albitization of feldspars, as mentioned above, creates a 2:1 exchange of

Na^+ for Ca^{2+} and this relationship can be seen in basinal fluids all over the world. The linear relationship between these saline brines has been defined as the 'basinal fluid line' (BFL). The equation of the BFL, as defines by Davisson and Criss (1996), is:

$$Ca_{excess} = (0967)Na_{deficit} + 140.3 \text{ ..... } (21)$$

The excess of Ca^{2+} and deficit of Na^+ can be interpreted by applying the equations and determining the slope and amount of shift. The effects of mixing, dolomitization, influence of halite dissolution and albitization can be seen on this graph. These trends are displayed in Figure 3-4 from Davisson and Criss (1996).

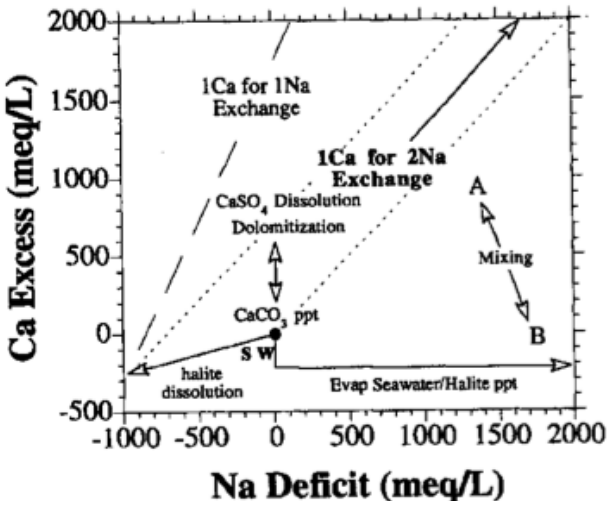

Figure 3-7. Diagenetic effects on basinal fluids as seen on a $Ca_{excess}/Na_{deficit}$ plot (Davisson and Criss, 1996).

Isotopes are employed to gain further information into brine alteration. Strontium, oxygen and deuterium are commonly used to trace brine origin and reactions with host rock (Stueber and Walter, 1991). This study has obtained oxygen and deuterium isotopic data, and while the age of the brine cannot be determined, some insight into the origin of the water can be gained by comparing the results to published research.

Discussion of Historic Arbuckle Data

Arbuckle aquifer data from all over the state of Kansas has been obtained by the Kansas Geological Survey. Na^+, Ca^{2+}, Mg^{2+}, Cl^- and SO_4^{2-} concentrations are available from this dataset. A significant portion of the data was obtained in the 1950s and 60s when oil production was high from overlying formations and brine disposal in the Arbuckle formation was common. Most of the samples are from shallow depths within the Arbuckle. Samples

come from a variety of processes and could be considered of questionable validity relative to modern sampling and analytical techniques. The data obtained in this work will be compared to this historical data in Chapter 6. The historical data is plotted as Cl^- ratios against seawater evaporation curves in Figure 3-8.

Several trends can be observed in these ratios in Figure 3-8. Na^+/Cl^- ratios have a strong linear relationship and closely follow the seawater evaporation curve. It is important to note that the data continues below the seawater composition and approaches the origin. It has been identified that this can only occur by the dissolution of evaporite minerals such as halite by a dilute, (possibly) meteoric water (Davisson and Criss, 1996). Mixing between primary and secondary brines and even meteoric water has been postulated as an origin for Cambro-Ordovician brines in Kansas (Dingman et al, 1968). Ca^{2+} increases linearly relative to Cl^- and trends above the seawater evaporation curve. Coupled with a depletion in Mg^{2+}, this is a typical signature of diagenetic dolomitization as discussed above. Ca^{2+} and Mg^{2+} approach the origin of the graph below seawater concentrations, indicating mixing with meteoric waters. SO_4^{2-} shows no trend with depth, as has been observed in previous studies of Kansas brines (Dingman et al, 1968). SO_4^{2-} is depleted below seawater values and has most likely been influenced by biological reduction and to some degree of $CaSO_4$ precipitation.

The Arbuckle reservoir has lower salinity values than the overlying Mississippian group aquifers (Dingman et al, 1968). It has been postulated that the Cambro-Ordovician Arbuckle aquifer has been flushed with meteoric water and concentrated due to downward migration of high saline brines from above (Dingman et al, 1968). It is clear from the Cl^- ratio plots that there has been some mixing that has occurred within the Arbuckle. The Chapter 6 states in detail how produced brine data obtained in this work fits with these trends.

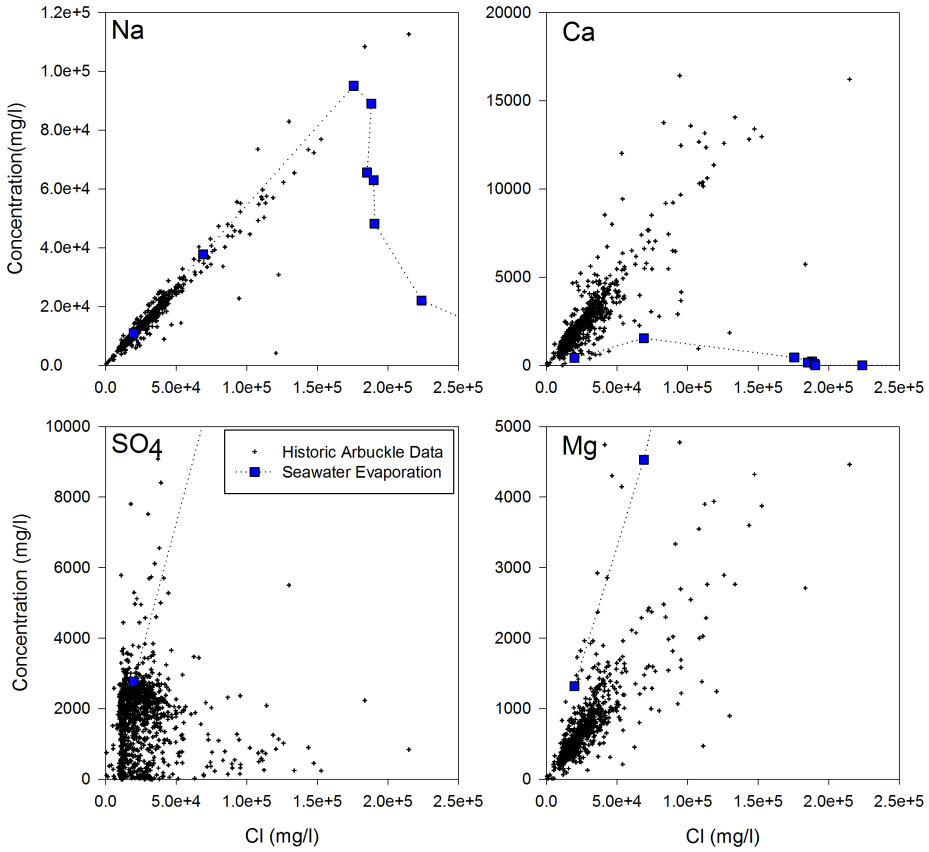

Figure 3-8. Historic Arbuckle data plotted against Cl^- with the seawater evaporation curve.

Chapter 4 - Methods and Materials

Two experimental wells were drilled in January through March of 2011 in Sumner County, south-central Kansas to provide aqueous and mineralogical samples for this project. These two wells (KGS 1-32 & KGS 1-28, Fig. 3-3) are 864 meters apart (see Fig. 3-2) and coring penetrated the entire Arbuckle formation until the Precambrian basement rock at ~5200`.

Methods in Mineralogical Characterization

Formation rock samples used in this study were obtained from 1600 feet of core retrieved from well KGS 1-32. The cored interval was 3540`-5179` which contained the the entire Mississippian (~3660`-4050`) and Arbuckle (4164`-5140`) formations. As the 60` core sections were retrieved from the hole, they were laid out in two 30` sections, marked for every foot, oriented top to bottom, and cut into three feet sections. These 3` sections were stored in a climate controlled tent to prevent fracturing of the core due to freezing.

The whole cores were then transported from the field site to Weatherford Laboratories® in Houston, TX where they were slabbed, photographed and lithologically described in detail. Whole core analyses at Weatherford provided porosity and permeability data for the core. 179 core plugs of 1.5" x 2" (diameter x length) were cut from the whole core for mineralogical description by thin section studies, X-ray Diffraction, Scanning Electron Microscopy and Computer-aided Tomography scan studies. Core plugs were visually described and photographed using a Canon® PowerShot® SD4000 IS camera.

Core chips were obtained from the whole core sections about every 15 feet from the ends of the 3` sections using a chisel and hammer while core sections were in the climate controlled tent. These core chips were sealed in oxygen impermeable Remel® bag (Mitsubishi Gas Company, Remel®, Cat No. 2019-11-02), along with an O_2 absorber pouch (Mitsubishi Gas Company, AnaeroPouch® Anaero; Cat. No. 23-246-379) to prevent elemental oxidation. The bags were flushed with nitrogen gas before being sealed and stored. These core chips were stored frozen on dry ice and transported to Kansas State University where they were stored in a freezer at -2°C.

Figure 4-1. (A) Core sections stored on pallets in climate controlled tent awaiting transportation to Weatherford Laboratories in Houston, TX. (B) Marking the depth and orienting the 30` core sections before cutting into smaller sections. (C) Whole core sections without aluminum sleeves marked with depth and top-bottom orientation descriptions. (D) Collecting core chips from the end of 3` core sections.

Well cuttings were also obtained from the well site during drilling of the core. As the drilling mud was circulated, cuttings were collected every 50 feet by a rig hand and quickly transferred into a Remel® bag with O_2 absorber (same as core chips described above). The cuttings were flushed with N_2 gas before being sealed and stored. The well cuttings were stored under dry ice in the field and transferred to Kansas State University where they were stored in the freezer.

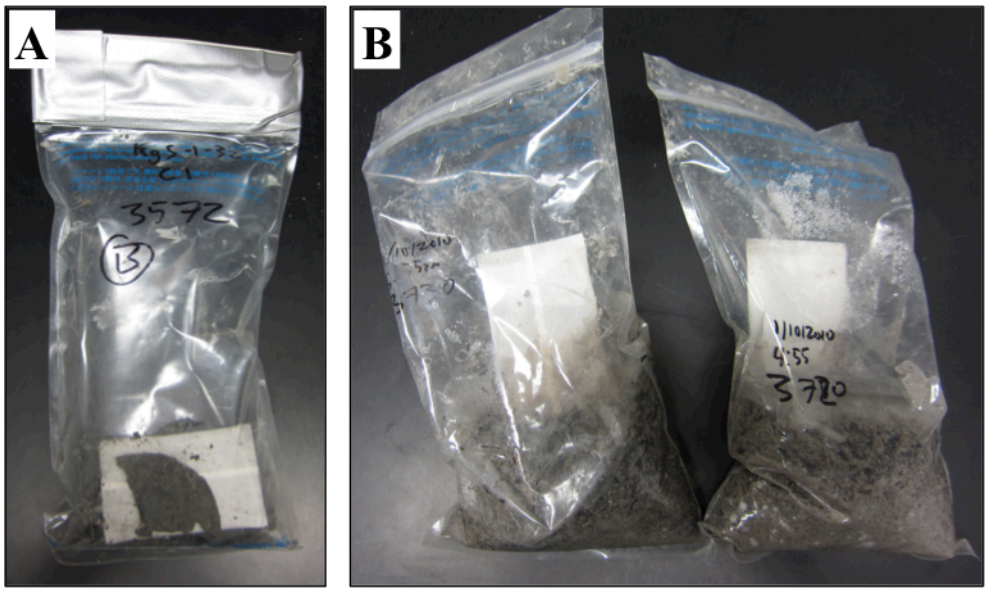

Figure 4-2. Core chips (A) and well cuttings (B) stored in Remel® bags with O_2 absorbers. Both are flushed with N_2 gas to remove oxygen.

Thin sections cut from core plugs were vacuum impregnated with blue epoxy by Spectrum Petrographics® and polished to 30μm thickness. Thin sections were analyzed and photographed using a Nikon® Eclipse® E600 POL polarizing petrographic microscope equipped with a SPOT® Insight® QE (Model # 4.2) camera. Pictures were captured and modified using SPOT Basic™ software.

X-Ray Diffraction (XRD) analyses on the core samples for mineralogical identification were performed at the Department of Agronomy at Kansas State University using a Phillips® XRD with a Cu Kα radiation source (λ=1.5406 Å) target and 2θ range of 2° – 70°. Step size was 0.02° with 0.6 seconds per step. Seven samples were analyzed at Panalytical® using copper x-rays in a Bragg Brentano configuration on a X'Pert Pro system using programmable slits and a fast linear X'Celerator detector. A reflection spinner stage was used and samples were made spinning to ensure data with good counting statistics. The measurement time varied from sample to sample to achieve better signal to noise and to get all trace phases accounted for.

Scanning Electron Microscopy (SEM) at the National Energy Technology Laboratory in Pittsburgh, PA was used via FEI® Quanta® 600 field emission gun and Aspex Instruments® with backscattered electron imaging coupled with energy dispersive spectroscopy. Core plug 31-19 (4977`) was imaged and was used in the core flow experiment.

X-ray computed tomography (CT scans) studies were used to examine internal pore structure of the cores at the National Energy Technology Laboratory in Morgantown, PA using a Medical CT scanner with a voxel resolution of $(0.25\ mm)^2$ x 1 mm. Core plugs 33-5 and 31-19 were scanned and 31-19 was scanned after the flow-through experiment.

Methods in Hydrogeochemical Characterization

Water samples were collected from specific depth intervals from drill stem tests (DST) during the drilling of both wells (Table 3-1 summarizes the samples collected). DSTs are a common method used in the oil industry to test reservoir fluids and pressure during the drilling process. A special tool is attached to the drilling joints and lowered into the uncased well to the desired depth. Inflatable 'packers' isolate a particular zone and the screen is opened, allowing fluid to enter the pipe. The water will rise a certain distance according to the pressure of the well. Once the test is concluded, the pipe is drawn out of the well and water can be collected. The first fluid to come out of the pipe as it is drawn out of the well contains drilling mud, making collection undesirable. Water closer to the testing tool is the cleanest and is considered to have minimal to no contamination by drilling fluid (Wenger et al, 2004).

The water was collected from the stands closest to the tool to reduce the amount of potential contamination by drilling mud. Three samples from each DST were collected to reduce uncertainty due to possible contamination via drilling fluids. Water was collected in 5 gallon buckets and immediately transferred into the following sample containers: one 2 gallon HDPE jug (Cat. No. 02923K), two Fisherbrand® 50 mL centrifuge tubes (Cat. No. 0644320), two Nalgene® 125 mL amber HDPE bottles (Cat. No. 20040004), two Thermo Scientific® 500 mL clear HDPE bottles (Cat. No. 02912323), one Fisherbrand® 250 mL glass bottle (Cat. No. 02911760) and one Fisherbrand® 60 mL glass bottle (Cat. No. 02911757) (Fig. 4-3). These samples were sealed with tape, transferred to K-State geochemistry lab on ice and stored cold in refrigerators until analyses.

Figure 4-3. Sample containers for water collection for each DST and swabbed waters.

Sample Name	Date	Well	Depth Interval (ft)	Depth Median (ft)
DST 1	1/9/11	KGS 1-32	3664 - 3690	3677
DST 2	1/23/11	KGS 1-32	4465 - 4575	4520
DST 3	1/24/11	KGS 1-32	4280 - 4390	4335
DST 4	1/25/11	KGS 1-32	4175 - 4190	4182
DST 5	3/5/11	KGS 1-28	5133 - 5233	5183
DST 6	3/5/11	KGS 1-28	5026 - 5047	5036
DST 7	3/6/11	KGS 1-28	4917 - 4937	4927
DST 8	3/6/11	KGS 1-28	4866 - 4885	4876
Swab 1	7/29/11	KGS 1-28	4995 - 5015	5005
Swab 2	8/11/11	KGS 1-32	5000 - 5020	5010
Swab 3	6/11/12	KGS 1-33	4924 - 4932	4928
Swab 4	6/12/12	KGS 1-34	4872 - 4878	4875
Swab 5	6/14/12	KGS 1-35	4374 - 4386	4380

Table 4-1. Drill stem test and swab intervals in wells KGS-1-32 and KGS-1-28. Samples were taken throughout the drilling process as indicated by the date. 4 DST samples were taken from KGS-1-32 and 4 taken from KGS 1-28. One swabbed sample was taken from KGS 1-28 and 4 taken from KGS 1-32. Each sample was collected over a depth interval in the well. The median depth is used for graphical presentation.

Two samples from each DST were prepared for geochemical analysis. Both were filtered with a 0.45 µm Milipore® filter. One was acidified with Optima grade nitric acid (65-70%) to pH <2 for Inductively Coupled Plasma-Optical Emission Spectroscopy (ICP-OES) to provide major cation data and the second one was unacidified for Ion Chromatographic (IC) analysis for total anion data. The samples were analyzed for major and minor elemental chemistry at Activation Laboratories® (Ancaster, Ontario). ICP-OES analyses were run on a Varian® 730-ES Axial ICP with SVS1 sample introduction using EPA method 200.5.

IC analyses was run on 100µL of sample diluted (1:50 and 1:1000) in deionized water and measured for conductivity. Quantitation was by peak area against a standard curve using an Inorganic Venture® (AL-LFS-2, lot F2-MEB 427095) mixed standard containing chloride, sulfate, bromide, phosphate, nitrate, and fluoride ions (chloride stock concentration of 1.500 mg/ml). IC analyses was conducted using a Dionex® 120 with a Dionex® IonPac® AS9-HC (4x250 mm) (Product # 051786 (supplied by Thermo Scientific® #010-21-15)) column with a 9 mM Sodium Carbonate mobile phase and a flow rate of 1 ml/min. Standard measurements and calculated standard deviations for ICP-OES and IC are presented in Table 4-2

Analyte Symbol	K	Mg	Mn	Ca	Fe	Li	Na	P	S	Sr	Cl	Br	SO4
Unit Symbol	mg/L	mg/L	mg/L	mg/L	mg/L	mg/L	mg/L	mg/L	mg/L	µg/L	mg/L	mg/L	mg/L
Detection Limit	0.1	0.1	0.01	0.1	0.01	0.05	0.1	0.02	1	10	0.03	0.03	0.03
Analysis Method	ICP-OES	ICP-OES	ICP-OES	ICP-OES	ICP-OES	ICP-OES	ICP-OES	ICP-OES	ICP-OES	ICP-OES	IC	IC	IC
IC Ref Std Meas	-	-	-	-	-	-	-	-	-	-	15.2	9.97	15.1
IC Ref Std Cert	-	-	-	-	-	-	-	-	-	-	15	10	15
NIST 1643e (ICP) Meas	2.2	7	0.04	28.9	0.09	0.05	19.2	-	-	300	-	-	-
NIST 1643e (ICP) Cert	2.034	8.037	0.03897	32.3	0.0981	0.0174	20.74	-	-	323.1	-	-	-
SLRS-5 (ICP) Meas	0.8	2.4	0.01	10.2	0.1	-	5.4	-	-	60	-	-	-
SLRS-5 (ICP) Cert	0.839	2.54	0.0433	10.5	0.0912	-	5.38	-	-	53.6	-	-	-
KSU_30 Orig	-	-	-	-	-	-	-	-	-	-	118000	236	341
KSU_30 Dup	-	-	-	-	-	-	-	-	-	-	118000	235	331
Method Blank Method Blank	< 0.1	< 0.1	< 0.01	< 0.1	< 0.01	< 0.05	< 0.1	< 0.02	< 1	< 10	-	-	-
Method Blank Method Blank	-	-	-	-	-	-	-	-	-	-	< 0.03	< 0.03	< 0.03
NIST 1643e (ICP) STDEV	0.117	0.733	0.001	2.404	0.006	0.023	1.089	-	-	16.334	-	-	-
SLRS-5 (ICP) STDEV	0.028	0.099	0.024	0.212	0.006	-	0.014	-	-	4.525	-	-	-
IC Ref Std STDEV	-	-	-	-	-	-	-	-	-	-	0.141	0.021	0.071

Table 4-2. Standards measured by ICP-OES and IC and calculated standard deviations.

After the completion of well KGS 1-32 and 1-28 a series of 5 swab tests were performed to obtain a sample from deeper within the formation at the proposed injection depth (see Table 4-1 for sample depths). These samples were collected in a similar way to the DSTs, with the difference being in the manner in which the water was pumped from the formation. After the wells were cased, they were perforated between the desired interval

(Table 4-1). The well filled with water and a bailer was dropped into the well to retrieve the water. The first phase of water retrieved from all tests was black with iron sulfide precipitates and then became relatively clear. Once the water was clear it was continuously monitored for temperature (°C), pH, conductivity (µS/cm), resistivity, oxidation reduction potential (ORP) (mV), dissolved oxygen (DO) (mg/l) and salinity using a HACH® Hydromet Hydrolab® MS5® Water Quality Multiprobe (Cat. No. 003078HY). The Hydrolab® was connected to a hand-held PDA (Trimble® Recon® handheld 400 64/256 Yellow BT/802; Cat. No. 69670) for display and recording of values for each measurement. The Hydrolab® was calibrated for pH (using pH buffers of 4 and 7) and conductivity (standards of 0.500 mS/cm [Cat. No. 013770HY] and 47.6 mS/cm [Cat. No. 013650HY]). Once the water achieved stability within about 10% the water was sampled in the same manner as the DST samples. The samples were prepared for analysis by High Resolution Inductively Coupled Plasma Mass Spectroscopy (HR-ICP-MS) in the same manner as was described for ICP-OES and IC for DST samples. HR-ICP-MS was run at Activation Laboratories® (Ancaster, Ontario) using a Element2® (Finnigan®, Germany) using a dilution factor of 1000. Standard measurements and calculated standard deviations of major elements measured by HR-ICP-MS are presented in Table 4-3.

Analyte Symbol	Ca	Fe	Li	Mg	Mn	Na	Sr	K
Unit Symbol	µg/L	µg/L	µg/L	µg/L	µg/L	µg/L	µg/L	µg/L
Detection Limit	5	1	0.05	0.2	0.05	5	0.01	1
Analysis Method	HR-ICP-MS	HR-ICP-MS	HR-ICP-MS	HR-ICP-MS	HR-ICP-MS	HR-ICP-MS	HR-ICP-MS	HR-ICP-MS
NIST 1643e	31398	97	18.65	7519.4	37.48	18707	322.27	2129
NIST 1643e	31512	97	18.94	7793.7	37.31	18707	320.13	2128
Certified Value	32300+-1100	98.1+-1.4	17.4+-1.7	8037+-98	38.97+-0.45	20740+-260	323.1+-3.6	2034+-29
STDEV	491.398	0.538	0.819	258.972	0.912	1173.962	1.534	54.560

Table 4-3. Standards measured by HR-ICP-MS and calculated standard deviations for major cations.

Field analyses of alkalinity, ferrous iron and total iron were performed using a HACH® DR2800 spectrophotometer. Alkalinity was measured using HACH® method 10239 with the TNT® 870 reagent test (Cat. No. TNT870) with a range of 25 mg/l to 400 mg/l $CaCO_3$. Ferrous iron was measured using HACH® method 8146 with the AccuVac® Ferrous iron reagent (Cat. No. 2514025) with a range of 0.02 mg/l to 3.00 mg/l Fe^{2+}. Field samples were diluted 5:1 with deionized water prior to test to fall within testable range. Total iron was measured using HACH® method 8008 with the AccuVac® FerroVer® iron reagent (Cat. No.

2507025) with a range of 0.02 mg/l to 3.00 mg/l total iron. Field samples were diluted 5:1 with deionized water to stay within range of testing.

Figure 4-4. (A) Monitoring physical chemistry of swabbed water using HACH Hydrolab MS5 at KGS 1-32. (B) Black water produced during the first minute of each swab test. (C) Conducting field analyses of swabbed water.

Stable isotope values of δ^2H and $\delta^{18}O$ for 12 brine samples were measured using stable isotope mass spectrometry (SIMS) (Picarro G1301) in the Stable Isotope Mass Spectrometry Lab in the Department of Biology at Kansas State University. The precision of the Picarro G1301 was ~50 ppmv. After filtering through a 0.2 µm filter to remove particulates, approximately 2 µg of sample was injected into the Picarro water analyzer for determination of δ^2H and $\delta^{18}O$. Inside the Picarro analyzer, the injected water sample was converted to vapor and carried by a N_2 carrier stream to the analyzer where the relative abundance of heavy and

light isotopes was measured. Due to the adsorptive nature of water, there is a slight memory effect between samples as water molecules from one injection linger on the surface of the analyzers internal plumbing. To remove the memory effect, a total of 6 injections were made into the analyzer per sample. The data from the first three were removed from the analysis (due to memory effect), and the last three were averaged (as recommended in the Picarro instrument user‘s manual). The average value represents a raw data point that is then corrected to four secondary standards (Evian bottled water [δ^2H = -71.00‰ and $\delta^{18}O$ = -9.90‰], KSU de-ionized water [δ^2H = -37.05‰ and $\delta^{18}O$ = -6.18‰], El Dorado [δ^2H = -106.00‰ and $\delta^{18}O$ = -14.30‰] and KSU de-ionized enriched water [δ^2H = -2.00‰ and $\delta^{18}O$ = 4.30‰]) that are analyzed along with each batch of samples. The standards have been calibrated to National Institute of Standards and Technology (NIST) accepted standards (Greenland Ice Sheet Precipitation (GISP: δ^2H = -189.5‰ and $\delta^{18}O$ = -4.78‰), Standard Light Arctic Precipitation (SLAP: δ^2H = -428.0‰ and $\delta^{18}O$ = -5.5‰), and Vienna Standard Mean Ocean Water (VSMOW: δ2H = 0‰ and δ18O = 0‰)) (Coplen, 1994). The δ^2H and $\delta^{18}O$ values of the standards span the entire range of expected isotope values for the samples submitted. In order for correction of drift in the analyzer during a batch of samples, a working standard of known isotope ratios was analyzed every four samples. Finally, the raw isotope data was corrected to the three standards analyzed with the measured water samples.

Supercritical Flow-Through Experiment

Flow through experiments were conducted using the Core Flow System 839Z apparatus at NETL – Pittsburgh, PA. This system uses a Hassler type core holder that enables high confining pressure and temperature settings (see Fig. 4-5 for Hassler cell diagram). Confining pressure is applied by pumping deionized water in the core holder to a specific pressure, monitored by a gauge (see Fig. 4-6). The core holder is located in a oven that controls the temperature of the experiment. Fluid used to flow through the core is stored in two 2 liter accumulators (Fig. 4-7. These accumulators are controlled by two separate pumps that regulate the flow rate and pressure that is introduced into the core. The pumps force deionized water into the accumulators where it pushes a piston, forcing the fluid into the piping leading to the core holder (see Fig. 4-8). Brine is stored in one accumulator while the second houses the CO_2. The CO_2 accumulator is chilled to around 4°C to keep the CO_2 in a

liquid phase. The CO_2 will become supercritical when it enters the core holder. The two fluids mix when they pass through the core. This two-phase flow is intended to simulate a near injection zone scenario. The fluids pass through the core at a rate determined by the pumps and the porosity of the core and exit down stream in a single pipe (see Fig 4-7). This down stream flow passes through two back pressure regulators that step down the pressure of the fluid to room temperature. One of the back pressure regulators is heated to prevent the freezing of the CO_2 when it becomes depressurized. Samples for geochemical analyses were collected at the end of the downstream piping.

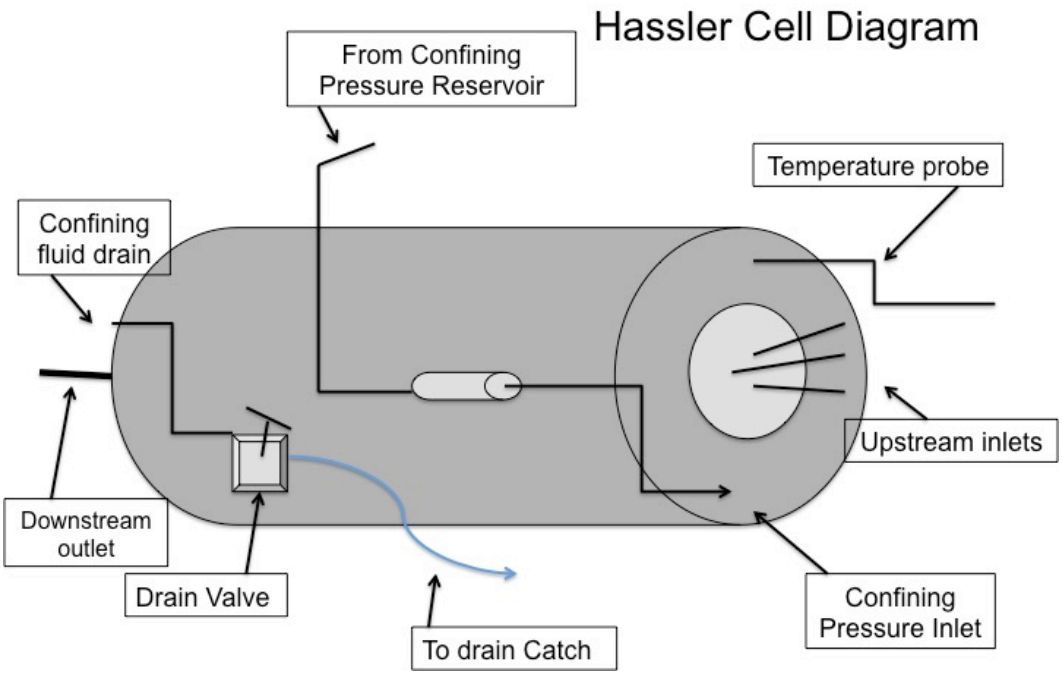

Figure 4-5. Diagram of Hassler-type cell used in NETL flow experiment.

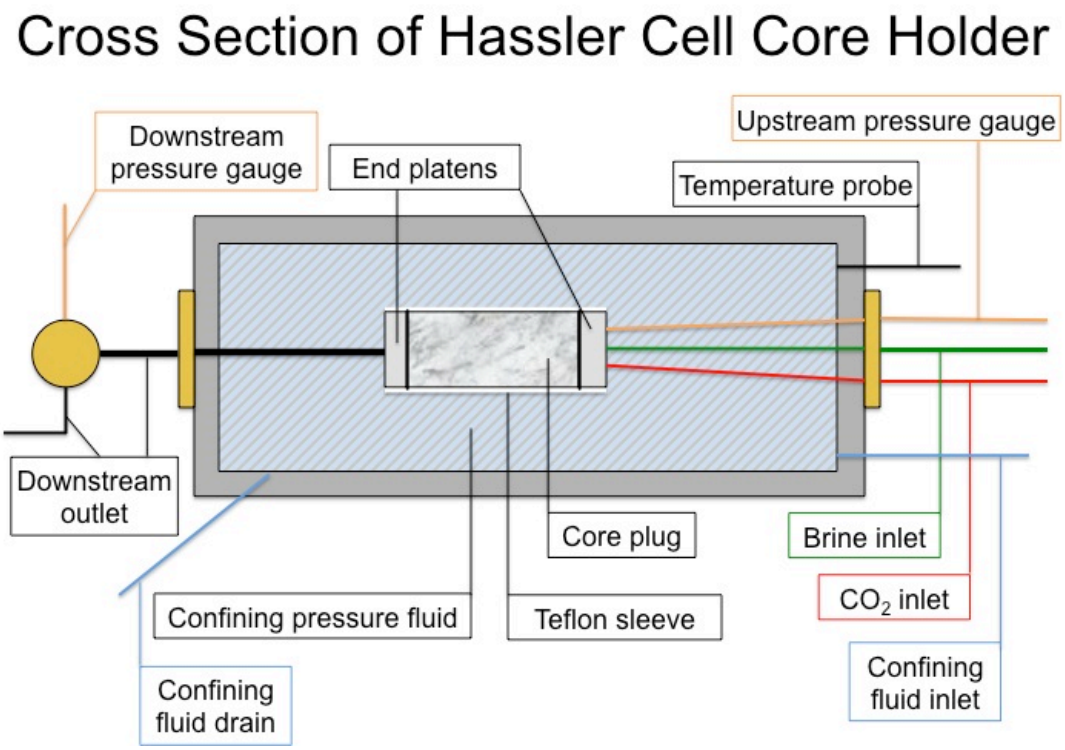

Figure 4-6. Cross section of core holder with major components and piping labeled.

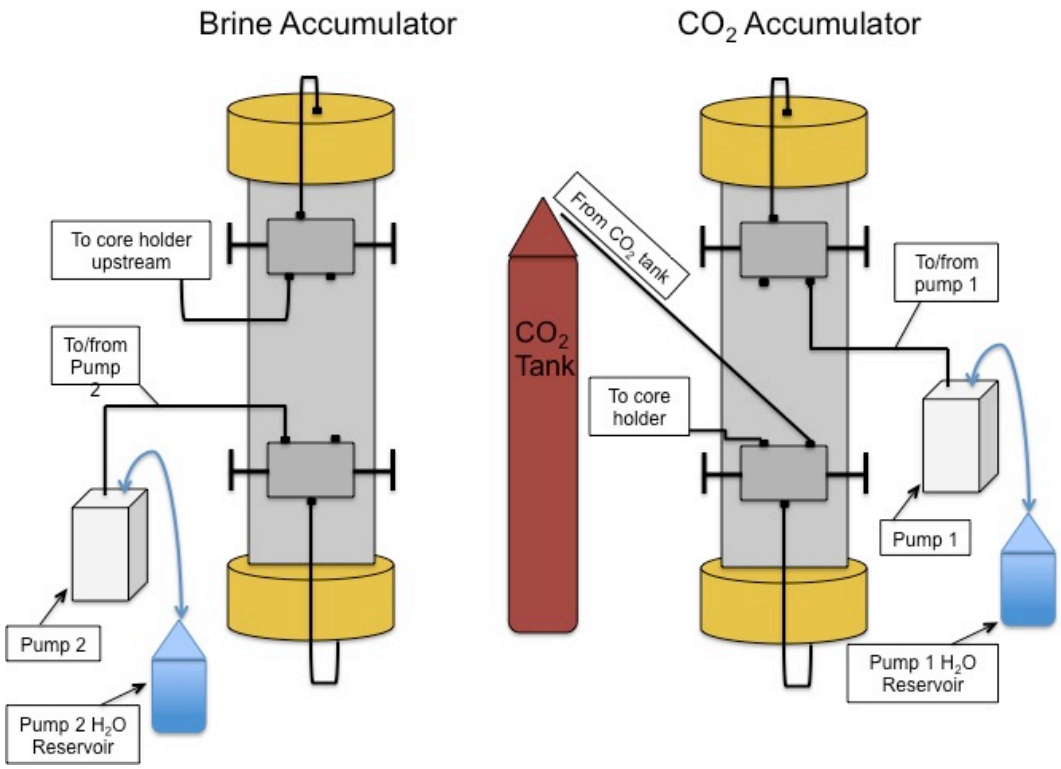

Figure 4-7. Diagram of CO_2 and brine accumulators used to introduce fluid to core.

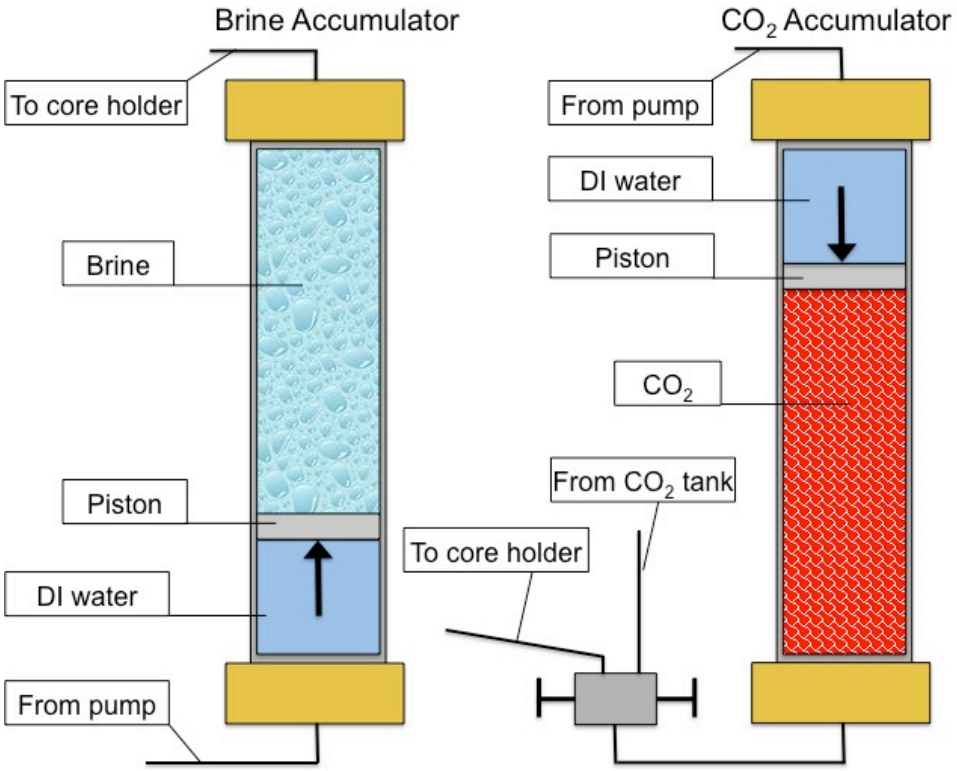

Figure 4-8. Cross section of accumulators showing how fluid is introduced.

The core plug (depth 4977', sample 31-19) was wrapped in a heat shrink Teflon sleeve according to the instrument protocol and inserted into the Hassler type core holder. Confining pressure of 2100 psi was applied to the core holder. Temperature was set to 40°C and the system was allowed to equilibrate (T & P corresponding to in situ conditions in the injection zone). Flow began with brine only at 0.2 ml/min for 12 hours to saturate the core and establish equilibrium conditions. After 12 hours, brine flow was stopped and the core was flooded with CO_2 for several minutes, simulating injection of CO_2 and the initial dehydration phase. Two phase flow was initiated with brine and CO_2 being pumped into the core at a constant rate of 1 ml/min and pressure was maintained with a back pressure regulator.

Effluent was collected every hour in 125 ml amber HDPE Nalgene® bottles for ICP-OES and IC analyses by Activation Laboratories (procedure described above). pH was measured as the effluent was collected and alkalinity was measured by spectrophotometer (HACH® TNTplus® 870 total alkalinity, Cat. No, TNT870). The pH and alkalinity measurements do not reflect conditions inside the core and are subject to CO_2 degassing. This would be solved by installing a high temperature pH probe in-line and collecting samples in a

pressurized vessel or by using a spectrophotometric method as developed by Shao et al (2012). Future flow experiments hope to utilize these instruments and techniques.

Chapter 5 - Results

Mineralogical Characterization

Mineralogical results obtained from XRD, SEM and thin section are presented in this chapter. Dolomite and microcrystalline quartz are the most abundant minerals found within the Arbuckle formation. Certain zones show an abundance of iron sulfide/oxide minerals. Several unidentified argillaceous minerals are present in minor abundance. Important textures that these minerals display in thin section are highlighted here and their significance to geochemical reactions with injected CO_2 are discussed in Chapter 6. Porosity textures displayed in formation rocks are described and presented with photomicrographs. Three intervals of interest within the Mississippian and Arbuckle formations have been chosen for detailed description in this chapter. Thin sections from these intervals are described to show depth-wise changes in mineralogy. Core plug and thin section samples are referenced using their depth in feet followed a unique sample number. For example: 4955.85` (30-56). Due to large amounts of data, see Appendix A for data not presented in this chapter, including core plug and thin section descriptions and additional XRD analyses.

XRD

X-ray diffraction of samples has revealed the dominant mineralogy of the Arbuckle to be dolomite with lesser amounts of microcrystalline quartz. The presence of quartz in samples masked peaks of minor minerals, such as pyrite, that were observed in thin section otherwise. All of the samples analyzed had dolomite and quartz as the dominant minerals, similar to Figure 5-1. See Appendix A for the rest of the XRD graphs.

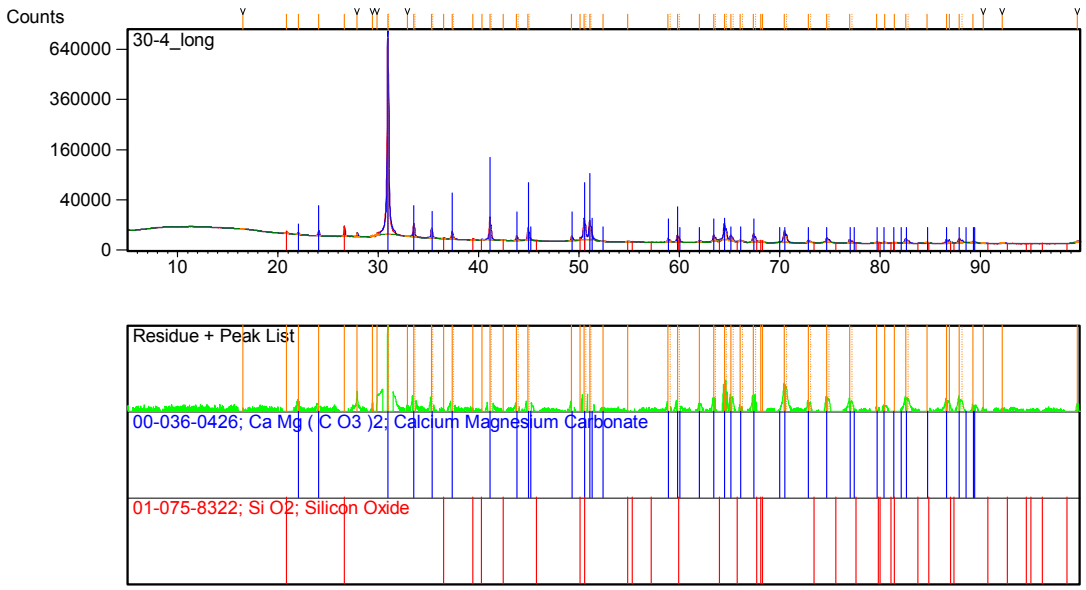

Figure 5-1 XRD Analyses of 30-4 (4903`) from the top of the proposed injection zone. Note strong dolomite and quartz peaks, the most common pattern observed in the Arbuckle.

Dolomite Mineralogy and Textures

Dolomite is the most common mineral in the Arbuckle and displays a diversity of habits in its occurrence throughout the formation (Fig. 5-2). The most common occurrence is a fine to coarse grained intergrown mosaic of dolomite (Fig. 5-2, A & B). This replacement mosaic most likely formed early in the diagenetic history of the Arbuckle as it is cross cut by fractures, silica nodules and argillaceous zones. Some depths reveal the mosaic to be entirely fine grained or entirely coarse grained. A few depths have a mixed/graded fine to coarse grained texture with other depths showing distinct zones of fine and coarse grained dolomite. Pore spaces are commonly filled with large, euhedral dolomite crystals that are more recent than the mosaic (Fig. 5-2, D & F). Some large fractures and vugs are filled with saddle dolomite (Fig. 5-2, E & G). The saddle dolomite displays its diagnostic sweeping extinction in thin section and is commonly associated with Fe oxide/sulfide minerals. Certain cores from specific depths contain dolomite that shows zoning with dark interiors of crystals surrounded by a clear outer rim(Fig. 5-2, D).

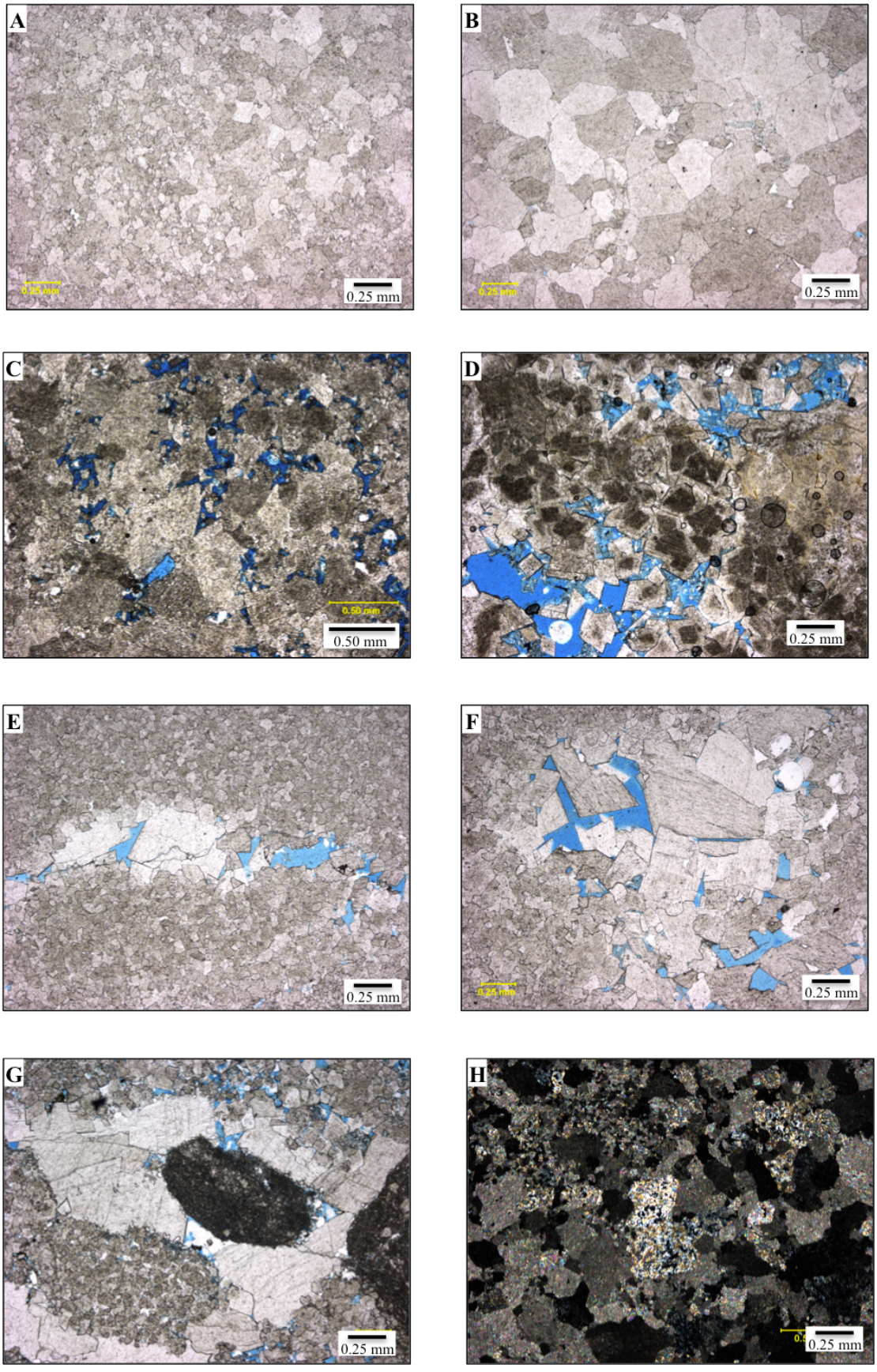
A
0.25 mm
B
0.25 mm
C
0.50 mm
D
0.25 mm
E
0.25 mm
F
0.25 mm
G
0.25 mm
H
0.25 mm

Figure 5-2. Dolomite in the Arbuckle. A) 4955.85` (30-56), PPL, 4x zoom; Fine grained inter-grown anhedral dolomite replacement mosaic. B) 4916.6` (30-17), PPL, 4x zoom; Large grained intergrown anhedral dolomite replacement mosaic. C) 4925.7` (30-26), PPL, 4x zoom; Large grained, subhedral to anhedral dolomite crystals. Fine grained dolomite growing in pore spaces. D) 4979.1` (17-27), PPL, 4x zoom; Porous dolomite with subhedral to euhedral dolomite rhombs growing in porous zones. Interiors of rhombs are cloudy with a rim of clear dolomite. Some wispy red Fe-oxide is present in crystal boundaries. E) 4187.75` (13-3), PPL, 4x zoom; Fracture filling dolomite, large rhombs grow into fracture in fine grained dolomite mosaic. F) 4923.7` (30-24), PPL, 4x zoom; Large dolomite rhombs growing into 2 mm size vug in fine grained dolomite mosaic. G) 4187.0` (12-47), PPL, 4x zoom; Large, inter-grown vug-filling saddle dolomite (sweeping extinction evident in cross polarized light, refer to thin section supplemental file). Dark nodule of fine grained dolomite with high organic matter. H) 4937.05` (30-38), XPL, 4x zoom; Coarse grained dolomite mosaic. Silica is observed replacing the dolomite crystals. Note dark specks in mineral grains as replacement silica.

Silica Mineralogy and Textures

Silica is extremely common throughout the Arbuckle and can be found in a variety of forms (Fig. 5-3). Silica most commonly occurs as microcrystalline chert, forming nodules. Nodules can range from <0.25 mm to a few cm. Chert nodules can display a layering, with a thin brown layer between each layer of silica. This brown layer could be a Fe carbonate mineral such as siderite or organic matter. Other chert nodules display a pattern of silica textures that repeats at various depths. This pattern typically consists of a boundary layer or radiating chalcedony followed by microcrystalline quartz and finally with large grained megaquartz mosaic filling the interior of the nodule. This is a common texture found in chert nodules (Alonso-Zarza et al, 2002). Chalcedony occurs as small spherule as well, with a well-defines radiating habit, indicative of void filling chalcedony (Hesse, 1989). Some large chert nodules do not display any sort of ordering as described above. They contain random arrangements of elongate quartz, microcrystalline chert and mosaic megaquartz crystals (0.25-0.1 mm). Silica can be observed filling small pore spaces and filling in fractures. Highly porous silica textures are common in the lower Arbuckle. These textures could be the result of

dissolution or could indicate recent silica precipitation. Opaque oxide/sulfide minerals are commonly observed as inclusions in nodules and in porous silicified zones. Boundaries between chert and dolomite commonly have an abundance of opaque oxide/sulfide minerals.

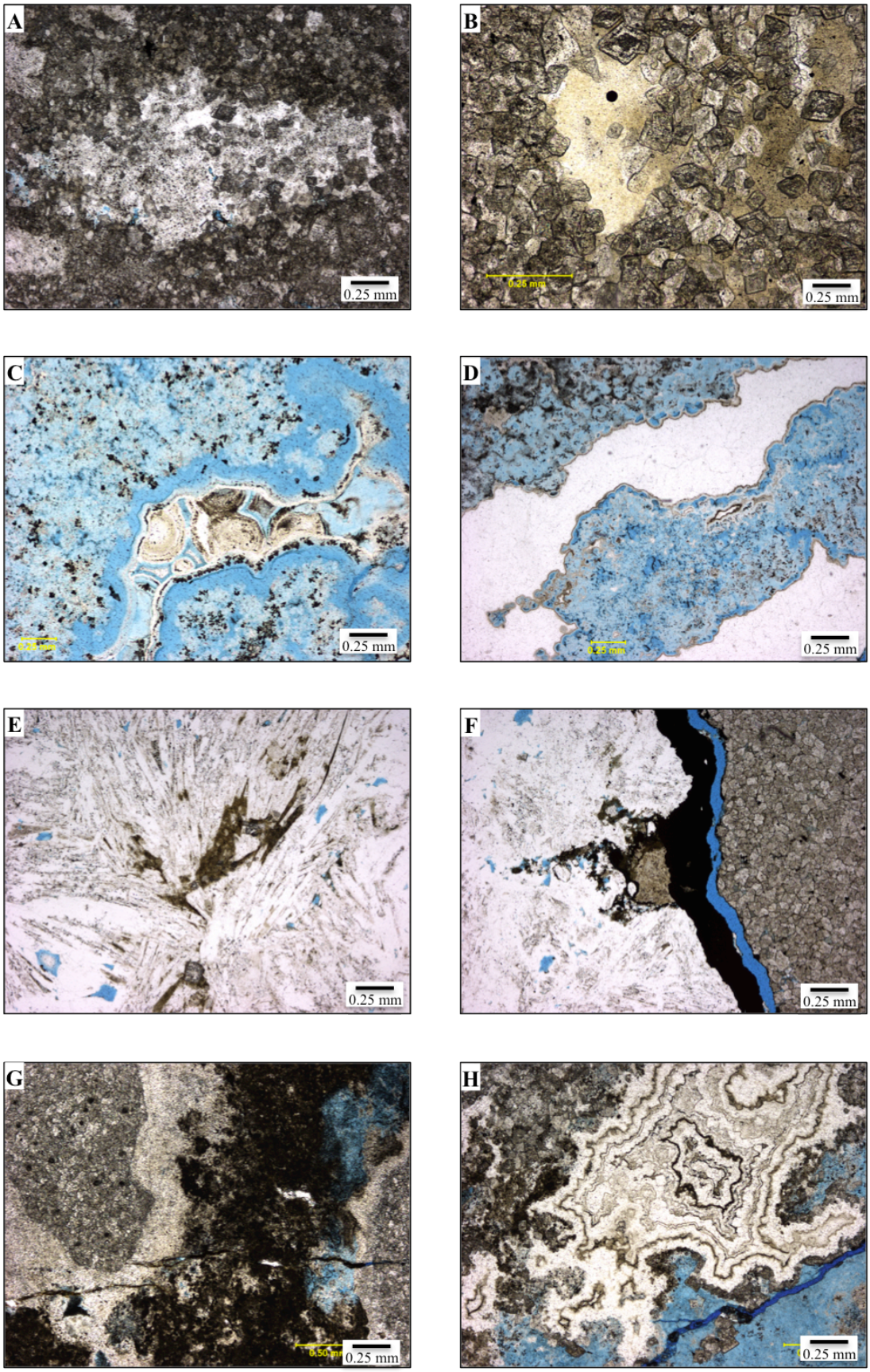
A
0.25 mm
B
0.25 mm
C
0.25 mm
D
0.25 mm
E
0.25 mm
F
0.25 mm
G
0.25 mm
H
0.25 mm

Figure 5-3. Occurrence of silica within the Arbuckle. A) 4977.8` (31-19), PPL; Chert nodule filling small vug in dolomite. Isolated dolomite rhombs embedded in microcrystalline chert. B) 4515.3` (19-51), PPL; Microcrystalline quartz nodule filling vug and surrounding pore space. Isolated dolomite rhombs in silica; microcrystalline quartz specked with pyrite. C) 4955.85` (30-56), PPL; Rounded chalcedony in porous silicified matrix. Dark, opaque specks are pyrite. D) 4955.85` (30-56), PPL; large grained megaquartz chert with rim of microcrystalline chert and chalcedony. Porous silica texture is prevalent along with pyrite. E) 4504.0` (19-41), PPL; Elongated, lathe-like quartz crystals with inclusion of clay material. Small anhedral quartz crystals surrounded by elongated crystals. F) 4504.0` (19-41), PPL; Silica texture as described in E in contact with Fe rich mineral filling fracture between dolomite replacement mosaic and chert. Accumulation of pyrite at silica-dolomite boundary demonstrates the potential for the development of preferential reaction paths along similar boundaries. G) 4985.75` (31-27), PPL; Microcrystalline chert surrounding dolomite "island". Partially silicified clay rich matrix present as dark band in center of image with another chert rimmed dolomite "island" in bottom right corner. H) 4985.75` (31-27), PPL; Chert nodule exhibiting layered appearance. Dark layer between chert layers could be Fe-carbonate or organic matter. Nodule grew inward, as is typical of silica gels. Chert fills porosity in dolomite surrounding the nodule.

Oxide, Sulfide and Argillaceous Minerals and Textures

In addition to extensive dolomite and chert throughout the formation, opaque oxide/sulfide minerals are present in minor abundance throughout the formation. These minerals occur in a wide variety of forms, as evident in Figure 5-4. XRD analysis could not identify minor amounts of these minerals and could have been masked by strong quartz peaks. So while an exact identification by XRD is not available, the opaque mineral is most likely pyrite, as in its associated studies under thin section and will be referred as such throughout the discussion.

Pyrite is observed as small inclusions in dolomitic matrix and as large 0.25 mm nodules in argillaceous matrix. Laminations 0.2 mm wide occur at chert-carbonate boundaries

and between zones within dolomite. The opaque minerals can be observed as coating the edges of pore spaces and sometimes completely filling the pore space. Pyrite nodules up to 0.25 cm are observed in fractures and are associated with saddle dolomite. Pyrite also occurs as small inclusions in chert nodules and in porous silica textures.

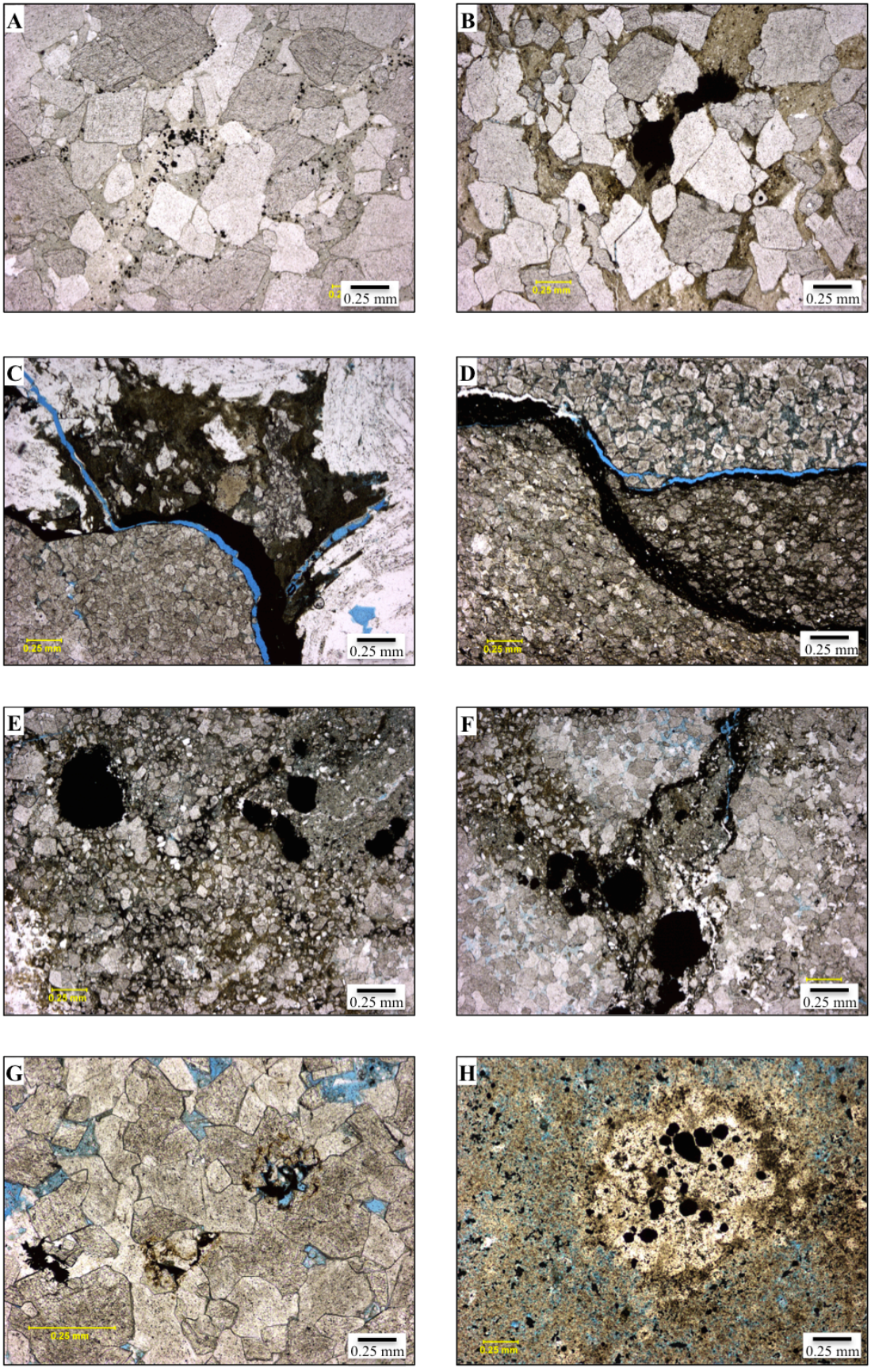
A
0.25 mm
B
0.25 mm
C
0.25 mm
0.25 mm
D
0.25 mm
0.25 mm
E
0.25 mm
0.25 mm
F
0.25 mm
G
0.25 mm
0.25 mm
H
0.25 mm
0.25 mm

Figure 5-4. Oxide, sulfide and argillaceous minerals. A) 4570.1 (20-50), PPL; Coarse grained dolomite mosaic with dolomicrite cement. Small pyrite crystals in dolomitic cement. B) 4570.1 (20-50), PPL; Coarse grained dolomite with argillaceous matrix. Large pyrite nodules in matrix with numerous small pyrite crystals in matrix. C) 4504.0 (19-41), PPL; Fe oxide/sulfide filling fracture between fine grained dolomite mosaic and chert nodule. Brecciated area with dolomite and argillaceous material between oxide/sulfide layer and chert. D) 4388.8 (17-36), PPL; Lamination of black Fe oxide/sulfide along bedding plane. E) 4388.8 (17-36), PPL; Large pyrite nodules in argillaceous dolomite. Abundant pyrite is filling porosity within clay material. F) 4388.8 (17-36), PPL; Large pyrite nodules associated with argillaceous material infilling permeable zone through dolomite. G) 4365.8 (17-3), PPL; Coarse grained dolomite mosaic with pyrite filling walls of pore spaces. H) 4515.3 (19-51), PPL; Chert nodule with pyrite inclusions. Pyrite abundant in porous, silicified matrix.

Porosity

Porosity is highly variable throughout the Arbuckle. Some depths with a tight dolomite mosaic have no porosity visible in thin section. Some dolomite mosaics have isolated intercrystalline porosity. Micro fracture porosity is common and can be observed crosscutting different textures. Some fractures and large pores have dolomite rhombs growing, which has reduced porosity over time. Well connected intercrystalline porosity is observed as well, though is less common. These zones usually have some degree of porous matrix material. In the upper Arbuckle we see the dissolution of peloids and sponge spicules, forming mouldic porosity. Vugs are common throughout the formation, and are usually partially filled with dolomite rhombs. Porous silica is common in the lower Arbuckle, with potential preferential flow paths evident. See Chapter 6 for NMR well logs and porosity measurements conducted by Weatherford Laboratories.

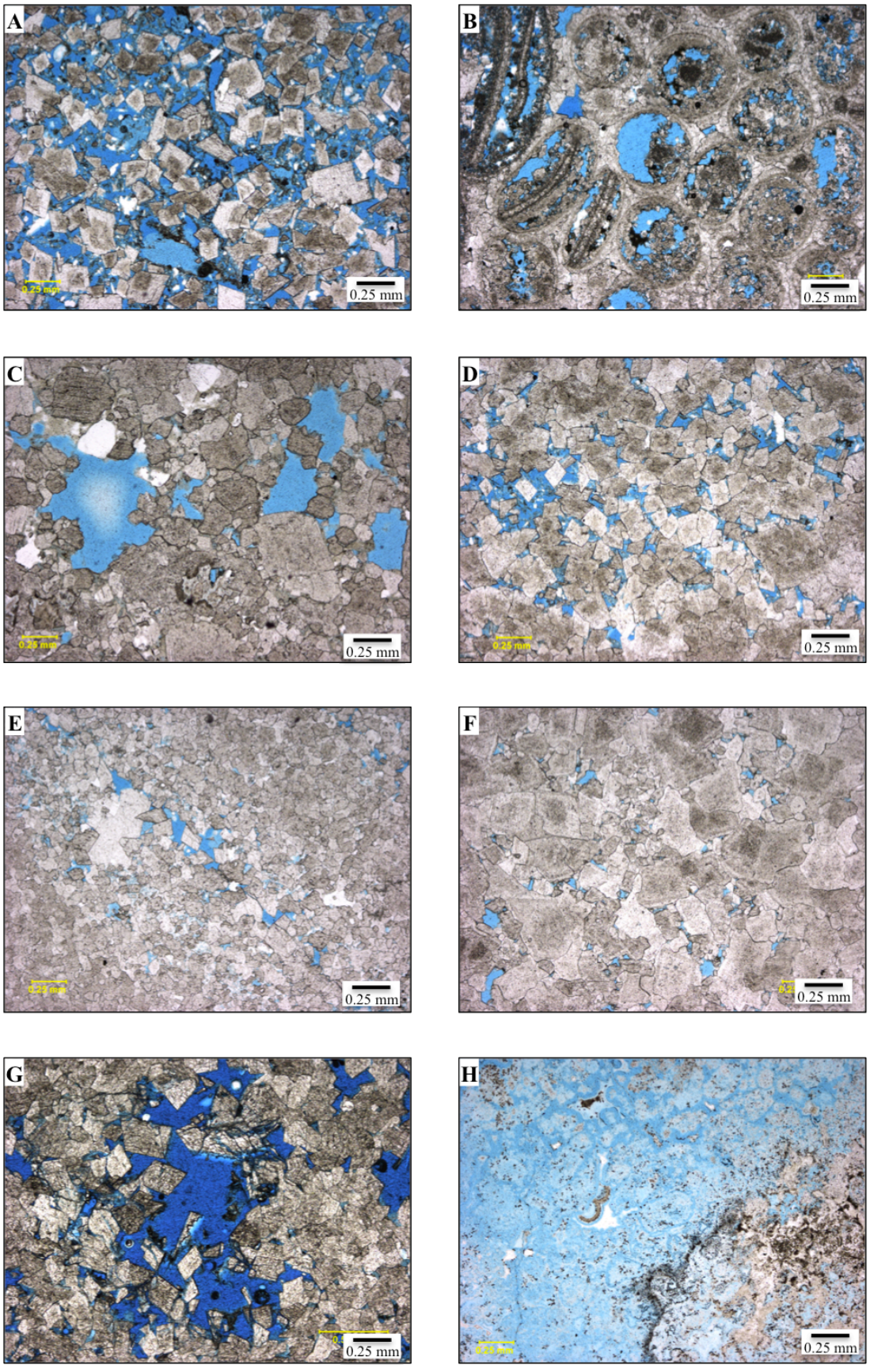
A
0.25 mm
B
0.25 mm
C
0.25 mm
D
0.25 mm
E
0.25 mm
F
0.25 mm
G
0.25 mm
H
0.25 mm

Figure 5-5. Porosity Textures. A) 4365.8` (17-3), PPL; High well connected (intercrystalline) porosity within dolomite. Clay and micritic dolomite creating matrix porosity. B) 4187 (12-47), PPL; Dissolved peloids and sponge spicules create a mouldic porosity texture. Pores are not well connected. C) 4923.7 (30-24), PPL; Mixed intercrystalilne and pinpoint vug porosity with minimal connectivity. D) 4365.8 (17-3) PPL; Zone of connected intercrystalline porosity within low porosity dolomite mosaic. E) 4187.2 (13-3), PPL; Partially filled fracture with moderate intercrystalline porosity. F) 4916.6 (30-17), PPL; Isolated intercrystalline porosity with little to no connectivity. G) 5074.6 (33-25), PPL; Isolated 2 mm size vug with euhedral dolomite crystals growing. H) 4955.85 (30-56), PPL; Highly porous silicified matrix. Almost all material is micritic silica with some dark oxides.

SEM Micrographs

SEM images of core plug 31-19 (4977`) are presented in Figure 5-6. Plug 31-19 is an autoclastic breccia within the middle portion of the injection zone and shows significant silicification. In Figure 5-6, A, B and C show a area in increasing magnification, as do D, E and F images. These images show the chert-carbonate boundary in detail. Euhedral dolomite is visible with some surface imperfections and micro fractures (Fig. 5-6, A & F). These features allow for greater surface area which can speed up geochemical reactions with acidified brine. Authegenic quartz crystals can be observed along the outer edge of the chert nodule (Fig. 5-6, F). This same feature is observed in thin section where large quartz crystals form the outer edge of chert nodules and microcrystalline chert and chalcedony fill the nodule. Large, vuggy pore spaces are visible and are a result of past brecciation.

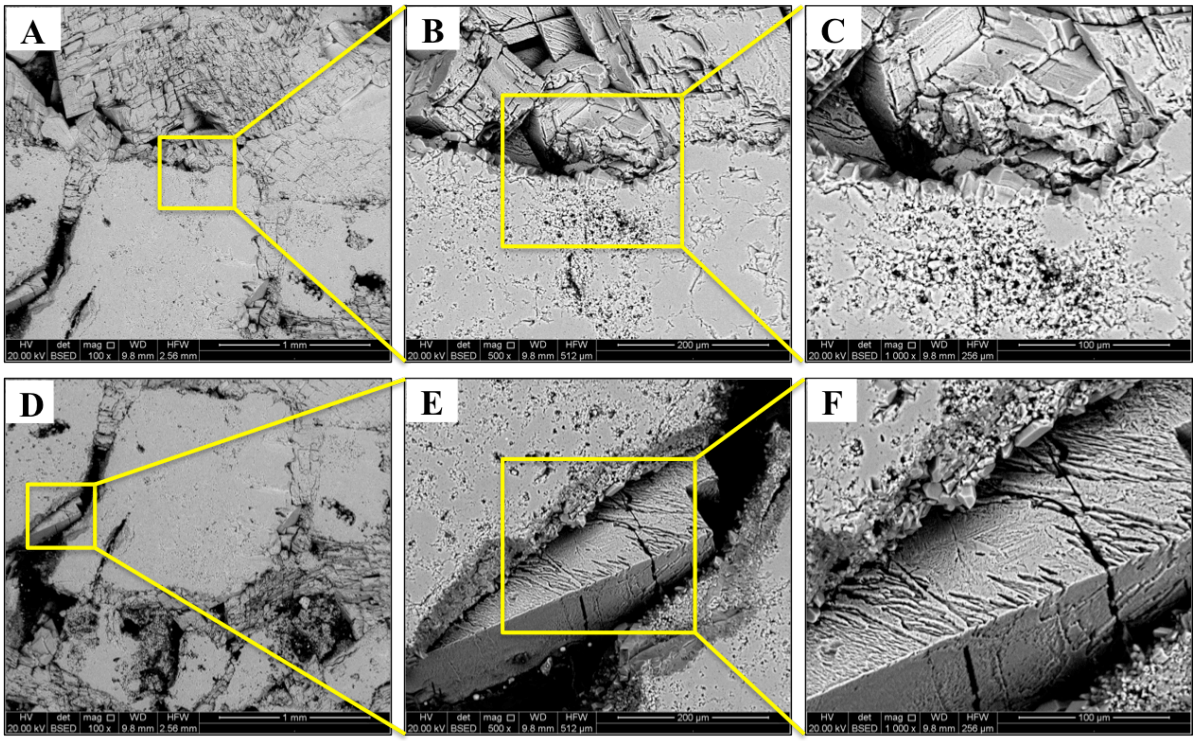

Figure 5-6. SEM micrographs of core plug 31-19. Two sets of images show progressive magnification (A & D 100x; B & E 500x; C & F 1,000x).

CT Scans

CT scan images reveal the internal structure of core plugs. Core plug 31-19 (4977`) from the middle injection zone and 33-5 (5054`) from the bottom of the injection were imaged and studied. Core 31-19 is within the proposed injection zone, used in flow experiment and was scanned before and after the flow experiment to document any changes that occurred during the course of the experiment. The before and after montages are presented in the flow-through experimental results section (see Figs. 5-22 and 5-23). The image montages presented in Figure 5-7 and 5-8 represent 1 mm slices of the core plug along the horizontal axis (A) and the vertical axis (B). These images are combined in a montage and assigned a color gradient that defines the density of the core plug. The bright (hot) colors represent dense material and the dark (cold) colors represent less dense material or open spaces. Core 31-19 is an autoclastic breccia and the heterogeneity in internal structure can be observed in the CT scan. The white areas are dense chert deposits while the dark areas are open flow pathways. Examination of the vertically oriented montage (Fig 5-7, B) reveals no single flow path through the core, though there are a few vugs and occasional porous zones throughout the

core. This core has significant mineral and textural heterogeneity as revealed by thin section and SEM studies. CT scans reflect that heterogeneity through a wide range of densities.

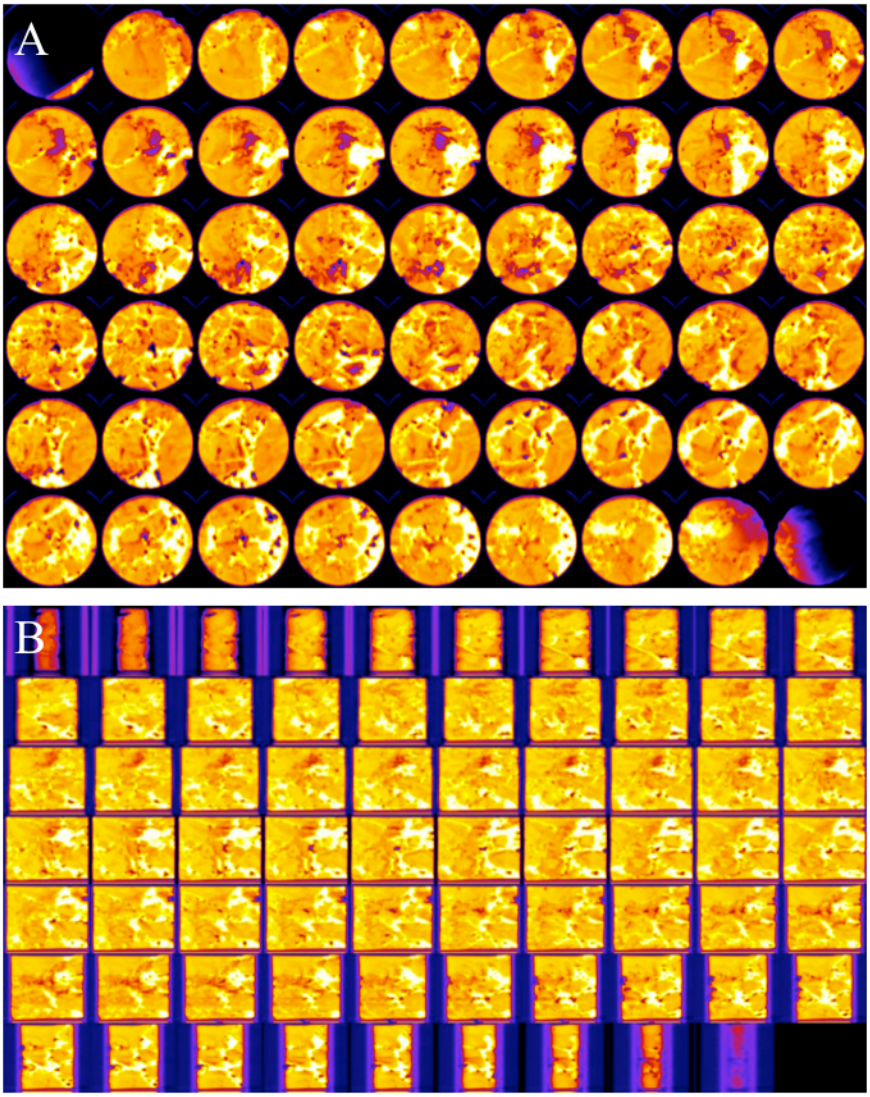

Figure 5-7. CT scan image montage of core 31-19 (4977`). 1 mm slices along the horizontal axis (A), and the vertical axis (B). Colors represent density with the bright (hot) colors being the most dense while dark (cold) colors are least dense (e.g. porosity).

A second core was scanned but not used for the flow experiment. Core plug 33-5 (5054`) is from the deepest point in the proposed injection zone and differs greatly from core 31-19 described above. 33-5 is a homogenous dolomite with a few millimeter to centimeter scale vugs. It has no evidence of sillicification and is exclusively dolomite. It is a representative sample of a tight, well crystallized dolomite that is common in the Arbuckle. Only bright colors are visible in this core plug with the exception of a few vugs (black areas).

Some small vugs are isolated in the interior of the core, but are not connected by porous dolomite. Because of its low porosity, CO_2 acidified brine attempting to flow through this rock will most likely develop worm holes where the acidified brine can pass quickly through.

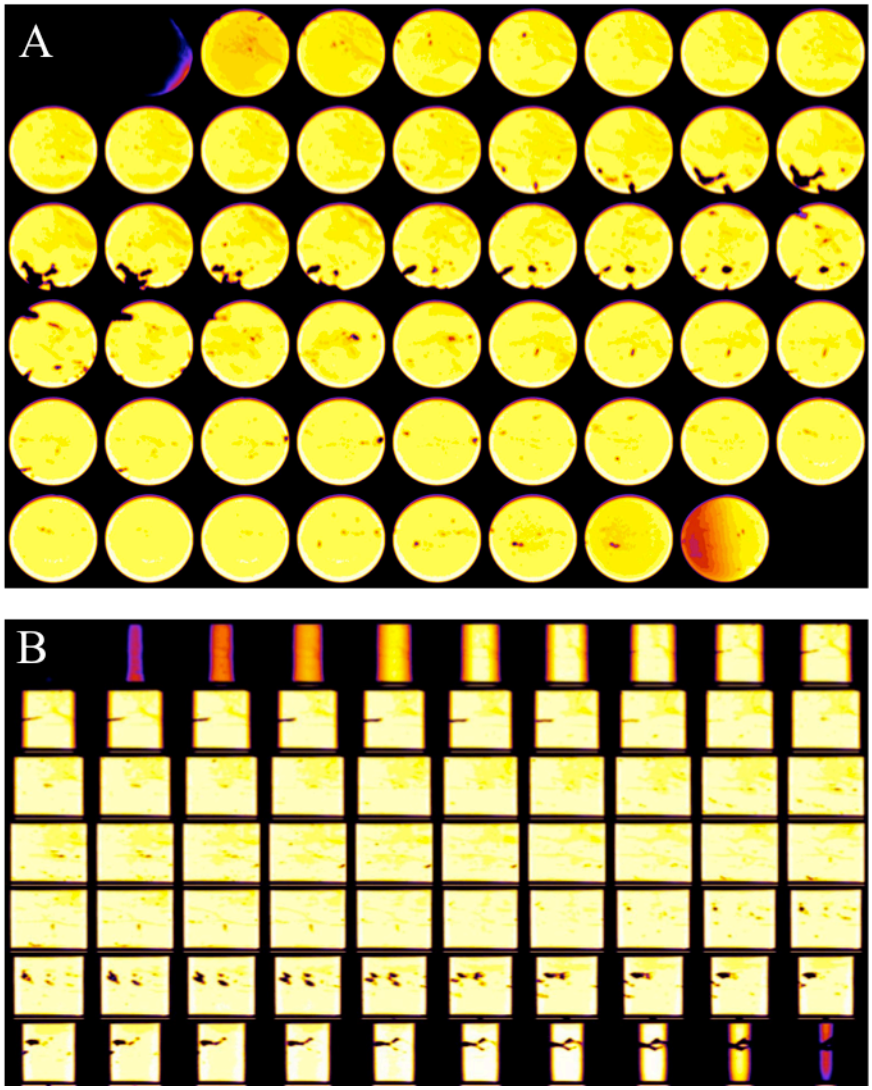

Figure 5-8. CT scan image montage of core 33-5 (5054`). 1 mm slices were examined along the horizontal axis (A), and the vertical axis (B). Colors represent density with the bright (hot) colors being the most dense while dark (cold) colors are least dense.

Intervals of Interest

The mineralogy of three intervals within the Mississippian and Arbuckle formations are highlighted below with thin section descriptions and images. These intervals are the economically important Mississippian pay zone, a potential baffle zone in the upper Arbuckle

(differentiating the lower and upper Arbuckle) and the proposed CO_2 injection zone. Remainder of thin section data are presented in Appendix A and supplemental files.

Mississippian Pay Zone Mineralogy

The Mississippian pay zone is not in the Arbuckle, but is the oil producing zone of the Mississippian oil reservoir overlying the Arbuckle. The mineralogy of this zone is important to this study because of the potential for enhanced oil recovery with the injection of CO_2. This secondary project has the potential to increase production yields, adding economic benefit to the CO_2 sequestration project.

This interval encountered in KGS 1-32 is a cherty dolomite mudstone with a significant amount of tripolite chert. The tripolite chert facies is an important producing facies in central Kansas and is described as containing sponge spicules, chert microporosity, dissolution and vuggy porosity and clay infilling fractures (Watney, 2000). Chert nodules larger than 1 cm were observed in thin section with microporous chert as a matrix between micritic dolomite rhombs. Depth 3686` displays a non-tripolite chert variety. The chert at this depth displays radial undulose extinction, common in evaporate replacement cherts in a low temperature setting (Hesse, 1989). Possible anhydrite crystals were observed in thin sections at this depth that could be undergoing chert replacement. Three thin sections from this depth are described below and images presented in Figure 5-9.

3670.6` (3-11)

Fine grained cherty dolomite with subhedral to euhedral micritic dolomite rhombs. Chert is abundant as infilling porosity and present as microporous tripolitic matrix. Oil stain in dolomite as parallel oriented splotches are present. Silicified sponge spicules and fossil fragments are common. Few opaque minerals are present as small (<0.2 mm) crystals infilling porosity.

3681.95` (3-22)

Fine grained cherty dolomite with subhedral to euhedral micritic dolomite rhombs. Common <2 cm size porous chert nodules with micritic dolomite inclusions. Presence of microporous tripolitic chert matrix. Oil stain visible in dolomite and chert nodules and is present as parallel splotches.

3686.9` (3-27)

Fine grained porous dolomite with large quartz crystals growing, some euhedral. Highly birefringent mineral, likely anhydrite, present partially filling vug size pores and growing around dolomite. Quartz appears to be replacing anhydrite(?) and displays fibrous habit and radial undulose extinction typical of evaporite replacement silica.

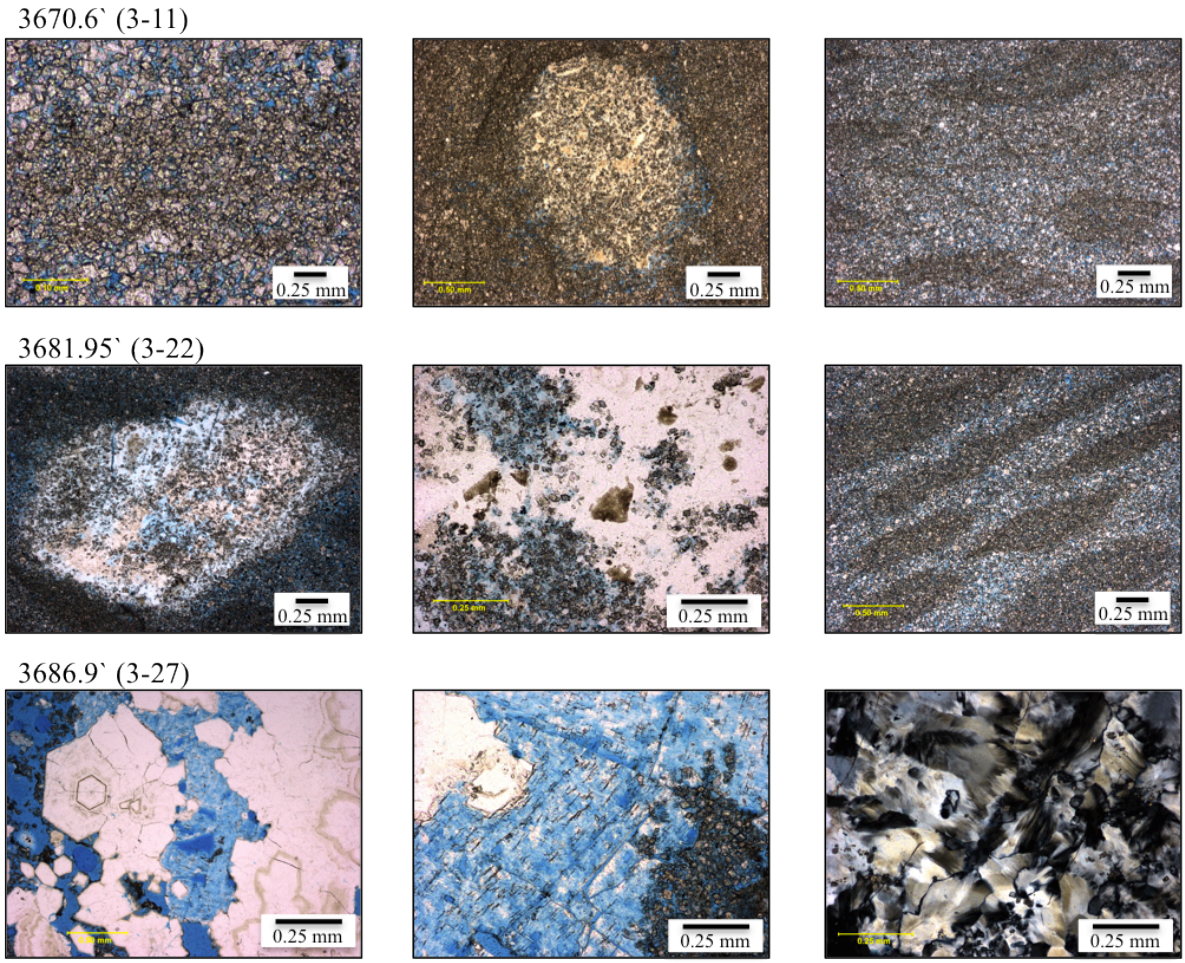

Figure 5-9. Mississippian Pay Zone Thin Sections

Baffle Zone Mineralogy

A low porosity zone has been identified between 4300` and 4550` using data compiled from whole core analyses and NMR logs. This low porosity zone could act as a baffle, or barrier to flow, as scCO2 migrates through the formation. This low flow zone has implications for geochemical reactions as the CO_2 could become more reactive as it has more time to react with formation minerals.

This interval is a dolomitic packstone with an increasing abundance of chert, argillaceous material, and sulfide minerals towards the lower section of the interval. The upper portion of this zone is porous with large dolomite rhombs infilling vugs and fractures. chert and clay material is not present in the upper portion of this zone. Abundant argillaceous material in the lower baffle zone reduced porosity significantly. Coarse grained dolomite replacement mosaic with little to no porosity is common in the lower baffle zone interval. Images and descriptions from 6 thin sections from this interval are presented in Figure 5-10.

4365.8` (17-3)

Coarse to fine grained intergrown dolomite mosaic with subhedral to anhedral crystal habit. Coarse grained dolomite exists in distinct zones. Few highly porous zones with small euhedral dolomite crystals and quartz crystals growing. Sporadic black, opaque oxide/sulfide mineral present. Few chert nodules with radiating chalcedony habit throughout.

4379.1` (17-27)

Coarse grained dolomite mosaic with subhedral to euhedral habit. Euhedral dolomite grains are large. High porosity with some silicification evident, euhedral dolomite crystals surrounded by porous silicified matrix. Dolomite is cloudy throughout with some crystals displaying a dark interior with lighter rim, suggesting biogenic influence on dolomitization. Area of large quartz and chert growing with no evidence of banding. Some porous zones have reddish clay material in association with opaque oxide/sulfide. Reddish stain also present in dolomite crystals suggesting Fe coatings.

4388.8` (17-36)

Coarse to fine grained dolomite with subhedral to euhedral habit. Some area contain a clay-matrix supported dolomite. Large nodules (0.25 mm) and smaller crystals of opaque oxide/sulfide mineral common in matrix supported areas. Dolomite crystals near fractures appear to be dissolving and replaced by clay material. Large silica nodule (>1 cm) present with a combination of microcrystalline quartz and megaquartz. Some inclusions of dolomite rhombs in chert nodules. Boundary between chert and dolomite fractured and filled with opaque oxide/sulfide mineral. Oxide/sulfide occurs as thin (<0.25 mm) laminations. Fracture porosity and matrix porosity common throughout. Fractures filled with clays and contain many black, opaque oxide/sulfide minerals.

4504.0` (19-41)

Fine grained dolomite mosaic in contact with larger chert nodule. Some zones of argillaceous material. Chert/silica is main mineral in this thin section. Elongated quartz crystals intergrown with megaquartz. Chert nodule isolated from zone of coarsely grained intergrown crystalline dolomite with subhedral habit by a large fracture (0.2 mm). Fracture filled with black, opaque oxide/sulfide mineral. Argillaceous zones contain euhedral dolomite rhombs and small chert nodules with opaque oxide/sulfide minerals. Fractures common in argillaceous zone.

4515.3` (19-51)

Coarse to fine grained intergrown dolomite mosaic with subhedral to anhedral habit. Porous zones contain some small euhedral dolomite rhombs. Some areas of fine grained dolomite with silicified micritic matrix. Large saddle dolomite being dissolved and replaced by porous silica. Small chert nodules surrounded by dolomite overgrowth. Zone of porous argillaceous material with abundance of opaque oxide/sulfide minerals. Fractures (<0.2 mm) common in the argillaceous zone, some filled with dolomite while others are filled with chert.

4570.1` (20-50)

Coarse grained dolomite mosaic with some clay/carbonate matrix support. Abundance of opaque oxide/sulfide minerals in matrix material. Some matrix appears dark and clay rich and appears to be healing fractures or filling flow paths. Visible porosity is low.

4365.8` (17-3)

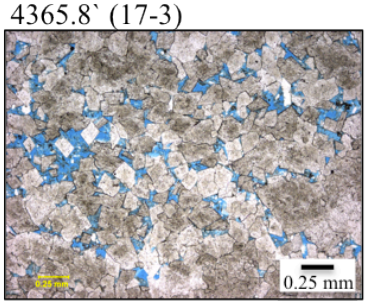

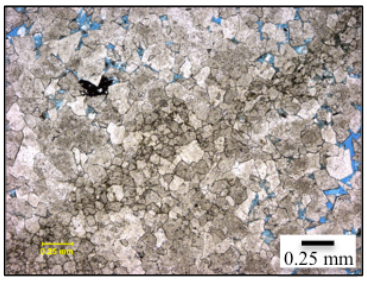

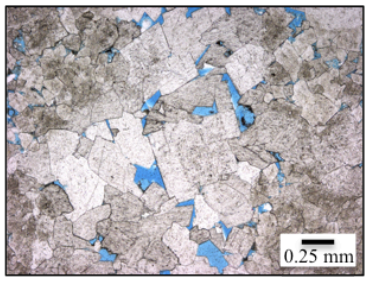

4379.1` (17-27)

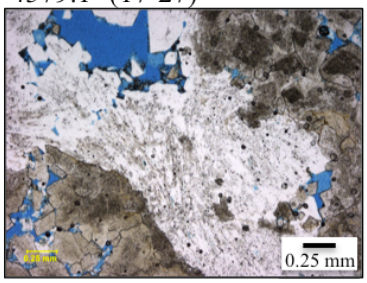

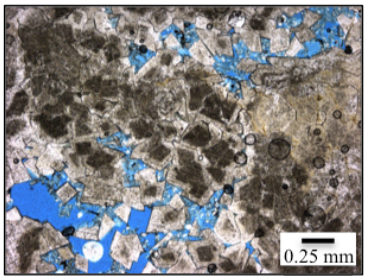

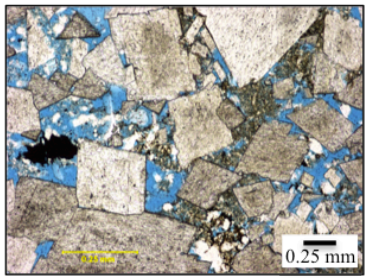

4388.8` (17-36)

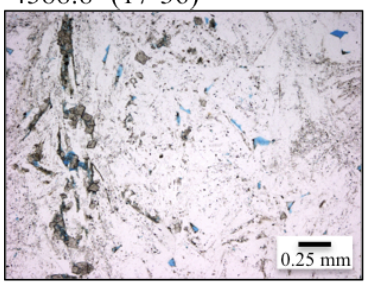

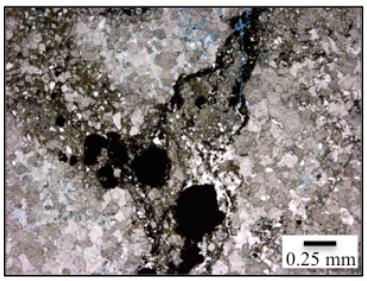

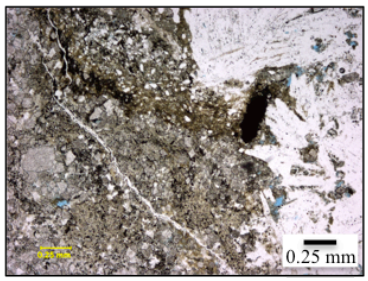

4504.0` (19-41)

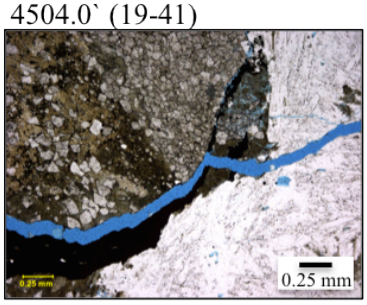

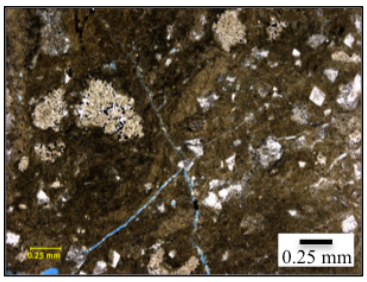

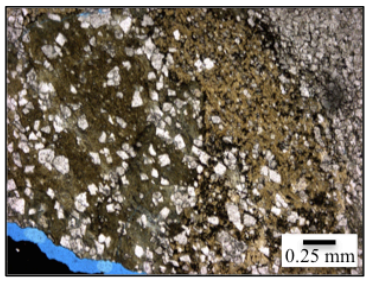

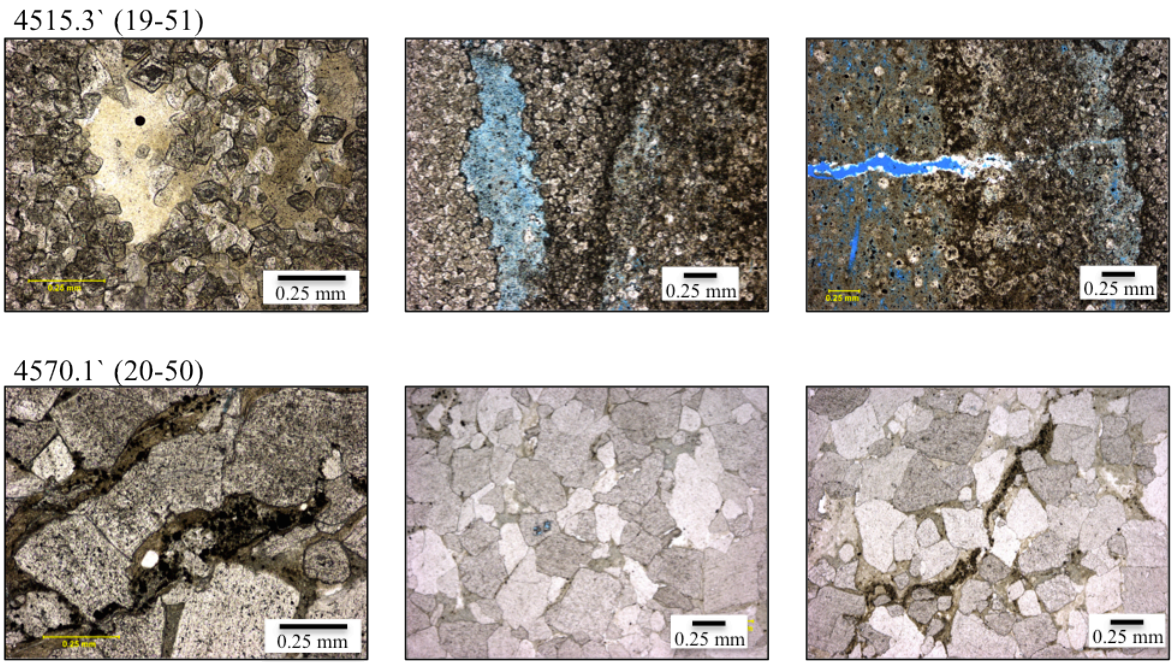

Figure 5-10. Baffle Zone Thin Sections

Injection Zone Mineralogy

The proposed CO_2 injection zone (~4900`-5050`) was the most important to characterize for this study because this zone will be exposed to injected CO_2 first. High porosity and permeability values provide an ideal zone for the injection of a large amount of CO_2 into the formation at this depth. Porosity and permeability data of the core plugs have been provided through whole core analyses completed by Weatherford Laboratory. NMR porosity values were obtained during the logging of KGS 1-32 and provided by the Kansas Geologic Survey and are presented in Chapter 6.

The injection zone is mainly a dolomitic packstone-wackstone becoming a cherty packstone in the lower portion of the interval. Zones of autoclastic breccia have also been identified. Dolomite replacement mosaic is predominant in the upper injection zone with an absence of significant chert nodules. A chert rich zone between 4970` and 5030` is observed. This zone has high porosity and an abundance of sulfide minerals and some argillaceous zones. The silica rich zone is confirmed with geochemical logs presented in Chapter 6. Thin section images and descriptions from 12 core pugs from the injection zone are presented in Figure 5-11.

4903.8` (30-4)

Fine grained subhedral to anhedral intergrown dolomite mosaic prevalent throughout. Dolomite crystals appear cloudy possibly due to organic matter inclusions or other impurities. Dolomite is exclusive mineral at this depth and displays replacement texture. Low intercrystalline porosity visible in thin section with some cm size vugs. Porosity was measured at 3.4%.

4916.6` (30-17)

Mixed coarse to fine grained intergrown dolomite mosaic. Crystals have with subhedral to anhedral habit with euhedral dolomite growing into large pore spaces. Small pores (<0.25 mm) create isolated, intercrystalline porosity throughout this depth. Some small opaque oxide/sulfides present in pore spaces.

4923.7` (30-24)

Coarse to fine grained intergrown crystalline dolomite with subhedral to anhedral habit. Some large euhedral dolomite crystals in porous zones. Chert nodules abundant with detrital quartz grains interspersed within coarse grained dolomite. Chert infilling of porosity near large grained dolomite crystals. Low, isolated vuggy porosity. Styolitic boundary between dolomite textures with more chert appearing as a matrix material.

4925.7` 30-26

Coarse to fine grained subhedral to anhedral dolomite mosaic with a large range in grain sizes. Some larger crystals appear to have undergone dissolution. Dolomite crystals are cloudy indicating the inclusion of organic matter. Well connected intercrystalline and matrix porosity are found at this depth. Some pores have a reddish brown (oxide/clay) coating. Porosity was measured at 5.2% from whole core analysis.

4937.05` (30-38)

Coarse grained subhedral to anhedral intergrown dolomite mosaic. Several silica textures are observed at this depth. Silica is observed partially replacing large dolomite crystals (?). These crystals retain their original morphology as they are replaced by the silica in small patches. Silica is observed infilling porosity between dolomite crystals. These pore filling silica nodules are less than 0.2 mm. A few opaque oxide/sulfide minerals are also present filling pore spaces. Porosity is low due to silica precipitation and was measured at 1.8%.

4949.4` (30-50)

Fine to coarse grained intergrown crystalline dolomite with subhedral to anhedral habit. Fine and coarse grained dolomite is well mixed throughout the thin section and do not occur in distinct zones. Some large euhedral dolomite growing in porous zones. A few zones of opaque oxide/sulfide infilling pores around dolomite. No silicification evident. Low, isolated intercrystalline porosity throughout. Micro fracture cross cuts dolomite mosaic.

4955.85` (30-56)

Fine to coarse grained intergrown dolomite mosaic with subhedral to anhedral habit. Distinct boundary between dolomite zone and highly silicified zone. Silicified zone dominated by porous, silicified matrix with large nodules of chert displaying radiating chalcedony habit. Chert nodules display layering with chalcedony at the border followed by microcrystalline chert and finally megaquartz in the center. Some chalcedony has brown color in plain light. Megaquartz is observed in contact with dolomite. Porous silicified zone appears to have skeletons of chalcedony and other chert nodules and could have undergone dissolution.

4967.4` (31-9)

Fine to coarse grained intergrown crystalline dolomite mosaic with subhedral to anhedral habit. Coarse and fine grained dolomite are well mixed and do not appear in distinct zones. Chert/chalcedony is observed infilling porosity with some 2.5 mm nodules of microcrystalline chert. Matrix of dolomicrite in some areas. Some opaque oxide/sulfide minerals throughout. Low fracture and isolated intercrystalline porosity.

4977.8` (31-19)

Highly silicified with various silica textures visible. Silicification concentrated in fracture boundaries and within pore spaces. Silica nodules have chalcedony outer edges with larger quartz grains in the interior. Silicification of carbonate mud evident with some isolated islands of carbonate mud(?)/dolomicrite(?) matrix still present. Euhedral quartz grains observed with a secondary, fracture filling dolomite growing around. Porosity is controlled by extensive fractures with slight porosity visible in silicified matrix. Porosity was measured at 8.8%. Large euhedral saddle dolomite infilling fractures. Saddle dolomite is associated with opaque oxide or sulfide minerals.

4985` (31-27)

Extremely heterogeneous dolomite and silica textures throughout this depth. Fine grained dolomite mosaic is prevalent. Saddle dolomite is observed filling large fractures and is associated with an opaque mineral, possibly an oxide or sulfide. Abundance of dolomicrite in some zones with matrix porosity. Partial silicification of dolomicrite and infilling of porosity is extensive. Silica nodules have layered appearance with oxide (?) precipitate separating the layers. Silica occurs as chalcedony, chert and megaquartz. This range of silica types can be observed in nodules where larger quartz crystals occur in the center while smaller, more fibrous chalcedony occurs at the margins. Chert nodules have isolated islands of dolomite mosaic. Fractures are observed crosscutting silica nodules and dolomite mosaic. Porosity was measured at 4.7% and occurs mainly as fracture and matrix porosity.

4990.1` (32-5)

Coarse to fine grained intergrown crystalline dolomite with subhedral to anhedral habit. Low isolated, intercrystalline porosity present. Small opaque oxide/sulfides. No evidence of silicification

5054.6` (33-5)

Coarsely crystalline, intergrown subhedral to anhedral dolomite mosaic. No evidence of dolomite dissolution. No silicification visible in thin section. Vuggy porosity with some isolated intercrystalilne porosity. Porosity measured at 2.3%. Quartz grains and small opaque mineral uncommon throughout.

4903.8` (30-4)

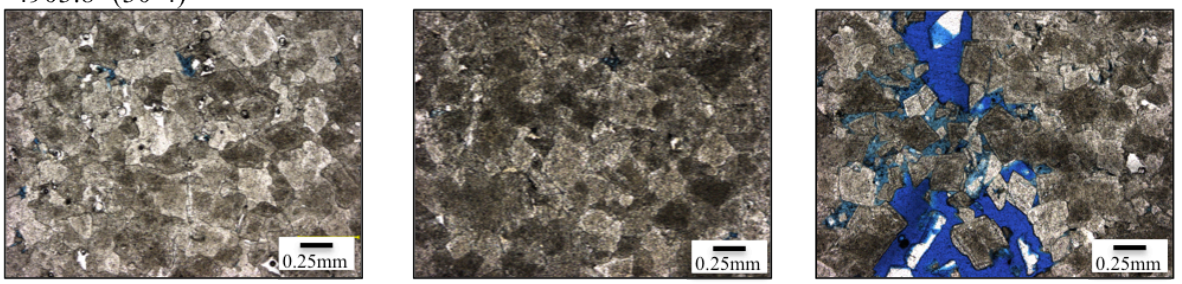

4916.6` (30-17)

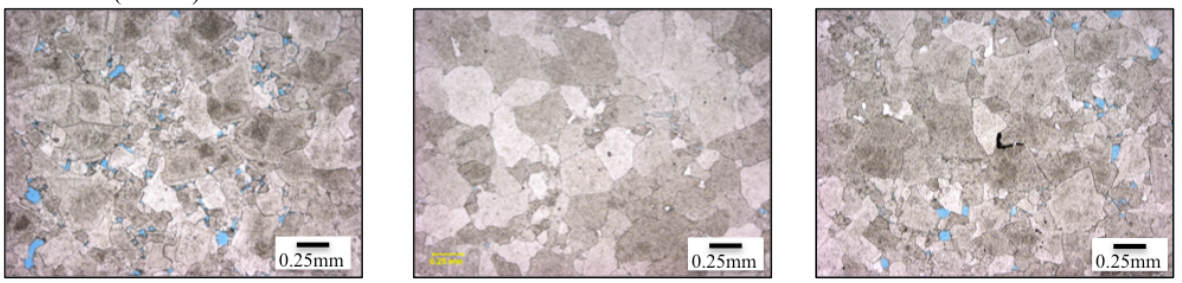

4923.7` (30-24)

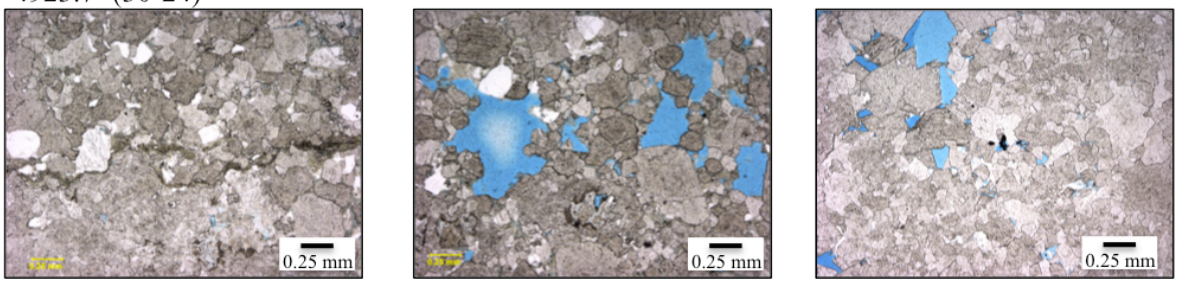

4925.7` (30-26)

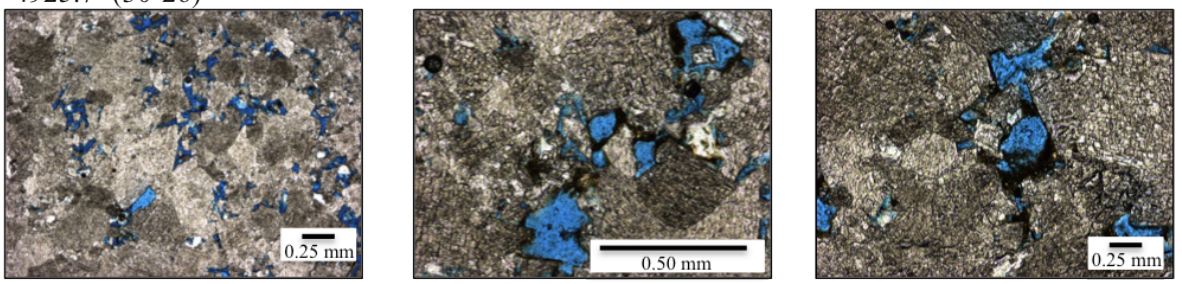

4937.05` (30-38)

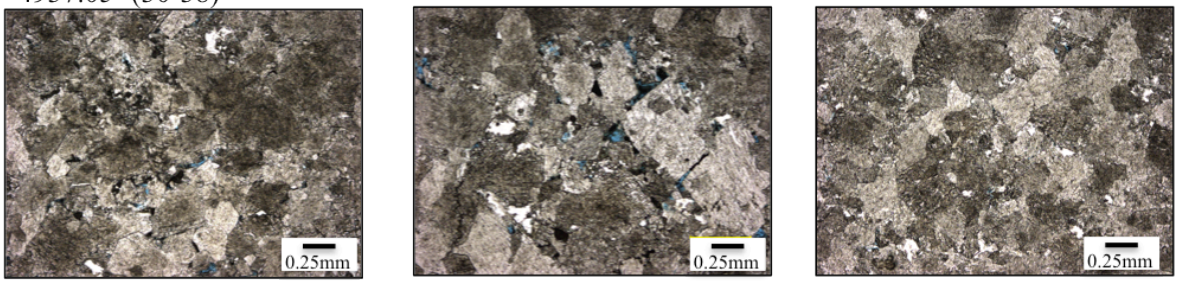

4949.4` (30-50)

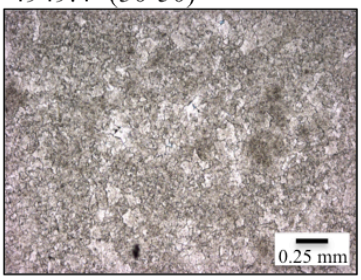

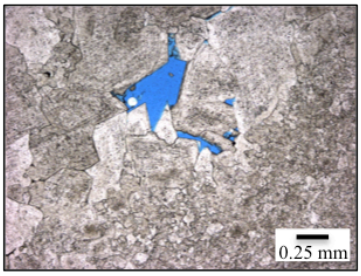

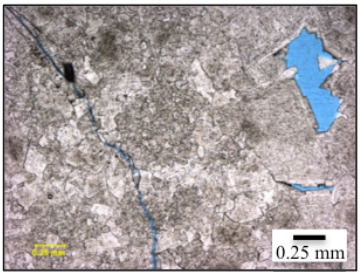

4955.85` (30-56)

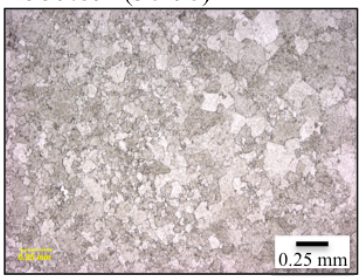

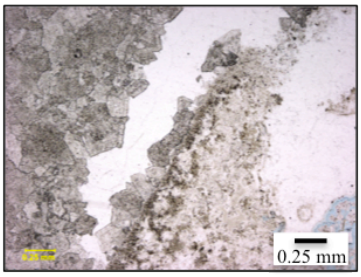

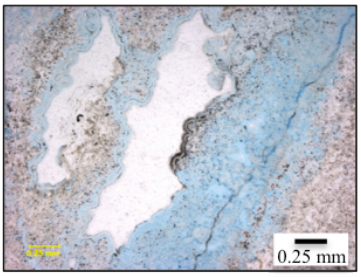

4967.4` (31-9)

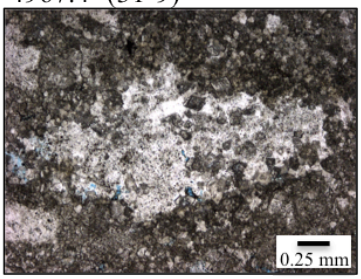

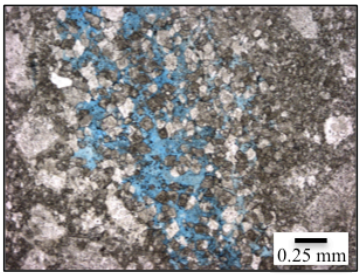

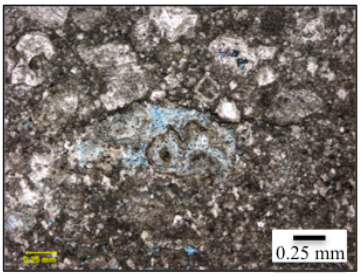

4977.8` (31-19)

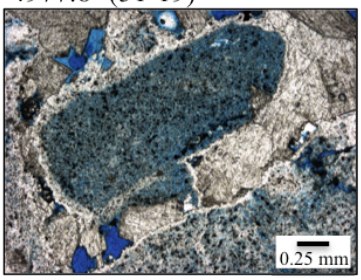

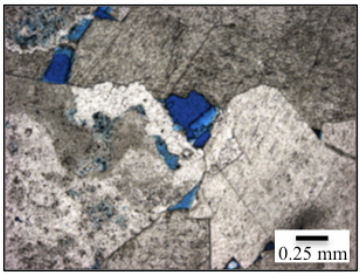

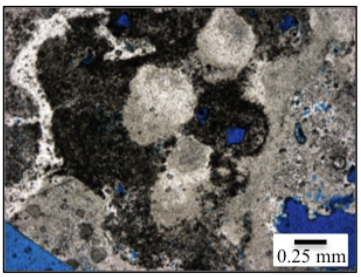

4985.75` (31-27)

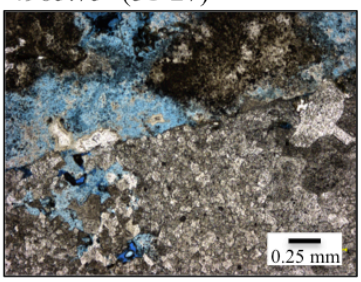

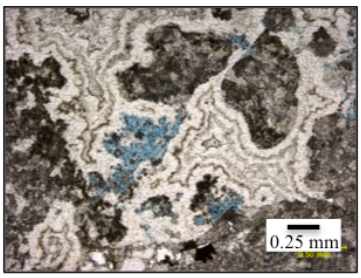

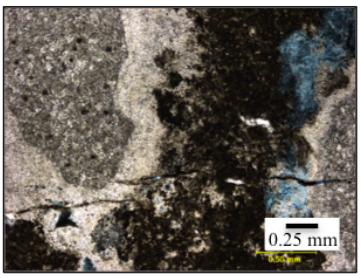

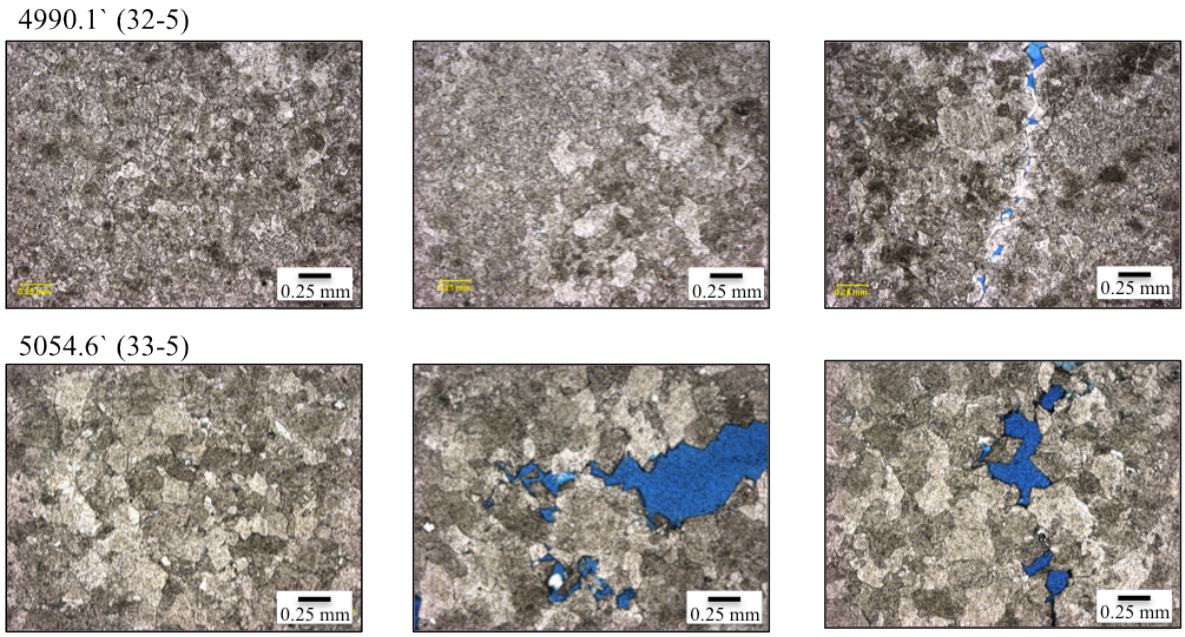

Figure 5-11. Injection zone thin section images.

Hydrogeochemistry Results

Analyzed brine samples obtained from wells KGS 1-32 and 1-28 are plotted to represent a vertical profile of the Arbuckle aquifer, demonstrating changing hydrogeochemistry with depth. The Arbuckle is a Na-Ca-Cl type brine with total dissolved solid (TDS) values ranging from 54,002 at the shallowest (4182`) to 191,717 mg/l at the deepest depth (5036`). pH ranges from 6.4 to 7.5 within the Arbuckle with total alkalinity values between 124 and 378 mg/l HCO_3^-. On a piper diagram, the Arbuckle brines plot to the left on the quadralinear plot, indicating the brine is becoming more enriched in Ca^{2+} and Mg^{2+} with depth (Fig. 5-12). Lower Arbuckle data is clustered in the piper diagram while the upper Arbuckle samples are somewhat set apart and more depleted in Ca^{2+}. This shift to the right for the upper Arbuckle indicates possible influence of meteoric water and has been previously described by Dingman (1968) for Cambro-Ordovician waters in Kansas. The increasing importance of Ca^{2+} with depth can be seen in the cation ternary diagram in Figure 5-10. The major elemental composition and physical parameters of the brine in the Mississippian, Arbuckle and Reagan sandstone/granite wash formations can be found in Table 5-1. The complete composition can be found in Appendix B.

			mg/L	mg/L	mg/L	mg/L	mg/L	mg/L	mg/L	µg/L	mg/L	mg/L	mg/L	mg/L
Well	**Sample Name**	**Depth**	**K**	**Mg**	**Mn**	**Ca**	**Fe**	**Na**	**S**	**Sr**	**Cl**	**Br**	**SO_4**	**CO_3**
1-32	**DST 1**	**3677**	702	1890	0.89	11300	0.29	58000	233	417000	119,000	464.0	703	42
1-32	**DST 4**	**4182**	347	347	1.17	1500	0.09	15900	271	55400	30,500	79.7	873	192
1-32	**DST 3**	**4335**	424	460	0.59	2150	0.07	17400	553	71300	32,000	75.9	1610	180
1-32	**Swab 5**	**4380**	398	933	3.80	3907	12.84	25585	-	132335	47,598	97.1	986	375
1-32	**DST 2**	**4520**	834	880	1.10	5030	0.05	31500	345	158000	65,800	120.0	1060	124
1-32	**Swab 4**	**4875**	900	1764	2.21	10527	1.77	50565	-	324045	103,326	190.9	543	280
1-28	**DST 8**	**4876**	1280	1450	0.61	8670	0.16	48400	247	262000	102,000	176.0	3320	134
1-28	**DST 7**	**4927**	1280	1430	0.70	8820	0.08	48600	208	274000	103,000	198.0	3140	132
1-32	**Swab 3**	**4928**	907	1802	3.06	10550	10.97	49842	-	330609	104,390	196.3	478	378
1-28	**Swab 1**	**5005**	1160	1790	0.2	10600	0.03	57500	136	335000	114000	235	425	199
1-32	**Swab 2**	**5010**	961	1910	1.27	11784	8.68	54791	-	383469	106,013	225.5	389	155
1-28	**DST 6**	**5036**	1430	1630	0.81	10300	0.09	54300	148	334000	118,000	235.0	336	74
1-28	**DST 5**	**5183**	1080	1160	2.20	7310	0.20	38300	136	253000	84,400	190.0	346	-

Table 5-1. Major ion chemistry from DST and swabbed water samples (- indicates data not available).

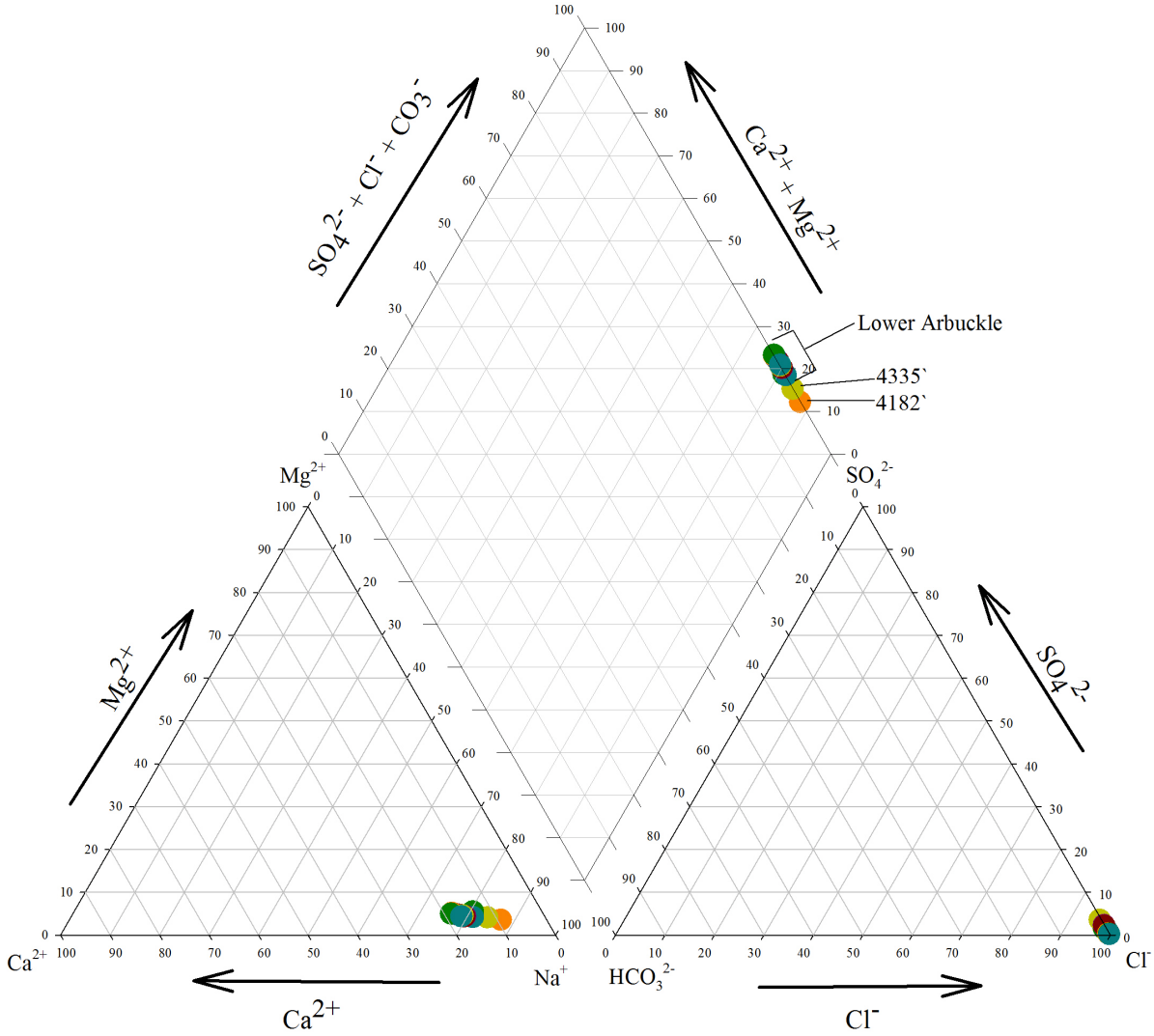

Figure 5-12. Piper diagram of brine from KGS 1-32 and 1-28. Trend of increasing concentration of Cl^- and Ca^{2+} with depth.

Depth Profiles

Figure 5-13 shows the depth profiles of major element concentrations in the Arbuckle, Mississippian and granite wash formations. DST and swab data are plotted as separate trends due to different sampling and analytical methods. The differences in data between sampling and analytical methods are discussed in Chapter 6. Within the Arbuckle, concentrations of major elements increase linearly with depth (Cl^-, Na^+, Ca^{2+}, Sr^{2+}, Mg^{2+}, K^+) while redox sensitive species fluctuate throughout the formation (SO_4^{-2}, S, Fe, Mn, P).

It is evident from the depth profiles that the chemistry of the overlying Mississippian aquifer is significantly different than the trend observed within the Arbuckle. In general

salinity values are higher and concentrations of trace metals, such as Zn, W, Pb and Sb, are higher in the Mississippian aquifer.

The chemistry of the Regan Sandstone/granite wash formation below the Arbuckle displays different chemical composition as well. This is expected since it is a sandstone layer in contact with a 'granite wash' formation and the crystalline granitoid basement rock. The formation water has lower concentrations of major elements than the deepest Arbuckle samples.

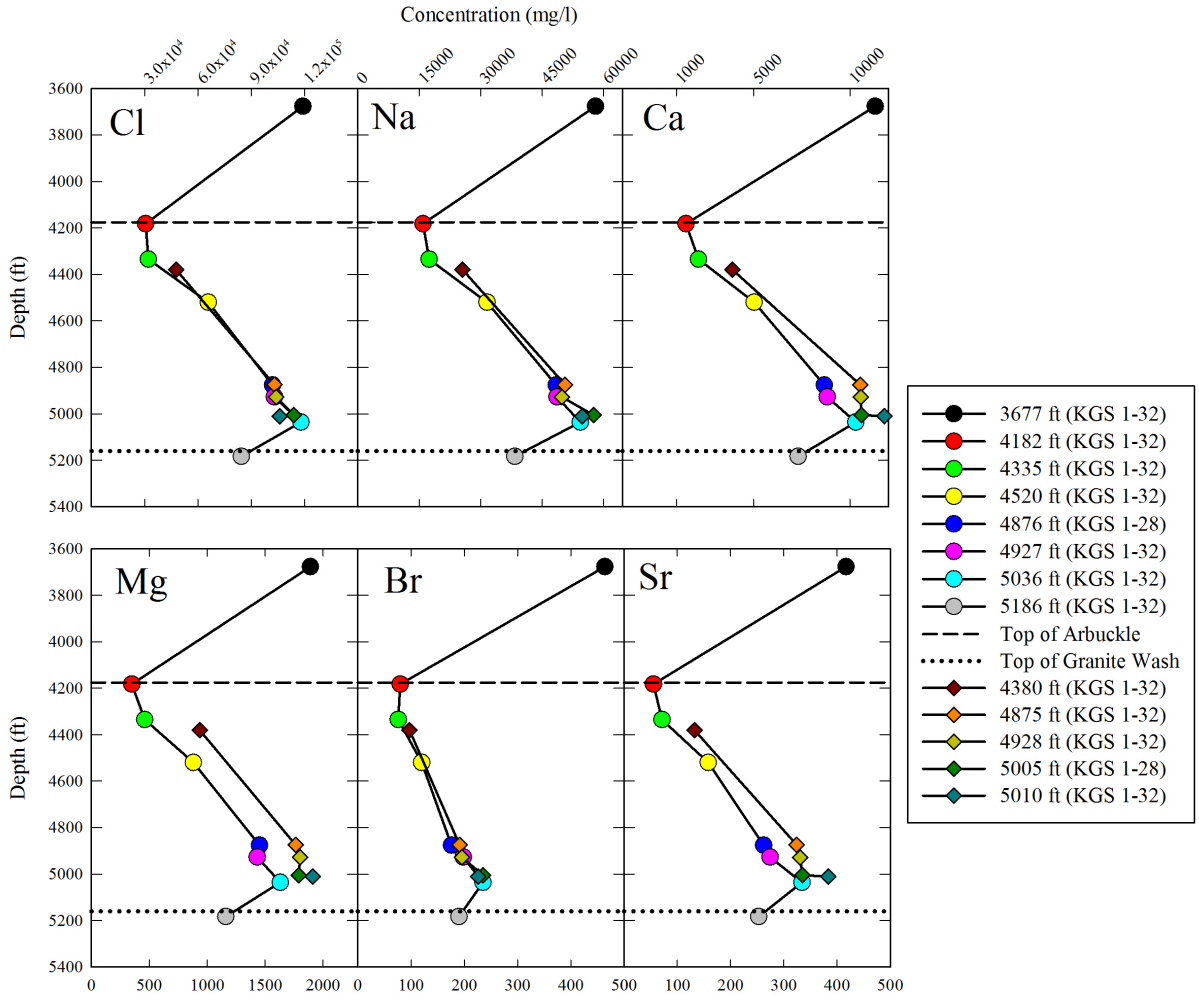

Figure 5-13. Depth profile of major elements within the Mississippian, Arbuckle and Granite wash formations. Circles represent DST samples and diamonds are swab samples. Dashed line represents the top of the Arbuckle and the dotted line represents the top of the granite wash. These elements show a clear trend of increasing with depth within the Arbuckle. Mississippian samples are much higher in concentration. There is good agreement between DST and Swab data for these elements.

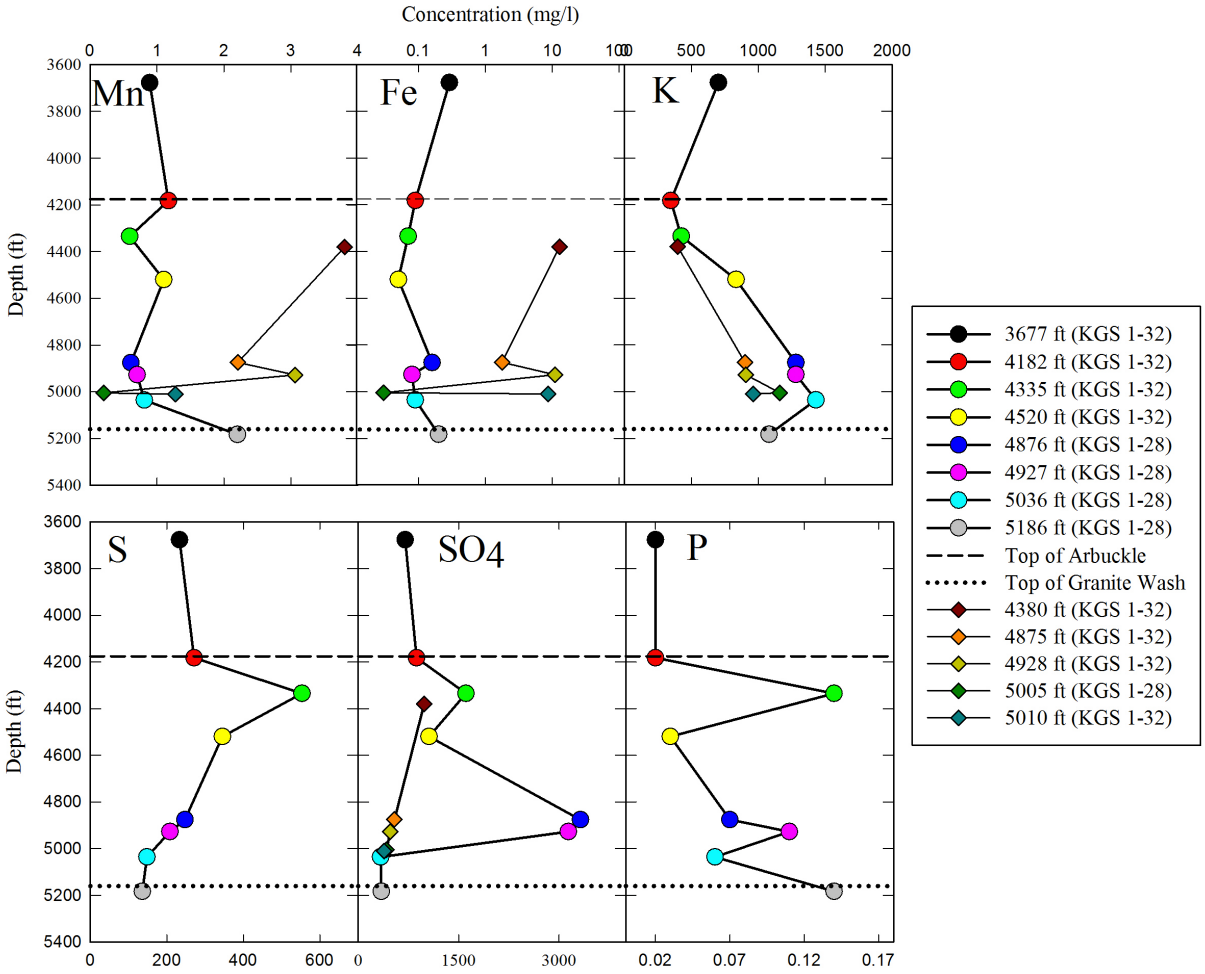

Figure 5-14. Depth profile of minor, redox sensitive elements. These elements show variation with depth due to changing redox conditions. There is less agreement between DST and swab data than elements presented in Figure 6-1. HR-ICP-MS data for S and P are not available. Circles represent DST samples and diamonds are swab samples. Dashed line represents the top of the Arbuckle and the dotted line represents the top of the granite wash.

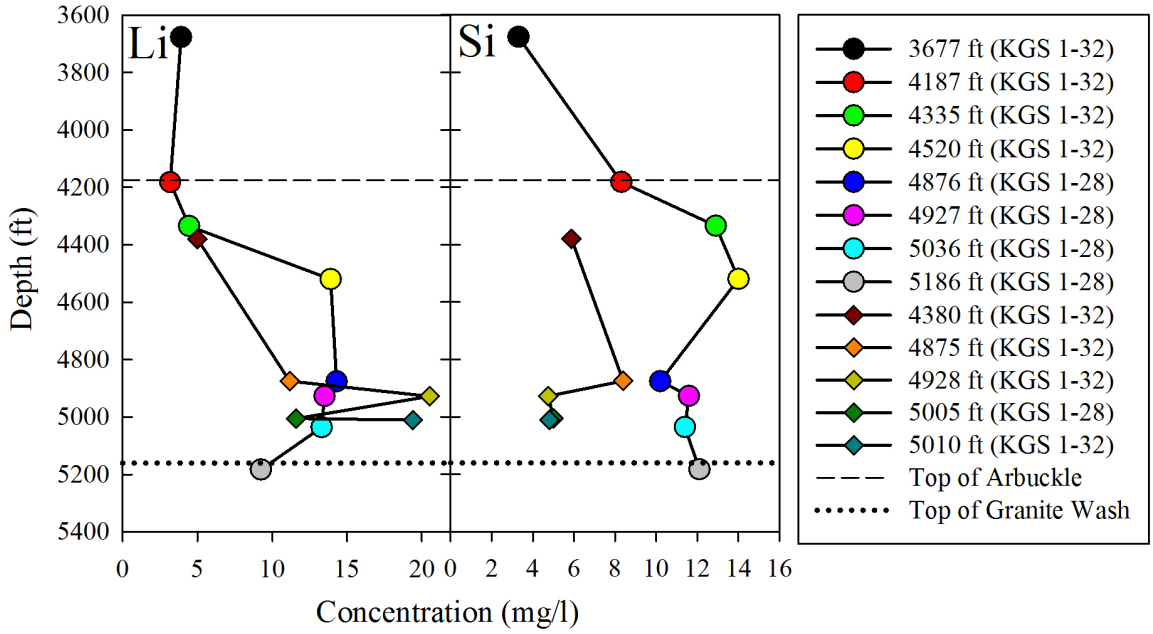

Figure 5-15. Depth profile of Li and Si. These elements variation is noticed throughout the formation. Circles represent DST samples and diamonds are swab samples. Dashed line represents the top of the Arbuckle and the dotted line represents the top of the granite wash.

Chloride Ratios

Chloride ratios with major ions show strong linear correlation within the Arbuckle samples which suggests similar processes have affected brine chemistry throughout the depth of the formation (Figs. 5-16 & 5-17). The seawater evaporation curve is plotted on these graphs with data compiled by Fontes and Matray (1993). The brines pass the gypsum stability field but do not reach the halite stability field. Na^+ concentrations closely follow the trend observed during the evolution of seawater with a slight downward shift. Ca^{2+} show an excess while Mg^{2+} is deficient relative to the evaporation curve. K^+ shows a strong linear trend, but is depleted relative to seawater evaporation. Br^- is also slightly depleted relative to seawater evaporation curve. Sr^{2+} is strongly enriched relative to seawater evaporation and follows the same trend as Ca^{2+}. SO_4^{2-} shows no clear trend with depth and is depleted relative to seawater data. Li^+ is enriched relative to seawater evaporation It does not show a clear linear trend with depth and it appears to be clustered into two groups (upper and lower Arbuckle) which has implications for mixing, discussed in Chapter 6.

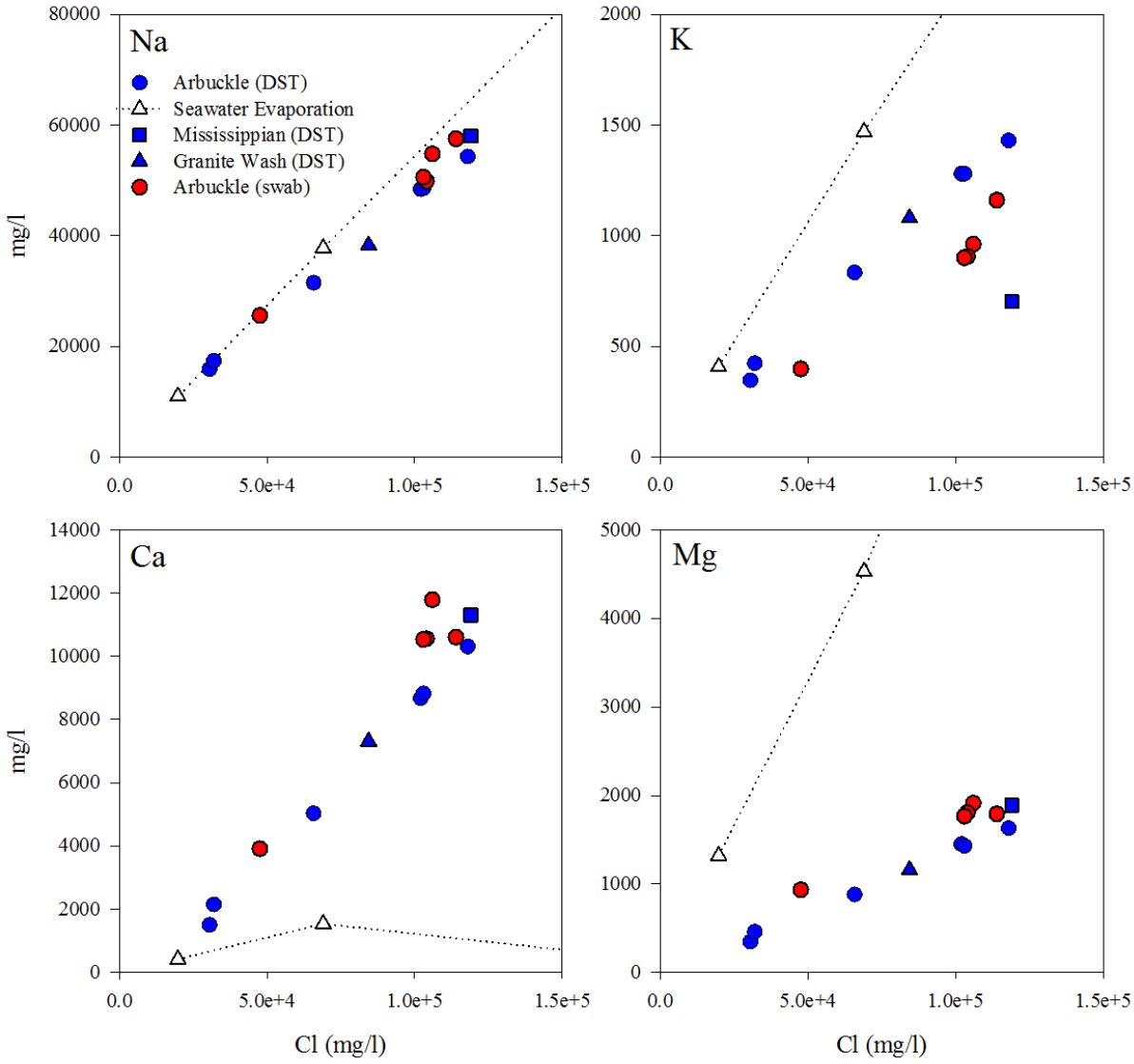

Figure 5-16. Cl^- ratios for Na^+, K^+, Ca^{2+} and Mg^{2+}. Data From DST samples are displayed in blue while swab data are in red. Mississippian data symbol is the square, Arbuckle are the circles and granite wash is the triangle. Seawater evaporation curve is the doted line with mineral precipitation stages marked as open triangles.

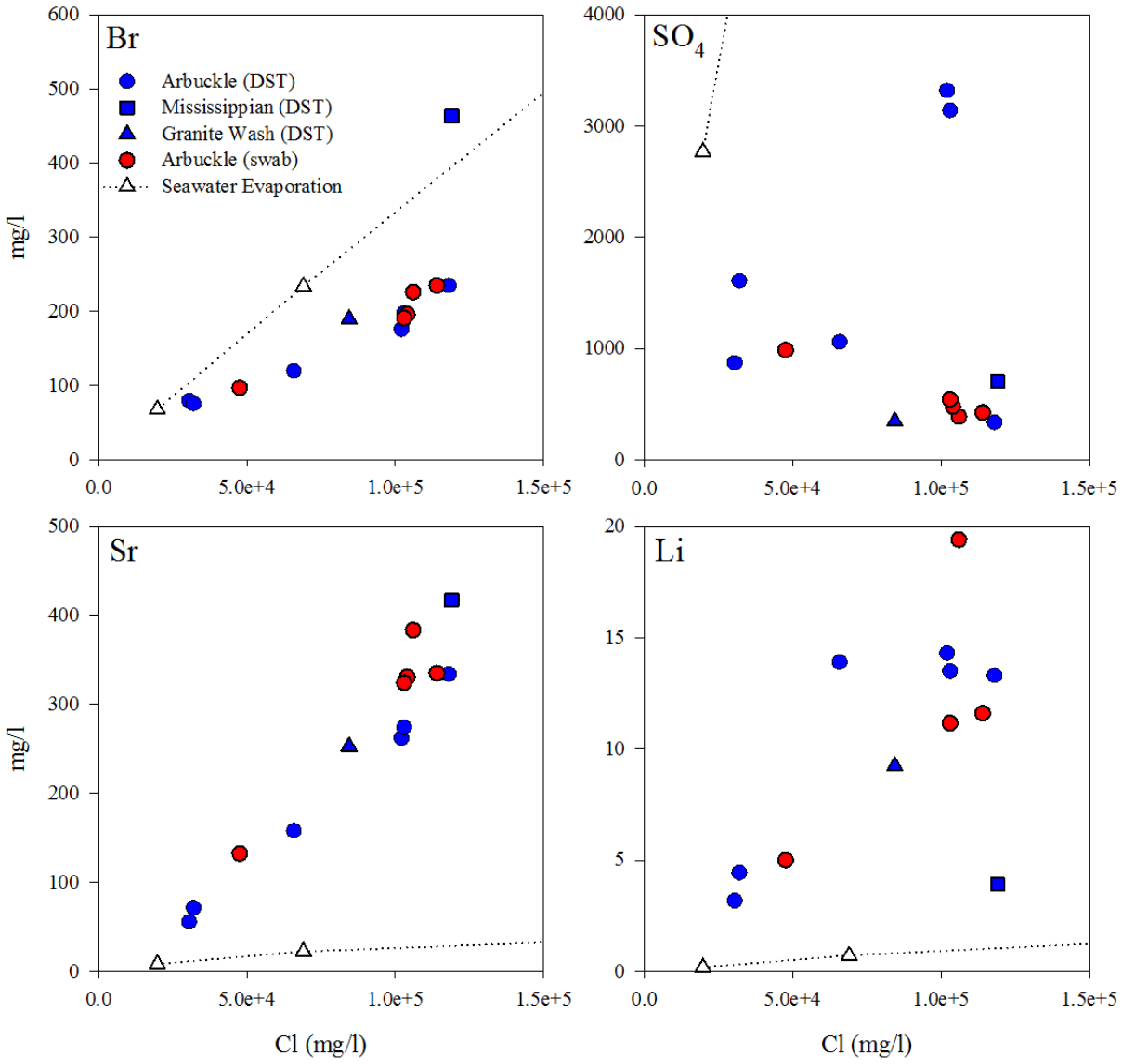

Figure 5-17. Cl^- ratios with Br^-, SO_4^{2-}, Sr^{2+} and Li^+. Data are presented as described in Figure 6-3.

Iron in Formation Waters

Iron is a potentially important species that could sequester CO_2 by precipitating Fe carbonates such as siderite (Lammers et al, 2011). The behavior of Fe in the Arbuckle is complex as revealed by analyses of brine samples. Total Fe concentrations range from 0.03 mg/l to 0.16 mg/l in the Arbuckle waters as measured by ICP-OES from DST samples (see Table 5-2). The concentration of Fe does not increase linearly with depth, but rather varies with a peak at 4876` and a minimum at 5036`, which corresponds to the peak in SO_4^{2-} at 4876`

and a minimum of SO_4^{2-} at 5036` (Fig. 5-14). The brine is highly reducing (-169 mV Eh at 5010') and it is possible that the amount of soluble Fe is greater in the formation that what was measured by ICP-OES. Swab data analyzed by HR-ICP-MS reveal much higher Fe concentrations, ranging from 1.7 mg/l to 12.8 mg/l, which is a substantial departure from the DST data and could represent more sophisticated analytical techniques and/or that the swab samples captured redox sensitive species better than the DST samples.

Upon sampling wells KGS-1-28 and 1-32 during swab testing, the first minute of water pumped from the well was dark black, indicative of the precipitation of amorphous iron sulfide (FeS^-). High levels of H_2S gas was observed as the water was brought to the surface. Sulfide is less soluble at lower temperature and pressures which helps explain degassing of H_2S during the swab test (Xiao, 2009). Sulfide could have bonded with Fe to form FeS^- compounds as the water was exposed to atmospheric conditions, causing the water to appear black.

ICP-OES analysis of an unfiltered swab sample from well KGS 1-28 gave total Fe concentrations of 0.51 mg/l compared with 0.3 mg/l for the filtered sample. Similarly, HR-ICP-MS analyses of this same depth from KGS 1-32 gave Fe concentrations of 12.9 mg/l for the unfiltered sample and 8.67 mg/l for the filtered sample (filtered through 0.45 μm). Variations in the measured Fe concentration could signify the iron concentrations in the formation are much higher than measured, with much of the iron precipitating out of solution as FeS^- as it depressurizes and reacts with oxygen.

Swab samples analyzed spectrophotometricly in the field do in fact reveal much higher Fe concentrations. Unfiltered and diluted samples tested by spectrophotometer yielded total Fe concentrations between 8 mg/l and 49.4 mg/l. They decrease with depth, correlating with the sulfate concentration. Ferrous Fe measured in the field shows an interesting trend with depth. Fe II/III ratio increases with depth, signifying the brine is becoming more reducing with depth. This idea is supported by decreasing ORP measurements with depth. This data shows changing redox conditions with depth that are thought to be controlled mostly by microbial communities.

The variation between Fe concentrations measured in the field by spectrophotometer and those measured by ICP-OES demonstrate the inherent problems in analyzing samples from depth with accuracy. The low values obtained by ICP-OES are probably due to the

precipitation of FeS^{-} in the samples where it eventually settles to the bottom of the sampling container and is excluded from analyses.

Depth	Well	Sample Name	ICP-OES mg/l	HR-ICP-MS mg/l	SPM Fe Total	SPM Fe II	FeII/III	ORP mV
3677	1-32	DST 1	0.29	-	-	-	-	-
4182	1-32	DST 4	0.09	-	-	-	-	-
4335	1-32	DST 3	0.07	-	-	-	-	-
4380	1-32	Swab 5	-	12.84	49.4	8.15	0.16	-48
4520	1-32	DST 2	0.05	-		-	-	-
4875	1-32	Swab 4	-	1.77	16.75	5.35	0.32	-156
4876	1-28	DST 8	0.16	-	-	-	-	-
4927	1-28	DST 7	0.08	-	-	-	-	-
4928	1-32	Swab 3	-	10.97	8	7.7	0.96	-168
5005	1-28	Swab 1	0.03	-	-	-	-	-172
5010	1-32	Swab 2	-	8.67	-	-	-	-176
5036	1-28	DST 6	0.09	-	-	-	-	-
5183	1-28	DST 5	0.2	-	-	-	-	-

Table 5-2. Iron concentrations as measured by ICP-OES, HR-ICP-MS and spectrophotometer (SPM) in KGS 1-28 and 1-32. Dashes indicate analyses were not conducted on the sample.

Elevated Fe concentrations in the brine are also observed during the flow through experiment where Fe concentrations increased from 0.03 mg/l to 6.96 mg/l during the first 12 hours of flow with no CO_2 (further discussion in the flow results section). In the presence of sulfide, Fe can be reduced which makes it more soluble and mobile in the aquifer (Afonso et al, 1992). The presence of H_2S, reduced Fe and $scCO_2$ has been shown experimentally to lead to mineral carbonation reactions (Lammers et al, 2011). Since H_2S gas is already present in the Arbuckle, these reactions need to be taken into account in modeling CO_2 injection into the Arbuckle.

Stable Isotopes

Oxygen and hydrogen isotopic data are presented in Figure 5-16 with the global meteoric water line and Figure 5-17 as a depth profile. In Figure 5-16 the data falls along a linear, evaporative trend deviating from the global meteoric water line (GMWL) within the

Arbuckle. Depth 3677` (Mississippian) data do not fall on this line and are more enriched in both heavy isotopes.

Depth profiles of $\delta^{18}O$ and $\delta^{2}H$ show that there is not a continuous linear increase with depth. Samples at 4335` and 4388` show a strong depletion with respect to $\delta^{18}O$ and $\delta^{2}H$. These samples occur in a high porosity zone in the upper Arbuckle above the baffle zone. Implications for vertical communication within the Arbuckle is discussed in Chapter 6. Depth 4182` does not fit the trend of enrichment with depth because it is more enriched than two data points below it (4335` and 4388`). This enrichment could indicate communication between the Mississippian and upper Arbuckle aquifers.

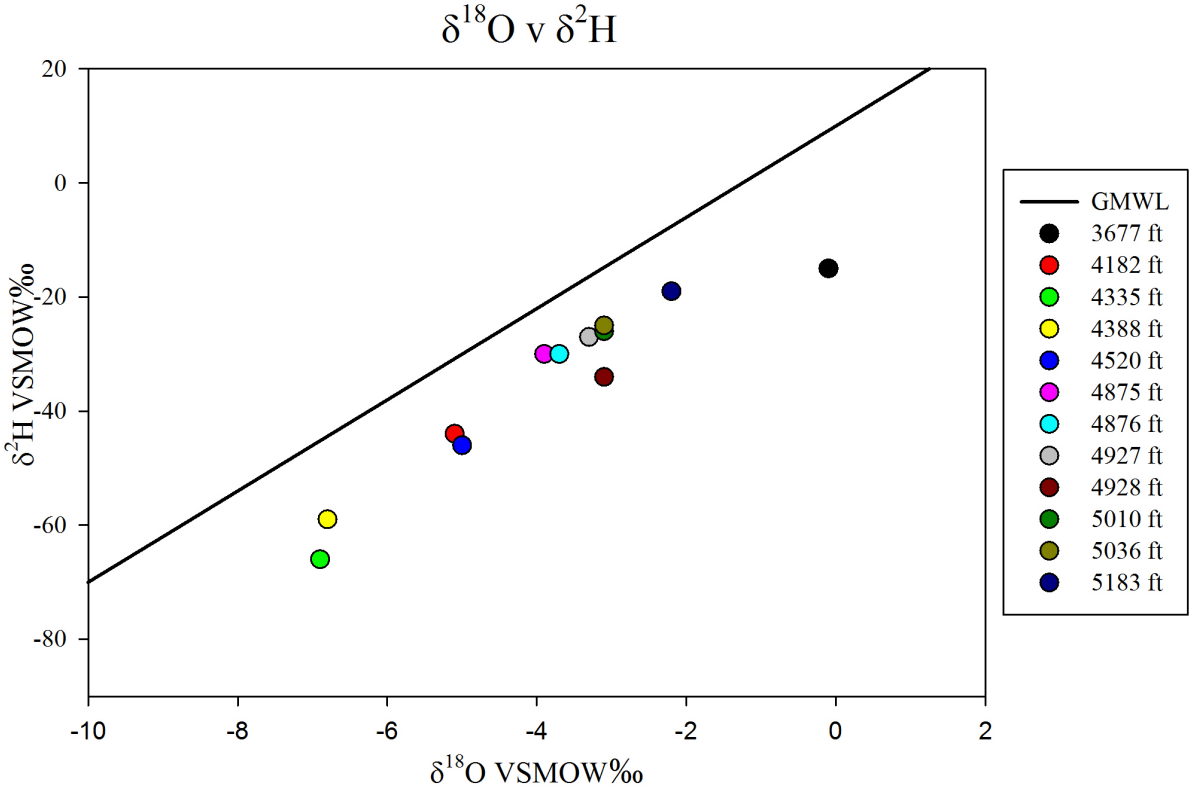

Figure 5-18. $\delta^{18}O$ v $\delta^{2}H$ isotopes in the Mississippian, Arbuckle and Granite wash formation

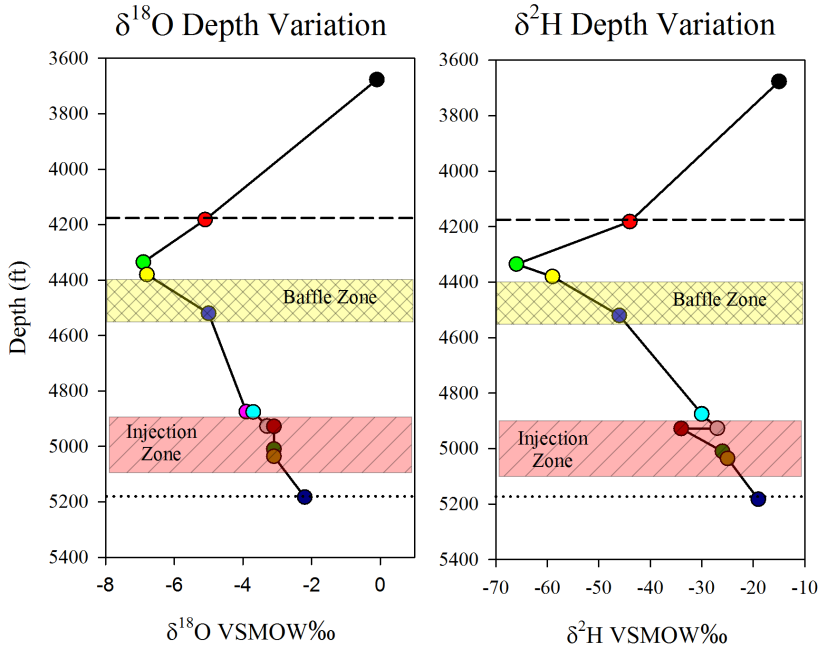

Figure 5-19. Depth profile of $\delta^{18}O$ and $\delta^{2}H$ within the Mississippian, Arbuckle and granite wash formations. Note anomalous depletion at 4335` and deviations from the trend in swabbed samples (yellow, pink and brown symbols). Yellow cross hatched box represents the baffle zone and the red box with diagonal lines represents the injection zone. Symbol colors and dashed/dotted lines are the same as Figure 5-16.

Supercritical Flow Experimental Results

Time Series

Effluent collected from the downstream outlet of the flow through apparatus is discussed and displayed as a time series in the following section and figures therein. During the saturation phase, where only brine was flowed through the core at low rates for 13 hours, the following changes in chemistry were observed (Fig. 5-18). Decreases in Cl^- (-6%), Na^+ (-6%), Ca^{2+} (-7%), Mg^{2+} (-11%), SO_4^{2-} (-13%) and S (1%) from original brine concentrations. Fe (+23200%), Mn (+835%) and P (+350) substantially increased during the saturation phase. During the first 5 hours after CO_2 was introduced into the system Fe, P and S decrease in solution while Cl^-, Na^+, Ca^{2+}, Mg^{2+}, Mn and SO_4^{2-} increased. This trend continued for the next five hours with the exception of SO_4^{2-} and Mn which showed fluctuation. A reverse trend was seen in the last 8 hours with Fe, S, P and SO_4^{2-} increasing while Cl^-, Na^+, Ca^{2+} and Mg^{2+} decreasing. Here it will be discussed how elemental concentrations changed with time. We will start with Cl^-, Na^+ and Ca^{2+} first because they are the major species present within the brine.

Cl^- decreased from original brine concentrations of 114,00 mg/l to 107,000 mg/l (-6%) from during the saturation phase. Cl^- concentrations rose once CO_2 was injected and increased to 116,000 mg/l and stayed within 3% of that value until the overnight sample, where it increased to 119,000 mg/l (2%). Cl^- decreased to its previous value of 116,000 mg/l and stayed within 3% of 116,000 mg/l through the next three hours. Cl^- decreased to 110,000 mg/l (-5%) during the last hour.

Na^+ decreased from original brine concentrations of 57,500 mg/l to 54,100 mg/l (-6%) during the saturation phase. It then increased in hours 1-3 by 1% each hour to 55,200 mg/l after CO_2 was introduced. Na^+ concentrations stayed fairly constant around 55,200 mg/l through hour 7. Overnight Na increased to 57,600 mg/l (4%) and then decreased by 1% each hour for three hours to 54,800 mg/l. Na^+ concentrations increased to 55,300 mg/l (1%) in hour 24. A somewhat opposite trend was seen in Na^+ when compared with Cl^-.

Ca^{2+} decreased from original brine concentrations of 10,600 mg/l to 9900 mg/l (-7%) during the initial saturation phase. Once CO_2 was introduced in hour 1, Ca^{2+} increased to 10,200 (3%) over three hours and then stayed within 1% of 10,200 mg/l through hour 7. Ca^{2+}

increased to 10,600 (3%) in the overnight sample. Ca^{2+} slightly decreased during the last 4 hours to 10200 (-1%)

Mg^{2+} decreased from original brine concentrations of 1790 mg/l to 1610 mg/l (-11%) during the saturation phase. Once CO_2 was introduced Mg^{2+} increased by 2% by hour 4. Mg^{2+} decreased in hour 5 by 2% and slightly increased through hour 7. Overnight Mg increased 2% from hour 7 and then decreased by 1% for the last 4 hours.

K^+ did not change substantially during the course of the experiment. It stayed within 2% of original brine concentrations (1160 mg/l) through the entire experiment.

Fe dramatically increased from original brine of 0.03 mg/l to 6.96 mg/l (23,200%) during the initial brine phase. Once CO_2 was introduced Fe values fell 50% in the first hour to 3.6 mg/l and continued to decrease through the over night sample to 1.73 mg/l (-48%). Fe concentrations increased from 1.73 mg/l to 2.56 (147%) over the last four hours.

Mn also increased substantially from original brine concentration of 0.2 mg/l to 1.67 mg/l (835%) during the saturation phase. Mn decreased to 1.5 mg/l (11%) once CO_2 was introduced. During hour 2 and 3 Mn increased to 1.56 mg/l and 1.63 mg/l, respectively (4% each hour). Mn decreased during hour 4 and 5 to 1.57 mg/l (2% each hour). During hour 6, 7 and the overnight sample Mn increased by 1% each hour to 1.66 mg/l. Mn stayed with 2% of 1.62 mg/l during the last four hours of the experiment.

pH was 5.30 for the saturation phase with brine only and remained significantly unchanged to ~5.33 after the first hour of two phase CO_2 and brine flow before dropping to 4.97 between hour 2 and hour 4. pH climbed again to 5.44 by hour 6 and then decreased to the lowest recorded pH of 4.76 at hour 7. As expected due to prolonged over night degassing, the sample recorded the highest pH at 5.66. For the last four hours pH was stable at 5 (+/- 0.04) (see Fig. 5-19).

Alkalinity was measured spectrophometrically after effluent was collected by HACH DR2800 spectrophotometer. Alkalinity values increase from a original value of 199 mg/l to 368 mg/l during the initial saturation phase. After CO_2 was introduced alkalinity values dropped to 225 mg/l within one hour. As pH continues to decrease, alkalinity values begin to increase, reaching 413 mg/l at hour 4. Alkalinity then begins to decrease until hour 6, when pH reaches 5.44. Alkalinity then increases at hour 7 and shows a peak in the overnight

sample. The last four hours are relatively steady (428-466 mg/l) and higher than the beginning of the experiment (Fig. 5-19).

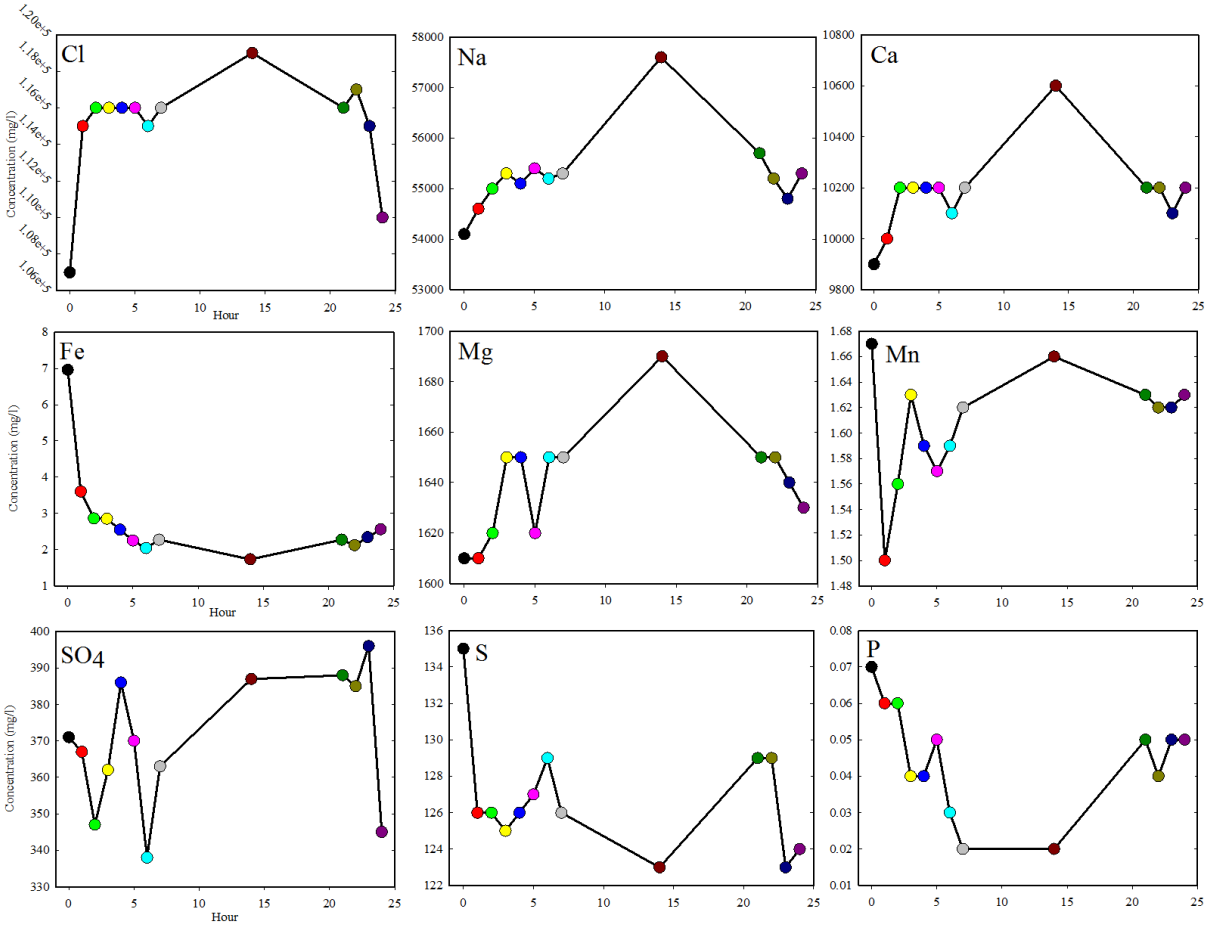

Figure 5-20. Time series plots of changing major ion chemistry during flow-through experiment.

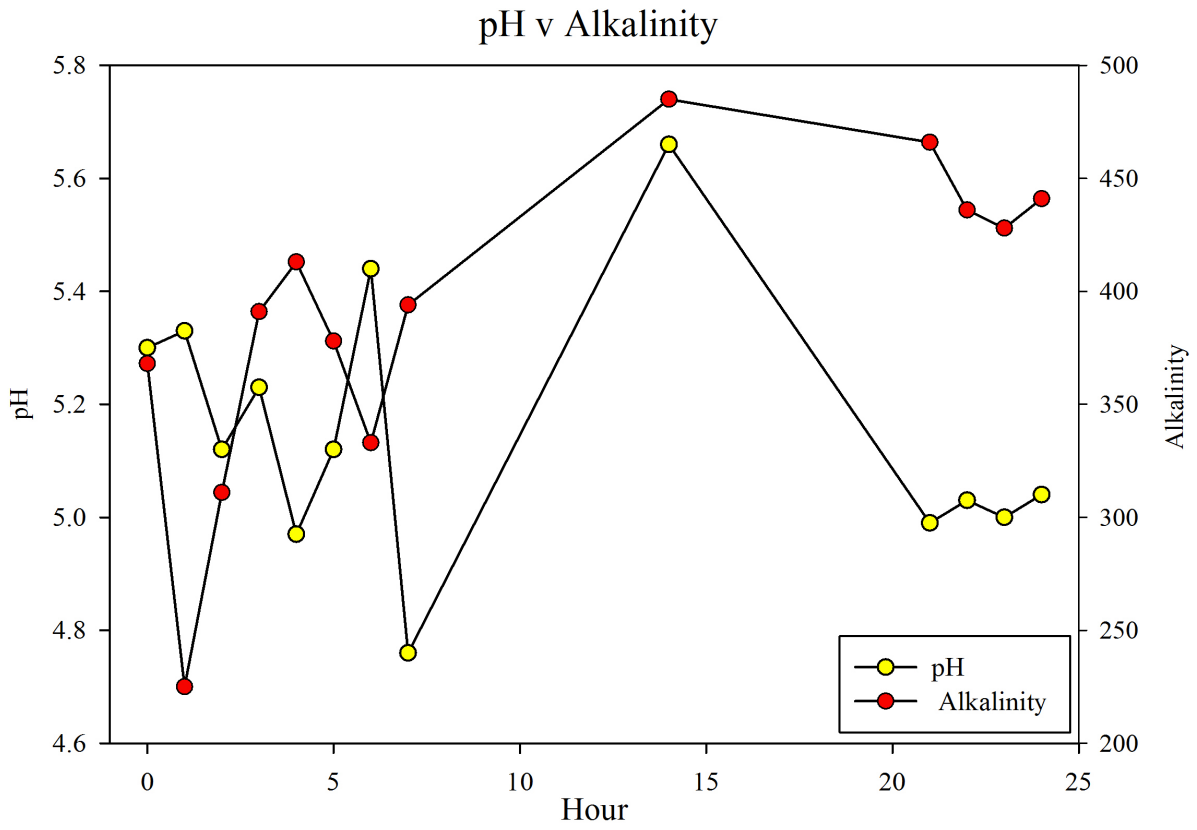

Figure 5-21. Time series plot of pH and alkalinity measurements on the effluent.

CT Scan

CT scans of core 31-19 before and after reactions with brine and CO_2 reveal changes in the interior of the core. Because the experiment was short (24 hrs) extensive changes were not observed, but several small scale changes can be observed in Figure 5-22. The core appears to have undergone a decrease in less dense material (dark areas) in the after injection image (Fig. 5-22, B). There appears to be an increase in bright, or dense material which could be due to the precipitation of minerals throughout the experiment. Figure 5-23 shows detail of slices taken from a montage to highlight some changes. Porosity is not completely infilled, but there is an obvious decrease in the extent of the porosity of the rock. Decreases in major cations during the last 5 hours of the flow experiment could be due to the precipitation of minerals within the core plug. Higher resolution CT images are needed to quantify the porosity changes and extent of mineralization.

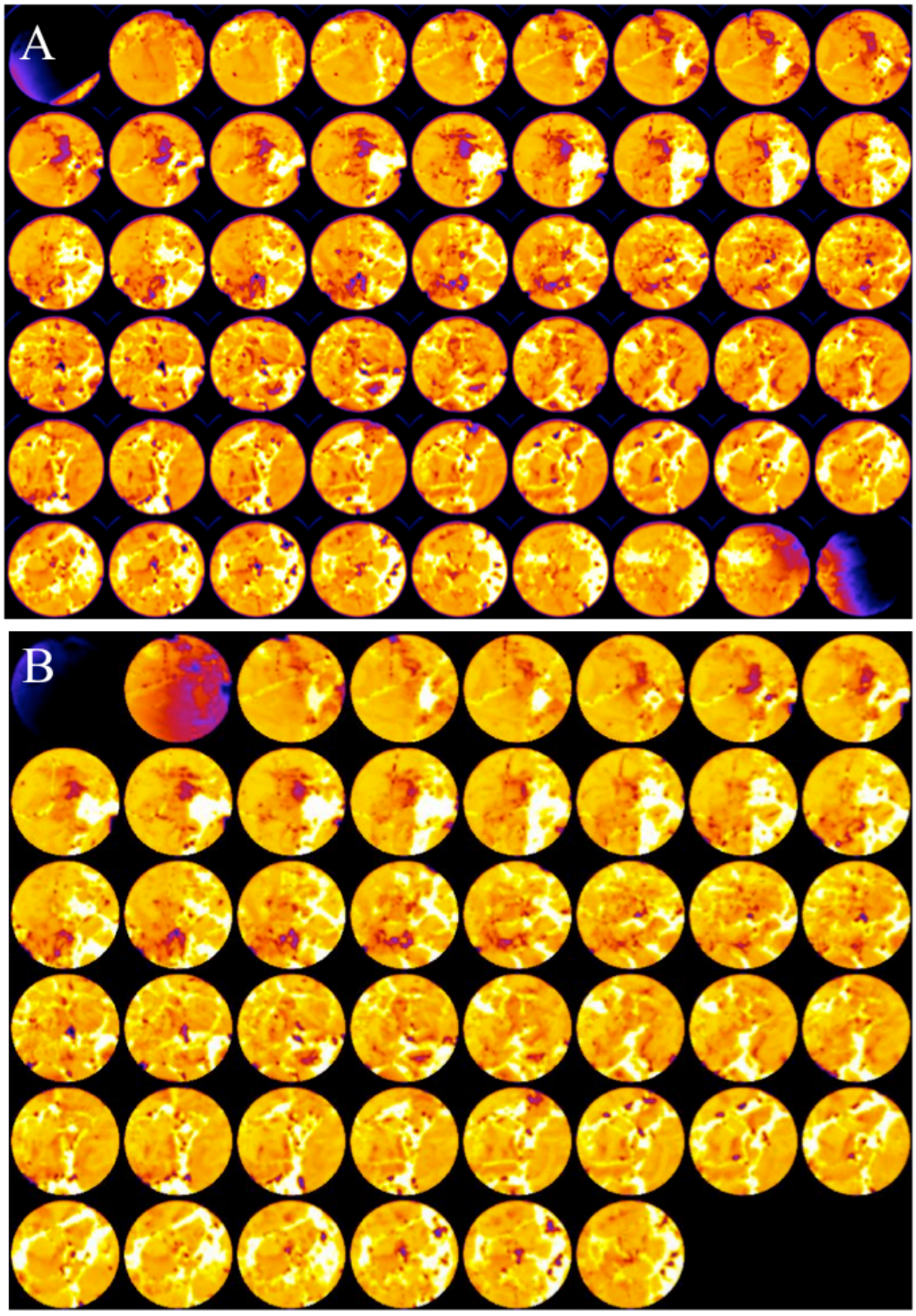

Figure 5-22. 3D CT scans of core 31-19 (4977`) before (A) and after (B) flow experiment. There appears to be an increase in dense material in the after image, indicating mineral precipitation.

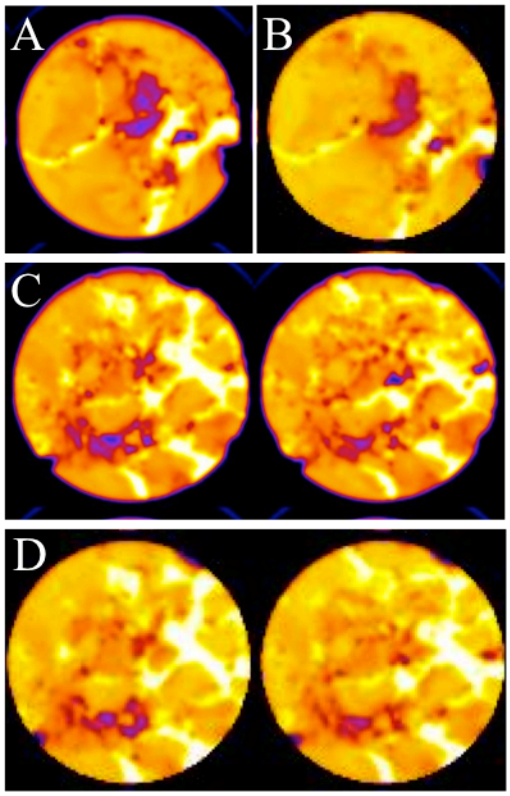

Figure 5-23. Slices from before and after montage showing an increase of dense material. Large vug present in A (before) has visibly decreased in intensity in the after image (B). Another example from the core shows veins of silica surrounded by an extensive porosity (dark areas in C). (D) The extent of porosity has visibly decreased in the after image.

Chapter 6 - Discussion

Discussion on Mineralogical Characterization

The Arbuckle is a dolomitic aquifer system with an abundance of silica rich zones. Argillaceous material and sulfide minerals are also common at certain depths throughout the formation. Dolomite appears mainly as a replacement mosaic and also occurs as fracture and pore filling crystals. Silica is present in a wide variety form including chalcedony, chert, microporous chert and quartz. Argillaceous material is concentrated to fractures where it has been infilled and is commonly associated with oxide/sulfide minerals. Extensive heterogeneity between boundaries of carbonate, chert and argillaceous material indicate that reactions will not be uniform throughout the formation. By identifying small scale mineralogical heterogeneity in thin section and what textures they create, we were able to identify reactions with CO_2 acidified brine. The three intervals of interest are discussed in detail in this chapter and how mineralogy and textures could be affected by CO_2 acidified brine. Porosity data and geochemical log data obtained from KGS 1-32 is presented here to demonstrate changes throughout the intervals of interest

Summary of Mississippian Pay Zone Mineralogy

The Mississippian pay zone has considerable economic importance to oil producers in Kansas and a successful tertiary oil recovery by injection of CO_2 could reduce the costs associated with CO_2 sequestration. A brief discussion of the mineralogy and how it could react with CO_2 is given here.

The dominant mineralogy of the pay zone is dolomite with an abundance of chert and minor amounts of anhydrite(?). The dolomite observed in thin sections from this interval does not display the intergrowth of dolomite mosaic that is typical of the Arbuckle. It is generally more fine grained with well connected intercrystalline porosity. Increased porosity is expected, since it has been a productive oil reservoir.

Chert nodules are common and range in size from 0.25 mm to a few cm. Euhedral quartz crystals are observed at 3686` depth and occur along with fibrous chert; at places it seems chert is representing sulfate replacement. Anhydrite that fills pore spaces between dolomite and quartz and appears to be undergoing silicification has also been noticed here. Oil

stain is evident in dolomite as well as in some chert nodules. One idea is that the fine grained, porous dolomite could react quickly with CO_2 saturated brine, increasing porosity and releasing oil trapped in pore spaces leading to enhanced oil recovery.

Summary of Baffle Zone Mineralogy

The potential of a geologic baffle, or low porosity zone, within the Arbuckle has important implications for the migration of a CO_2 plume after injection has taken place. It is important to understand the baffle zone mineralogy with possibly reactions with CO_2. As the CO_2 plume migrates vertically, it could become 'stuck' at the baffle. This would slow the vertical migration and increase the reactivity of the plume as it has longer time to dissolve into brine and react with existing minerals. While this baffle does not have caprock integrity, multiple low porosity zones within a targeted aquifer are beneficial to effective CO_2 storage (Eisinger, 2011). Since the plume could be more reactive within this interval, the mineralogy of the low porosity zone is of particular interest (Fig. 6-1).

The porosity of the baffle zone is significantly lower than the proposed injection zone. As seen in Figure 6-1, porosity drops significantly around 4400` as shown by NMR well logs and porosity analyses. The extensive silicification of open pore space and infilling by argillaceous material could have reduced the porosity in this zone.

Petrographic studies reveal this zone is heterogeneous with an abundance of silica precipitates and argillaceous material to be present within an otherwise dolomitic lithology. Clayey minerals typically have more reactive surface area and could react faster in presence of CO_2. The abundance of Fe-oxide minerals found in the baffle zone, usually within the argillaceous zones, suggests Fe could be released if the clay material reacts with CO_2 for long periods of time.

Geochemical logs have shown that there is a high amount of silica in formation rocks within the baffle zone (Fig. 6-2). There are only a few thin zones where the silica content peaks, but it is generally higher than the silica content of the injection zone. Silica concentration is similar to the Mg concentration in the baffle zone (Fig. 6-2), while silica content is lower than the Mg content measured in the injection zone (Fig. 6-3). This high silica content is confirmed in thin section, where silica (as microcrystalline chert and megaquartz) is present in nearly all depths analyzed. Thin sections also reveal the extensive

heterogeneity that occurs at chert-carbonate boundaries. If preferential reaction pathways form along these boundaries, pyrite and argillaceous materials will be exposed to acidified brine. This would release Fe, S, K and possibly other species into solution as they dissolve.

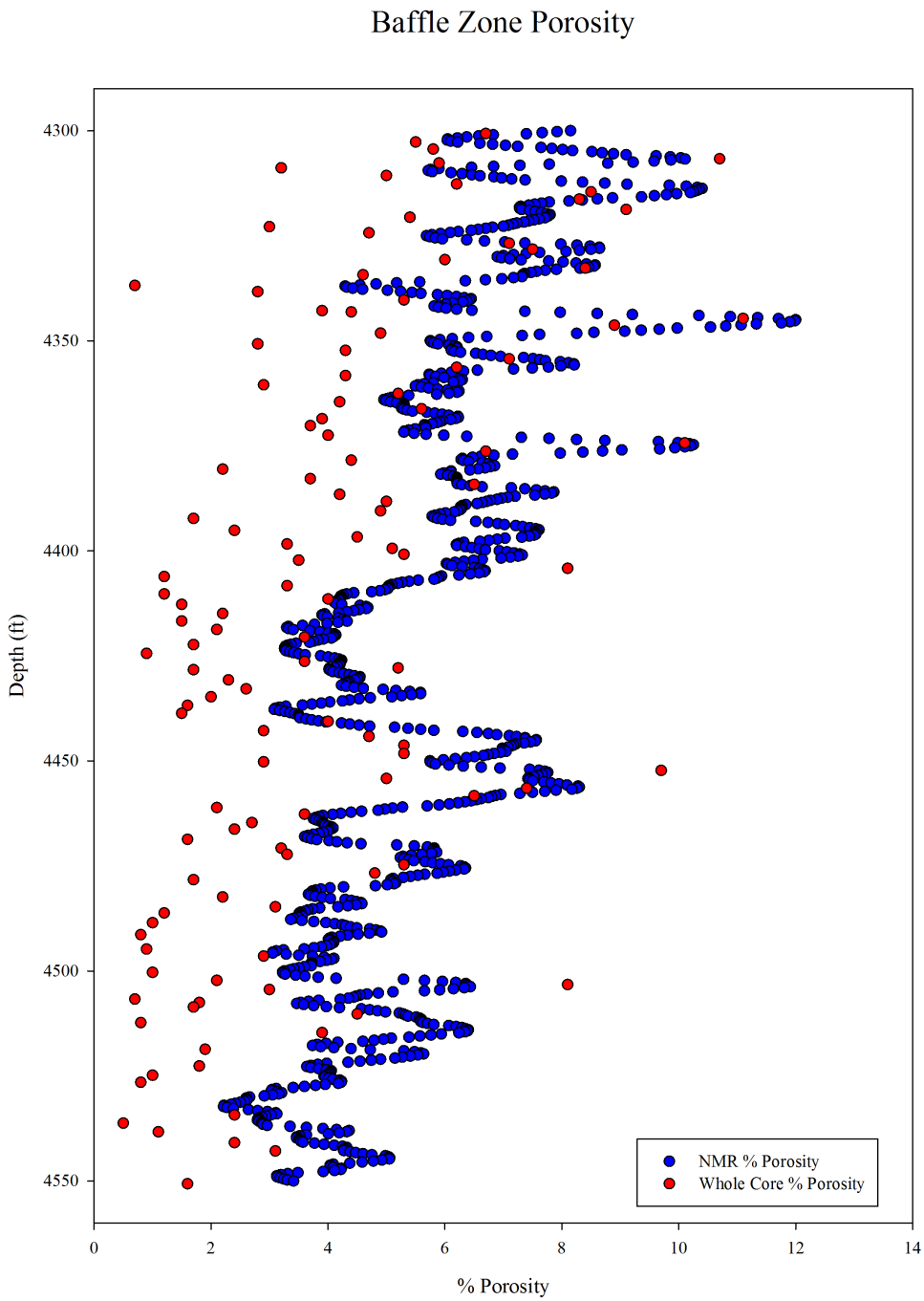

Figure 6-1. Porosity percent of potential baffle zone (~4330`-4550`) within Arbuckle. NMR and Weatherford porosity analyses data are plotted.

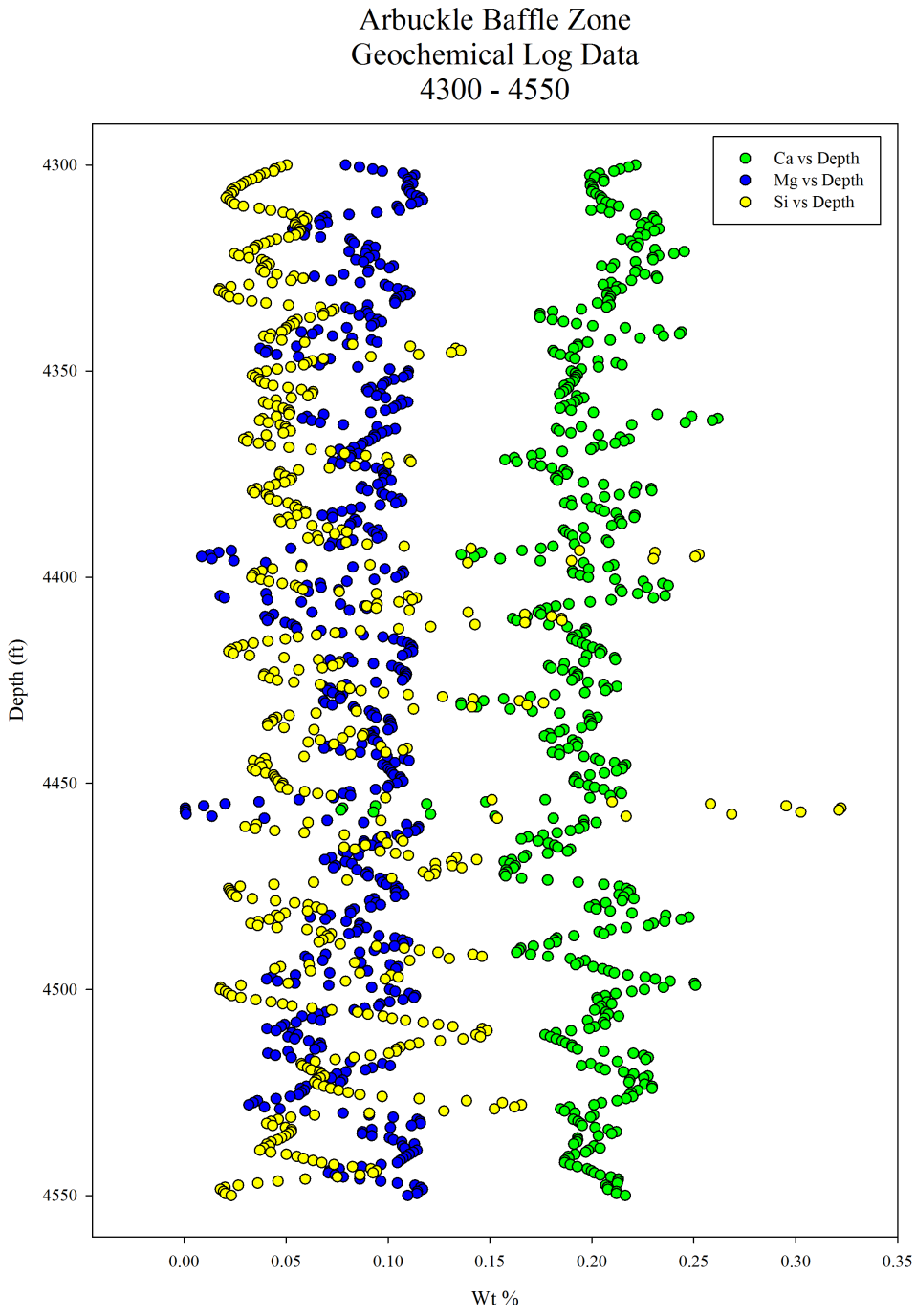

Figure 6-2. Geochemical log of Arbuckle baffle zone. Ca, Mg, and Si are plotted on this graph.

Summary of Injection Zone Mineralogy

The dominant mineralogy of the injection zone is dolomite with interspersed cherty nodules. Dolomite appears to have replaced most if not all of the calcite. Dolomitic textures range from dolomicrite, coarsely to finely crystalline anhedral to subhedral mosaic, and coarsely crystalline pore filling euhedral dolomite. Large, fracture filling saddle dolomite is also observed within the thin sections and usually occurs with an opaque mineral, probably pyrite.

Silica (chert or quartz) is observed throughout the injection zone with some increase in the lower portion of the injection zone. Geochemical logs showing Ca, Mg and Si concentration show a zone of increased silicification between 4965` and 5030` (Fig. 6-3). Four thin sections from this siliceous interval (31-9, 31-19, 31-27, 32-5) confirm the abundance of silica as well as highlight the diversity of silica textures. Chert is observed replacing dolomicrite and as well developed euhedral dolomite rhombs. Clusters of dolomite surrounded by chert is common in the lower injection zone. This might imply that the silicification occurred diagenetically after extensive dolomitization (Kolkas and Friedman, 1998).

Silica minerals range from radiating chalcedony to microcrystalline chert to megaquartz to well developed hexagonal quartz. SEM images of core plug 31-19 (used in flow cell experiment, Fig. 5-6) show hexagonal quartz present in porous areas. Silica nodules infilling porosity shows chalcedony at pore edges with larger, megaquartz precipitating in the interior nodule. Porous silica is common in the injection zone and could have formed from the replacement of micritic material or could be the result of partial dissolution of chert. This porous silica has important implications for CO_2 injection. We anticipate these high porosity zones will have more reactive surface area, allowing CO_2 to react with minerals at faster rates. Opaque Fe- oxides/sulfide minerals are common in these porous silica zones, and Fe and other metals could be released into solution upon reaction with CO_2.

The chert-carbonate boundary is of particular interest in context of the effects of CO_2 acidified brine on the structure and texture minerals. Fractures are common at the chert-carbonate boundary and the heterogeneity that has developed at these boundaries indicates complex reaction mechanisms could develop once CO_2 acidified brine comes in contact with these zones. Some fractures are open while others are filled with clay material or opaque

oxide/sulfide minerals. The increased pressure of injected CO_2 could reactivate fractures and provide flow paths for CO_2.

Extensive heterogeneity in targeted CO_2 storage sites forces the CO_2 to take a more convoluted path as it flows through the reservoir. This could allow for more laterally extensive migration, enabling more contact with formation minerals. It has been shown that heterogeneity could initially inhibit the trapping of CO_2 as a residual fluid as it flows through preferential paths at high flow rates (Flett et al, 2007).

Experimental studies have shown that dissolution rates of minerals were impeded by the precipitation of an amorphous silica layer on crystal surfaces (Daval et al, 2011). This experiment was conducted on olivine, but has implications for high silica content in carbonate aquifers as well. Precipitation of silica at low pH values could impede the dissolution of clay or iron minerals, slowing their release into solution. If future experimental work finds silica layers precipitating on carbonate mineral faces, it would have profound effects on limiting the buffering capacity of the brine. Without buffering capacity enabled by the dissolution of minerals, less CO_2 can be dissolved in brines reducing solubility trapping mechanisms.

Porosity is highly variable throughout the injection zone, ranging from 1.6% to 8.8% with depth. Porosity values measured at Weatherford Laboratories are plotted with porosity values obtained by NMR logs in Figure 6-4. Porosity values are significantly higher in the injection zone than the baffle zone. A high porosity zone exists within the same interval as the zone of high silica content (4965`-5030`). Porosity values from NMR logs are consistently higher than porosity data measured at Weatherford Laboratories. This discrepancy is anticipated because of the different techniques. Porosity is not available for the entire injection zone because 5000`-5050` was not cored due to loss of circulation while drilling. While whole core measurements are considered to be more precise, NMR logs provide a continuous profile that reveals small scale changes in porosity with depth.

Thin section petrography has revealed a large range of porosity types including inter-crystalline matrix, presence of fractures and occasional vugs (see Fig. 5-5). Large pore spaces and fractures allow CO_2 to travel further through the formation while small pores and matrix porosity with high surface area will slow the CO_2 plume and facilitate quicker reactions. The coincidence of high silica content and increased porosity in the injection zone indicate reactions more complex than carbonate dissolution could occur in the near well environment.

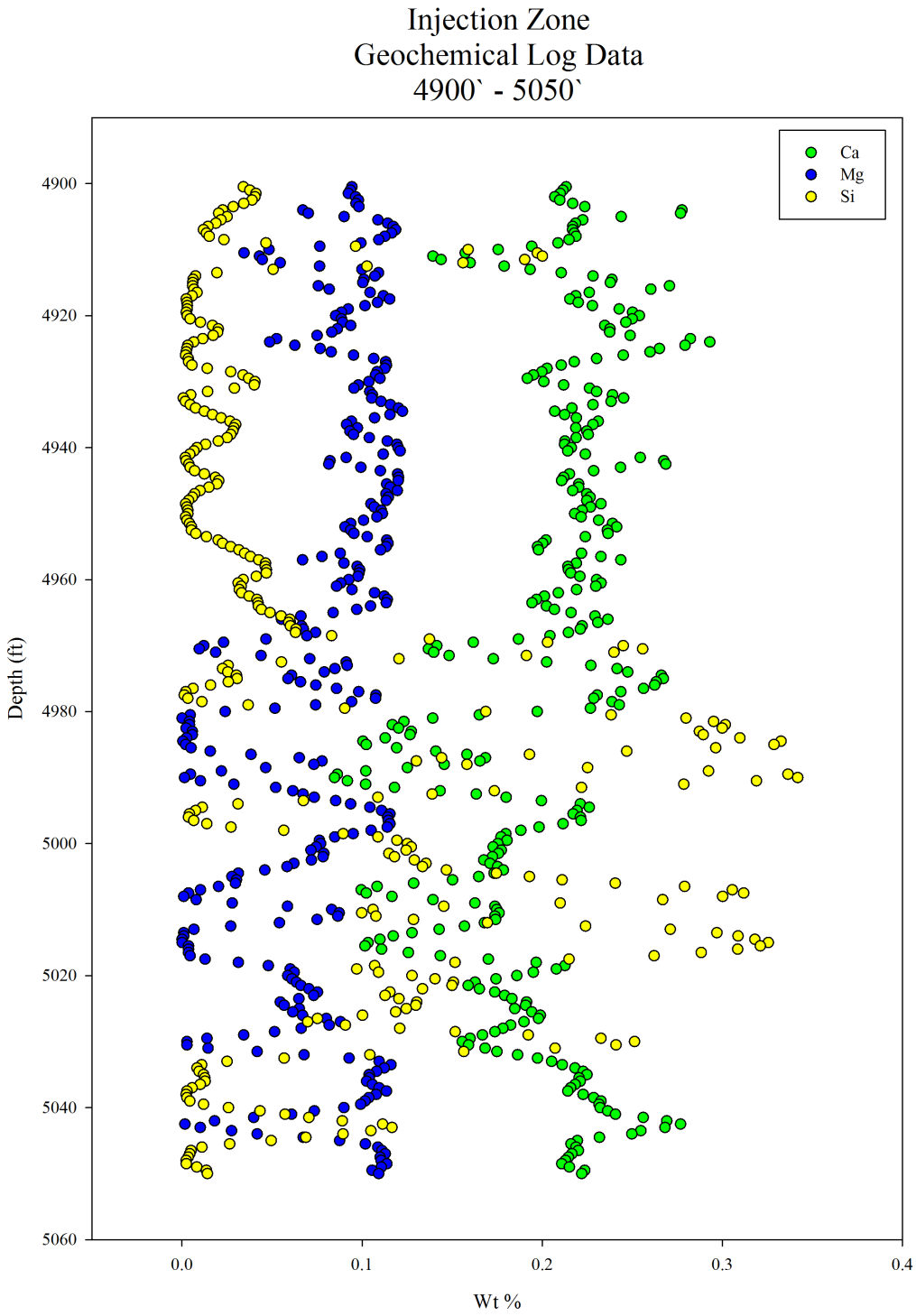

Figure 6-3. Geochemical log of the proposed Arbuckle injection zone (4900`-5050`)

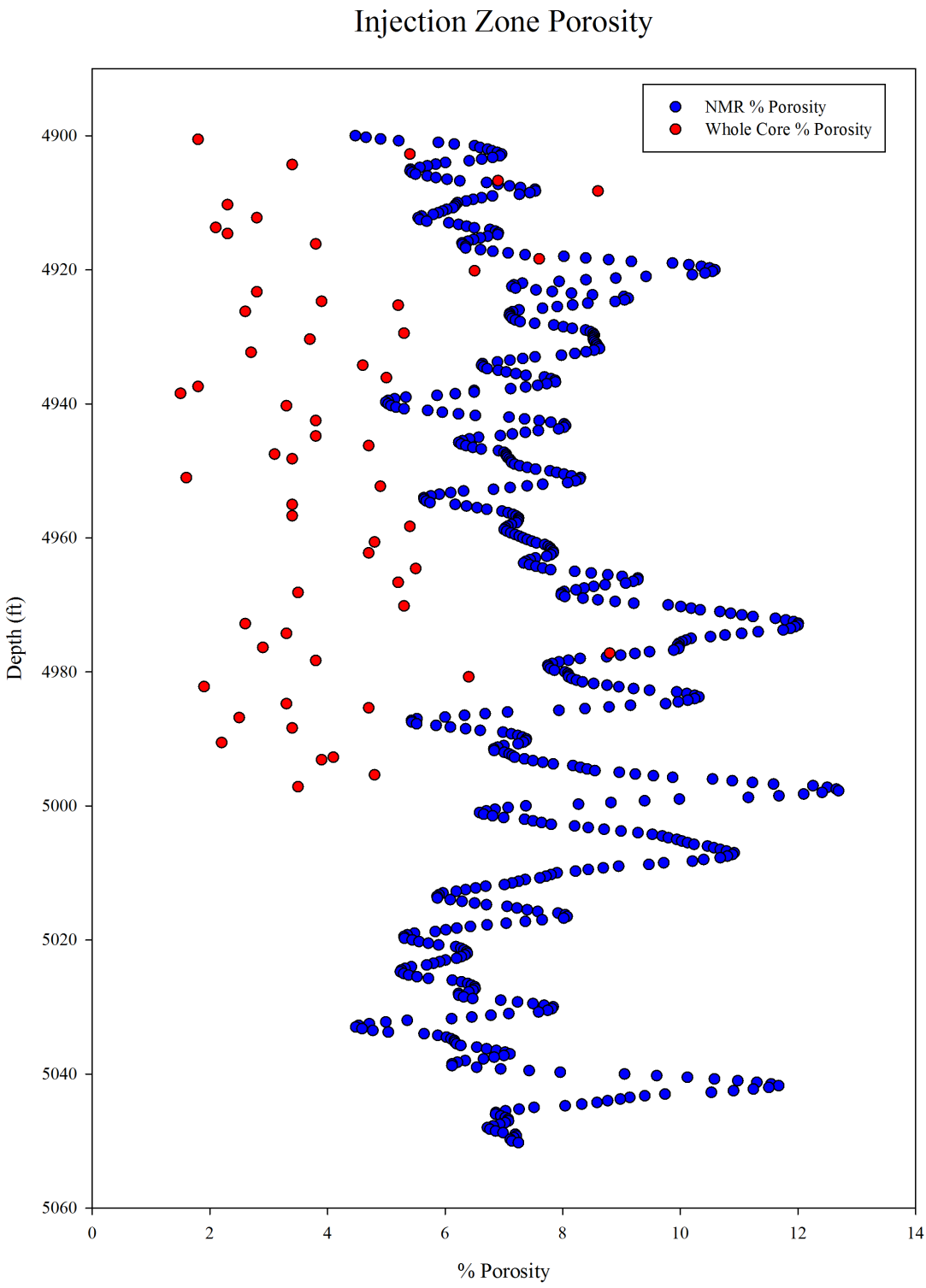

Figure 6-4. Percent porosity of the injection zone as measured by NMR logging tool (blue circles) and whole core porosity measurements (red circles).

Discussion of Hydrogeochemistry

Evolution of Arbuckle Brine

With only one vertical profile it is statistically unreasonable to draw definitive conclusions about the origin and evolution of Arbuckle brine without more laterally extensive data, however, clear trends are observed with increasing depth in the experimental wells. Vertical connectivity of Arbuckle brines can provide information into how an injected CO_2 plume will migrate through the formation. This connectivity was examined by looking at the evolution of the Arbuckle brine.

Brines produced from KGS 1-32 and 1-28 fit well with historical data presented in Chapter 3 (Fig. 6-5). The concentrations of elements measured in this work are all above seawater concentrations while some Arbuckle data have concentrations lower than seawater that approach the origin of the graph. This indicates that some Arbuckle brine has formed from a secondary brine that has an origin from the dissolution of halite. These brines are most likely produced from the west and east of the field sites. A detailed examination of the historical data is beyond the scope of this work. In this section a comparison has been made between produced brine from KGS 1-32 and 1-28 and brines formed from the seawater evaporation process (refer to Figs. 5-14 and 5-15).

Compared to modern seawater evaporation curves (Fontes and Matray, 1993), Arbuckle brine is heavily depleted in Mg^{2+} and SO_4^{2-}, slightly depleted in K^+ and Br^-, and enriched in Ca^{2+} and Sr^{2+} (see Fig. 5-16 & 5-17). As mentioned in the background chapter (Chapter 2), albitization of feldspars and dolomitization of calcite are two diagenetic processes thought to exert significant influence on Ca^{2+} and Na^+ concentrations in brines. The Na^+ composition of Arbuckle water closely follows the seawater evaporation curve which suggests albitization has not affected Na^+ in Arbuckle brine (Houston et al, 2011). Absence of alumnosilicate minerals from the formation mineralogy reinforces this conclusion. Enrichment of Ca^{2+} and Sr^{2+} accompanied by depletion of Mg^{2+} and SO_4^{2-} could be due to the process of dolomitization through the following equation (Carpenter, 1978; Houston et al, 2011):

$$2CaCO_3 + Mg^{2+} = CaMg(CO_3)_2 + Ca^{2+} \quad \text{.....(22)}$$

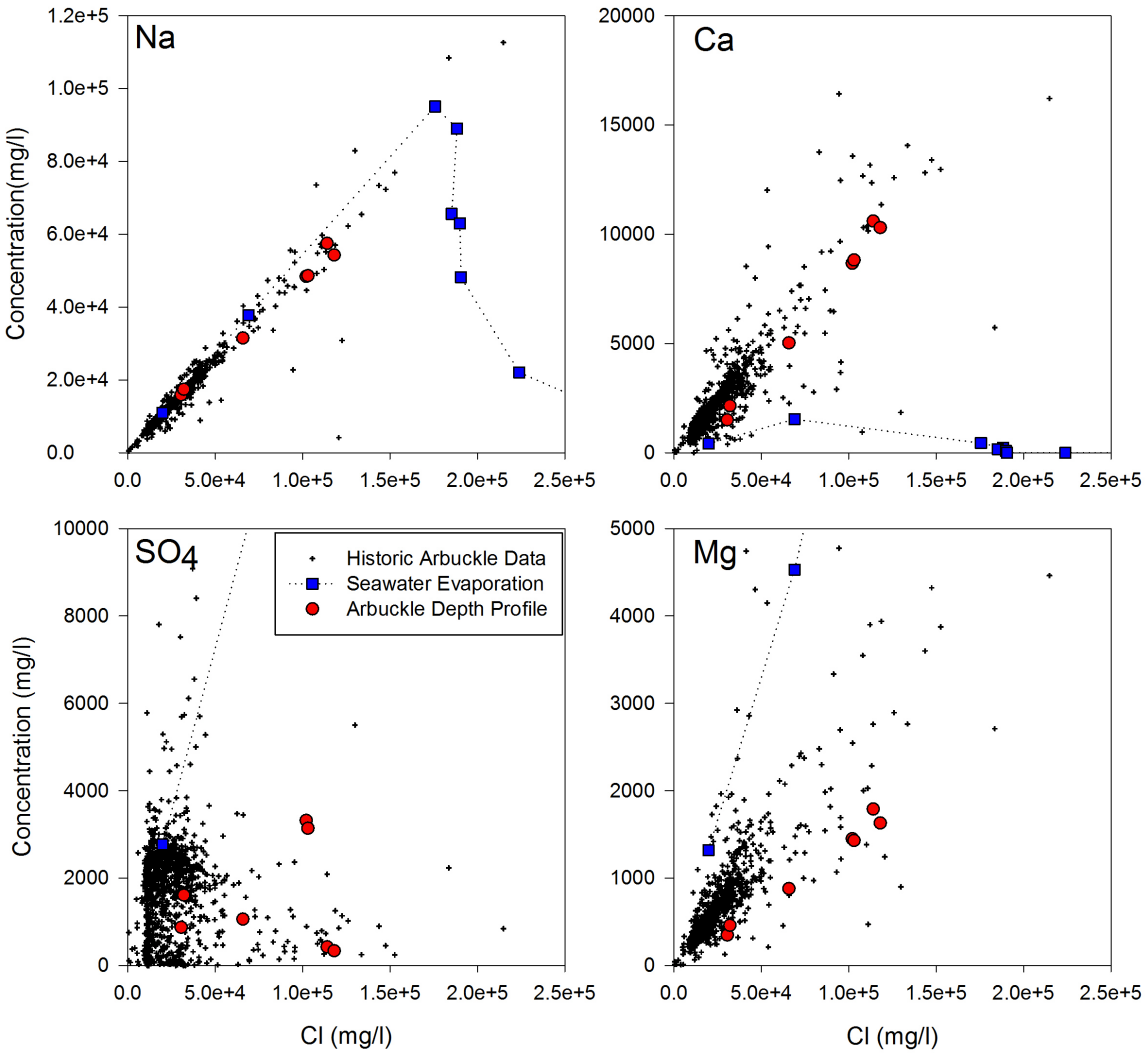

Figure 6-5. Historic Arbuckle data plotted with Arbuckle data from KGS 1-32 and 1-28 and compared with seawater evaporation curve.

Extensive dolomite was observed in the mineralogical investigation of the core from KGS 1-32 and replacement textures are prevalent in thin section. If dolomitization of calcite is responsible for the Ca^{2+} enrichment of the brine, a plot of (Ca^{2+} + Mg^{2+}) against Cl^- should fall along the seawater evaporation curve for these elements (Davisson and Criss, 1996). This relationship is clearly shown in Figure 6-6, providing further evidence that dolomitization has exerted significant influence on the hydrogeochemistry of Arbuckle brine.

Another method for examining the effect of diagenetic changes within a saline aquifer is a Ca/Mg vs Ca/Sr molar ratio graph. With this plot the effects of carbonate replacement and recrystallization can be interpreted. Figure 6-7 shows the relationship between the brine

collected from KGS 1-32 and 1-28. There are two distinct trends with the upper Arbuckle which plots in the lower left corner while the lower Arbuckle, Mississippian and granite wash plot in a more linear trend towards the upper left. These two trends have been described by McIntosh et al (2004) and represent the effects of dolomitization and calcite recrystallization. These trends are displayed as the dashed arrows in Figure 6-7. The lower Arbuckle brines have been more affected by dolomitization than the upper Arbuckle, which show a calcite recrystallization trend. The lithology compiled through well logs and core description show there is limestone in the upper Arbuckle and this is clearly shown in the brine chemistry. The differing chemical trends is further evidence that the upper and lower Arbuckle are not well connected.

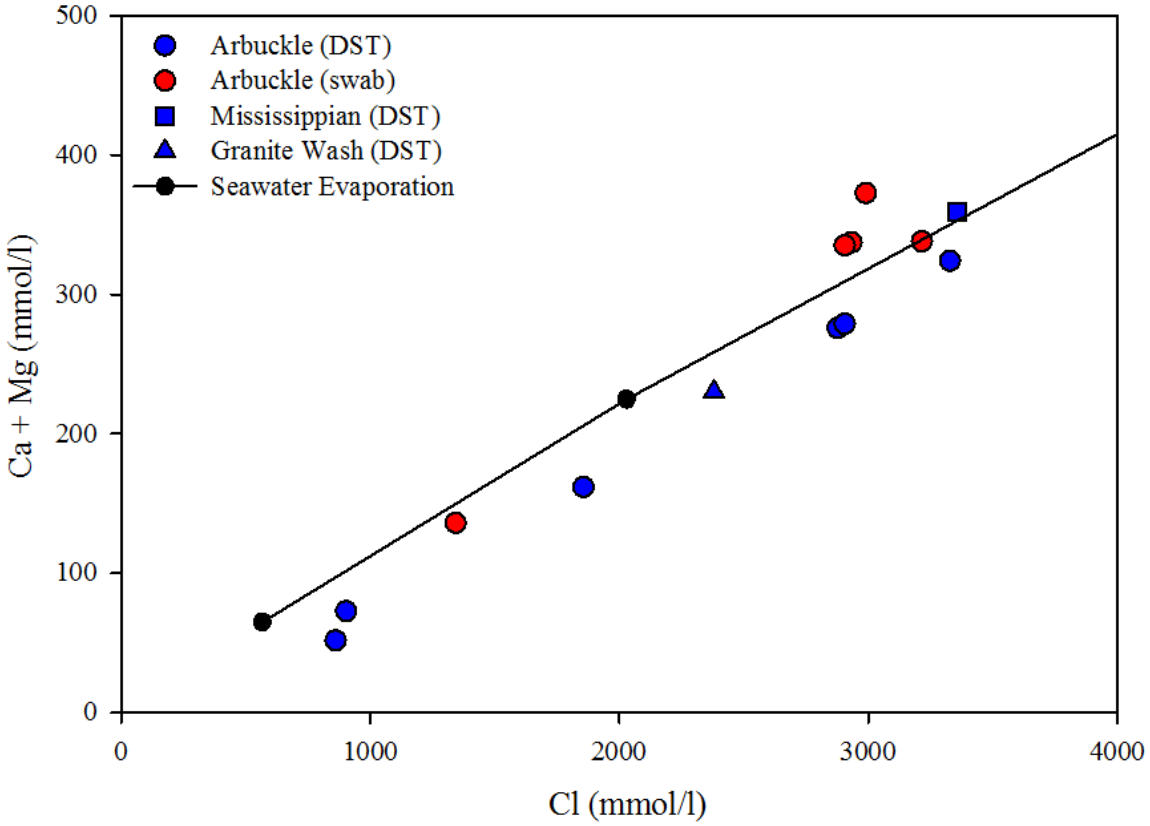

Figure 6-6. (Ca^{2+} + Mg^{2+}) plotted against Cl^- with the seawater evaporation curve, showing influence of dolomitization on Arbuckle brines.

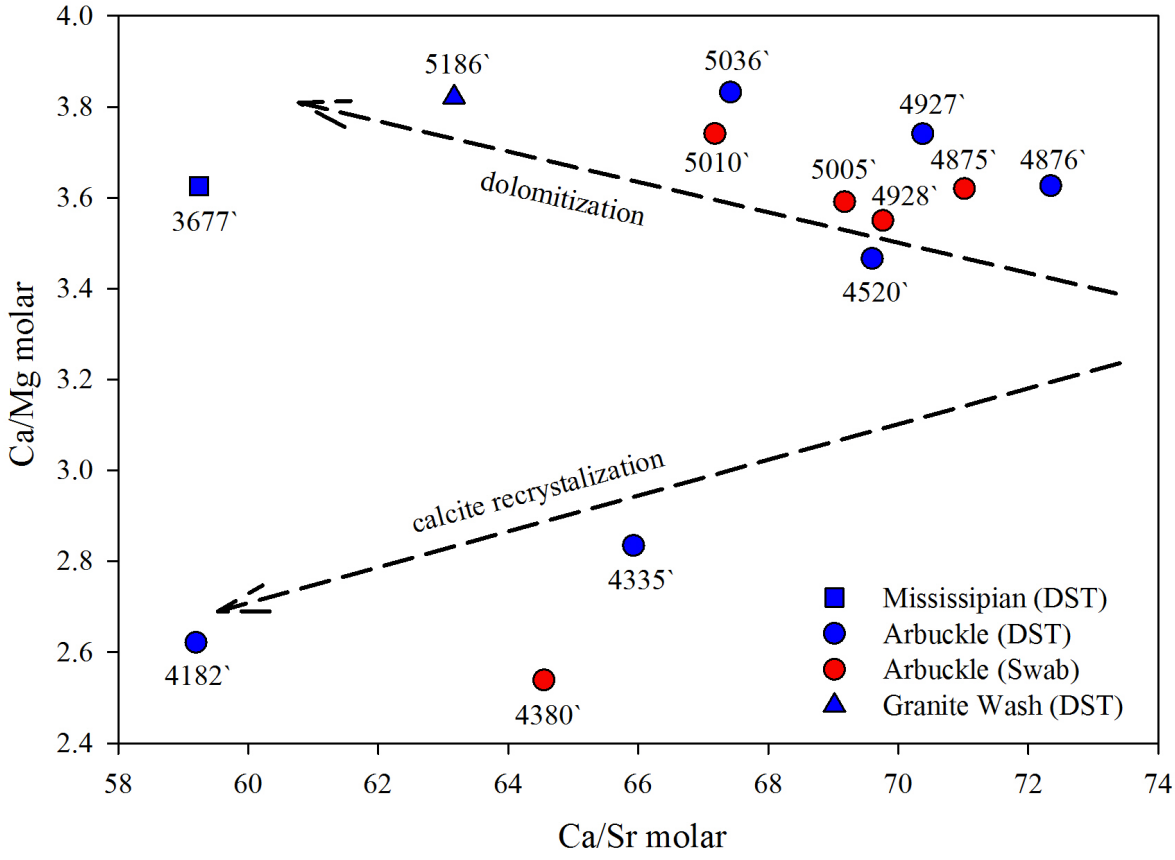

Figure 6-7. Ca/Sr vs Ca/Mg molar ratios showing trends of dolomitization and calcite recrystallization; *(trends from McIntosh, 2004).*

Using the $Ca_{excess}/Na_{deficit}$ graph proposed by Davisson and Criss (1996), and introduced in Chapter 3 of this work, we can see that the Arbuckle brine has a positive Ca^{2+} excess and Na^{+} deficit (Fig. 6-8). The data obtained in this work correlates well with historical data also plotted in Figure 6-8. The lower Arbuckle has more of an excess than the upper Arbuckle, which correlates with the molar ratios in Figure 6-7. The upper Arbuckle has possibly experienced calcite recrystallization which explains the lack of substantial Ca^{2+} excess. The lithological profile of the Arbuckle obtained from logs and whole core description describe some limestone in the upper Arbuckle. The historical data extends into the negative quadrants, which indicates influence of halite dissolution. The excess Ca^{2+} within the Arbuckle has implications for the geochemical reactions initiated with the injection of CO_2 into the subsurface. With low alkalinity values, bicarbonate ions that form from the dissolution of supercritical CO_2 into the brine could supersaturate the brine with respect to

calcite over a relatively short time period (Wang et al, 2011). This could induce early precipitation of calcite, potentially filling the porosity of the injection zone.

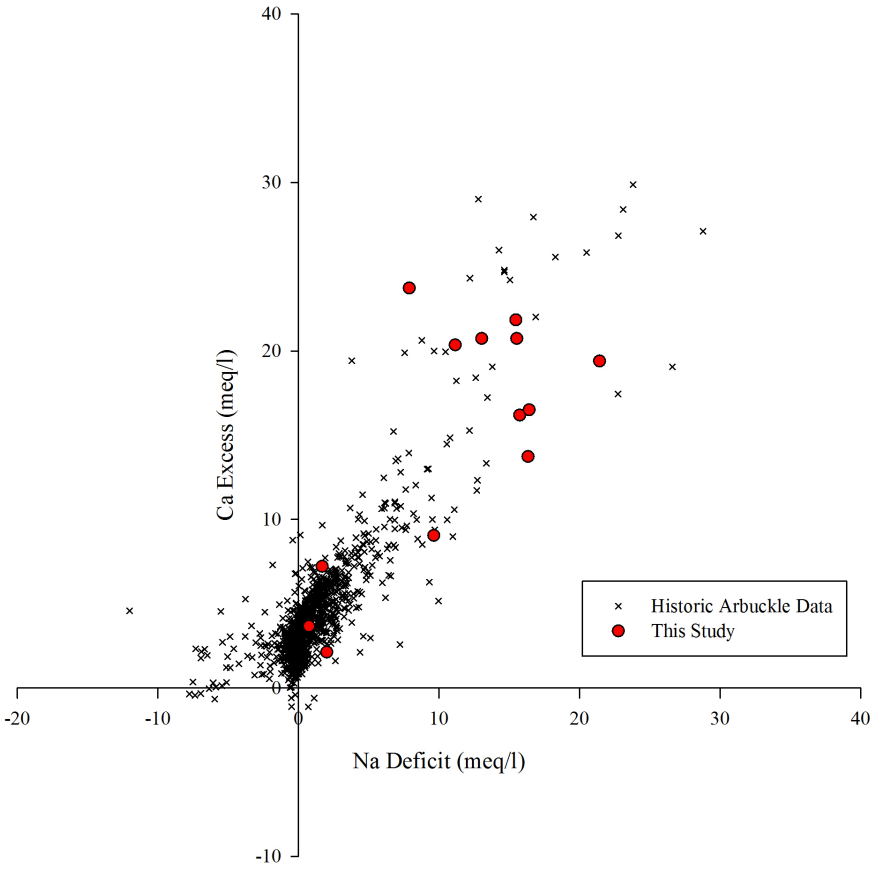

Figure 6-8. $Ca_{excess}/Na_{deficit}$ plot with historic Arbuckle data and samples obtained in this work.

SO_4^{2-} shows no clear trend with chloride in the Arbuckle and is deficient with respect to seawater evaporation. Two mechanisms are believed to have the most effect on sulfate levels in saline conditions: diagenetic alterations (formation of $CaSO_4$ during seawater evaporation and/or dolomitization) and the microbial reduction of sulfate into sulfide (Wilson and Long, 1993). The formation of gypsum is given by the following reaction:

$Ca^{2+} + SO_4^{2-} \rightarrow CaSO_4$ ……(23)

And the microbial reduction of sulfate to sulfide is given by the following reaction, where CH_2 represents organic matter:

$SO_4^{2-} + 2CH_2O \rightarrow H_2S + 2HCO_3^-$……(24)

The precipitation of $CaSO_4$ is not likely to be the source of sulfate deficiency because no gypsum has been observed in thin section or XRD analyses of the cores of Arbuckle rocks.

While gypsum formation cannot be ruled out, the observation of high H_2S gas concentrations during sampling of the lower depths of KGS 1-28 and 1-32 implies biological sulfate reduction contributes substantially to the SO_4^{2-} deficit at depth within the Arbuckle (Penny, 2003). Biological sulfate reduction is a common process in hypersaline evaporative environments (Sonnenfeld, 1984).

The low SO_4^{2-} concentrations observed at 5036` and 5010` is accompanied by a spike in concentration higher in the formation at 4927` and 4876`. This is a common occurrence within subsurface waters and is the result of 'microbial stratification'. The sulfide precipitation created by the sulfate reducers rises in the formation where it is utilized by sulfide oxidizing bacteria, releasing sulfate (Maier et al, 2000). Geochemical data reinforce the idea of microbial stratification which has been confirmed through DNA work conducted at the University of Kansas (Scheffer, 2012). The effect of high or low sulfate on CO_2-brine-mineral reactions is important to consider because sulfate could impede the precipitation of carbonates.

Concentrations of K^+ are depleted with respect to seawater evaporation. The diagenetic mechanisms for K^+ depletion in a saline aquifer involve the formation of silicate minerals such as K-feldspar and illite (Wilson and Long, 1993). These diagenetic reactions are given by the following equations (Carpenter, 1978):

$$2K^+ + 3Al_2Si_2O_5(OH)_4 \rightarrow 2H+ + 2KAl_2AlSi_3O_{10}(OH)_2 + 3H_2O \ldots\ldots\ldots (25)$$

$$2K^+ + KAl_2AlSi_3O_{10}(OH)_2 + 6SiO_2 \rightarrow 2H^+ + 3KAlSi_3O_8 \ldots\ldots\ldots (26)$$

$$2K^+ + Al_2Si_2O_5(OH)_4 + 4SiO_2 \rightarrow 2KAlSi_3O_8 + H_2O + 2H^+ \ldots\ldots\ldots (27)$$

Equation 25 shows kaolinite in the presence of K^+ forming illite. In the presence of silica and K^+ ions, illite can be transformed to K-feldspar via equation 26. Equation 27 shows that kaolinite in the presence of K^+ ions and silica can be altered to K-feldspar. Significant argillaceous zones were observed in the core that could act as a sink for K^+ ions. These argillaceous zones are though to have filled porosity and contribute to the baffle zone between the upper and lower Arbuckle. The dissolution of clay minerals is an important reaction to take into account during the injection of CO_2. If the clay minerals have formed in pore spaces, fractures and flow paths they could readily react with CO_2 acidified brine. Dissolution of phyllosilicate minerals such as phlogopite ($KMg_3Si_3AlO_{10}(F,OH)_2$), though we have not detected this mineral in our rock samples, can provide divalent cations into solution that can

be available for the precipitation of carbonate minerals (Shao et al, 2010). The dissolution of clay minerals in a carbon sequestration scenario is complex and needs further examination.

The depth profile of Si presented in Figure 5-15 shows an increase in concentration at 4520`, which is within the potential baffle zone. A high degree of silicification is evident in thin sections from this zone which could be contributing to high silica concentrations in the brine. The correlation between high Si in baffle zone brine samples and extensive mineral occurrences of quartz in this zone is not replicated in highly silicified zones within the injection zone. In the baffle zone, high Si concentrations in the brine and formation rock correlates with low porosity. In the injection zone the high silica concentrations found in formation rocks is associated with higher porosity and a lower Si concentration in the brine. This could indicate that high Si in brine is contributing to ongoing silicification in the baffle zone while it has slowed down in the injection zone.

Brine Mixing Within the Arbuckle

Cl^- and Br^- are considered conservative anions during the evaporation of seawater. Br^- concentration remains the same until potassium salts begin to precipitate where it begins to leave solution (Carpenter, 1978; Fontes and Matray, 1993). Arbuckle brines analyzed in this study have not reached that level of evaporative enrichment with some species just passing the gypsum precipitation stage (Figs. 5-16 & 5-17). Because of the conservative nature of the Cl^-/Br^- ratio, deviations from the seawater evaporation curve can indicate mixing between primary and secondary brine, or waters of meteoric origin (Fontes and Matray, 1993). Figure 6-9 shows the Cl^-/Br^- ratio plotted against Cl^- concentrations. Brines in the Arbuckle and granite wash show a general horizontal trend with an upward shift from the seawater evaporation curve. This upward shift represents a depletion in regards to Br^- might indicate mixing with a secondary brine formed from the dissolution of halite (Fontes and Matray, 1993). Within the Arbuckle data, there are two distinct groupings, the upper Arbuckle and the lower Arbuckle. Similar groupings are evident in the Li data presented in Figure 5-15. Lithium is not affected by major diagenetic processes and is therefore mainly influenced by groundwater mixing (Fontes and Matray, 1993). Stable isotope values also display clustering of upper and lower Arbuckle data (Figs. 5-18 & 5-19). These grouping indicate the effect of the baffle zone in terms of vertical connectivity in the Arbuckle in this study area.

The Mississippian brine sample plots below the evaporation curve indicating the presence of a primary brine formed from the evaporation of seawater (Fontes and Matray, 1993). It is interesting to note here that Mississippian brine samples contain higher TDS than the underlying Arbuckle brines. This has been noted in previous studies on Kansas brines (Dingman et al, 1968). Elemental concentrations in brine are expected to increase with depth (White et al, 1965). This could indicate that the Arbuckle aquifer has mixed with lower salinity groundwater.

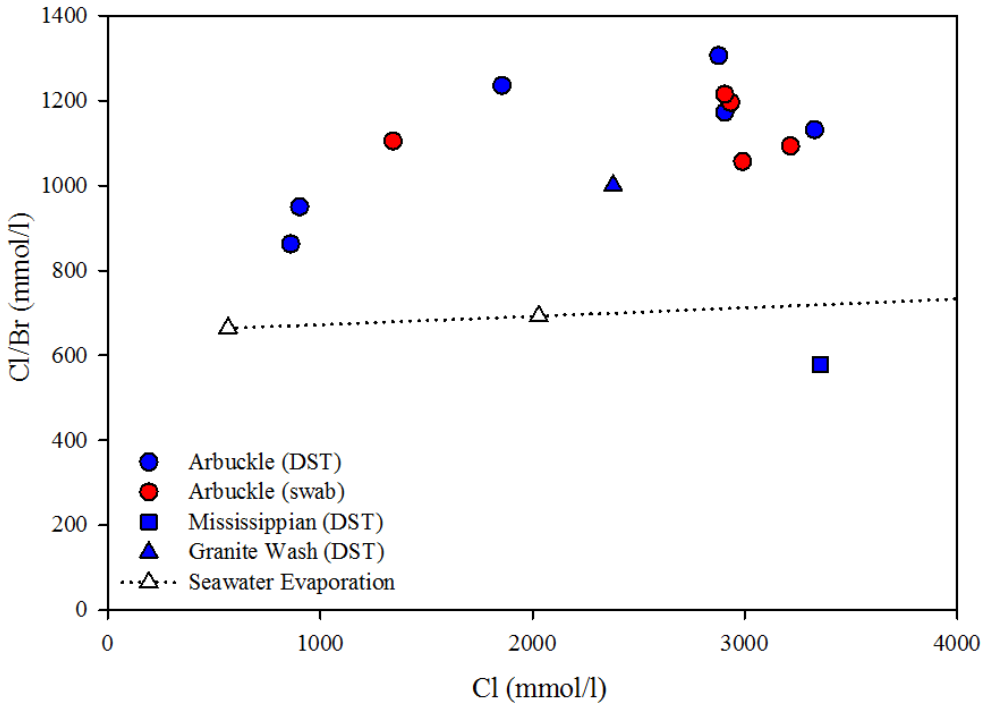

Figure 6-9 Cl/Br ratio plotted against Cl concentration compared to Cl/Br ratio of seawater evaporation.

A groundwater mixing model for brines in the midcontinent United States has been proposed by Musgrove and Banner (1993). Three end members were described and brines classified into distinct groups based on major element (Cl^-, Br^-, Na^+, Ca^{2+}) concentrations and stable isotopic values of $\delta^{18}O$ and $\delta^{2}H$. End member 1 is a low salinity ground water of meteoric origin, end member 2 is a secondary brine originating from the dissolution of halite and end member 3 is an evolved seawater that could have originated in the Anadarko Basin (Musgrove and Banner, 1993; Garven et al, 1995). Mixing between these end members is common and three mixing groups have been described. Brines analyzed from KGS 1-32 and 1-28 fall into group 3 brines with two exceptions. Group 3 has been described as mixing

between a primary brine (evolved seawater, end member 3) and a brine formed from the dissolution of halite (end member 2). The exceptions to this grouping found in our data is at 4335` and 4388` and are significantly more depleted in ^{18}O and ^{2}H than the rest of the Arbuckle. This water to our understanding falls into group 2 as described by Musgrove and Banner (1993) which have a strong dissolved halite signature. This has significant implications for the connectivity of the groundwater flow system in the Arbuckle. The 4335` and 4388` samples occur above the baffle zone in the Arbuckle and are within a high porosity zone. This zone could have increased flow rates, enabling faster mixing rates than the lower Arbuckle. The group 2 brines have been described as regional groundwater flowing from the west and has a distinctive meteoric origin. Our interpretation is that as the groundwater migrated eastward it mixed with downward migrating brines formed from dissolution of halite (Musgrove and Banner, 1993). The 4335` and 4388` depths are more depleted in Br^-, typical of brines formed from the dissolution of halite (Carpenter, 1978).

When plotting the ^{18}O and ^{2}H values against Cl^-, two trends seem to emerge (Fig. 6-10) to infer some explanations. From 4335` to 5035` there is a linear trend indicating mixing between end member 2 brine (shallow Arbuckle) and an end member 3 brine (deep Arbuckle). Depth 4176` (top of the Arbuckle) seems to fall on a different trend than the rest of the Arbuckle data. It could be in a linear relationship with Mississippian brines, indicating there is connectivity between the top of the Arbuckle and Mississippian formation in this location. More isotope data would be needed from the Mississippian formation to confirm this interpretation. Below the top of the Arbuckle, the high porosity zone could be bringing a halite derived water with a more meteoric signature from the west. Another important aspect of this data is the observation that the deep Arbuckle samples seem to have a grouping of isotopic values distinct from upper Arbuckle values. An even spread between the data would indicate the Arbuckle is well mixed. Depth 4520` is an intermediate point between the two groups and this sample is located within the baffle zone. The low porosity baffle zone present in the Arbuckle could be limiting the mixing between upper and lower Arbuckle creating the clustering of stable isotope values as well as Cl^-/Br^- ratios and Li^+ concentrations.

The differing mixing regimes between the lower and upper Arbuckle are important to take into account in characterizing an aquifer for CO_2 injection. An upward migrating CO_2 plume will encounter different brine chemistry as well as a possibly higher flow rate on a

more regional scale. Connection between the upper and lower Arbuckle needs to be well characterized to determine how fast the CO_2 plume will pass through the baffle zone and enter the upper Arbuckle. Reactions between CO_2 and minerals in the baffle zone could open flow pathways and increase mixing between upper and lower Arbuckle. High concentrations of argillaceous minerals could be reactive in the presence of $scCO_2$ and dissolve to release metals such as Fe and Mn into solution. Monitoring the upper Arbuckle chemistry for changes in isotopic values and metal concentrations will reveal if the CO_2 plume has migrated through the baffle zone.

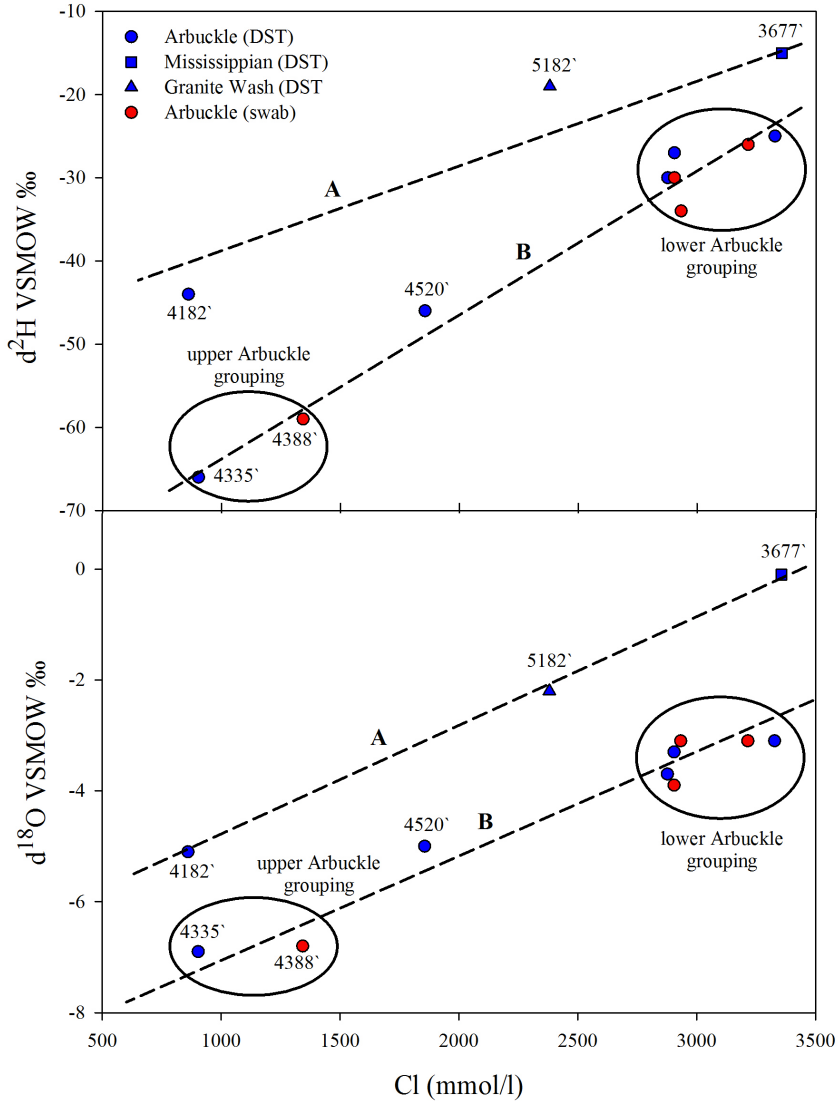

Figure 6-10. Stable isotope data plotted against Cl^- showing mixing between two end members in the Arbuckle. Circles represent isotopic groupings and dashed lines are hypothetical mixing lines.

What is the Role of Iron and Sulfur in Arbuckle Brine?

After analyses of brine samples from the Mississippian and Arbuckle aquifers, iron was found to play a significant role in the hydrogeochemistry of the systems. Iron is a reactive species that plays an important role in every hydrologic system, possibly more so in subsurface water environments. Ferric (Fe III) iron can be utilized by anaerobic microbes as an electron donor. The process of microbial iron reduction is believed to play an important role in the cycling of Fe species in groundwater systems (Hansel et al, 2003). Discrepancies between measured iron concentrations was discussed briefly in Chapter 5. It is safe to assume that iron concentrations of Arbuckle brine are on the high end of what was measured, with a substantial amount present in the form of suspended solids of amorphous FeS^{-}. FeS^{-} (or Fe-S complexes) is an unstable precursor to pyrite formation (Palandri et al, 2005, Pyzik and Sommer 1981). Iron reducing bacteria can coexist with sulfate reducing bacteria in groundwater systems. Reduced iron can react with H_2S created by the reduction of sulfate to for Fe-S complexes (Hansel et al, 2004, Poulton et al, 2003 & 2004). The ratio of Fe II/III increases with depth in the Arbuckle, following trends of decreasing sulfate, decreasing ORP, and increased sulfide. The question that is raised is how this reduced iron will react with injected CO_2 is an important topic to explore and research has been conducted that sheds light onto the reactions between reduced iron, sulfur species and CO_2 (Palandri et al, 2004; Lammers et al, 2011; Ghaderi et al, 2011).

In order to reduce CO_2 capture costs and potentially increase carbonate mineralization it has been proposed to co-inject SO_2 and/or H_2S with CO_2 (Palandri et al, 2004). These sulfur species act as reducers once injected into an aquifer. Researchers have examined the ability for injected sulfides to reduce Fe (III+) (oxy)hydroxides and release Fe^{2+} into the brine. Reduced iron reacts with bicarbonate to form siderite (Lammers et al, 2011; Palandri et al, 2004, 2005):

$$Fe^{2+} + HCO_3^{-} \leftrightarrow FeCO_3 + H^{+} \quad \text{.....(28)}$$

This is a favorable reaction leading to stable, permanent storage of CO_2 in mineral form as siderite. In these studies it was necessary to have a reducing agent to speed the release of Fe II into solution. This is not an issue in the Arbuckle as high concentrations of reduced Fe are already in solution, or present as suspended colloids of amorphous FeS^{-}. This reduced Fe could quickly react with dissolved CO_2 to form siderite. The reaction has potential advantages

and disadvantages regarding CO_2 storage and a potential thermodynamic hurdle to cross before siderite can precipitate.

Precipitation of siderite has been shown to occur in CO_2 sequestration scenarios (Palandri et al, 2005; Lammers et al, 2011). Increasing the ability to store CO_2 as minerals is a huge advantage in carbonate aquifers where mineralization reactions are limited. The rate of this reaction could have important implications on the continuing viability of an aquifer to accept injected CO_2. Studies so far have examined the effects of a CO_2 and sulfide injection on iron (oxy)hydroxide minerals (Palandri et al, 2005; Lammers et al, 2011) and have not examined the effects of injecting into a brine that already has high levels of ferrous iron in solution. The rate limiting factor in these experiments was the dissolution of the iron oxyhydroxide minerals and release of ferrous iron. Since Fe^{2+} already exists in solution or as suspended colloids, the rate limiting step for precipitation of iron carbonates in the Arbuckle would be the dissolution of CO_2 into brine and the subsequent dissociation of carbonic acid leading to the availability of carbonate. Reactions could be fast enough to block pore spaces, limiting the ability of the aquifer to accept CO_2 over meaningful periods of time. Quick mineral reactions leading to reduced permeability is a potential disadvantage of high iron concentrations in the aquifer. This quick precipitation of siderite would most likely occur in pore water and around suspended colloids rather than on mineral surfaces making the precipitated carbonate less stable. As the chemical equilibrium between the formation brine and injected CO_2 evolves, the Fe carbonates could dissociate, releasing the trapped CO_2 into solution.

Before the Fe can react with carbonate, it has to overcome the saturation state of iron sulfide species such as Fe-sulfide complexes and pyrite. Iron and sulfide have a strong affinity for each other and carbonate activity has to exceed that of the sulfide species if these carbonate reactions are to take place. This will depend on how quickly and how much CO_2 can dissolve into the brine. Palandri et al (2004) conducted simulations examining reactions between CO_2, H_2S and hematite. They found that if 1.25 mol% H_2S is added to the CO_2 stream then siderite will be favored over the precipitation of iron sulfide minerals. This suggests that the amount of CO_2 that needs to be dissolved in brine containing H_2S in high initial concentrations will be significant. Dissolution of carbonate minerals in the formation will add to the carbonate concentration of the brine. It is likely that injected CO_2 could enable

the precipitation of amorphous FeS and eventually FeS_2 with such high sulfide contents. This will sequester the H_2S gas while increasing the relative CO_2 content in the brine. The concentration of H_2S in solution will decrease to the point where Fe carbonate minerals will precipitate.

The presence of high concentrations of reduced iron and sulfur species in the injection zone zone brine adds significant complexity to the geochemical reactions induced by the injection of $scCO_2$. Previous studies revealed that the injection of CO_2 into an aquifer with high levels of H_2S causes the exsolution of H_2S gas into the leading edge of injected CO_2 plume (Ghaderi et al, 2011). This could lower concentrations of sulfide species in the brine, enabling iron to form carbonate rather than sulfide minerals.

This exsolution could also transport H_2S gas into upper zones of the formation where sulfide species are low and sulfate is high, complicating reactions between CO_2, acidified brine and formation minerals. These species need to be carefully monitored during injection to determine what reactions are taking place. Quick precipitation of iron sulfide minerals could result in blocked porosity leading to increasing injection pressures. If injection pressure builds up too much, fractures could develop allowing the CO_2 plume to migrate away from the near well bore environment. Local, small scale fractures in the injection zone are not a compromising issue for the integrity of the seal 1000+ feet above, but make monitoring the path of the CO_2 plume significantly more difficult.

Discussion of Supercritical Flow-through Experiment

Cl^- is assumed to be a conservative element and was interpreted as a tracer during this experimental process. Ratios of Cl^- with major elements reveal trends among potential reactions and identify experimental artifacts that have affected these flow results. The ratios are generally clumped with the exception of three data points, hour zero, hours 8-20 and hour 24 (Fig. 6-11). Hour zero and hour 24 show lower Cl^- concentrations than was analyzed in the original brine. This could represent a dilution event that occurred during the experimental process. The pipes were flushed with brine before the experiment to remove any other fluids in the piping, but the flushing might have left some residual fluid in the piping. Dilution with a residual fluid could account for the 6% decrease in both Cl^- and Na^+ concentrations during the brine only flow stage.

Another possibility for the initial decrease in concentration of Cl^- is the precipitation of halite once the brine was introduced into the core. Collected brine was not stored at formation pressure and will have equilibrated to the lower storage pressure. By reapplying the formation pressure, changes in the chemical equilibrium could have induced precipitation of halite. It has been observed in previous flow experiments that NaCl can precipitate upon the injection of CO_2 and increasing the pressure of a brine (Izgec, 2008). At low flow rates the possibility of mineral precipitation increases, which imitates the current experiment (Izgec et al, 2008). The low flow rate of the saturation phase could have induced the precipitation of NaCl as the brine was first introduced. This hypothesis is supported by the observation that not all elemental concentrations decreased in this first phase and Cl^- and Na^+ both decreased by 6%. Fe shows a considerable increase in the brine phase, which implies Fe was mobilized from the core into solution as the re-pressurized brine was passed through. Mn^{2+} concentrations also increase considerably during the brine phase and could be due to similar processes as described for Fe. Association of Fe and Mn^{2+} in sedimentary formations is ubiquitous and similar behavior is expected. The large decrease observed in concentrations of Fe and increase in equivalent bicarbonate alkalinity could result from precipitation of siderite. No direct evidence of siderite was observed in the retrieved core, hence these decreases are likely caused by precipitation of the observed iron oxyhydroxides or oxides. The mechanism contributing to the increase in P during the saturation phase is not clear. Both of these

scenarios (dilution and halite precipitation) are plausible to explain elemental decreases/increases during the saturation phase and it is unreasonable to confirm one or the other. It is likely both hypotheses contributed to changing brine composition during the initial saturation phase.

The potential dilution event at hour 24 is similar to the hour zero event, except Cl^-, Br^-, Mg^{2+} and SO_4^{2-} are the only species that decrease. Na^+, Ca^{2+}, Fe, S and Mn^{2+} slightly increase during this time. At this point in the experiment, no residual fluid is present that could have contributed to dilution. Our hypothesis is that deionized water leaked from the CO_2 accumulator as it was being pumped into the system. As described in the methods chapter, the accumulators use DI water to move a piston, thereby injecting the fluid in the accumulator. Near the end of the experiment, the CO_2 accumulator could have emptied all of the CO_2 it contained. With the pumps still pumping DI water into the piston chamber, some could have leaked around the piston and entered the piping. This accounts for the decrease in Cl^-, but does not take into account the increases in other species such as Ca^{2+} and Na^+. There could be Na^+ rich minerals in the form of argillaceous material contributing to Na^+ increase. Similarly if there was precipitation of halite that accounted for the decrease in Cl^-, Na^+ concentrations would decrease by the same magnitude since Halite has a 1:1 Na:Cl ratio. This is the best plausible explanation that can be given with the conditions of the experiment and the changing concentrations of elements with time.

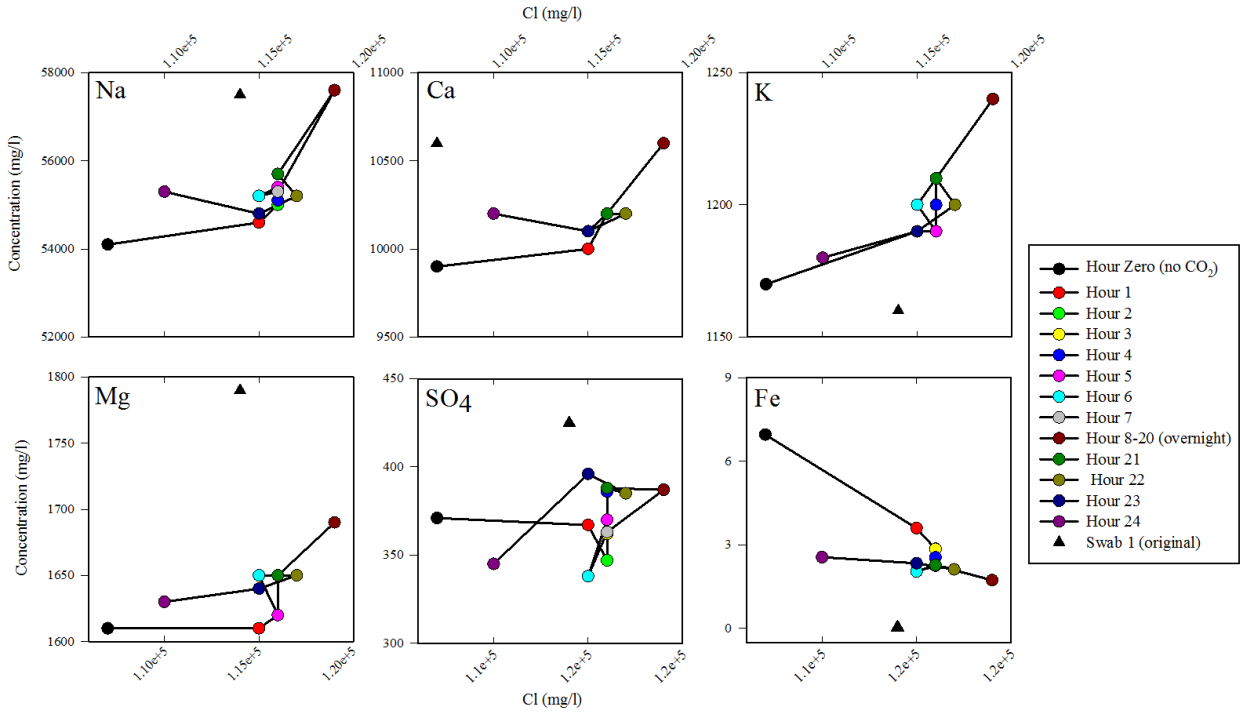

Figure 6-11. Chloride ratios with Na^+, Ca^{2+}, K^+, Mg^{2+}, SO_4^{2-}, and Fe during flow-through experiment. Lines are hypothetically connected to show changes in the trend as time proceeded. SO_4^{2-} was plotted to determine the way variation of SO_4^{2-} would be affected by changing brine concentration. It seems Fe, Mg, and SO_4^{2-} are readily forming or precipitating during hour 2 and hour 6.

The overnight sample (hour 8-20) also show deviation from the general trend observed in the time series results. Due to inaccessibility of the experiment during the overnight runs, the sample had to be collected in a large beaker. The concentrations of Cl^-, Na^+, Ca^{2+}, Mg^{2+}, Mn^{2+}, and SO_4^{2-} all increase during this time, as is evident in the spike in the time series. These species have been concentrated by evaporation of the brine effluent as it resided in the beaker (even though it was covered in parafilm) for a considerable period of time. Fe and S decreased in this sample, which could be due to the precipitation of FeS_2 as was seen when the swabbed water samples were taken from depth. During this evaporative enrichment event, concentrations of Ca^{2+}, Mg^{2+} and Na^+ increased close to, or exactly similar to, original brine concentrations. P decreased to its original brine concentration of 0.02 mg/l.

When comparing the measured pH values to alkalinity values, it appears that the two parameters show an inverse relationship (Fig. 5-21). When pH decreases over the first four

hours of CO_2 injection the alkalinity values increase, indicating dissolution of carbonate minerals. A subsequent increase in pH inhibits carbonate dissolution, reducing alkalinity values. The first 7 hours show strong variation of both pH and alkalinity. This suggests complex reaction are taking place in the initial hours of the experiment as the system attempts to attain a new equilibrium. The overnight sample shows higher values for both pH and alkalinity and it cannot be well interpreted. Degassing of CO_2 allows pH to rise. Bicarbonate would be expected to decrease as carbonate minerals are precipitated out or CO_2 is degassed. It shows an increase possibly due to evaporative enrichment, or more likely, that it does not respond to degassing effects as quickly as pH measurements. The drastic increase in pH relative to alkalinity during the overnight sample supports the stronger effect of degassing on pH. It can be estimated that the pH would follow a roughly linear trend to the relatively stable values during the last four hours of the experiment.

Alkalinity and pH values can also be compared to major elements analyzed in the flow effluent to determine correlations between parameters (Figs. 6-12 & 6-13, respectively). Cl^- and Na^+ do not show a strong correlation with pH throughout the course of the flow experiment. Ca^{2+} and Mg^{2+} do show an inverse correlation with pH. This is expected as Ca^{2+} and Mg^{2+} are present in the dolomite core. Acidic conditions will dissolve Ca^{2+} and Mg^{2+} (along with carbonate) from the core increasing their concentrations in the effluent. The Mg^{2+} concentrations seem to show a delayed response to pH values while Ca^{2+} has a closer relationship. Fe does not show a clear relationship with pH. Fe is more responsive to the redox conditions of the water and less on the pH. Mn^{2+} seems so have an inverse relationship with pH, but it is not a clear correlation. SO_4^{2-} has a good inverse correlation with pH while S has a positive correlation. These species are sensitive to redox conditions, as was seen in the stratification with depth due to microbial action, and seem to be affected by pH variations with injected CO_2.

Alkalinity values seem to correlate more closely to major elements than pH. Alkalinity values are less susceptible to the rapid change observed in pH values once the effluent has been collected. Even if alkalinity values are not exactly what they were at pressure in the core flow experiment, the trend that it shows is expected to be the same. Alkalinity values follow the trend of Cl^- and Na^+ with good agreement, though if these species affect alkalinity or vice versa is unknown. Ca^{2+} and Mg^{2+} concentrations show high positive correlation with

alkalinity values. The dissolution of dolomite in the core releases Ca^{2+}, Mg^{2+} and CO_3^-. Fe shows no significant correlation with alkalinity as with pH indicating redox conditions play a greater role in the mobilization of solid Fe into solution. Surprisingly Mn^{2+} shows a strong positive correlation with alkalinity. There is a slight delay in the alkalinity response, but it appears that Mn^{2+} is more mobile with increasing alkalinity in this experimental system.

SO_4^{2-} also shows a strong positive correlation with alkalinity values while S has a negative correlation. High sulfate in the formation could inhibit carbonate precipitation in favor of the precipitation of sulfur species. Elemental sulfur can be precipitated in high pressure flow experiments which could have affected elemental sulfur concentrations throughout the experiment (Guo et al, 2009). The brine used in the flow experiment has low sulfate values compared to brine collected less than 100 feet above in the Arbuckle. The correlation between SO_4^{2-} and alkalinity suggest that higher sulfate concentrations could play a significant role in geochemical reactions. This interaction between injected CO_2 and high SO_4^{2-} concentrations could be reduced due to distance from the injection zone. CO_2 could be dissolved in the brine before migrating upwards into the high sulfate zone, minimizing the impacts of high sulfate on CO_2 dissolution and carbonate mineral precipitation.

Heterogeneity within the core has significant effects on the geochemical reactions expected during CO_2 injection. Because of high flow rates during the experiment and a heterogeneous core plug, reactions cannot be predicted to follow specific paths and differ substantially from field reactions (Li et al, 2008). It has been known that geochemical reactions in the near well bore environment will be heterogeneous due to increased flow rates and initial mixing between brine and CO_2 as the injected fluid is forced into pore spaces (Bemer et al, 2010). Due to the uneven distribution of reactants, preferential dissolution will occur, resulting in the creation of worm holes (Bemer et al, 2010). Based on the mineralogical examination of Arbuckle core, we think these preferential paths will occur along silica-carbonate boundaries. These boundaries have been observed to have been previously fractured and filled with clay or oxide/sulfide minerals. The reactions along these boundaries will result in fluctuations in regard to metal species released into the brine. During the flow experiment, we observed fluctuating concentrations, indicating the effects of heterogeneous material to geochemical reaction rates in the near well bore environment. The ions that fluctuated the

most were redox sensitive metals such as P, Fe and Mn. The preliminary reactions in this system could have been predominantly with argillaceous minerals and not carbonate phases.

During the experiment, CO_2 and brine were injected as separate fluids and combined while flowing within the core plug. Due to the high salinity of the brine, the dissolution of CO_2 could have been inhibited. This would leave the brine as the dominant phase during the reaction and could explain the stability of Ca^{2+} and Mg^{2+} concentrations throughout the experiment. The core plug was an autoclastic breccia with a combination of large pore space and micro porosity. In the microporous regions of the core the effect of salinity decreases and dissolution of CO_2 in the brine could have increased. Higher reactive surface area in the microporous region would increase reactions between minerals and acidified CO_2. Thin section studies revealed the presence of argillaceous minerals and small pyrite crystals. Faster reactions with these minerals explain the dramatic increases in Fe and Mn^{2+} throughout the experiment.

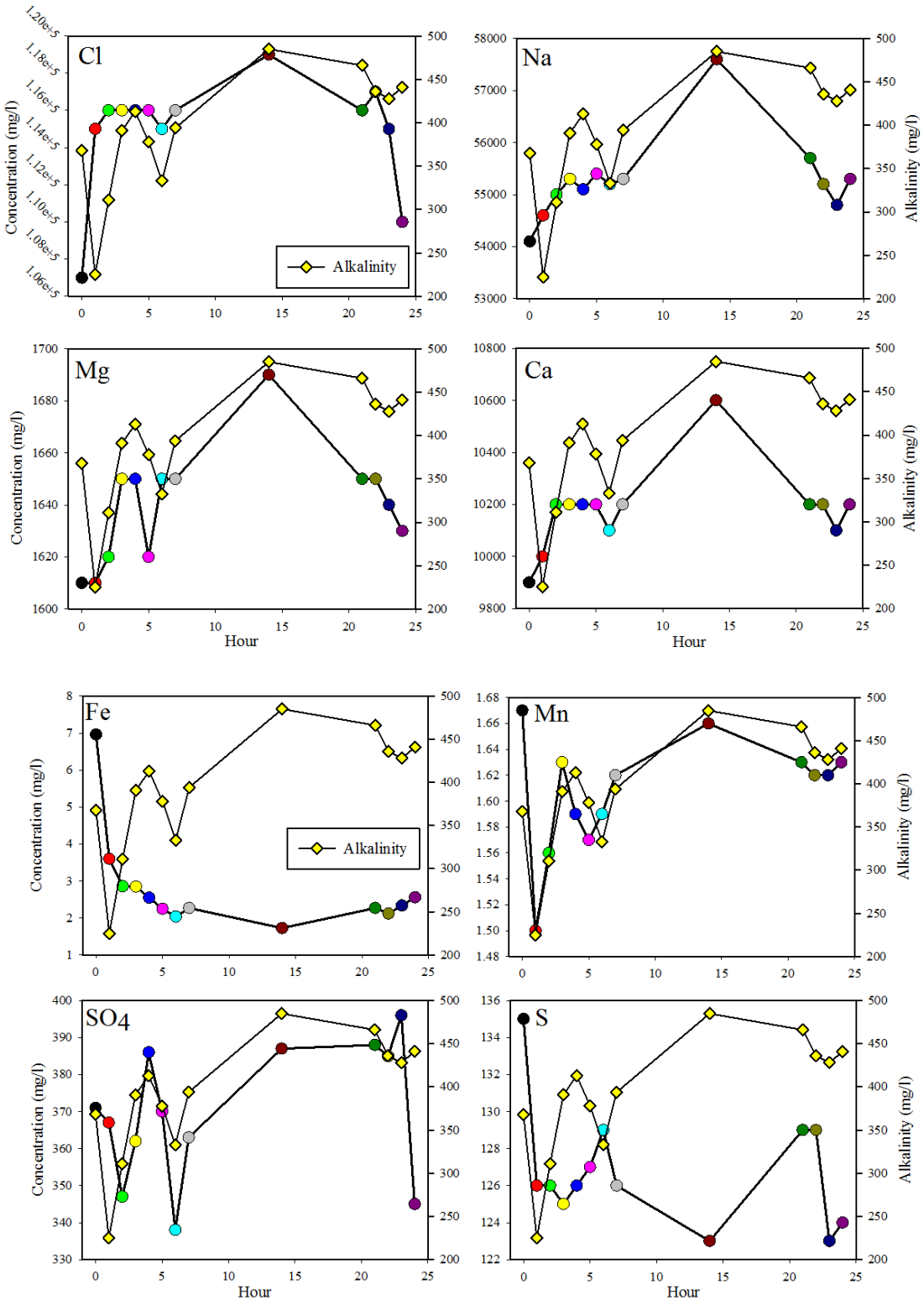

Figure 6-12. Change in major and minor elements and anions as a time series with change in alkalinity.

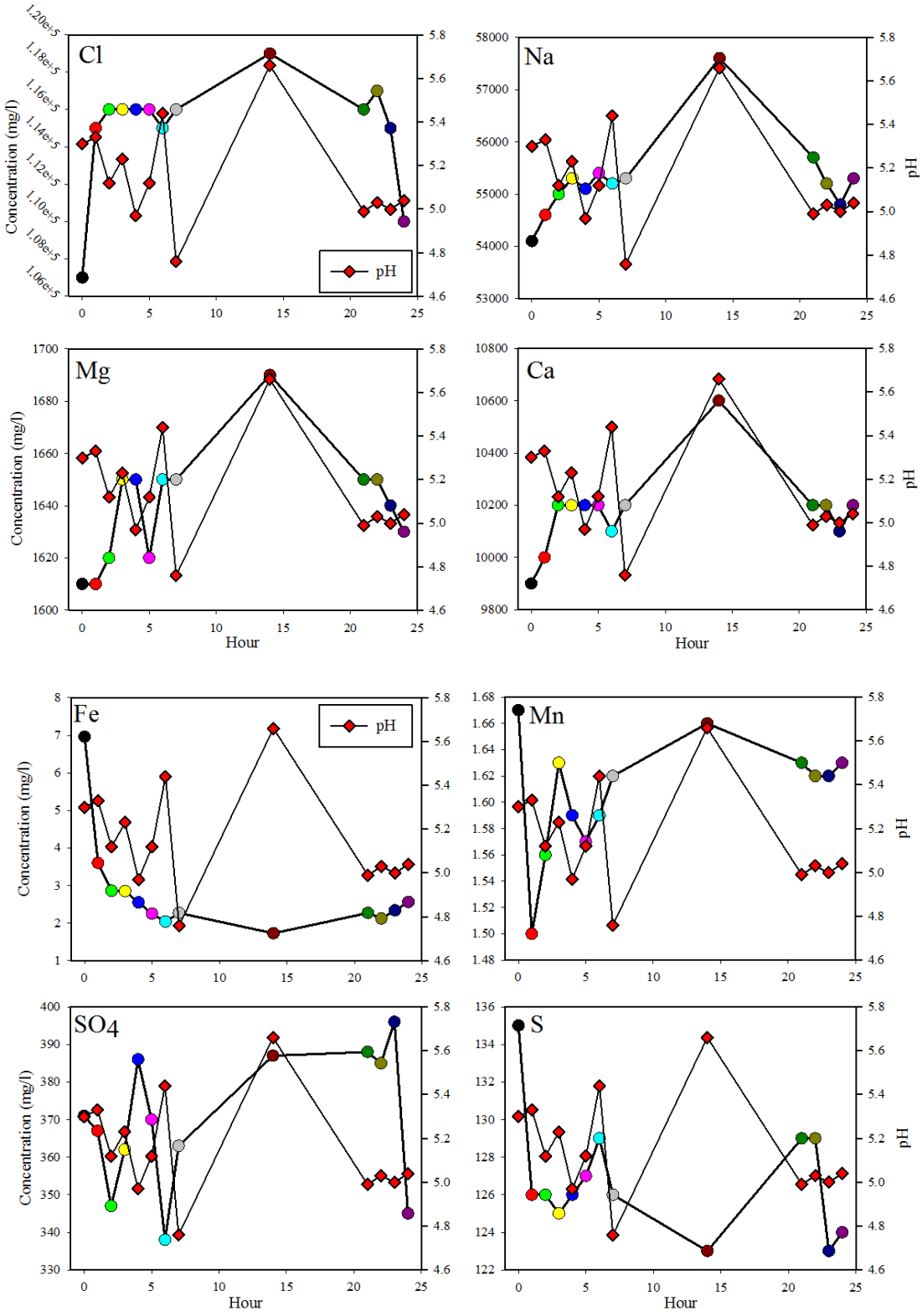

Figure 6-13. Changes in major and minor elements and anions as a time series with change in pH.

Chapter 7 - Conclusion

There is growing consensus in the scientific community that the anthropogenic release of CO_2 and its build up in the atmosphere is affecting Earths climate. In addition to increasing energy efficiency and developing renewable sources of energy, several mitigation techniques have been proposed to curb CO_2 emissions. One of the mitigation methods proposed is the storage of CO_2 in geologic formations. Of the geologic formations being examined in this avenue of research, sedimentary basins show the most promise toward long term secure storage of significant quantities of CO_2. Sedimentary basins are ideal for several reasons: they are non-potable, isolated from fresh drinking water sources, and at necessary pressure and temperature to sustain supercritical CO_2 conditions. The Arbuckle saline aquifer that underlies most of Kansas is well suited for small scale injection and storage of CO_2. The Arbuckle has been successfully used as an oil field disposal well for over 50 years. The characterization of the Arbuckle mineralogy and brine chemistry coupled with supercritical flow-through experiments have provided information on how the formation will react upon CO_2 injection.

The dominant mineralogy of the Arbuckle is dolomite with abundant cherty nodules. At certain zones fractures and brecciation are associated with argillaceous minerals and pyritic crystals. The top of the Arbuckle is limestone rich while the lower portions are exclusively dolomite. This mineralogy is reflected in the hydrogeochemistry as Ca^{2+} is in excess while Mg^{2+} is depleted throughout the aquifer. Ca/Mg vs Ca/Sr molar ratio plots show the effect of dolomitization in the lower Arbuckle while the upper Arbuckle has a calcite recrystallization signature. The correlation between hydrogeochemistry and mineralogy is also seen via the behavior K^+ ion which is depleted in the aquifer due to interactions with clay minerals from the argillaceous zones. Mineral interactions with injected CO_2 will change the elemental ratios of the brine and this can be used to determine the extent of reactions that are occurring in the subsurface.

From mineralogical and hydrogeochemical examination of the Arbuckle aquifer it can be determined that the baffle zone plays a significant role in isolating the upper and lower portions of the formation. Porosity measurements and NMR logs clearly show a low porosity zone between 4400` and 4550` that correlates well with changes in the hydrogeochemistry. Chloride and bromide can be considered conservative tracers in the formation and can be used

to monitor geochemical reactions by examining brine chemistry after CO_2 injection. Cl^-/Br^- ratios indicate that there is separation between the upper and lower Arbuckle. Stable isotope data indicate the upper Arbuckle is influenced by a brine of meteoric water with salinity derived from the dissolution of halite as it migrates westward. The lower Arbuckle is more enriched in $\delta^{18}O$ and $\delta^{2}H$ and could be sourced in the Anadarko basin. The distinct groupings of the upper and lower Arbuckle shown in the Cl/Br ratios and stable isotope data provide evidence for the hydrolic connectivity between these zones within the aquifer. The baffle zone has important implications to the injection and subsequent migration of CO_2 in the Arbuckle. An upward migrating CO_2 plume will be hindered by the low porosity zone and will migrate further in a horizontal direction. Geochemical reactions between minerals, CO_2 and brine will be more extensive at the bottom of the baffle zone and as the plume slowly migrates upward through the low porosity zone. There is a high likelihood that worm holes could develop through this low porosity zone providing preferential pathways for the CO_2 plume to migrate through into the upper Arbuckle.

Iron is present in the Arbuckle in significant quantities and will play an important role in the long term storage of CO_2. Strong reducing conditions and high concentrations of ferrous iron in the injection zone could allow fast carbonate precipitation reactions. Flow experiments showed that Fe decreased once CO_2 was introduced, possibly due to the precipitation of Fe carbonates such as siderite. The quick reaction of ferrous iron in solution and in presence of injected CO_2 could prove unstable in the long term and dissociate once conditions change. Along these lines, the last few hours of the flow experiment showed increase of Fe, potentially from the dissolution of early precipitations of siderite that became unstable as the chemical system evolved. Flow experiments with Arbuckle cores demonstrated dissolution reactions with Ca, Mg, Fe, Mn, SO and S during the first 7 hours while variations in Fe, Mn, SO_4 and S during the last hours of the experiment indicate reactions with non carbonate minerals in the system

CO_2-brine-mineral reactions will be between minerals dolomite, calcite, silica/quartz, pyrite, anhydrite and argillaceous clay material. Small and large scale heterogeneity of mineral occurrences are observed throughout the formation which will create complex mineral-brine-CO_2 interactions. Heterogeneous mineralogy occurs predominantly at the chert/carbonate interface where previous fractures and flow paths have been in filled with

argillaceous and pyritic materials. These zones will be highly reactive upon the injection of CO_2 and will release cations from non carbonate minerals, increasing the possibility of mineral trapping mechanisms in the long run. Fluctuations in brine chemistry observed during supercritical flow experiment showed the effect of heterogeneity on geochemical reactions. Complex reactions will develop in the aquifer with different kinetic rates as CO_2 migrates through heterogeneous material.

The overall conclusion is with possible reactions inferred in the injection zone and their rates obtained, carbonate aquifers with high salinity can prove effective in sequestration. However, special attention needs to be considered towards intricate textural relations within the cores and water chemistry. The stratigraphy of the Arbuckle formation and overlying Mississippian reservoir creates a secure CO_2 storage situation that will allow CO_2 to be physically secure over time frames needed to induce chemical trapping mechanisms. There is no immediate sign of water quality degradation of the shallow aquifer due to injection.

Information gathered in this work will be used to implement a detailed monitoring program once CO_2 has been injected. This future work will be an important stage in assessing the viability and safety of geological carbon storage. Monitoring changes in stable isotopic concentration and Cl/Br ratios will allow future researchers to examine the reactions that have occurred within the aquifer and determine the rates of these reactions. Monitoring will also allow researchers to examine the effect of the baffle zone on the migration pathways of injected CO_2. Slight chemical changes in the upper Arbuckle brine could indicate diffused migration through the baffle zone while rapid changes could indicate migration of CO_2 through the baffle zone along fractures or worm holes that have developed due to dissolution. Utilizing elemental ratios and isotopic changes for mixing between brines has been well established, and this work introduces their use in monitoring the migration and effects of injected CO_2. This geochemical work to some extent also demonstrates no imminent contamination threats due to low volume CO_2 injection into the Arbuckle.

References

Afonso, M. D. and W. Stumm (1992). "Reductive Dissolution Of Iron(III) (Hydr)Oxides By Hydrogen-Sulfide." Langmuir **8**(6): 1671-1675.

Alonso-Zarza, A. M., Y. Sanchez-Moya, et al. (2002). "Silicification and dolomitization of anhydrite nodules in argillaceous terrestrial deposits: an example of meteoric-dominated diagenesis from the Triassic of central Spain." Sedimentology **49**(2): 303-317.

Bachu, S. (2002). "Sequestration of CO_2 in geological media in response to climate change: road map for site selection using the transform of the geological space into the CO_2 phase space." Energy Conversion and Management **43**(1): 87-102.

Bachu, S., and Adams, JJ. (2003). "Sequestration of CO_2 in geological media in response to climate change: capacity of deep saline aquifers to sequester CO_2 in solution." Energy Conservation and Management. **44**: 20. p 3151-3175.

Bachu, S. (2007). "Carbon dioxide storage capacity in uneconomic coal beds in Alberta, Canada: Methodology, potential and site identification." International Journal of Greenhouse Gas Control **1**(3): 374-385.

Bachu, S. (2008). "CO_2 storage in geological media: Role, means, status and barriers to deployment." Progress in Energy and Combustion Science **34**(2): 254-273.

Basbug, B., Gumrah, F., et al. 2005. "Simulating the Effects of Deep Saline Aquifer Properties on CO_2 Sequestration." Canadian International Petroleum Conference. 2005-139.

Bathurst, R. G. (1974). "Marine Diagenesis Of Shallow-Water Calcium-Carbonate Sediments." Annual Review of Earth and Planetary Sciences **2**: 257-274.

Bemer, E. and J. M. Lombard (2010). "From Injectivity to Integrity Studies of CO_2 Geological Storage Chemical Alteration Effects on Carbonates Petrophysical and Geomechanical Properties." Oil & Gas Science and Technology-Revue De L Institut Francais Du Petrole **65**(3): 445-459.

Birkle, P., B. M. Garcia, et al. (2009). "Origin and evolution of formation water at the Jujo-Tecominoacan oil reservoir, Gulf of Mexico. Part 2: Isotopic and field-production evidence for fluid connectivity." Applied Geochemistry **24**(4): 555-573.

Birkle, P., K. Pruess, et al. (2008). "Using Laboratory Flow Experiments and Reactive Chemical Transport Modeling for Designing Waterflooding of the Agua Fria Reservoir, Poza Rica-Altamira Field, Mexico." Spe Reservoir Evaluation & Engineering **11**(6): 1029-1045.

Bradshaw, J., S. Bachu, et al. (2007). "CO_2 storage capacity estimation: Issues and development of standards." International Journal of Greenhouse Gas Control **1**(1): 62-68.

Brennan, S. T. and T. K. Lowenstein (2002). "The major-ion composition of Silurian seawater." Geochimica Et Cosmochimica Acta **66**(15): 2683-2700.

Brosse, E., G. Badinier, et al. (2010). "Selection and Characterization of Geological Sites able to Host a Pilot-Scale CO_2 Storage in the Paris Basin (GeoCarbone-PICOREF)." Oil & Gas Science and Technology-Revue De L Institut Francais Du Petrole **65**(3): 375-403.

Cantucci, B., G. Montegrossi, et al. (2009). "Geochemical modeling of CO_2 storage in deep reservoirs: The Weyburn Project (Canada) case study." Chemical Geology **265**(1-2): 181-197.

Carpenter, A. 1978. "Origin and Chemical Evolution of Brines in Sedimentary Basins." Oklahoma Geological Survey. Circular 79, 60-77

Carr, T. R., D. F. Merriam, et al. (2005). "Use of relational databases to evaluate regional petroleum accumulation groundwater flow, and CO_2 sequestration in Kansas." Aapg Bulletin **89**(12): 1607-1627.

Chalbaud, C., M. Robin, et al. (2010). "Brine/CO_2 Interfacial Properties and Effects on CO_2 Storage in Deep Saline Aquifers." Oil & Gas Science and Technology-Revue D Ifp Energies Nouvelles **65**(4): 541-555.

Chi, G. X. and M. M. Savard (1997). "Sources of basinal and Mississippi Valley-type mineralizing brines: mixing of evaporated seawater and halite-dissolution brine." Chemical Geology **143**(3-4): 121-125.

Daval, D., O. Sissmann, et al. (2011). "Influence of amorphous silica layer formation on the dissolution rate of olivine at 90 degrees C and elevated pCO_2." Chemical Geology **284**(1-2): 193-209.

Davisson, M. L. and R. E. Criss (1996). "Na-Ca-Cl relations in basinal fluids." Geochimica Et Cosmochimica Acta **60**(15): 2743-2752.

Davisson, M. L., T. S. Presser, et al. (1994). "Geochemistry Of Tectonically Expelled Fluids From The Northern Coast Ranges, Rumsey-Hills, California, Usa." Geochimica Et Cosmochimica Acta **58**(7): 1687-1699.

DeVries, T., Primeau, F, et al. (2012) "The Sequestration Efficiency of the Biological Pump." Geophysical Research Letters. **39:**L13601.

Dingman, R. and Angino, E. 1968. "Chemical composition of Kansas Brines as an Aid in Interpreting Change in Water Chemistry with Depth." Chemical Geology. **4**:325-339.

Domenico, P. A. and G. A. Robbins (1985). "The Displacement Of Connate Water From Aquifers." Geological Society of America Bulletin **96**(3): 328-335.

Druckenmiller, M., Maroto-Valer, M. "Carbon Sequestration Using Brines of Adjusted pH to form Mineral Carbonates." 2005. Fuel Processing Technology. **86**: 1599-1614.

Eisinger, C. and J. Jensen (2011). "Reservoir Characterization for CO_2 Sequestration: Assessing the Potential of the Devonian Carbonate Nisku Formation of Central Alberta." Oil & Gas Science and Technology-Revue D Ifp Energies Nouvelles **66**(1): 47-65.

Emberley, S., I. Hutcheon, et al. (2004). "Geochemical monitoring of fluid-rock interaction and CO_2 storage at the Weyburn CO_2-injection enhanced oil recovery site, Saskatchewan, Canada." Energy **29**(9-10): 1393-1401.

Espinoza, D. N. and J. C. Santamarina (2010). "Water-CO_2-mineral systems: Interfacial tension, contact angle, and diffusion-Implications to CO_2 geological storage." Water Resources Research **46**.

Figueroa, M. P., F. Barrera, et al. (2008). "Chalcedony (a crystalline variety of silica): Biogenic origin in electric organs from living Psammobatis extenta (family Rajidae)." Micron **39**(7): 1027-1035.

Fischer, S., A. Liebscher, et al. (2010). "CO_2-brine-rock interaction - First results of long-term exposure experiments at in situ P-T conditions of the Ketzin CO_2 reservoir." Chemie Der Erde-Geochemistry **70**: 155-164.

Flett, M., R. Gurton, et al. (2007). "Heterogeneous saline formations for carbon dioxide disposal: Impact of varying heterogeneity on containment and trapping." Journal of Petroleum Science and Engineering **57**(1-2): 106-118.

Fontes, J. C. and J. M. Matray (1993). "Geochemistry And Origin Of Formation Brines From The Paris Basin, France .1. Brines Associated With Triassic Salts." Chemical Geology **109**(1-4): 149-175.

Fontes, J. C. and J. M. Matray (1993). "Geochemistry And Origin Of Formation Brines From The Paris Basin, France .2. Saline Solutions Associated With Oil-Fields." Chemical Geology **109**(1-4): 177-200.

Franseen, E. K., A. P. Byrnes, et al. (2003). Geological Controls of Variable Character of Arbuckle Reservoirs in Kansas: An Emerging Picture. Kansas Geological Survey Open-file report. Lawrence, KS, Kansas Geological Survey**:** 11.

Garcia, B., V. Beaumont, et al. (2010). "Experiments and geochemical modelling of CO_2 sequestration by olivine: Potential, quantification." Applied Geochemistry **25**(9): 1383-1396.

Garven, G. (1995). "Continental-Scale Groundwater-Flow And Geologic Processes." Annual Review of Earth and Planetary Sciences **23**: 89-117.

Gaus, I. (2010). "Role and impact of CO(2)-rock interactions during CO_2 storage in sedimentary rocks." International Journal of Greenhouse Gas Control **4**(1): 73-89.

Ghaderi, S. M., D. W. Keith, et al. (2011). "Evolution of hydrogen sulfide in sour saline aquifers during carbon dioxide sequestration." International Journal of Greenhouse Gas Control **5**(2): 347-355.

Gislason, S. R., D. Wolff-Boenisch, et al. (2010). "Mineral sequestration of carbon dioxide in basalt: A pre-injection overview of the CarbFix project." International Journal of Greenhouse Gas Control **4**(3): 537-545.

Gledhill, D. K. and J. W. Morse (2006). "Calcite dissolution kinetics in Na-Ca-Mg-Cl brines." Geochimica Et Cosmochimica Acta **70**(23): 5802-5813.

Gunter, W. D., S. Bachu, et al. (2004). "The role of hydrogeological and geochemical trapping in sedimentary basins for secure geological storage of carbon dioxide." Geological Storage of Carbon Dioxide. S. J. Baines and R. H. Worden. London, Geolgical Society, London. **233:** 129 - 145.

Gunter, W. D., B. Wiwchar, et al. (1997). "Aquifer disposal of CO_2-rich greenhouse gases: Extension of the time scale of experiment for CO_2-sequestering reactions by geochemical modelling." Mineralogy and Petrology **59**(1-2): 121-140.

Guo, X., Z. M. Du, et al. (2009). "Sulfur deposition in sour gas reservoirs: laboratory and simulation study." Petroleum Science **6**(4): 405-414.

Han, W. S., B. J. McPherson, et al. (2010). "Evaluation Of Trapping Mechanisms In Geologic Co(2) Sequestration: Case Study Of Sacroc Northern Platform, A 35-Year CO_2 Injection Site." American Journal of Science **310**(4): 282-324.

Hanor, J. S. (1994). "Physical And Chemical Controls On The Composition Of Waters In Sedimentary Basins." Marine and Petroleum Geology **11**(1): 31-45.

Hansel, C. M., S. G. Benner, et al. (2003). "Secondary mineralization pathways induced by dissimilatory iron reduction of ferrihydrite under advective flow." Geochimica Et Cosmochimica Acta **67**(16): 2977-2992.

Hansel, C. M., S. G. Benner, et al. (2004). "Structural constraints of ferric (hydr)oxides on dissimilatory iron reduction and the fate of Fe(II)." Geochimica Et Cosmochimica Acta **68**(15): 3217-3229.

Hesse, R. (1989). "Silica Diagenesis - Origin Of Inorganic And Replacement Cherts." Earth-Science Reviews **26**(4): 253-284.

Houston, S., C. Smalley, et al. (2011). "The relative importance of buffering and brine inputs in controlling the abundance of Na and Ca in sedimentary formation waters." Marine and Petroleum Geology **28**(6): 1242-1251.

IPCC, 2005. IPCC special report on carbon dioxide capture and storage. Prepared by Working Group III of the IPCC [Metz, B., Davidson, O., de Coninck, H.C., Loos, M., Meyer, L.A., (Eds.)]. Cambridge University Press, Cambridge, United Kingdom/New York, NY, USA, 442 pp.

IPCC (Intergovernmental Panel on Climate Change). Climate change 2007: The physical science basis. Fourth assessment report, IPCC Secretariat, Geneva, Switzerland, 2007.

Izgec, O., B. Demiral, et al. (2008). "CO2 injection into saline carbonate aquifer formations I: laboratory investigation." Transport in Porous Media **72**(1): 1-24.

Jorgensen, D. G. (1989). "Paleohydrology of the Anadarko Basin, Central United States." Oklahoma Geological Survey Circular **90**: 179-193.

Kaszuba, J. P., D. R. Janecky, et al. (2005). "Experimental evaluation of mixed fluid reactions between supercritical carbon dioxide and NaCl brine: Relevance to the integrity of a geologic carbon repository." Chemical Geology **217**(3-4): 277-293.

Kharaka, Y.K. and Smalley, W.C. (1976) "Flow of Water and Solutes Through Compacted Clays." AAPG Bulletin. **60:** 6. 973-980.

Kharaka, Y. K., P. Campbell, et al. (2010). "Geologic storage of carbon dioxide: Potential environmental impacts of CO_2-organic interactions." Geochimica Et Cosmochimica Acta **74**(12): A511-A511.

Kharaka, Y. K., D. R. Cole, et al. (2006). "Gas-water-rock interactions in Frio Formation following CO_2 injection: Implications for the storage of greenhouse gases in sedimentary basins." Geology **34**(7): 577-580.

Kharaka, Y. K., J. J. Thordsen, et al. (2009). "Potential environmental issues of CO_2 storage in deep saline aquifers: Geochemical results from the Frio-I Brine Pilot test, Texas, USA." Applied Geochemistry **24**(6): 1106-1112.

Kharaka, Y. K., J. J. Thordsen, et al. (2010). "Changes in the chemistry of shallow groundwater related to the 2008 injection of CO_2 at the ZERT field site, Bozeman, Montana." Environmental Earth Sciences **60**(2): 273-284.

Kolkas, M. M. and G. M. Friedman (1998). "Diagenetic history and geochemistry of the Beekmantown-Group dolomites (Sauk sequence) of New York, USA." Carbonates and Evaporites **13**(1): 69-85.

Lagneau, V., A. Pipart, et al. (2005). "Reactive transport modelling of CO_2 sequestration in deep saline aquifers." Oil & Gas Science and Technology-Revue De L Institut Francais Du Petrole **60**(2): 231-247.

Lammers, K., R. Murphy, et al. (2011). "CO_2 Sequestration through Mineral Carbonation of Iron Oxyhydroxides." Environmental Science & Technology **45**(24): 10422-10428.

Lemieux, J. M. (2011). "Review: The potential impact of underground geological storage of carbon dioxide in deep saline aquifers on shallow groundwater resources." Hydrogeology Journal **19**(4): 757-778.

Little, M. and Jackson, R. (2010). "Potential Impacts of Leakage From Deep CO_2 Geosequestration on Overlying Freshwater Aquifers." Environmental Science and Technology. **44**: 9225-9232.`

Thibeau, S., Ngheim, L.X., Ohkuma, H., (2007). "A Modeling Study of the Role of Selected Minerals in Enhancing CO_2 Mineralization During CO_2 Aquifer Storage". Society of Petroleum Engineers. 109739.

Li, L., C. I. Steefel, et al. (2008). "Scale dependence of mineral dissolution rates within single pores and fractures." Geochimica Et Cosmochimica Acta **72**(2): 360-377.

Little, M. G. and R. B. Jackson (2010). "Potential Impacts of Leakage from Deep CO_2 Geosequestration on Overlying Freshwater Aquifers." Environmental Science & Technology **44**(23): 9225-9232.

Liu, F. Y., P. Lu, et al. (2012). "CO_2-brine-caprock interaction: Reactivity experiments on Eau Claire shale and a review of relevant literature." International Journal of Greenhouse Gas Control **7**: 153-167.

Liu, Q. and M. M. Maroto-Valer (2010). "Investigation of the pH effect of a typical host rock and buffer solution on CO_2 sequestration in synthetic brines." Fuel Processing Technology **91**(10): 1321-1329.

MacFarlane, A. 2000. "Revisions to the Nomenclature for Kansas Aquifers." Kansas Geological Suvery. Bulletin 244.

Matter, J. M., T. Takahashi, et al. (2007). "Experimental evaluation of in situ CO_2-water-rock reactions during CO_2 injection in basaltic rocks: Implications for geological CO_2 sequestration." Geochemistry Geophysics Geosystems **8**.

McGrail, B. P., H. T. Schaef, et al. (2006). "Potential for carbon dioxide sequestration in flood basalts." Journal of Geophysical Research-Solid Earth **111**(B12).

McIntosh, J., Walter, L., Martini, A. 2004. Extensive Microbial Modification of formation water Geochemistry: Case Study from the Midcontinent Sedimentary basin, United States. Geological society of America Bulletin. 116, No 5-6; 743-759.

Merriam, D. "The Geologic History of Kansas: State Geological Survey of Kansas", Bulletin 162. University of Kansas Publications. Lawrence KS, 1963. P146-151.

Musgrove, M. and J. L. Banner (1993). "Regional Groundwater Mixing And The Origin Of Saline Fluids - Midcontinent, United-States." Science **259**(5103): 1877-1882.

Newell, D. L., J. P. Kaszuba, et al. (2008). "Significance of carbonate buffers in natural waters reacting with supercritical CO_2: Implications for monitoring, measuring and verification (MMV) of geologic carbon sequestration." Geophysical Research Letters **35**(23).

Nordbotten, J. M., M. A. Celia, et al. (2005). "Injection and storage of CO_2 in deep saline aquifers: Analytical solution for CO_2 plume evolution during injection." Transport in Porous Media **58**(3): 339-360.

Palandri, J. L. and Y. K. Kharaka (2005). "Ferric iron-bearing sediments as a mineral trap for CO2 sequestration: Iron reduction using sulfur-bearing waste gas." Chemical Geology **217**(3-4): 351-364.

Palandri, J. L., R. J. Rosenbauer, et al. (2005). "Ferric iron in sediments as a novel CO_2 mineral trap: CO_2-SO_2 reaction with hematite." Applied Geochemistry **20**(11): 2038-2048.

Parkhurst, D.L, and CAJ Appelo (1999). "User's guide to PHREEQC (version-2)- A computer program for speciation, batch-reaction and one-dimensional transport, and inverse geochemical calculations." U.S. Geological Survey. 312 pp.

Pfingsten, W., B. Paris, et al. (2006). "Tracer and reactive transport modelling of the interaction between high-pH fluid and fractured rock: Field and laboratory experiments." Journal of Geochemical Exploration **90**(1-2): 95-113.

Penny, E., M. K. Lee, et al. (2003). "Groundwater and microbial processes of Alabama coastal plain aquifers." Water Resources Research **39**(11).

Portier, S. and C. Rochelle (2005). "Modelling CO_2 solubility in pure water and NaCl-type waters from 0 to 300 degrees C and from 1 to 300 bar - Application to the Utsira Formation at Sleipner." Chemical Geology **217**(3-4): 187-199.

Poulton, S. W. (2003). "Sulfide oxidation and iron dissolution kinetics during the reaction of dissolved sulfide with ferrihydrite." Chemical Geology **202**(1-2): 79-94.

Poulton, S. W., M. D. Krom, et al. (2004). "A revised scheme for the reactivity of iron (oxyhydr)oxide minerals towards dissolved sulfide." Geochimica Et Cosmochimica Acta **68**(18): 3703-3715.

Preston, C., M. Monea, et al. (2005). "IEA GHG Weyburn CO_2 monitoring and storage project." Fuel Processing Technology **86**(14-15): 1547-1568.

Pyzik, A. J. and S. E. Sommer (1981). "Sedimentary Iron Monosulfides - Kinetics And Mechanism Of Formation." Geochimica Et Cosmochimica Acta **45**(5): 687-698.

Rickels, W. and Lontzek, T. 2012. "Optimal global Carbon Management with Ocean Sequestration." Oxford Economic Papers. **64**:323. 323-349.

Sakurai, S., T. S. Ramakrishnan, et al. (2006). "Monitoring saturation changes for CO_2 sequestration: Petrophysical support of the Frio Brine Pilot Experiment." Petrophysics **47**(6): 483-496.

Scheffer, A., Roberts, J., et al. (2012) "Geochemical and Microbiological Characterization of the Arbuckle Saline Aquifer, a Potential CO_2 Storage Reservoir; Implications for hydraulic Separation and Caprock Integrity." Thesis: University of Kansas.

Shao, H. B., J. R. Ray, et al. (2010). "Dissolution and Precipitation of Clay Minerals under Geologic CO_2 Sequestration Conditions: CO_2-Brine-Phlogopite Interactions." Environmental Science & Technology **44**(15): 5999-6005.

Sonnenfeld, P. 1984. "Brines and Evaporites." Academic Press. Orlando, FL. p. 245-356.

Sorai, A., T. Ohsumi, et al. (2007). "Feldspar dissolution rates measured using phase-shift interferometry: Implications to CO_2 underground sequestration." Applied Geochemistry **22**(12): 2795-2809.

Stueber, A. M. and L. M. Walter (1991). "Origin And Chemical Evolution Of Formation Waters From Silurian-Devonian Strata In The Illinois Basin, Usa." Geochimica Et Cosmochimica Acta **55**(1): 309-325.

Taberner, C., G. Zhang, et al. (2009). Injection of Supercritical CO_2 into Deep Saline Carbonate Formations, Predictions form Geochemical Modeling. 2009 SPE EUROPE/EAGE Annual Conference and Exhibition. Amsterdam, The Netherlands, Society of Petroleum Engineers. **SPE 121272:** 11.

Tan, H. B., W. B. Rao, et al. (2011). "Hydrogen, oxygen, helium and strontium isotopic constraints on the formation of oilfield waters in the western Qaidam Basin, China." Journal of Asian Earth Sciences **40**(2): 651-660.

Tarkowski, R. and M. Wdowin (2011). "Petrophysical and Mineralogical Research on the Influence of CO_2 Injection on Mesozoic Reservoir and Caprocks from the Polish Lowlands." Oil & Gas Science and Technology-Revue D Ifp Energies Nouvelles **66**(1): 137-150.

Tesmer, M., P. Moller, et al. (2007). "Deep reaching fluid flow in the North East German Basin: origin and processes of groundwater salinisation." Hydrogeology Journal **15**(7): 1291-1306.

Thibeau, S., Ngheim, L.X., Ohkuma, H., (2007). "A Modeling Study of the Role of Selected Minerals in Enhancing CO_2 Mineralization During CO_2 Aquifer Storage." Society of Petroleum Engineers, 109739.

Wang, W. L., M. Q. Hu, et al. (2011). "CO_2 Fixation in Ca^{2+}-/Mg^{2+}-Rich Aqueous Solutions through Enhanced Carbonate Precipitation." Industrial & Engineering Chemistry Research **50**(13): 8333-8339.

Wellman, T. P., R. B. Grigg, et al. (2003). Evaluation of CO_2-Brine-Reservoir Rock Interaction with Laboratory Flow Tests and Reactive Transport Modeling. SPE International Symposium on Oilfield Chemistry. Houston, TX, Society of Petroleum Engineers. **SPE80228:** 9.

Wenger, L. M., C. L. Davis, et al. (2004). "Impact of modern deepwater drilling and testing fluids on geochemical evaluations." Organic Geochemistry **35**(11-12): 1527-1536.

Wigand, M., J. W. Carey, et al. (2008). "Geochemical effects of CO_2 sequestration in sandstones under simulated in situ conditions of deep saline aquifers." Applied Geochemistry **23**(9): 2735-2745.

Wigand, M., J. P. Kaszuba, et al. (2009). "Geochemical effects of CO_2 sequestration on fractured wellbore cement at the cement/caprock interface." Chemical Geology **265**(1-2): 122-133.

Wilson, T. P. and D. T. Long (1993). "Geochemistry And Isotope Chemistry Of Ca-Na-Cl Brines In Silurian Strata, Michigan Basin, Usa." Applied Geochemistry **8**(5): 507-524.

White, D.E. (1965). "Saline waters in sedimentary rocks," *in* Young, A., and Galley, J.E., eds., Fluids in subsurface environments: American Association of Petroleum Geologists Memoir 4: 342-346.

Xie, X. N., J. J. Jiao, et al. (2003). "Regional variation of formation water chemistry and diagenesis reaction in underpressured system: example from Shiwu depression of Songliao basin, NE China." Journal of Geochemical Exploration **78-9**: 585-590.

Xu, T. F., J. A. Apps, et al. (2003). "Reactive geochemical transport simulation to study mineral trapping for CO_2 disposal in deep arenaceous formations." Journal of Geophysical Research-Solid Earth **108**(B2).

Xu, T. F., J. A. Apps, et al. (2004). "Numerical simulation of CO_2 disposal by mineral trapping in deep aquifers." Applied Geochemistry **19**(6): 917-936.

Xu, T. F., Y. K. Kharaka, et al. (2010). "Reactive transport modeling to study changes in water chemistry induced by CO_2 injection at the Frio-I Brine Pilot." Chemical Geology **271**(3-4): 153-164.

Appendix A - Mineralogy Data

Core Plug Descriptions

Depth	Core #	Length	Weight (g)	Description
3541.90	1-2	2 1/4 "	175.44	Micritic limestone, some skeletal fragments?, mottled gray/light gray, longitudinal fracture, filled with sparry cement, small sparry clasts
3547.25	1-8	3 3/16 "	250.589	micritic texture, latitudinal lenticular beds of dark shale?(>1mm), skeletal fragments 2mm -> 6mm, mainly gray with thin light color beds ~7 thicker (1mm) darker beds (shale)
3554.60	1-15	3 1/8"	228.96	gray-black bioclstic wakestone possible pyrite crystals .5 mm, longitudinal fractures ~.5, longitudinal layering of bioclasts, bioclast size range 1mm-1cm, shell fragments
3580.30	1-41	3 1/8"	166.167	noncydrilical, top dark olive green with fractures (1mm-2mm) filled with light color mineral (calcite, contact with lighter limestone, highly fractured random fractures, core is fractured, vitreous surface is revealed, fractures in lighter portion ~4 mm, fracture crystals in green portion reddish
3592.90	1-53	2 15/16 "	231.309	med-light gray, lighter clasts (1.5 cm- .5 cm), yellow coloration, possible pyrite crystals with 1mm, a few bioclasts present (shell fragments fine grained) (micritic), slight longitudinal fracture
3600.25	2-1	1 1/2 "	80.252	crumbly, no full core, olive color, pink clay on surfaces, red material (fine grained) formed in vug or cavity?, shiny surfaces, oriented along bed plane
3608.00	2-9	3 1/16 "	236.423	gray-light red sandstone, Fe rich, fine grained, fractures present, filled with red mineral (Fe-oxide), no lithic fragments, fractures are latitudinal ~1mm-3mm thick, also longitudinal
3628.15	2-29	1 3/4 "	132.041	light to med-gray, speckled with light color word? (bioclasts?), layers of darker grey, fine grained material, non porous, speckled portion appears porous, small grains of pyrite visible
3638.30	2-39	3 1/16 "	237.077	light gray, micritic with bioclasts (3mm) mottled with olivine green color, sparry clasts visible 2 mm, apparent porosity, longitudinal fracture, small darker line
3649.40	2-50	1 1/2 "	59.896	dark grey/black, greenish layers, crumbly, reddish layers in cross section, pinkish clay covering
3661.30	3-2	2 3/16 "	163.23	light grey, fine grained, very few larger crystals, longitudinal fracture > 1mm, small clast matrix possible
3665.80	3-6	2 1/4 "	121.731	broken, exposed side clastic, mid size grains, grayish-yellow green shale, other half micritic calcite, white, vug 1 cm x 3 cm, has calcite recrystallization, long and flat fractures intersection vug, shale side has large (2.5 cm) chert clast
3670.60	3-11	2 7/8 "	199.568	brown to light brown, tripolite chert matrix, brecciated chert clasts (.5 cm x 1 cm) - (2cm - 2 cm), some chert matrix appears dissolved with flow lines, above is more brecciated, main breccia clasts are grey, brown (oil stain) inclusions in chert, oil smell
3678.90	3-19	2 15/16 "	190.063	brown, chert clasts (2 cm x 1 cm) (1 cm x 1 cm), dissolved tripolite, brown tripolite, oil smell, possible vug in tripolite area
3681.95	3-22	1 5/8 "	106.212	brown to light brown, oil stains in chert, clastic chert (irregular ~2 cm), vugs in chert (1mm x 2mm), pyrite on end?, oil smell

3684.20	3-25	3 "	194.172	brown, tripolite chert, angular grey to dark grey, chert clasts, some oil stains visible in chert clast (4 x 2cm) (3 mm x 2mm), brown chert matrix swirled with lighter color, has oil smell, small vug in chert
3686.90	3-27	3 1/16 "	191.29	brown, calcite almost completely filling vug (1 cm x 1.5 cm), Fe-oxidized particle, large chert (2cm x 3 cm), vug near chert, oil smell, oil stain on chert, slight tripolite flow
3689.90	3-30	2 15/16 "	202.134	brown, tripolite chert, small chert clasts (grey), large vug, almost filled with calcite crystals (5 cm x 4 cm), mostly brown, area around grey chert clasts are lighter color, gray surrounded by white thin light brown, large vug filled with calcite, oil smell
3693.75	4-2	2 7/8 "	189.804	brown, darker chert bands, darker surrounded by lighter chert, clacite (.5 cm x 1.5 cm), vugs in chert (1mm -> 2 mm), chert (3.5 cm x 2.5 cm), oil smell
3699.75	4-8	2 7/8 "	197.85	greyish brown linear-orientated dark lines, mottled dark to light-brown gray chert clasts (2mm x 2 mm) - (1.5 x 1.5 cm), chert clasts have oil staining, lenticular beds
3705.75	4-14	2 7/8 "	206.613	grey, vugs (1mm), oil stains, dolomite (2mm), porous tripolite
3709.10	4-18	2 3/4'	198.7	grey-brown, alternating light brown with longitudinal layering
3714.10	4-23	2 7/8 "	213.65	light brown -> light grey, limey mudstone light laminated bedding, planes with brown matrix, no clasts, fractures, vugs, slight oil smell
3717.90	4-26	3 "	222.036	light brown, longitudinal layering, lime mudstone, vug <1mm
3722.40	4-31	2 15/16 "	219.329	light grey, fine grained, wispy white color opposite blue line, longitudinal fracture, very thin (2 mm?), no apparent filling, uniform except white wispy material
3728.40	4-37	3 1/8 "	231.565	greyy to light grey, longitudinal layering, crinoidal packstone, dark bands of chert
3731.85	4-40	3 "	231.629	light grey, top has calcite crystals sparry, fractures longitudinal, filled in with darker material, smaller filled in vug on other side, calcite , some wispy white areas
3733.70	4-42	3 "	254.083	grey to light grey color, sparry calcite, filling 1.5 cm x .5 cm vug with possible pyrite in vug also, longitudinal fracture, chert with crinoids included in it, darker band of chert longitudinal
3739.80	4-48	3 5/16 "	251.354	grey to light grey, limy , micritic limestone, thin laminations, mostly grey with some white layers, dispersed, possible purer calcite, possible saw burns on ends
3746.90	4-55	3 1/8 "	238.256	light brown to grey, dark grey scattered (chert), sparry calcite inclusion in dark cert, latitudinal bedding in light grey chert, calcite .5 cm in black chert, 2 cm long fracture filled with calcite in light grey chert
3754.70	5-3	3 1/8 "	243.182	grey to light grey, micritic limy mud, inform with thin discontinuous darker layer, no fractures/vugs, clasts
3762.60	5-11	3 1/4 "	248.545	grey to light grey, two longitudinal fractures 1 mm wide filled with dark material (mud), .25 cm x .25 cm chunk missing from under a fracture, pyrite crystal in darker or black chert, longitudinal layering of different chert and mudstone .25 x .25 cm sparry calcite inclusion in light grey chert

3767.70	5-16	3 1/8 "	237.138	light to med grey, portion of one end grey-blue-dark could be a dark dust, slightly mottled with specks of dark material, facture, longitudinal, travels one side entirely, one end entirely and partway down other side and only a little into opposite end, thin, filled in with dark material -> black chert?, dark chert inclusions surrounded by lighter color
3777.50	5-26	3"	230.012	grey and light brown/grey, latitudinal layering of mudstone and chert, very find longitudinal fracture along the sharp contact, 2mm fracture filled with sparry calcite, sparry calcite inclusion in light brown/grey chert, faint latitudinal fracture in grey material
3789.15	5-38	3 1/8 "	230.434	med to light grey, sub-horizontal bedding, laminated with dark areas, large sparry white calcite filling vug completely, core is chipped on one end exposing calcite, longitudinal fracture, small micro fractures, some saw burns
3795.30	5-44	3 1/8"	237.907	light grey-grey, calcite (sparry) crystals inclusion (1cm x 1cm), latitudinal calcite filled fracture (2 mm wide), scattered crinoids (.1 cm x .4 cm)
3804.90	5-53	2 15/16 "	219.131	light grey to grey, micritic lime mud, uniform with a dark bedding plan and running in the middle, small filled vug of calcite at one end, only 1 mm deep into core, thin word? Laminations throughout, black specks near one side
3832.15	6-21	2 15/16 "	216.17	med-dark grey, micritic, laminated with dark material, multiple fractures, one longitudinal, extending to both ends, one angular, sub latitudinal meeting long fracture, large (3.5 x 2 cm) vug filled in with sparry white calcite, another filled vug on opposite side (2 x 2) possibly connected, calcite on one end as well
3837.10	6-26	3 1/16 "	226.988	light brown, wood grain texture, dolomite or calcite inclusions, 1-3 cm size, longitudinal layering, longitudinal fracture filled with dolomite or calcite
3856.10	6-45	3 1/16 "	229.905	grey to med grey, laminated beds of darker material, somewhat mottled, uniform throughout, possible 2 micro fractures in core side
3861.20	6-50	3 1/4 "	239.669	light brown to grey, vugs filled in with dolomite or calcite (1 cm x 1 cm) (.5 cm x .5 cm), possible latitudinal fracture between latitudinal layering of shale
3867.90	6-56	3 1/8 "	233.415	light grey, wave laminations, uniform throughout two small (.5 x .25 cm) chert nodules, no fracture visible
3870.60	6-59	2 7/8 "	219.028	grey, light grey, 2 longitudinal fractures, dolomite crystal, longitudinal layering, possible slight longitudinal fracture, chip missing from top of core
3876.90	7-5	3 1/4 "	237.507	grey, peloidal limestone, slight laminations uniform large dark chert nodule with 3-4 fractures not extending into limestone
3884.60	7-13	3 "	229.715	grey with light brown chert present, peloidal limestone, definite longitudinal layering present, peloids distributed throughout entire core, chip of chert from top, packstone
3893.90	7-22	2 7/16"	164.753	dark brown, dolomite crystals, Fe-oxidized in dolomite crystal, dolomite crystal size (2 cm x 3 cm), (.5 cm x .5 cm), translucent bluish chert (.2 cm x .5 cm), porous
3896.20	7-25	2 15/16 "	201.024	brown to dark grey brown, thinly laminated, inclusions of bluish chert (.5 cm x .5 cm) (1 x 1mm), dark specks visible, mottled in layers

3902.80	7-31	2 15/16 "	202.087	dark brown, dolomite crystals (1.5 cm x 1 cm), (.5 cm x .5 cm), translucent bluish chert (.5 cm x .5 cm), longitudinal layering, vug partially filled with dolomite, slight longitudinal fracture (very fine)
3912.90	7-41	3 1/16 "	229.735	grey to light grey, slight lamination, swirled with lighter color, micritic, slightly dolostone, no large area of differentiation
3915.90	7-44	3 "	227.6	light grey, longitudinal layering, siltstone, alternating grey and dark grey layering, wispy shale laminations
3922.40	7-51	3 1/16 "	231	grey to light grey, silty dolostone, laminations present, not continuous along length, swirly, some have tiny >1mm cherts, longitudinal fracture along entire length, splits into smaller fractures, other microfractures visible
3925.90	7-54	3 1/16 "	230.58	grey-light brown, pink calcite (1.5 cm x 1.5 cm), chert with dolomite in it, pyrite surrounded by chert, vug
3930.10	8-2	3 1/16 "	230.964	med grey, silty dolostone, wispy laminations, not continuous, uniform throughout
3937.45	8-9	3 1/8 "	234.605	dark grey, porous, longitudinal banding, longitudinal fracture, chert, wispy shale, vug filled in with chert
3940.20	8-12	3 1/16 "	238.684	med-grey, uniform, no evidence of laminations, small (.6 x .3 cm) chert nodule on one end, longitudinal fracture, does not reach ends, filled in with calcite or chert
3945.80	8-17	3 3/8"	243.296	grey to light brown, vug partially filled with chert (.5 cm x .5 cm), translucent bluish chert, dolomite (1 cm x 1 cm)
3954.90	8-26	3 3/16 "	238.41	med-light grey, silty dolostone, slight laminations, wispy shale layers- discontinuous, some light grey nodules
3967.80	8-39	2 "	153.764	grey siltstone, wispy laminations of lighter grey color (shale possibly), longitudinal layering, possible dolomite crystal on end, Saw burn makrs on core
3969.90	8-41	2 1/16 "	151.311	med-dark grey, silty dolostone, swirled laminations, pockets of light colored material, longitudinal fracture extending entire length, filled with dark material
3979.30	8-51	2 1/16 "	152.822	dark to med-grey silty dolostone, longitudinal fracture, partially filled with dark material, some calcite perhaps, 1 mm pyrite grain, some smaller grains, shale laminate near fracture
3988.20	8-60	2 "	153.477	grey with light grey patches, pyrite crystals scattered in core, very tight, not porous, longitudinal layering
3991.90	9-2	2 "	152.004	med-dark grey, slight shale laminations, silty dolostone, light-colored masses, possibly Si rich area? on one end, sarry calcite visible, small pyrite grains visible
4001.10	9-12	2 1/16 "	154.720	med grey-brown, uniform throughout, silty dolostone, a few light colored Si-inclusions, possible pyrite grain, no shale laminae
4009.15	9-20	2 1/16 "	157.890	light-grey brown dolomite, silty-broken laminations of lighter (Si?) material, uniform except for lighter inclusions, no shale laminations present
4013.00	9-24	2 1/16 "	152.191	light-grey brown, silty dolomitic, oil smell, small patchy shale laminations, sharp contact between laminations and more silty area, lamination zone has some light colored areas, possibly cherty above uniform
4026.70	10-7	2 "	147.679	light grey-brown, silty dolomitic shale, indistinct, wavy shale bedding, Z (1mm) size vugs, empty, 2 mm size chert no, slight longitudinal fractures on one end, oil smell

4029.90	10-10	2 "	147.683	med grey-brown, more coarse grained, heterogeneous, wavy shale laminations, indistinct bedding, indistinct nodules, dark and light, some areas of sparry crystals, some chert, visible porosity in parts
4035.90	10-16	2 1/16 "	147.171	olive grey, high shale content with dolomite, wavy laminations, indistinct chert nodules, small vugs around chert, oil smell, indistinct bedding
4052.30	10-33	2 1/16"	154.847	dark grey-olive, shaley dolomitic silt, mudstone, wispy laminations of shale, slight micro fractures visible at one end
4065.20	10-46	2 1/16 "	155.906	medium grey-brown, shale laminations, some Si-silt, sub mm size, chert mm size black inclusions, possibly fossils?
4066.90	10-47	2 "	153.783	light grey -> white, fine grained sandstone, quartzite, 45 degree longitudinal fracture, filled with dark material, vertical (longitudinal) fracture, thick (1mm) filled with white-yellow material with possible Fe-oxidization, latitudinal fractures near one end filled with white quartz, large (2cm x 2cm) with quartz nodule (quartzite), small black flecks throughout
4072.90	10-53	2 "	149.873	med-grey, quartz right sandstone with carbonate mud, wispy shale laminations, indistinct bedding, heterogeneous sand carbonate, Fe oxidation visible in spots, dark specks throughout, visible porosity
4077.20	10-58	2 1/16 "	154.718	light-med grey, fine grain sandstone with carbonate mud, irregular nodules of chert (light color) 1 mm size vug, contact above chert, bioturbation, lighter above
4083.63	11-5	2 1/16 "	151.732	light-med grey, fine grain sandstone with carbonate mud, chert nodules on lower part, fractured, Fe oxidation visible in some parts
4094.10	11-16	2 "	152.639	grey to light grey, fine grained sandstone and carbonate mud, chert horizontal bed, irregular not planar (1cm thick), Fe-oxide on one end, fine grained quartz crystals
4097.30	11-19	2 1/16 "	155.737	light grey-brown, fine grain sandstone with carbonate mud, bioturbated, browner bedding, irregular browner, fine grained material interbedded in SS, Fe oxidation visible on some grains
4111.60	11-33	2 1/16 "	149.642	med-grey, broken off on one side, pyrite, lithoclasts, porous
4119.10	11-41	2 "	145.780	light to med-grey, sandstone, visible porosity, bioturbation, mottled appearance, black lithoclasts present, sub-mm size, some Fe-oxidation
4121.10	11-43	2 1/16 "	149.350	light grey to dark grey, bioturbated pyrite, Fe-oxidation on the top, porous, lithoclast, some lithoclasts have Fe oxidation surrounding it, shale mud
4123.50	11-45	2 1/16 "	148.015	light to med grey, coarse sandstone, visible porosity, visible quartz grains, black litholcasts with Fe-oxidation surrounding it, SS with carbonate mud filling pores, ~70% sand
4135.85	11-57	2 "	152.261	dark grey, complete longitudinal fracture, Fe-oxidation on side around fracture, fine grained quartz, bioturbated, partial longitudinal fracture, porous, pyrite, large amount of sand, sandstone
4152.40	12-15	2 "	148.605	light to med grey, fine grained SS, bioturbated, green-grey filling, swirled mottled appearance, porous, green area is fine grained, no visible porosity, no clasts

4157.20	12-20	2"	148.197	green -> blue, light grey, white, iron smell, longitudinal fracture, Fe-oxidation, lithoclasts (.3 cm), shale lens filling fracture, chert (white), vug (with chert filling it), porous
4159.70	12-22	2 "	136.965	light grey, SS, greenish blue, shale with interbedded SS, one side of core is broken near shale, latitudinal fracture with shale filling space, appears bioturbated, a few Fe-oxidation patches
4160.50	12-23	2 1/16 "	144.050	bluish-grey shale, porous, partial fracture on one end, Fe-oxidation, fine grain quartz crystals, bioturbated
4174.55	12-37		149.458	light-med grey, mottled layers of mudstone, wavy layers of mudstone, 60 degree longitudinal fracture, fracture is broken on core, filled with mudstone, mm size vugs, some Fe-oxidation, below fracture more sandy
4176.10	12-39	2 "	156.633	light grey to brown, vug, chert, latitudinal and longitudinal fractures filled with quartz silt, dolomudstone, sandy clasts, highly fractured, porous
4178.90	12-41	2 1/16 "	163.232	light grey, highly fractured quartz silt, porous, vugs filled with quartz, pyrite, Fe-oxidation near fracture, chert (white)
4187.75	12-47		154.795	light to med grey, oolitic grainstone with sharp contact with fine grained calcareous mud, boundary has chert nodule, oomoldic porosity, visible on side fractures present in carbonate mud, filled with chert
4187.20	13-3	2 "	161.539	light grey to brown, longitudinal fracture all the way through shale, chert fine grained quartz, interclast
4193.30	13-9	2 "	161.204	med grey, fine grained carbonate, parry calcite crystals present, some areas of large calcite crystals, mm size vugs, calcite on edges, visible porosity
4195.10	13-11	2 1/16 "	154.752	med-grey, fine grained carbonate mud with white sparite, brecciated, small (mm size) with calcite crystals present, no laminations or bedding present, mottled, visible porosity
4202.30	13-18	2 1/16 "	158.073	med green-grey, micritic carbonate with sparry inclusions, filled vugs, longitudinal fracture, filled with green-blue shale, carbonate above more grey, below, more green-grey, below fracture mottled, highly visible porosity, vugs filled with sparry calcite, some Fe-oxidation spots on end
4207.10	13-23	2 1/16 "	153.921	med grey-brown, micritic carbonate with sparrite filling vugs, no clear bedding possible fluid alteration of fractures, filled with sparrite, cm size open vug, calcite crystals present, visible porosity, strongly oxidized particles on one end
4212.60	13-28	2 "	150.009	brownish grey, packstone above with finer carbonate below, longitudinal of silty clay mud, mm size vugs above, pin point vugs below, coarser above, white calcite clasts, visible porosity
4213.80	13-29	2 1/16 "	152.802	light grey-blue with some white, highly fractured, brecciated chert, blue-grey chert fractured, filled with white, either pure white or packstone, very tight, no visible porosity
4221.90	13-37	2 1/16 "	154.945	grey sandstone, red dolomite veins traveling longitudinally, filled in longitudinal fracture with dolomite also possible quartz crystals on end
4225.70	13-41	2 "	145.736	med gray to bluish grey, fine grained tight, vuggy, interconnected vugs, vugs have chalky material growing (possible anhydrite), some vugs have sparry calcite visible, highly variable mottled, clastic, brecciated, indistinct bedding, possible large fracture filled with dark chert

4230.30	13-46	2 1/16 "	161.481	light grey with sharp contact to light brown, faint but numerous longitudinal fracture, dolomite crystals filling vugs, white chalks material filling some fractures
4235.90	13-51	2 1/16 "	153.082	light grey, fi ne grained carbonate, white areas of sparry calcite, mottled, no visible fractures or bedding, pin point vugs, Fe-oxidation on side, white areas chalky (chert?)
4243.00	13-59	2 "	141.477	light grey, numerous large vugs (3cm x 2cm) (1cm x 1cm) (2cm x 1cm) lined with dolomite, very sparry, vugs partially filled with dolomite, chunk out of one end
4247.00	14-4	2 "	156.291	light-med grey, mottled with white Si rich material, chalk, fine grained, pin point vugs, fluid enhanced discontinuous fractures, Fe-oxidation, no bedding present, some sparite visible
4252.50	14-9	2 1/8 "	154.808	grey/brown, large vug (4cm x 3cm) partially filled with dolomite, smaller vugs filled with dolomite, matrix is sparry, possible fracture along large vug edge, white spots on end (dolomite possible)
4262.60	14-19	2 "	147.895	med-grey, peloidal, dolomitic, 60 degree longitudinal fractures (2-3 mm wide), fractures filled with chert (blue-grey), highly fractured, long flat fractures, filled with bluish chert or white chalky material (chert)
4280.40	15-14		150.008	brownish grey, mottled with browner sparry crystals, mm-cm size vugs with crystal growth, pinpoint vugs, indistinct bedding,
4299.10	16-6	2 "	154.392	brownish grey, faint filled longitudinal fractures, chert (light brown), grain stone packstone, vugs filled in with chert
4308.10	16-15	2 "	159.596	med-dark grey, fine grained, mudstone, many discontinuous longitudinal microfractures filled with dark material, 5 mm size vugs, brown in color connected to fractures, sparry crystals present near vugs
4342.50	16-49	2 "	159.289	light brown, grey, bioturbated, dolomite, lighter grey spots in matrix, longitudinal fracture scattered fractured filled with dolomite
4365.80	17-13	2 "	149.200	dark grey, dark mudstone with areas of sparry crystals, vuggy large vug (2cm x .5cm) vug crystals are brown, calcite or dolomite, another 1.5 x .5 cm vug similar to above vug
4379.10	17-27	2 "	146.672	dark brown, very porous matrix, frosted white (dolomite?), bioclasts, sparry matrix
4388.80	17-36	1 11/16 "	120.773	med-dark grey, micritic mudstone below, fracture above fracture autoclastic breccia, some chert with clay, material in between clasts, fractures in mudstone with some fluid alteration, plug has some broken pieces
4394.60	17-42	2 1/8 "	147.475	dark grey/blue, crinoids scattered, large sparry dolomite crystal (1cm x 1cm), porous, various sizes of vugs, sparry matrix, longitudinal fracture
4399.85	17-47	2 1/16 "	154.795	med-grey, packstone with sparry crystals, fine brown crystals filling vugs, surrounded by sparry packstone, cm size vug with calcite crystals, elongated vugs, could be fractures, some chert nodules (mm size)
4406.35	17-54	2 "	159.232	grey/light brown, fractured (longitudinal), dolomite, peloidal packstone, fractures filled with matrix
4410.90	17-58	'2 1/8 "	162.959	grey to bluish grey, highly fractured, longitudinal fractures filled with chert, layers of mud stone of sparrite, some parts brecciated, one fracture is empty, ends uneven

4431.60	18-18	2 "	161.849	medium grey shale, vertical fractures, pyrite, longitudinal layering, whispy shale texture, mudstone lens?
4441.00	18-28	2 "	162.899	med-grey, dolomitic micrite, micro fractures present, below more porous, calcite with sparite, tight no visible porosity, some small vugs with calcite
4443.80	18-30	2 "	157.74	grey to light brown; many small (2mm) vugs with sparry crystals inside. Moderately porous texture. Packstone
4446.00	18-33	2 "	158.477	brown/grey, vugs filled with sparry crystals; longitudinal fracture filled with calcite; porous, sparry texture present
4451.90	18-38	2 "	152.107	light grey; longitudinal layering, rough, sparry texture
4460.80	18-47	2 "	163.349	light grey; longitudinal fracture, sparry texture; vug filled with brown material
4465.75	19-2	2 "	169.205	light grey to light brown; fine grained dolomite; scattered vugs, low visible porosity, possible black chert
4475.10	19-12	2 "	154.331	medium grey packstone; porous with scattered vugs filled with dolomite; longitudinal fracture; medium crystalline dolomite; sharp contact between light and dark dolomite
4496.10	19-33	2 "	160.312	light brown to light grey, finely crystalline dolomite; scattered vugs partially filled with dolomite crystals; oxidized iron particles; longitudinal fracture filled with dolomite; porous
4504.00	19-41	2 "	154.036	dark to light grey; large dolomite crystal (4x4cm); longitudinal fracture, vugs filled with dolomite; dark color surrounding large dolomite crystal
4507.85	19-22	2 "	163.289	light grey; fine grained dolomite; low visible porosity; longitudinal fracture and scattered vugs filled with dolomite, irregular bedding.
4515.30	19-51	2 "	158.391	light grey, tan, dark grey alternating layers; wavy layering that is bioturbated with white carbonate mud; apparent shell fragments
4519.00	19-56	2 "	164.72	light grey, fine grained dolomite; vugs filled with sparry dolomite; irregular bedding; low visible porosity; longitudinal fracture filled with dolomite; wispy shale laminations
4523.10	20-3	2 "	163.925	light grey to light brown; fine grained dolomite, occasional brown streaks throughout; otherwise uniform, no fractures of vugs; low visible porosity
4534.70	20-14	2 "	161.342	light grey to light brown; fine grained dolomite; fracture around entire core; vugs present, some partially filled with dolomite spar; chert nodule in fracture with vug
4543.40	20-23	2 "	159.883	light grey; fine grained dolomite; abundant vugs; no fracture, little visible inter crystalline porosity
4550.90	20-30	2 "	165.3	Medium grey; fine grained dolomite, tight matrix vugs filled with sparry dolomite; uniform throughout; longitudinal fracture.
4557.10	20-37	2 "	164.858	Light to medium grey; fine grained dolomite; low visible porosity; highly fractured, long and lat fractures interconnected, solution enhanced; some fractures filled, some connect to vugs
4570.10	20-50	2 "	159.983	grey-brown; sparry, coarsely crystalline dolomite; large fracture present, irregular and filled with briwn clay/shale material; below fracture sparry autoclastic breccia with brown matrix micro fractures present in brecciated zone.
4579.65	21-5	2 "	164.603	light olive grey; fine grained dolomite; wavy fractures, discontinuous; 1-5 mm vugs with sparry dolomite growing; dark shale filing fractures

4598.30	23-6	2 "	154.006	grey to white to blue-grey; fine grained dolomite; longitudinal fracture dividing dolomite from autoclastic breccia (chert possibly); large vugs in dolomite with large crystals of dolomite infilling; abundant vugs in dolomite/breccia boundary
4609.90	24-7	2 "	164.391	grey brown; autoclastic breccia; highly fractured with solution enhancement; vugs along fractures; micritic dolomite? Filling fracture; low visible porosity
4626.90	25-3	2 "	155.872	Light grey; fine grained dolomite; mottled; matrix of micrite between crystals; cm size vugs with dolomite crystals infilling
4632.90	25-30	2 "	160.54	olive grey; fine grained dolomite; longitudinal fracture, filled with micritic dolomite; 3mm vugs
4640.60	25-38	2 "	161.358	light grey-brown; fine grained dolomite some sparry crystals; 45 degree longitudinal fracture, pin point vugs; core plug broken exposing brown sparry crystals
4645.90	25-43	2 "	158.145	light to medium grey; fine grained dolomite; mottled; vuggy, 1mm-1,5cm; vugs filled with micritic dolomite; smaller vugs filled with sparry crystals; microfractures visible
4649.10	25-47	2 "	159.135	light olive grey; fine to coarse grained dolomite; vuggy, discontinuous 1-10mm vugs; crystals growing in vugs; good visible porosity, homogenous, no bedding planes
4683.40	26-4	2 1/16 "	148.931	dark grey-brown; brecciated fine grained dolomitel angular bedding plane, crystalline and brecciated below; highly fractured; large vug 2.5 x 1 cm, continuous through plug; smaller vugs in fracture zone; some vugs filled with a white carbonate mud.
4728.60	27-2	2 "	136.283	med to dark grey fine grained dolomite; brecciated; fractures large; vuggy, greater then 2mm; crystals growing inside vugs;
4732.40	27-6	2 "	154.057	dark olive grey; mottled; fine grained dolomite; 1-2mm size vugs; longitudinal fracture, thin, filled with white mud; chert nodule, 3.5x2cm; good visible porosity.
4743.90	27-17	2 "	150.298	light grey to white; fine grained dolomite; bedding layer visible; layers of chert present; also peloidal lime mud? In layers; healed fractures visible; rare mm size vugs
4748.25	27-22	2 "	150.744	medium to light grey; fine grained dolomite; large crosscut of chert with peloids and shell fragments; shale lamination of edges of chert inclusion; dolomite portion fractured.
4755.95	28-8-2	2 "	163.363	light grey; fine grained dolomite; extensively fractured, with apparent enhancement; lighter material around fractures; tight porosity; homogenous except fracture zones
4772.30	28-25	2 "	160.909	light grey; fine grained dolomite; fractured; sparry pink dolomite filling fractures; mm size vugs; low visible porosity
4778.30	28-38	2 "	155.865	Medium grey-brown; finely crystalline dolomite; vuggy, up to 2 cm; dolomite crystals growing in vugs; tight porosity
4790.10	28-43	1 3/4"	146.927	light grey; fine grained dolomite; slightly peloidal; homogenous throughout; pin point vugs; visible porosity; slight bedding; slight latitudinal fracture
4794.10	28-47	2 "		dark yellow grey crystalline dolomite; extensive pinpoint to 2mm vugs; white mud filling some vugs; no fractures
4801.30	29-3	2 "	158.36	med-light grey; micritic dolomite; longitudinal fractures; large area of sparry pink dolomite crystals in fractures and vugs, not completely filling space
4815.60	29-17	2 "	160.104	light grey; fine grained dolomite; vuggy (pinpoint to 1.5cm); dolomite crystals growing in vugs; tight porosity

4903.80	30-4	2 "	161.995	light to medium grey; fine grained peloidal dolomite; slight fractures; filled with white mud?; area of sparry pink dolomite filling entire vug
4906.35	30-7	1 5/8"	99.977	med grey, fine grained dolomite; vuggy, filled with pink dolomite crystals; fractures present, discontinuous, filled with white carbonate mud?
4913.35	30-14	2 "	157.42	light grey peloidal packstone; dolomite some crystallinity apparent; white carbonate filling vug/fracture/inter crystalline spaces; healed longitudinal fracture; low porosity
4916.60	30-17	2 "	161.896	light grey; fine grained dolomitic packstone; crystalline; no bedding, homogenous; two 45 degree fractures, filled with dolomite crystals and carbonate; tight porosity; core is broken
4923.70	30-24	2 "	158.279	light grey; fine grained dolomite; bedding plane evident, with greenish clay speckled throughout; fracture above bedding plane, filled with carbonate; above shale bed, 2-3mm vugs with dolomite crystals growing; tight porosity
4925.70	30-26	2 "	152.824	medium grey; finely crystalline dolomite with carbonate mud filling pinpoint vugs; vugs filled with dolomite crystals; tight to low porosity
4929.10	30-30	2 "	154.622	medium grey; fine to coarsely crystalline dolomite; vugs, pinpoint to 0.5cm; dolomite crystals growing in vugs;
4937.05	30-38	2 "	160.2	light grey; fine grained dolomite; some areas of sparry crystals; homogenous throughout; no fractures/vugs; tight porosity
4949.40	30-50	2 "	163.207	light grey; fine grained dolomite; vuggy (pinpoint to 2cm); dolomite crystals infilling vugs; longitudinal fracture, filled with carbonate; tight porosity
4955.85	30-56	2 "	153.495	light grey; fine grained dolomite; large chert nodule, white with wavy laminations, discontinuous; deep vug in fracture, dolomite crystals infilling; pin point vugs in dolomite
4967.40	31-9	2 "	162.104	light to medium grey; fine grained dolomite; longitudinal fracture, branching, filled with white carbonate; vuggy on one side, mm - 1cm stringy vugs, with dolomite crystals growing; tight porosity
4977.80	31-19	2 "	154.734	light to medium grey; autoclastic breccia; open fractures; large, sparry pink dolomite; strongly brecciated; vugs, fractures with fluid enhancement; Fe oxides present (2mm)
4985.75	31-27	2 "	160.433	Chert dominated with some fine grained dolomite; small (1-2mm) vugs in dolomite; silicified zone in dolomite, mottled; Fe oxide present;
4990.10	32-5	1"	90.445	Finely crystalline dolomite; pinpoint to mm size vugs; some silicified areas <2mm; mostly homogenous throughout
5054.60	33-5	2 "	164.763	light to medium grey; fine grained dolomite; latitudinal fracture, not significantly altered; small vugs ranging from pinpoint to 3 cm; druzy dolomite growing in vugs; mostly homogenous.
5074.05	33-25	2 "	141.9	Coarse grained dolomite with wispy argillaceous laminations; elongate vug with crystallization; healed longitudinal fracture
5078.10	33-29	2 "	152.628	light grey; fine grained crystalline dolomite; no visible porosity; slightly mottled
5085.80	34-3	2 "	151.403	Medium grey; finely crystalline dolomite; vuggy, 1mm -4cm; vugs filled with dolomite crystals; some white silicified areas.
510.90	34-22	2 "	157.45	light grey; fine grained crystalline dolomite; mottled with darker color; pinpoint vugs; carbonate matrix surrounding crystals in light areas.

5108.10	34-26	2 "	146.642	light to medium grey; coarsely crystalline sparry dolomite; tight porosity, no vugs; mottled; areas of large pink dolomite crystals; possibly dark chert
5117.00	34-35	2 "	146.464	dark brown; coarsely crystalline argillaceous dolomite; vuggy, pinpoint to 4 mm; zones of clay rich material; white crystals growing in vugs; calcareous matrix; no fractures
5127.00	34-45	2 "	160.028	medium grey-brown; finely crystalline dolomite; longitudinal fractures filled with clay; some calcareous matrix;
5142.65	34-60	2 "	143.857	light grey; sandy dolomite; dolo-ss transition; homogenous distribution of sand, no fractures; visible grain size, porous
5170.90	35-28	2 "	145.863	Igneous, granite; light to medium grey; yellow coloration on out side of core, sulfur?; dense, no porosity, large crystals, quarts, feldspars, pyrite
5176.90	35-34	2 "	151.4	Pink granitoid rock; biotite, quartz, k-spar

Thin Section Descriptions

3670.6` (3-11)

Fine grained cherty dolomite with subhedral to euhedral micritic dolomite rhombs. Chert abundant infilling porosity and present as microporous tripolitic matrix. Oil stain in dolomite as parallel oriented splotches. Silicified sponge spicules and fossil fragments common. Few opaque minerals present as small (<0.2 mm) crystals infilling porosity.

3681.95` (3-22)

Fine grained cherty dolomite with subhedral to euhedral micritic dolomite rhombs. Common <2 cm size porous chert nodules with micritic dolomite inclusions. Microporous tripolitic chert matrix. Oil stain visible in dolomite and chert nodules and is present as parallel splotches.

3686.9` (3-27)

Fine grained porous dolomite with large quartz crystals growing, some euhedral. Highly birefringent mineral, possibly anhydrite, present partially filling vug size pores and growing around dolomite. Quartz appears to be replacing anhydrite(?) and displays fibrous habit and radial undulose extinction typical of evaporite replacement silica.

4187.75` (12-47)

Coarse to fine grained intergrown crystalline dolomite, subhedral to anhedral. Crystal size is highly variable with distinct zones of fine grained dolomite. Some zones of micrite (dolomicrite). Large crystals of saddle dolomite filling fractures. High mouldic porosity in some zones. Possible fossil remnants rare. Some intercrystaline areas have been filled with chert. Large grains of quartz sporadic throughout.

4187.2` (13-3)

Coarse to fine grained intergrown crystalline dolomite, sub to anhedral. Large euhedral to subhedral dolomite crystals in small areas. Some silicification of pore space. Low porosity except in fractures and isolated intercrystalline porosity around large dolomite crystals. Some micritic or argillaceous zones near fractures.

4365.8` **(17-13)**

Coarse to fine grained intergrown crystalline dolomite. Sub to anhedral crystal habit. Coarse grained dolomite exists in distinct zones. Few highly porous zones with small euhedral dolomite crystals and quartz crystals growing. Sporadic black, opaque oxide/sulfide mineral present. Few chert nodules with radiating chalcedony habit.

4379.1` **(17-27)**

coarsely crystalline dolomite with sub to euhedral habit. Euhedral grains are large. High porosity with some silicification evident, euhedral dolomite crystals surrounded by porous silicified matrix. Dolomite is cloudy throughout, suggesting biogenic influence on dolomitization. Area of large quartz and chert growing with no evidence of banding. Some porous zones have reddish clay material in association with opaque oxide/sulfide.

4388.8` **(17-36)**

Coarse to fine grained crystalline dolomite with subhedral to euhedral habit. Fracture porosity and matrix porosity common throughout. Fractures filled with clays and contain many black, opaque oxide/sulfide minerals. Dolomite crystals near fractures appear to be

dissolving and replaced by clay material. Large silica nodule present. Large nodules of opaque mineral.

4504` (19-41)

Chert/silica dominates thinsection. Intergrown crystals, massive habit. Chert zone isolated by a large fracture from zone of coarsely grained intergrown crystalline dolomite with subhedral habit. Large fracture filled with black, opaque oxide/sulfide mineral. Zones of reddish clay material with euhedral dolomite crystals interspersed. Some shaley zones within chert.

4515.3` (19-51)

Coarse to fine grained intergrown crystalline dolomite with subhedral to anhedral habit. Some areas of fine grained dolomite with silicified micritic matrix. Small chert nodules surrounded by dolomite overgrowth. Zone of porous argillaceous material with abundance of opaque oxide/sulfide minerals. Fracture filled with dolomite.

4570.1` (20-50)

Coarsely crystalline dolomite with some matrix support. Abundance of oxides in matrix. Some matrix appears clay rich. Possible silicified dolomite rhombs. Shale rich zone rare.

4903.8’ (30-4)

Coarsely crystalline subhedral to anhedral intergrown dolomite. Dolomite crystals appear cloudy possibly due to organic inclusions or other impurities. Dolomite is exclusive mineral at this depth and appears to display replacement texture. Low intercrystalline porosity visible in thin section. Porosity was measured at 3.4%.

4916.6` (30-17)

Coarse to fine grained intergrown crystalline dolomite with subhedral to anhedral habit. Low isolated, intercrystalline porosity. Some small pyrite grains. No fractures visible.

4923.7` (30-24)

Coarse to fine grained intergrown crystalline dolomite with subhedral to anhedral habit. Some large dolomite crystals in porous zones. Chert nodules abundant with quartz grained interspersed within coarse grained dolomite. Chert infilling of porosity near large grained dolomite crystals. Low, isolated vuggy porosity. Some zones contain clay material.

4925.7' (30-26)

Coarsely crystalline subhedral to anhedral dolomite with a large range in grain sizes. Some larger crystals appear to have undergone dissolution. Dolomite crystals are cloudy and some. Intercrystalline and matrix porosity are found at this depth. Pore space is larger than 4903.8' and some pores have a reddish brown (oxide) coating. Porosity was measured at 5.2% from whole core analysis.

4937.05` (30-38)

Coarsely crystalline with subhedral to anhedral intergrown dolomite. Several silica textures are observed at this depth. Silica is observed partially replacing large dolomite crystals (?). These crystals retain their original morphology as they are replaced by the silica. Silica is also observed infilling porosity between dolomite crystals. Porosity is low due to silica precipitation and was measured at 1.8%.

30-50 (4949.4`)

Fine to coarse grained intergrown crystalline dolomite with subhedral to anhedral habit. No distinct zones between fine and coarse grained dolomite. Some large euhedral dolomite in porous zones. Low, isolated intercrystalline porosity throughout. A few zones of opaque oxide/sulfide infilling poresaround dolomite. No silicification evident.

30-56 (4955.85`)

Fine to coarse grained intergrown crystalline dolomite with subhedral to anhedral habit. Distinct boundary between dolomite zone and highly silicified zone. Silicified zone

dominated by porous, silicified matrix with large nodules of chert displaying radiating chalcedony habit. Chert nodules display layering, some chalcedony has brown color. Some large quartz grains with massive habit.

31-9 (4967.4`)

Fine to coarse grained intergrown crystalline dolomite with subhedral to anhedral habit. Chert/chalcedony infilling porosity. Silicification of dolomite rhombs evident. Matrix of dolomite in some areas. Low porosity, fracture and isolated intercrystalline. Some opaque oxides throughout

31-19 (4977.8')

Highly silicified with various silica textures visible. Silicification concentrated in fracture boundaries and within pore spaces. Silica nodules have chalcedony outer edges with larger quartz grains in the interior. Porous silica texture prevalent. Euhedral quartz grains observed with a secondary, fracture filling dolomite growing around. Porosity is controlled by extensive fractures with slight porosity visible in silicified matrix. Porosity was measured at 8.8%. Large euhedral saddle dolomite infilling fractures. Saddle dolomite is associated with opaque oxide or sulfide minerals.

4985` (31-27)

Heterogeneous dolomite textures, highly silicified with extensive fractures. Coarsely crystalline dolomite with a wide range of crystal sizes is prevalent. Saddle dolomite is observed filling large fractures and is associated with an opaque mineral, possibly an oxide or sulfide. Abundance of dolomicrite in some zones. Matrix porosity is observed in the dolomicrite. Partial silicification of dolomicrite and infilling of porosity is extensive. Silica nodules have layered appearance with oxide (?) precipitate separating the layers. Silica occurs as chalcondeny, chert and well defined quartz crystals. This range of silica types can be observed in nodules where larger quartz crystals occur in the center while smaller, more fibrous chalcondeny occurs at the margins. Porosity was measured at 4.7% and occurs mainly as fracture and matrix porosity.

4990.1` (32-5)

Coarse to fine grained intergrown crystalline dolomite with subhedral to anhedral habit. Low isolated, intercrystalline porosity. Small opaque oxide/sulfides. No evidence of silicification.

5054.6' (33-5)

Coarsely crystalline, intergrown subhedral to anhedral dolomite. No evidence of dolomite dissolution. No silicification visible in thin section. Vuggy porosity with some isolated intercrystalilne porosity. Porosity measured at 2.3%. Quartz grains and small opaque mineral uncommon throughout.

5074.05' (33-25)

Highly porous, euhedral to subhedral dolomite. Detrital quartz grains more prevalent at this depth. No evidence of microcrystalline silicification. Vuggy to intercrystalline porosity prevalent. Porosity measured at 11.8%. Reddish brown oxide coating some pore edges.

5078.1` (33-29)

Fine grained intergrown crystalline dolomite with anhedral habit. Moderate intercrystalline porosity. Interspersed bands of quartz grains. Large and small opaque oxide/sulfide minerals throughout. Texture typical of a carbonate-sandstone transition zone.

XRD Data

K-State

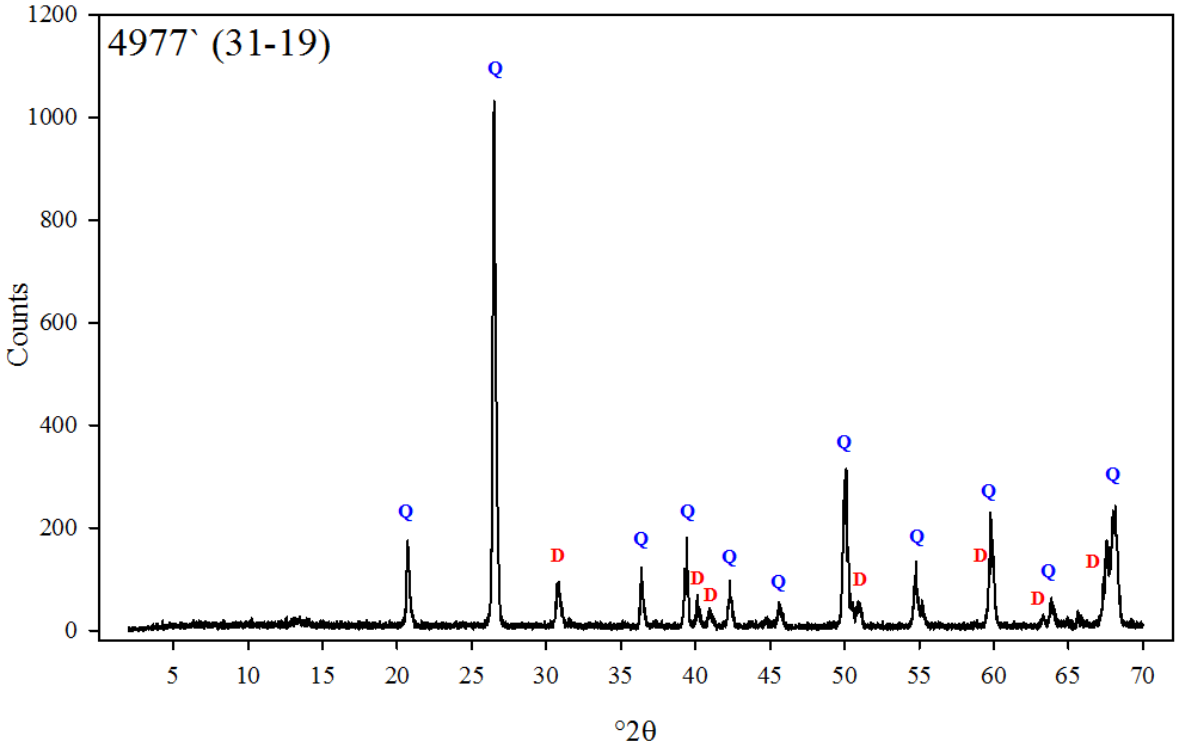

Figure A-1. Core 31-19 (4977`) from the injection zone and used in flow through experiment. Pattern shows strong quartz peaks with dolomite.

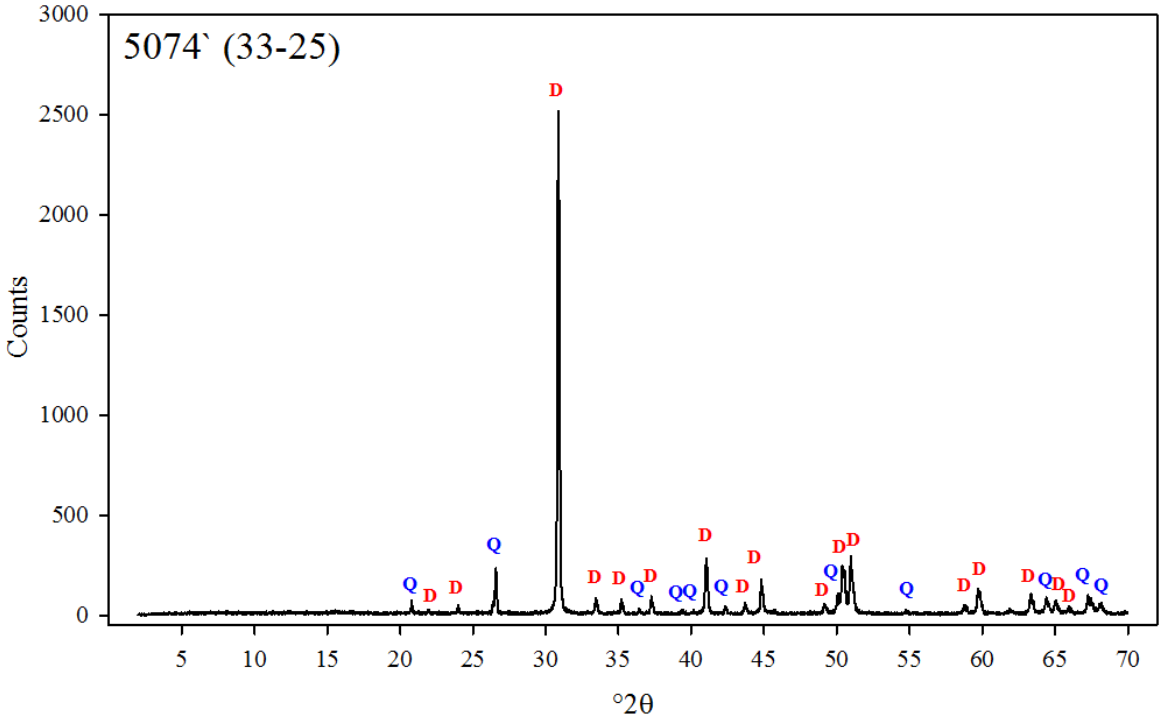

Figure A-2. Core 33-25 (5074`) from blow the injection zone showing strong dolomite peaks.

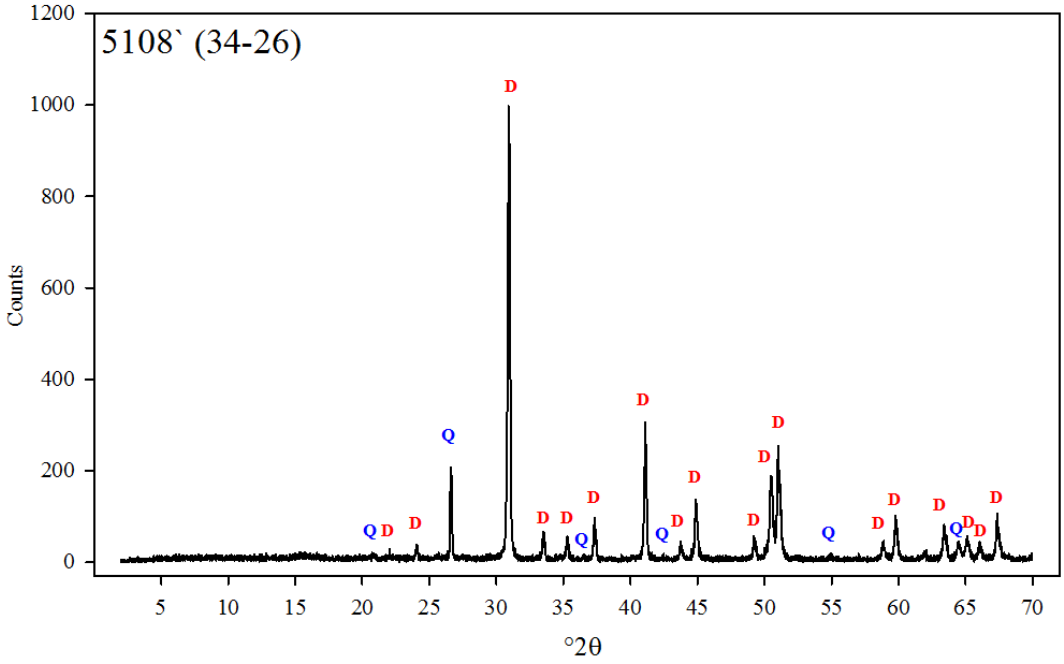

Figure A-3. Core 34-26 (5108`) from below the injection zone showing predominantly dolomite peaks with some quartz.

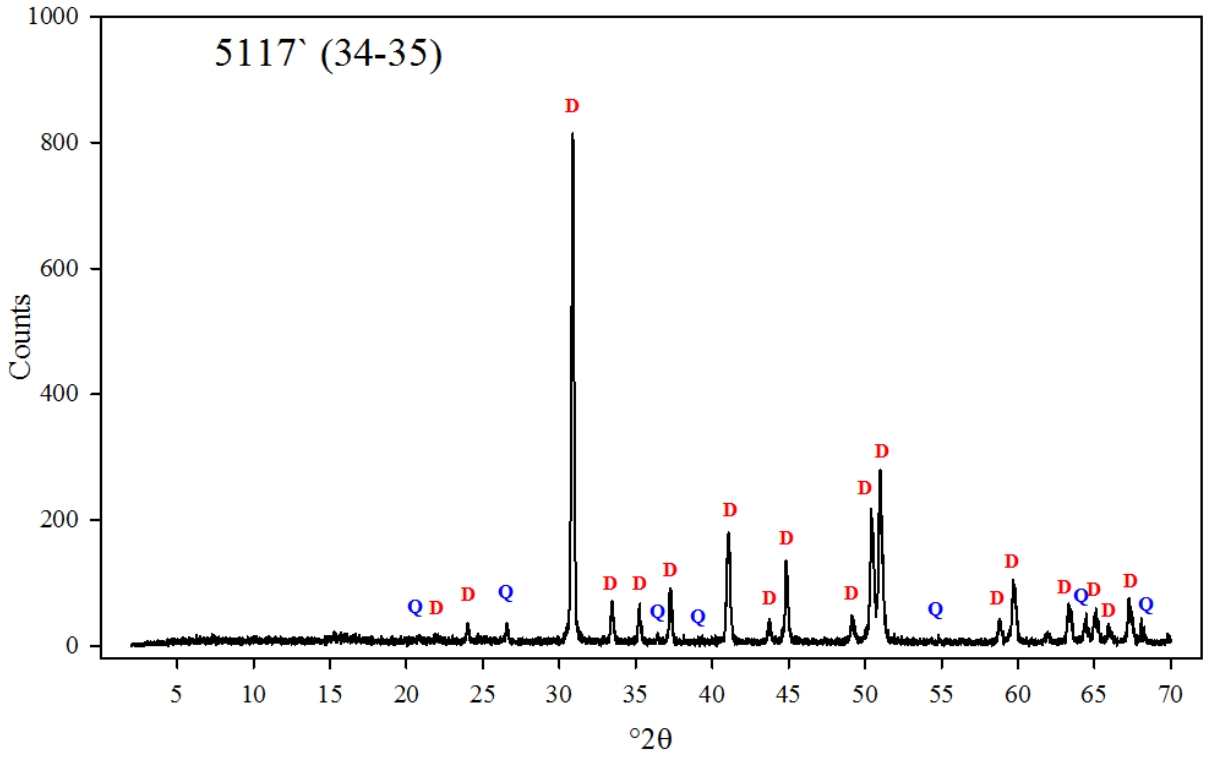

Figure A-4. Core 34-35 (5117`) from below the injection zone showing dolomite mineralogy.

Panalytical

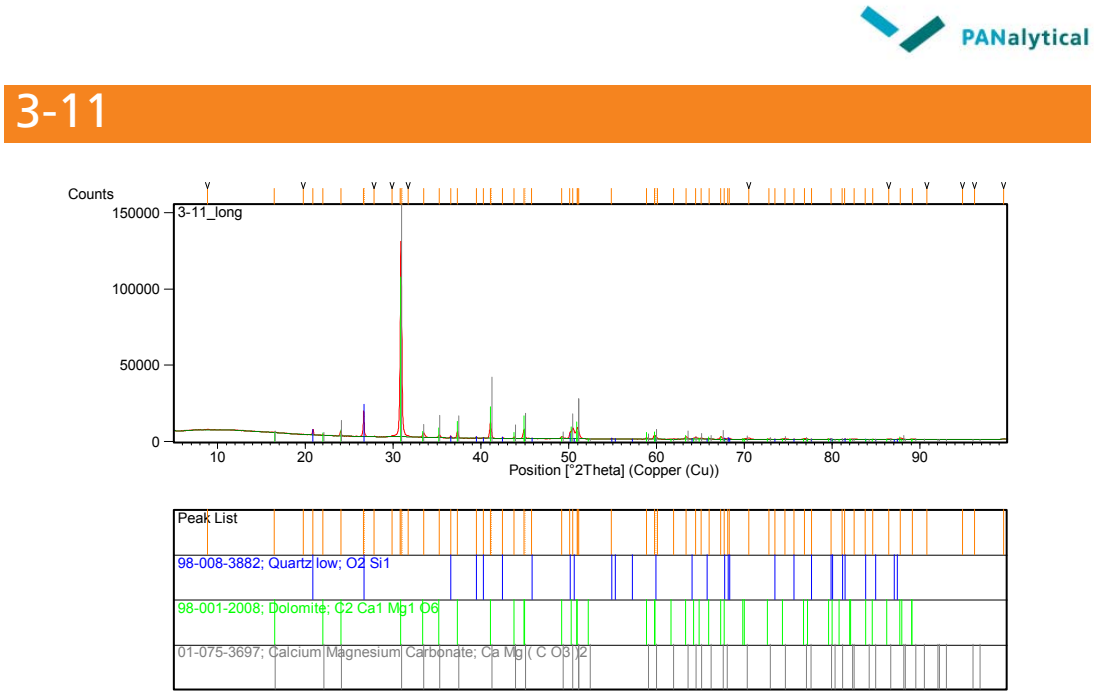

Figure A-5. Core 3-11 (3670.6`) from the Mississippian pay zone showing quartz and dolomite

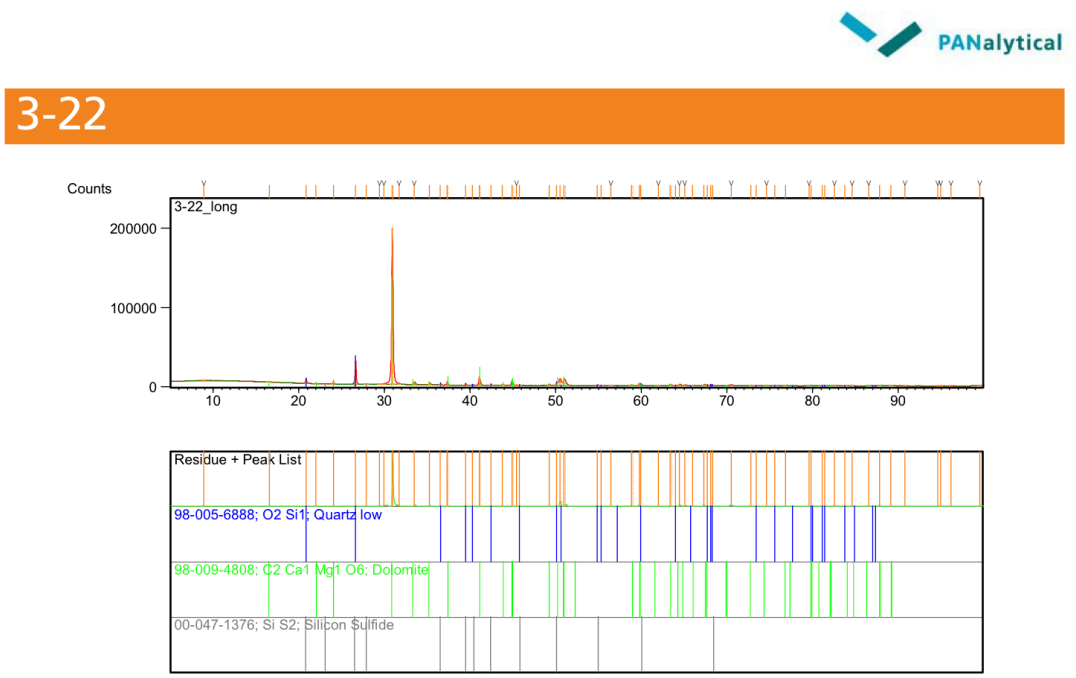

Figure A-6. Core 3-22 (3681.95`) from the Mississippian pay zone showing strong dolomite peak with minor quartz.

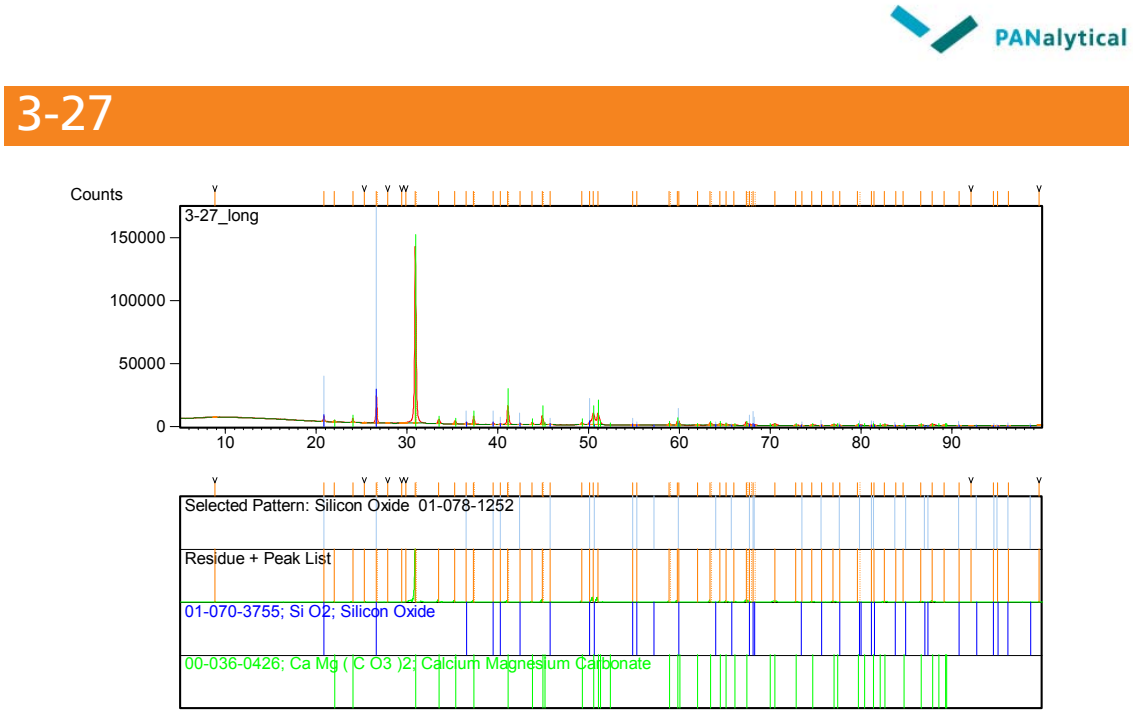

Figure A-7. Core 3-27 (3686.9`) from the Mississippian pay zone showing strong quartz peaks and dolomite.

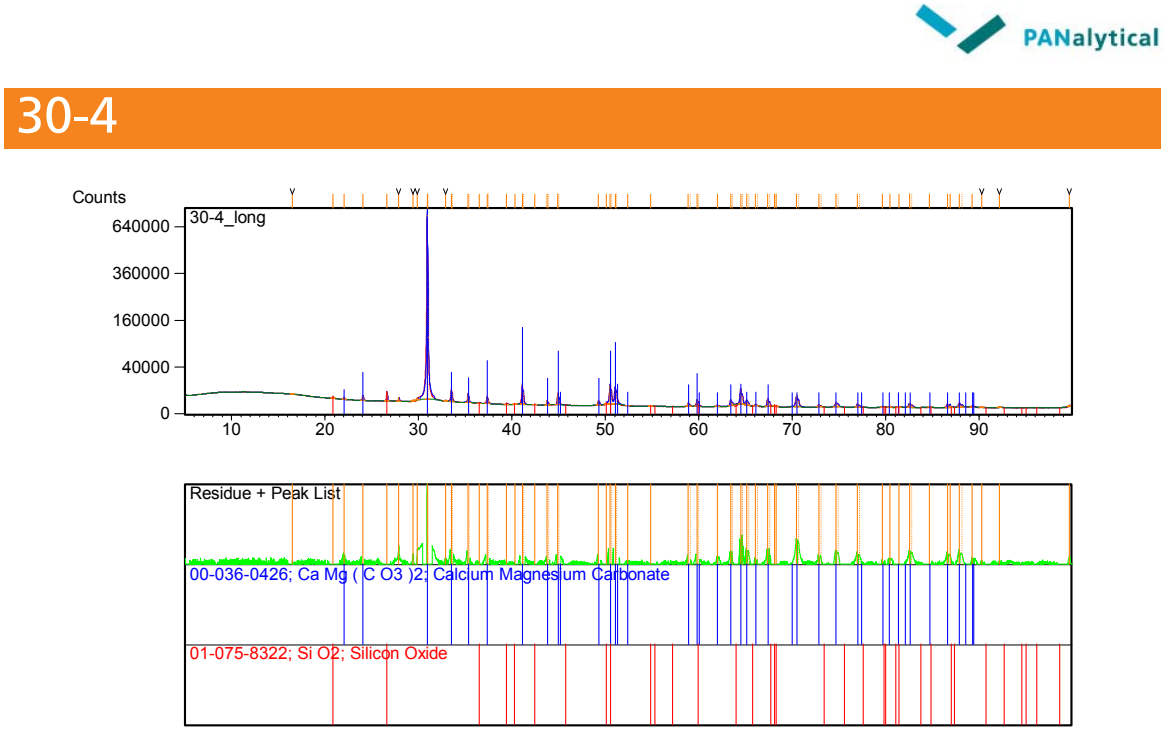

Figure A-8. Core 30-4 (4903.8`) from the injections zone showing a dolomite dominate mineralogy with minor quartz.

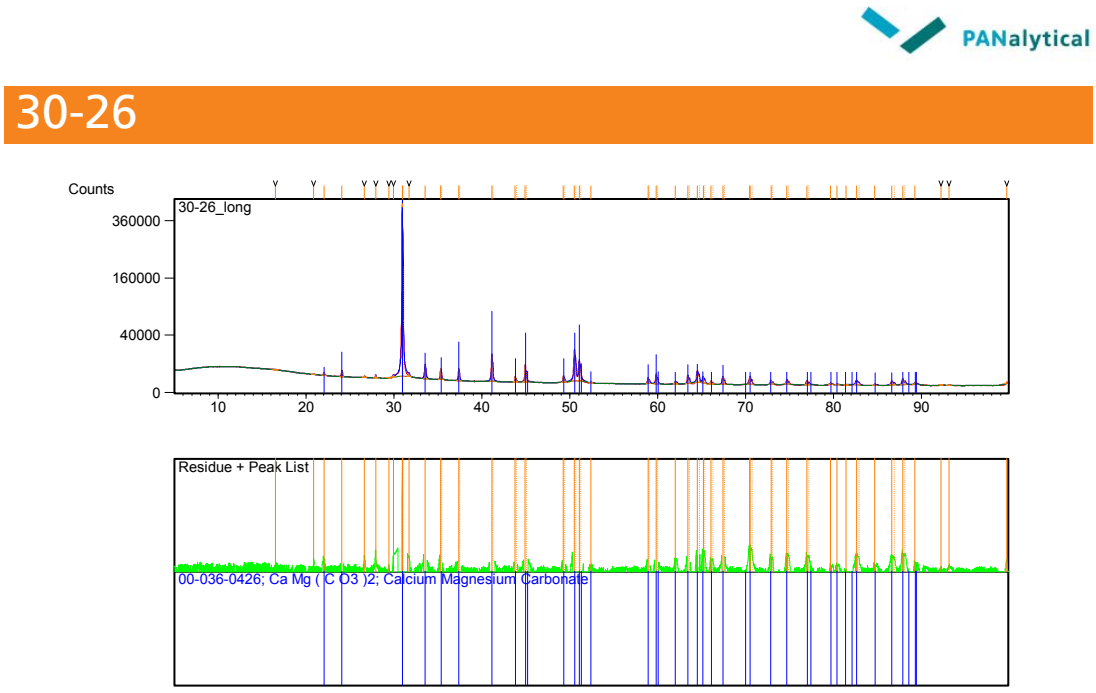

Figure A-9. Core 30-26 (4925.7) from the injection zone showing a pure dolomite mineralogy.

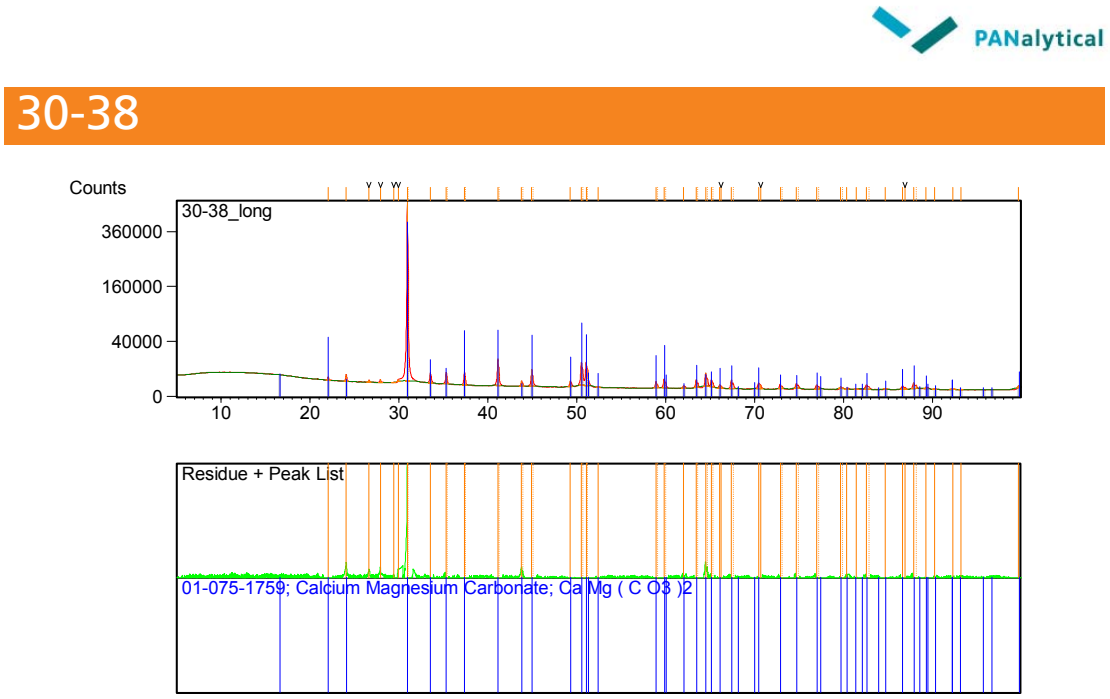

Figure A-10. Core 30-38 (4937.05`) from the injection zone that shows a pure dolomite mineralogy.

PANalytical

31-27

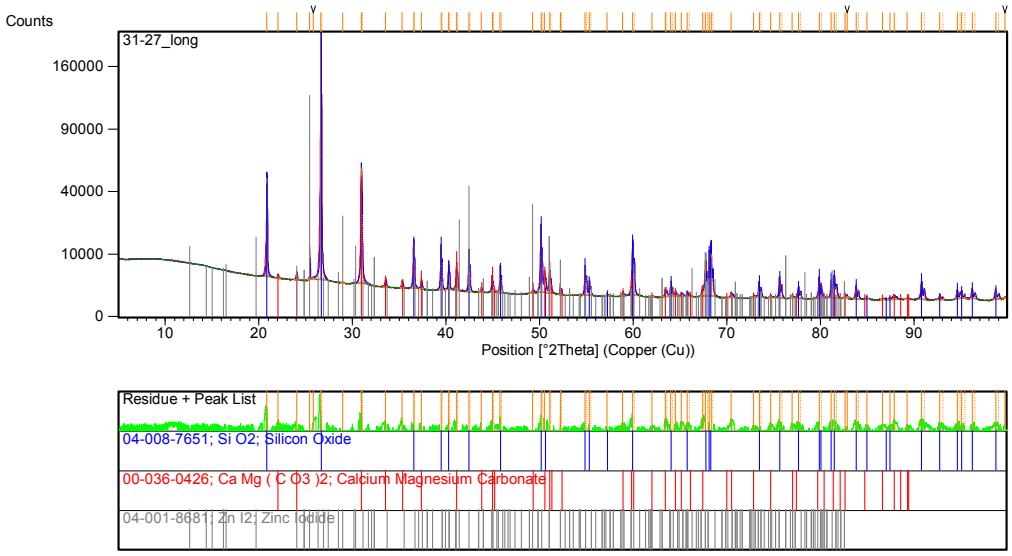

Figure A-11. Core 31-27 (4985.75`) from the injection zone showing strong quartz peaks with dolomite. An abundance of secondary peaks identified via software as zinc sulfide could represent argillaceous minerals observed in thin section.

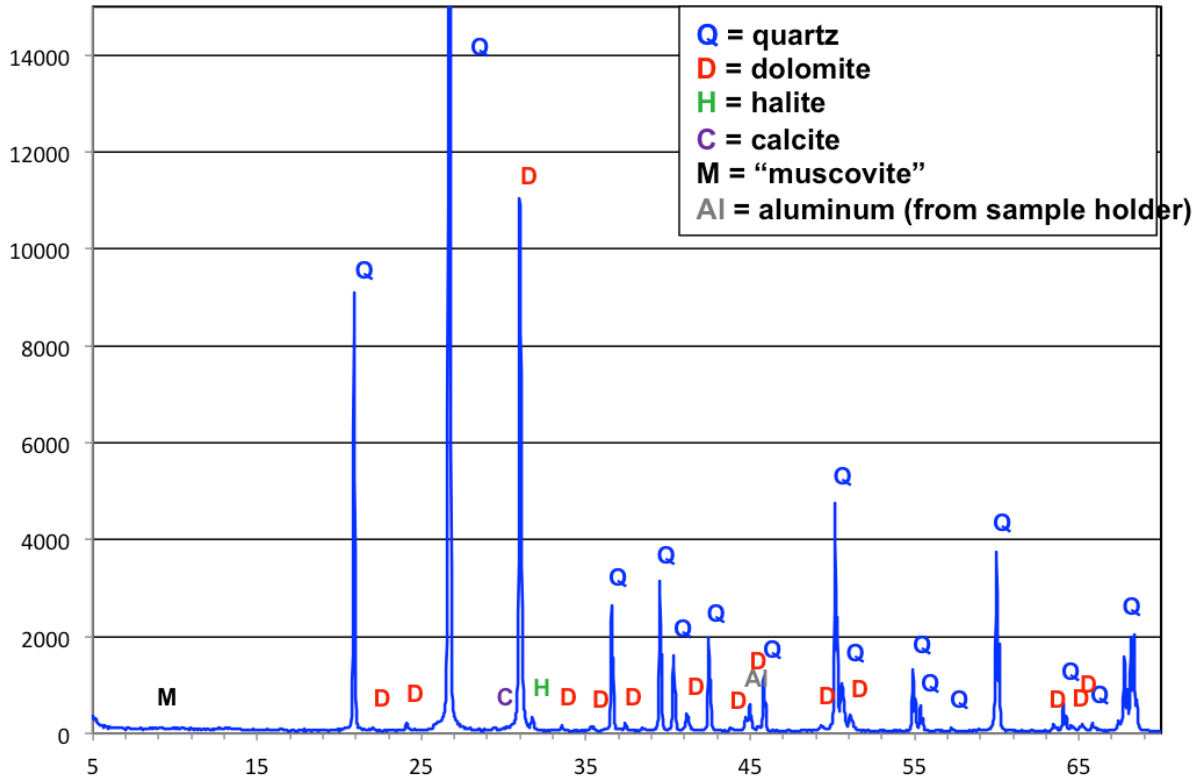

Figure A-12. Core 31-19 (4977`) from the injection zone and used in flow through experiment showing strong quartz and dolomite peaks with some minor clay minerals.

Appendix B - Hydrochemistry Data

Unit	Detection Limit	Analyte Symbol	DST-1 2/6 3664-3690	DST-1 1/6 3664-3690	DST-2 2/6 4465-4575	DST-2 4/6 4465-4575	DST-3 1/3 4280-4390	DST-3 2/6 4280-4390	DST-4 3/6 4175-4190	DST-4 4/6 4175-4190
µg/L	20	Ba	740	730	430	400	180	170	280	290
mg/L	0.1	Al	< 0.1	< 0.1	< 0.1	< 0.1	< 0.1	< 0.1	< 0.1	< 0.1
mg/L	0.1	K	691	702	834	830	424	411	347	278
mg/L	0.1	Mg	1880	1890	880	873	460	446	347	283
mg/L	0.01	Mn	0.89	0.89	1.1	1.06	0.59	0.49	1.17	1.36
mg/L	0.1	Si	2.9	3.3	14	15.1	12.9	13.3	8.3	4.5
µg/L	5	Ag	41	40	22	22	12	12	11	10
µg/L	30	As	< 30	< 30	< 30	< 30	< 30	< 30	< 30	< 30
µg/L	2	Be	< 2	< 2	< 2	< 2	< 2	< 2	< 2	< 2
µg/L	20	Bi	< 20	< 20	< 20	< 20	< 20	< 20	< 20	< 20
mg/L	0.1	Ca	10900	11300	5030	5080	2150	2150	1500	1130
µg/L	2	Cd	< 2	< 2	< 2	< 2	< 2	< 2	< 2	< 2
µg/L	30	Ce	30	< 30	< 30	< 30	< 30	< 30	< 30	< 30
µg/L	2	Co	< 2	6	4	4	< 2	< 2	< 2	< 2
µg/L	20	Cr	< 20	< 20	< 20	< 20	< 20	< 20	< 20	< 20
mg/L	0.01	Fe	0.09	0.29	0.05	0.04	0.07	0.04	0.09	0.67
µg/L	2	Cu	175	92	6	6	4	4	4	3
mg/L	0.05	Li	3.84	3.9	13.9	13.9	4.43	4.49	3.17	2.7
µg/L	5	Mo	16	8	< 5	< 5	< 5	< 5	58	102
mg/L	0.1	Na	56000	58000	31500	31900	17400	17300	15900	13700
µg/L	5	Ni	13	14	< 5	6	< 5	< 5	< 5	< 5
mg/L	0.02	P	0.03	0.02	0.03	< 0.02	0.14	0.03	< 0.02	0.06
µg/L	10	Pb	3510	180	< 10	20	< 10	< 10	< 10	10
µg/L	10	Sb	70	70	10	< 10	< 10	< 10	< 10	< 10
mg/L	1	S	219	233	345	346	553	552	271	246
µg/L	20	Se	20	< 20	< 20	< 20	< 20	< 20	< 20	< 20
µg/L	10	Sn	< 10	< 10	< 10	< 10	< 10	< 10	< 10	< 10
µg/L	10	Sr	402000	417000	158000	160000	71300	71500	55400	45000
µg/L	10	Te	< 10	< 10	< 10	10	10	< 10	< 10	< 10
µg/L	10	Ti	< 10	< 10	< 10	< 10	< 10	< 10	< 10	< 10
µg/L	10	Tl	< 10	< 10	< 10	< 10	< 10	< 10	< 10	< 10
mg/L	0.05	U	< 0.05	< 0.05	< 0.05	< 0.05	< 0.05	< 0.05	< 0.05	< 0.05
µg/L	10	V	< 10	< 10	< 10	< 10	< 10	< 10	< 10	< 10
µg/L	10	W	70	40	< 10	< 10	< 10	< 10	< 10	< 10
µg/L	10	Y	< 10	< 10	< 10	< 10	< 10	< 10	< 10	< 10
µg/L	5	Zn	6900	1780	32	45	< 5	6	< 5	5
mg/L	0.01	F	< 10	< 10	< 10	< 5	< 3	< 3	< 2	< 2
mg/L	0.03	Cl	116000	119000	65800	70800	32000	33100	30500	5090
mg/L	0.01	NO_2	< 10	< 10	< 10	< 5	< 3	< 3	< 2	< 2
mg/L	0.03	Br	455	464	120	132	75.9	77.4	79.7	< 6
mg/L	0.01	NO_3	146	39.8	< 10	< 5	< 3	< 3	< 2	< 2
mg/L	0.02	PO_4	< 20	< 20	< 20	< 10	< 5	< 5	< 4	< 4
mg/L	0.03	SO_4	689	703	1060	1150	1610	1670	873	718
mg/L	-	CO_3	-	42	124	-	180	-	192	-

Table B-1. DST water analysis from KGS 1-32 as measured by ICP-OES and IC. DST samples are numbered according to the DST sample number (DST-1, DST-2, etc.) the pipe it was collected from (1/6, 2/6, etc.) and the depth interval (3664`-3690`, etc.).

Unit	Detection Limit	Analyte Symbol	DST-1 2/6 3664-3690	DST-1 1/6 3664-3690	DST-2 2/6 4465-4575	DST-2 4/6 4465-4575	DST-3 1/3 4280-4390	DST-3 2/6 4280-4390	DST-4 3/6 4175-4190	DST-4 4/6 4175-4190
µg/L	20	Ba	740	730	430	400	180	170	280	290
mg/L	0.1	Al	< 0.1	< 0.1	< 0.1	< 0.1	< 0.1	< 0.1	< 0.1	< 0.1
mg/L	0.1	K	691	702	834	830	424	411	347	278
mg/L	0.1	Mg	1880	1890	880	873	460	446	347	283
mg/L	0.01	Mn	0.89	0.89	1.1	1.06	0.59	0.49	1.17	1.36
mg/L	0.1	Si	2.9	3.3	14	15.1	12.9	13.3	8.3	4.5
µg/L	5	Ag	41	40	22	22	12	12	11	10
µg/L	30	As	< 30	< 30	< 30	< 30	< 30	< 30	< 30	< 30
µg/L	2	Be	< 2	< 2	< 2	< 2	< 2	< 2	< 2	< 2
µg/L	20	Bi	< 20	< 20	< 20	< 20	< 20	< 20	< 20	< 20
mg/L	0.1	Ca	10900	11300	5030	5080	2150	2150	1500	1130
µg/L	2	Cd	< 2	< 2	< 2	< 2	< 2	< 2	< 2	< 2
µg/L	30	Ce	30	< 30	< 30	< 30	< 30	< 30	< 30	< 30
µg/L	2	Co	< 2	6	4	4	< 2	< 2	< 2	< 2
µg/L	20	Cr	< 20	< 20	< 20	< 20	< 20	< 20	< 20	< 20
mg/L	0.01	Fe	0.09	0.29	0.05	0.04	0.07	0.04	0.09	0.67
µg/L	2	Cu	175	92	6	6	4	4	4	3
mg/L	0.05	Li	3.84	3.9	13.9	13.9	4.43	4.49	3.17	2.7
µg/L	5	Mo	16	8	< 5	< 5	< 5	< 5	58	102
mg/L	0.1	Na	56000	58000	31500	31900	17400	17300	15900	13700
µg/L	5	Ni	13	14	< 5	6	< 5	< 5	< 5	< 5
mg/L	0.02	P	0.03	0.02	0.03	< 0.02	0.14	0.03	< 0.02	0.06
µg/L	10	Pb	3510	180	< 10	20	< 10	< 10	< 10	10
µg/L	10	Sb	70	70	10	< 10	< 10	< 10	< 10	< 10
mg/L	1	S	219	233	345	346	553	552	271	246
µg/L	20	Se	20	< 20	< 20	< 20	< 20	< 20	< 20	< 20
µg/L	10	Sn	< 10	< 10	< 10	< 10	< 10	< 10	< 10	< 10
µg/L	10	Sr	402000	417000	158000	160000	71300	71500	55400	45000
µg/L	10	Te	< 10	< 10	< 10	10	10	< 10	< 10	< 10
µg/L	10	Ti	< 10	< 10	< 10	< 10	< 10	< 10	< 10	< 10
µg/L	10	Tl	< 10	< 10	< 10	< 10	< 10	< 10	< 10	< 10
mg/L	0.05	U	< 0.05	< 0.05	< 0.05	< 0.05	< 0.05	< 0.05	< 0.05	< 0.05
µg/L	10	V	< 10	< 10	< 10	< 10	< 10	< 10	< 10	< 10
µg/L	10	W	70	40	< 10	< 10	< 10	< 10	< 10	< 10
µg/L	10	Y	< 10	< 10	< 10	< 10	< 10	< 10	< 10	< 10
µg/L	5	Zn	6900	1780	32	45	< 5	6	< 5	5
mg/L	0.01	F	< 10	< 10	< 10	< 5	< 3	< 3	< 2	< 2
mg/L	0.03	Cl	116000	119000	65800	70800	32000	33100	30500	5090
mg/L	0.01	NO_2	< 10	< 10	< 10	< 5	< 3	< 3	< 2	< 2
mg/L	0.03	Br	455	464	120	132	75.9	77.4	79.7	< 6
mg/L	0.01	NO_3	146	39.8	< 10	< 5	< 3	< 3	< 2	< 2
mg/L	0.02	PO_4	< 20	< 20	< 20	< 10	< 5	< 5	< 4	< 4
mg/L	0.03	SO_4	689	703	1060	1150	1610	1670	873	718
mg/L	-	CO_3	-	42	124	-	180	-	192	-

Table B-2. DST water analyses from KGS 1-28 as measured by ICP-OES and IC. DST samples are numbered according to the DST sample number (DST-1, DST-2, etc.) the pipe it was collected from (1/6, 2/6, etc.) and the depth interval (3664`-3690`, etc.).

Unit Symbol	Detection Limit	Analyte Symbol	Swab 1 Filtered	Swab 1 Unfiltered
µg/L	20	**Ba**	1350	1350
mg/L	0.1	**Al**	< 0.1	< 0.1
mg/L	0.1	**K**	1160	1160
mg/L	0.1	**Mg**	1790	1800
mg/L	0.01	**Mn**	0.2	0.26
mg/L	0.1	**Si**	5	5
µg/L	5	**Ag**	9	9
µg/L	30	**As**	< 30	< 30
µg/L	2	**Be**	< 2	< 2
µg/L	20	**Bi**	< 20	< 20
mg/L	0.1	**Ca**	10600	10600
µg/L	2	**Cd**	< 2	< 2
µg/L	30	**Ce**	< 30	< 30
µg/L	2	**Co**	< 2	< 2
µg/L	20	**Cr**	< 20	< 20
mg/L	0.01	**Fe**	0.03	0.51
µg/L	2	**Cu**	< 2	4
mg/L	0.05	**Li**	11.6	11.7
µg/L	5	**Mo**	< 5	< 5
mg/L	0.1	**Na**	57500	57500
µg/L	5	**Ni**	< 5	< 5
mg/L	0.02	**P**	< 0.02	< 0.02
µg/L	10	**Pb**	< 10	< 10
µg/L	10	**Sb**	< 10	< 10
mg/L	1	**S**	136	133
µg/L	20	**Se**	< 20	< 20
µg/L	10	**Sn**	< 10	< 10
µg/L	10	**Sr**	335000	335000
µg/L	10	**Te**	< 10	< 10
µg/L	10	**Ti**	< 10	< 10
µg/L	10	**Tl**	< 10	< 10
mg/L	0.05	**U**	< 0.05	< 0.05
µg/L	10	**V**	< 10	< 10
µg/L	10	**W**	< 10	< 10
µg/L	10	**Y**	< 10	< 10
µg/L	5	**Zn**	< 5	8
mg/L	0.01	**F**	< 10	< 10
mg/L	0.03	**Cl**	114000	114000
mg/L	0.01	**NO_2**	< 10	< 10
mg/L	0.03	**Br**	235	197
mg/L	0.01	**NO_3**	< 10	< 10
mg/L	0.02	**PO_4**	< 20	< 20
mg/L	0.03	**SO_4**	425	420

Table B-3. Swabbed sample 1 as measured by ICP-OES and IC. One filtered and one unfiltered sample were analyzed.

Unit	Limit Range	Analyte Symbol	Swab 2 Filtered	Swab 2 Unfiltered	Swab 3 Filtered	Swab 3 Unfiltered	Swab 4 Filtered	Swab 4 Unfiltered	Swab 5 Filtered	Swab 5 Unfiltered
µg/L	0.002	**Ag**	1.847	1.956	0.482	0.427	0.303	0.516	<0.002	<0.002
µg/L	0.5	**Al**	5337.9	596.7	875.0	6281.8	1622.5	410.5	<0.5	127.6
µg/L	0.02	**As**	137.34	13.99	111.31	229.56	74.46	149.69	18.61	72.35
µg/L	0.1	**B**	16713.4	17272.4	16960.6	12120.8	14779.4	10238.4	16312.6	14452.4
µg/L	0.01	**Ba**	2337.46	2235.49	1946.70	1713.99	1774.71	1785.79	438.00	426.08
µg/L	0.001	**Be**	<0.001	<0.001	<0.001	<0.001	<0.001	<0.001	<0.001	<0.001
µg/L	0.001	**Bi**	1.440	0.464	0.855	0.538	0.768	0.323	0.167	<0.001
µg/L	5	**Ca**	11783534	11572648	10549897	10031250	10526714	10040376	3907032	3843394
µg/L	0.001	**Cd**	1.116	1.141	0.730	3.219	1.036	1.071	1.386	0.946
µg/L	0.001	**Ce**	14.733	2.157	7.535	2.639	9.293	0.882	0.678	1.542
µg/L	0.001	**Co**	1.997	0.388	0.472	0.072	0.916	2.069	0.320	5.494
µg/L	0.01	**Cr**	60.66	8.44	11.20	18.15	63.61	40.15	2.05	55.70
µg/L	0.001	**Cs**	487.989	463.755	264.361	220.541	221.469	396.103	10.701	35.425
µg/L	0.05	**Cu**	655.26	273.63	141.74	77.09	114.11	113.70	41.31	132.98
µg/L	0.0005	**Dy**	0.3848	0.0591	1.2740	0.2155	0.1979	0.0366	0.0857	0.0955
µg/L	0.00005	**Er**	0.29762	<0.00005	1.07507	0.19303	0.11788	0.03161	0.05081	0.05506
µg/L	0.00005	**Eu**	1.54639	0.76163	1.57198	0.73210	0.84848	0.56515	0.14932	0.19215
µg/L	1	**Fe**	8677	12963	10972	768	1772	59169	12844	120799
µg/L	0.001	**Ga**	2.277	0.608	0.745	0.641	0.454	0.606	<0.001	0.866
µg/L	0.00005	**Gd**	0.55927	0.10300	0.79855	0.11763	0.29791	0.06348	0.06945	0.10408
µg/L	0.001	**Ge**	2.683	2.002	0.055	3.420	5.681	17.340	0.007	15.141
µg/L	0.00005	**Hf**	0.32834	<0.00005	0.15369	0.00850	0.04600	0.00138	<0.00005	<0.00005
µg/L	0.05	**Hg**	19.71	14.22	3.92	4.07	0.98	4.58	<0.05	<0.05
µg/L	0.00001	**Ho**	0.22924	0.01622	1.15083	0.16588	0.08515	0.00869	0.04659	0.06265
µg/L	0.0001	**In**	<0.0001	<0.0001	<0.0001	0.0330	0.0424	<0.0001	<0.0001	<0.0001
µg/L	1	**K**	961419	955099	906588	875609	900460	876618	398247	385065
µg/L	0.001	**La**	11.172	1.683	7.117	2.130	7.281	0.687	0.984	1.655
µg/L	0.05	**Li**	19407.14	21381.17	20523.90	8135.63	11156.01	3024.26	4991.85	2194.78
µg/L	0.00005	**Lu**	1.69391	0.05939	1.73644	0.29177	0.31954	0.12345	0.05194	0.13678
µg/L	0.2	**Mg**	1910104.6	1894266.7	1802167.1	1721037.7	1763510.8	1660561.2	933223.3	891900.1
µg/L	0.05	**Mn**	1273.76	1175.68	3062.69	2047.29	2206.12	2265.34	3802.15	3876.85
µg/L	0.005	**Mo**	2.953	1.055	6.953	0.476	5.242	17.797	9.247	<0.005
µg/L	5	**Na**	54791251	53838505	49841960	49247950	50564764	46844894	25584997	24238256
µg/L	0.0001	**Nb**	0.9196	1.1388	0.4873	4.2589	4.7184	8.9680	0.0563	0.8907
µg/L	0.0001	**Nd**	3.2259	0.5691	1.6896	0.5899	1.9164	0.2575	0.1558	0.4616
µg/L	0.05	**Ni**	15.22	<0.05	<0.05	<0.05	<0.05	8.67	<0.05	28.21
µg/L	0.005	**Pb**	16.147	19.350	4.869	4.655	7.855	8.859	2.795	7.553
µg/L	0.00005	**Pr**	1.78105	0.14018	1.46245	0.32923	0.67423	0.08356	0.12349	0.17995
µg/L	0.005	**Rb**	2885.129	2728.094	2649.431	2481.513	2555.514	2615.111	882.398	875.524
µg/L	0.0001	**Re**	<0.0001	<0.0001	0.0078	<0.0001	<0.0001	<0.0001	<0.0001	<0.0001

µg/L	0.001	**Sb**	1.777	3.552	1.844	0.626	0.596	4.751	0.425	<0.001
µg/L	0.01	**Sc**	<0.01	<0.01	<0.01	<0.01	<0.01	<0.01	<0.01	<0.01
µg/L	5	**Se**	1333	313	1179	1903	944	765	235	561
µg/L	30	**Si**	4796	7174	4750	8427	8392	8213	5874	9928
µg/L	0.0005	**Sm**	1.4057	0.1614	1.4839	0.2957	0.3363	0.1046	0.0879	0.1207
µg/L	0.01	**Sn**	<0.01	<0.01	<0.01	<0.01	<0.01	<0.01	<0.01	<0.01
µg/L	0.01	**Sr**	383468.64	367389.61	330608.57	306273.79	324044.71	328532.25	132335.30	133881.14
µg/L	0.0005	**Ta**	0.0135	<0.0005	0.0096	0.0255	0.0082	0.0179	0.0066	<0.0005
µg/L	0.00002	**Tb**	0.20610	0.02192	1.00714	0.14437	0.08494	0.00934	0.05057	0.05096
µg/L	0.001	**Te**	4.384	0.990	<0.001	0.962	6.494	1.141	2.075	1.862
µg/L	0.00002	**Th**	0.44932	0.00585	1.39042	0.22434	0.09560	0.02977	<0.00002	<0.00002
µg/L	0.01	**Ti**	61.72	11.56	6.78	10.96	18.70	9.36	3.75	16.75
µg/L	0.0001	**Tl**	0.4902	0.0679	0.0853	0.0296	0.0977	0.0986	<0.0001	0.0600
µg/L	0.0001	**Tm**	1.5735	0.0397	1.5313	0.2135	0.3492	0.1694	0.0531	0.0977
µg/L	0.0001	**U**	2.3791	0.1695	4.0591	0.2707	0.5720	0.1174	0.0581	0.1878
µg/L	0.001	**V**	7.954	1.367	2.451	2.163	3.441	2.492	0.090	4.341
µg/L	0.001	**W**	14.738	17.605	2.069	7.813	9.606	5.813	2.080	1.079
µg/L	0.0005	**Y**	5.6459	3.5689	3.8182	3.1511	3.9488	2.9238	1.5454	1.3988
µg/L	0.00005	**Yb**	0.99666	0.05925	1.33421	0.17103	0.23696	0.02462	0.06723	0.09140
µg/L	0.5	**Zn**	1713.7	575.5	518.8	285.5	523.6	864.9	140.3	1622.9
µg/L	0.001	**Zr**	8.439	1.468	3.215	1.792	3.486	1.082	0.377	1.292

Table B-4. HR-ICP-MS analyses of swabbed samples 2, 3, 4 and 5. Two samples from each test are presented, one filtered, the second unfiltered. Filtered samples were used in comparisons.

Unit	Analyte	Swab 2	Swab 3	Swab 4	Swab 5
mg/L	**F**	-0.50	-0.50	-0.50	-0.50
mg/L	**Cl**	106013.09	104390.13	103326.48	47598.38
mg/L	**NO_2 (as N)**	-0.50	-0.50	-0.50	-0.50
mg/L	**Br**	225.52	196.32	190.93	97.08
mg/L	**NO_3 (as N)**	-0.50	-0.50	-0.50	-0.50
mg/L	**PO_4 (as P)**	-1.00	-1.00	-1.00	-1.00
mg/L	**SO_4**	389.01	478.47	542.60	985.89
	dillution factor	50	50	50	50

Table B-5. IC analysis of swabbed samples 2-5.

Appendix C - Flow Through Experiment Data

Analyte	Unit	Hour zero	Hour 1	Hour 2	Hour 3	Hour 4	Hour 5	Hour 6	Hour 7	Hour 8-20	Hour 21	Hour 22	Hour 23	Hour 24
Ba	µg/L	580	600	590	590	590	590	580	580	590	580	580	580	580
Al	mg/L	0.5	0.1	0.2	0.1	0.1	0.1	< 0.1	0.1	< 0.1	< 0.1	< 0.1	< 0.1	< 0.1
K	mg/L	1170	1190	1190	1210	1200	1190	1200	1210	1240	1210	1200	1190	1180
Mg	mg/L	1610	1610	1620	1650	1650	1620	1650	1650	1690	1650	1650	1640	1630
Mn	mg/L	1.67	1.5	1.56	1.63	1.59	1.57	1.59	1.62	1.66	1.63	1.62	1.62	1.63
Si	mg/L	6.4	5.5	5.5	5.5	5.5	5.5	5.5	5.4	5.5	5.4	5.4	5.4	5.4
Ag	µg/L	15	14	14	14	14	13	13	14	14	14	14	14	13
As	µg/L	< 30	< 30	< 30	< 30	< 30	< 30	< 30	< 30	< 30	< 30	< 30	< 30	< 30
Be	µg/L	< 2	< 2	< 2	< 2	< 2	< 2	< 2	< 2	< 2	< 2	< 2	< 2	< 2
Bi	µg/L	< 20	< 20	< 20	< 20	< 20	< 20	< 20	< 20	< 20	< 20	< 20	< 20	< 20
Ca	mg/L	9900	10000	10200	10200	10200	10200	10100	10200	10600	10200	10200	10100	10200
Cd	µg/L	< 2	< 2	< 2	< 2	< 2	< 2	< 2	< 2	< 2	< 2	< 2	< 2	< 2
Ce	µg/L	< 30	< 30	< 30	< 30	< 30	< 30	< 30	< 30	< 30	< 30	< 30	< 30	< 30
Co	µg/L	10	< 2	< 2	< 2	< 2	< 2	< 2	< 2	< 2	< 2	< 2	< 2	< 2
Cr	µg/L	< 20	30	< 20	< 20	< 20	< 20	< 20	< 20	< 20	< 20	< 20	< 20	< 20
Fe	mg/L	6.96	3.6	2.86	2.85	2.55	2.25	2.04	2.27	1.73	2.27	2.12	2.34	2.56
Cu	µg/L	8	3	2	2	4	3	< 2	2	3	3	2	< 2	< 2
Li	mg/L	15.9	16.1	16.2	16.4	16.2	16.2	16.3	16.2	16.7	16.2	16.2	16.1	16.1
Mo	µg/L	< 5	10	< 5	< 5	< 5	< 5	< 5	< 5	< 5	< 5	< 5	< 5	< 5
Na	mg/L	54100	54600	55000	55300	55100	55400	55200	55300	57600	55700	55200	54800	55300
Ni	µg/L	50	43	8	5	< 5	< 5	< 5	< 5	< 5	< 5	< 5	< 5	< 5
P	mg/L	0.07	0.06	0.06	0.04	0.04	0.05	0.03	< 0.02	0.02	0.05	0.04	0.05	0.05
Pb	µg/L	20	< 10	< 10	< 10	< 10	< 10	< 10	< 10	< 10	< 10	< 10	< 10	< 10
Sb	µg/L	10	< 10	< 10	< 10	< 10	< 10	< 10	< 10	< 10	< 10	< 10	< 10	< 10
S	mg/L	135	126	126	125	126	127	129	126	123	129	129	123	124
Se	µg/L	< 20	< 20	< 20	< 20	< 20	< 20	< 20	< 20	< 20	< 20	< 20	< 20	< 20
Sn	µg/L	< 10	< 10	< 10	< 10	< 10	< 10	< 10	< 10	< 10	< 10	< 10	< 10	< 10
Sr	µg/L	315000	317000	323000	324000	324000	321000	321000	324000	336000	323000	322000	321000	322000
Te	µg/L	30	< 10	< 10	< 10	< 10	< 10	< 10	< 10	< 10	< 10	< 10	< 10	< 10
Ti	µg/L	< 10	< 10	< 10	< 10	< 10	< 10	< 10	< 10	< 10	< 10	< 10	< 10	< 10
Tl	µg/L	< 10	< 10	< 10	< 10	< 10	< 10	< 10	< 10	< 10	< 10	< 10	< 10	< 10
U	mg/L	< 0.05	< 0.05	< 0.05	< 0.05	< 0.05	< 0.05	< 0.05	< 0.05	< 0.05	< 0.05	< 0.05	< 0.05	< 0.05
V	µg/L	< 10	< 10	< 10	< 10	< 10	< 10	< 10	< 10	< 10	< 10	< 10	< 10	< 10
W	µg/L	< 10	< 10	< 10	< 10	< 10	< 10	< 10	< 10	< 10	< 10	< 10	< 10	< 10
Y	µg/L	< 10	< 10	< 10	< 10	< 10	< 10	< 10	< 10	< 10	< 10	< 10	< 10	< 10
Zn	µg/L	28	13	14	10	9	7	8	6	7	5	9	8	6
F	mg/L	< 10	< 10	< 10	< 10	< 10	< 10	< 10	< 10	< 10	< 10	< 10	< 10	< 10
Cl	mg/L	107000	115000	116000	116000	116000	116000	115000	116000	119000	116000	117000	115000	110000
NO_2	mg/L	< 10	< 10	< 10	< 10	< 10	< 10	< 10	< 10	< 10	< 10	< 10	< 10	< 10
Br	mg/L	204	252	240	240	237	236	228	245	238	245	236	227	225
NO_3	mg/L	< 10	< 10	< 10	< 10	< 10	< 10	< 10	< 10	< 10	< 10	< 10	< 10	< 10
PO_4	mg/L	< 20	< 20	< 20	< 20	< 20	< 20	< 20	< 20	< 20	< 20	< 20	< 20	< 20
SO_4	mg/L	371	367	347	362	386	370	338	363	387	388	385	396	345
CO_3^{2-}	mg/l	368	225	311	391	413	378	333	394	485	466	436	428	441
pH	-	5.3	5.33	5.12	5.23	4.97	5.12	5.44	4.76	5.66	4.99	5.03	5	5.04

Table C-1. Complete Analyses of flow through experimental data by ICP-OES and IC.